Acoustical Physics, Vol. 47, No. 5, 2001, pp. 503–506. Translated from Akusticheskiĭ Zhurnal, Vol. 47, No. 5, 2001, pp. 581–585.

Effect of the Variability of Hydrological Conditions on the Sound Field Interference Structure in a Shelf Region

A. A. Aredov, V. I. Neklyudov, and A. V. Furduev

Andreev Acoustics Institute, Russian Academy of Sciences, ul. Shvernika 4, Moscow, 117036 Russia

e-mail: bvp@akin.ru

Received December 18, 2000

Abstract—Computer simulations are performed to study the effect of internal waves and heating of the surface water layer on the behavior of the local spectral maximums of the interference sound field in coastal slope conditions, as applied to the operation of the self-sustained oscillator technique for monitoring the ocean. Results of testing the self-sustained oscillator technique on a 1-km-long propagation path are presented. *© 2001 MAIK "Nauka/Interperiodica".*

One of the promising new acoustic methods developed for monitoring the variability of the oceanic medium is the self-sustained oscillator technique, which was experimentally tested in full-scale conditions in the sea [1–4]. The main feature that determines the efficiency of this method and its capability for self-adaptation to the medium is that the medium to be monitored forms part of the self-sustained oscillator and serves as the feedback loop in it. In the self-sustained oscillator technique, a specific frequency, usually the one with the maximal amplitude, is selected from the whole spectrum of the space–time interference structure of the noise field and, at this frequency, the resonance amplification of the signal is performed. With fixed transmitting and receiving points, a change in the resonance frequency reveals some dynamic processes that occur both in the bulk of the medium and at its boundaries: internal waves, currents, cooling or heating of water, etc.

To predict the response of the self-sustained oscillator circuit, it is necessary to estimate the behavior of the local spectral maximums of the interference field. Computer simulations were performed to determine the type of motion of the interference maximum, namely, whether this maximum will move monotonically or in steps. In other words, whether the frequency of the self-sustained oscillator will vary smoothly with varying conditions in the water medium or not.

We estimated the effect of internal waves and the heating of the surface water layer on the interference spectrum for a broadband acoustic signal transmitted through a stationary propagation path on a measuring test bench. We used the ray program (developed at the Acoustics Institute), which allowed us to calculate the sound field at the reception point by combining the arriving rays with allowance for their phases. For the computer simulation, we used the parameters of the medium that corresponded to the region on the Black Sea shelf near Gelendzhik, where the experiments with the self-sustained oscillator technique [4] were carried out (at the base belonging to the southern branch of the Oceanology Institute, Russian Academy of Sciences).

The sound field was calculated for two propagation paths 1 and 5 km long with central frequencies of 6570 and 2500 Hz, respectively. The source and the receiver were set 1 m above the bottom. The sea depth linearly increased from 12 and 15 m near the source to 28 and 90 m near the receiver for the first and second paths, respectively.

Taking into account the bottom, we used a liquid halfspace model with the parameters typical of a sandy ground: a longitudinal wave velocity of 1.9 $(1 - i \times 0.01)$ km/s and a ground-to-water density ratio of 2.15. Figure 1 shows the sound velocity profiles for the summer season. The effect of an internal wave (a large-scale phenomenon compared to the path length) on the interference structure of the sound field was modeled by a change in the sound velocity in the discontinuity layer at depths from 7 to 50 m with a maximal deviation of 5 m/s from the mean profile (Fig. 1a). The heating of the surface was modeled as a smooth increase in the sound velocity at zero depth: by 2 and 10 m/s relative to the basic value for the distances 1 and 5 km, respectively (curves *1* and *2* in Fig. 1b). For the temperature range 15–20°C, such an increase (to the first approximation) corresponds to a change in the water temperature of 0.66 and 3.3°C, respectively.

The effect of the surface heating on the interference structure of the acoustic pressure spectrum at the receiver is represented in the form of three-dimensional

1063-7710/01/4705-0503$21.00

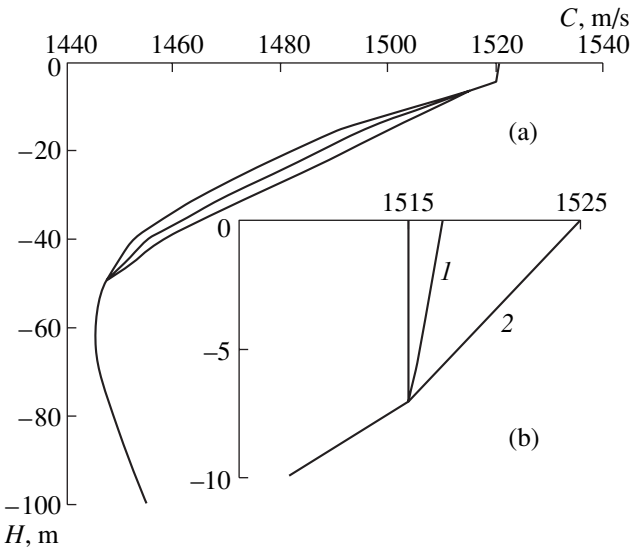

Fig. 1. Variation of the sound velocity profile in the calculations of the interference pattern: (a) in the case of the propagation of an internal wave and (b) in the case of the surface heating for the distances (*1*) 1 and (*2*) 5 km.

surfaces in Figs. 2a and 2b for the distances 1 and 5 km, respectively. The horizontal axes represent the frequency in hertz and the sound velocity in m/s, and the vertical axis represents the sound pressure in decibels relative to the maximal value. The data shown in Fig. 2a were obtained for the frequency range 6520–6620 Hz at a step of 5 Hz with the sound velocity at the surface increasing from 1515 to 1517 m/s at a step of 0.1 m/s. The data in Fig. 2b correspond to the frequencies 2450–2550 Hz taken at a step of 5 Hz and to the sound velocity at the surface increasing from 1515 to 1525 m/s at a step of 0.5 m/s. The choice of these parameters was dictated by the necessity to obtain smooth variations of the sound field interference structure.

In both figures, one can clearly distinguish the displacement of the interference maximums with varying surface temperature. The maximums move toward higher frequencies as the surface temperature increases. A smoother displacement of the interference structure for the 1-km distance (Fig. 2a) is explained by the smaller step of the sound velocity variation at the surface and, hence, a smaller temperature range.

For illustration, Fig. 2c shows the evolution of the spectrum for the 1-km distance in the form of a tint pattern in the coordinates representing frequency versus sound velocity at the surface. The tint intensity in the cells is proportional to the sound field level. The maximums of the interference pattern correspond to the almost parallel light strips. As the sound velocity at the surface varies, the maximums move smoothly with average rates of 15 Hz per 1 m/s of the sound velocity variation; when the temperature increases, the maximums move to higher frequencies. It should be noted that, for the interval of the ray departure angles ±40° selected for the calculations, we obtained up to 80 rays at the reception point with the focusing factor no less than 0.3 at the 1-km distance and up to 70 rays at the 5-km distance. Some of the rays propagated near the bottom without surface reflections, but most of the rays (~60%) were multiply reflected from the surface, which resulted in the aforementioned displacement of the signal spectrum with varying surface temperature.

The effect of an internal wave on the interference structure of the field is represented in Fig. 3 for the 5-km distance at frequencies near 2500 Hz in the form of a tint pattern. The interference was calculated for the case of the sound velocity variation in the discontinuity layer from minimal to maximal values within the internal wave period (Fig. 1a). We obtained a smooth displacement of the interference structure toward higher frequencies in the first half-period (an increase in the sound velocity) and toward lower frequencies in the second half-period (a decrease in the sound velocity) of the internal wave. From Fig. 3, it follows that the rate of motion of the interference maximums is ~5 Hz per 1 m/s of the velocity variation at a depth of 25 m.

On the whole, both the internal waves and the surface heating cause a monotonic displacement of the maximums of the sound field interference structure, which allows one to expect a distinct and unambiguous detection of this type of hydrophysical phenomena by the self-sustained oscillator technique.

The self-sustained oscillator method of monitoring the medium variability [4] was tested and studied for both short (~1 km) and long (~5 km) propagation paths. The operation of the regenerative circuit is characterized by the loop transmission factor *M*, which includes the response of the sound receiver, the trans-

mission factor of the amplifier channel with a filter, the automatic gain control, cables, the response of the source, and the frequency-dependent transmission factor of the propagation path. When $M < 1$, the circuit operates as a regenerator of the sea noise, and when $M \geq 1$, the circuit operates as a self-sustained oscillator whose frequency is determined by the spectral maximum of the ray (mode) interference at the reception point and by phase matching conditions.

The process of noise regeneration considerably increases the contrast in the variations of M and detects the maximum in the frequency dependence of M if the frequencies of the positive feedback are spaced at sufficiently small intervals, which occurs when the propagation path is sufficiently long. For example, on the 1-km path, the frequencies are spaced 1.5 Hz apart, and on the 5-km path, they are 0.3 Hz apart. Evidently, at $M = 1$, the circuit switches to the self-sustained oscillator mode, which corresponds to generation in the region of the ray interference maximum.

Figure 4 shows the results of the experiment for the path 1 km long. The left curve shows the regeneration-contrasted noise spectrum in a 2500-Hz frequency band with the maximum at a frequency of 6509 Hz. The observation of the time variation of the interference pattern, which presumably is quite informative for monitoring the path, makes the separation of rays and the detection of inhomogeneities possible; however, further methodical and theoretical development of this monitoring technique is necessary. We note that with the regenerative circuit, the position of the interference maximums on the frequency axis can be determined with high accuracy. The right plot in Fig. 4 illustrates this statement. This plot represents the same regeneration spectrum in a 37-Hz frequency band near the principal maximum of the interference pattern (about 6509 Hz) at $M = 0.9$. The experiment showed that the maximum can be traced with an accuracy of about 0.005 Hz at a frequency of 6500 Hz; i.e., with an accuracy of about 10^{-6}. Therefore, this method seems to be promising for the development of the interference tomography [5–8].

The experiment also revealed the interesting fact that the intervals between the positive feedback frequencies are constant. For the given example, all frequency separations between the peaks of the positive feedback proved to be equal to 1.56 Hz, which corresponds to the travel time of the dominant ray covering the whole path within 0.64 s. It should be noted that long-term observation of the spectra (like the spectrum presented in Fig. 4) showed that the frequency grid of positive feedback remains unchanged and equidistant for a long time, and the interference maximum is slowly displaced following changes in the propagation conditions along the path. Such a behavior of the regeneration spectrum in the region of the interference maximum suggests that self-sustained oscillations (when

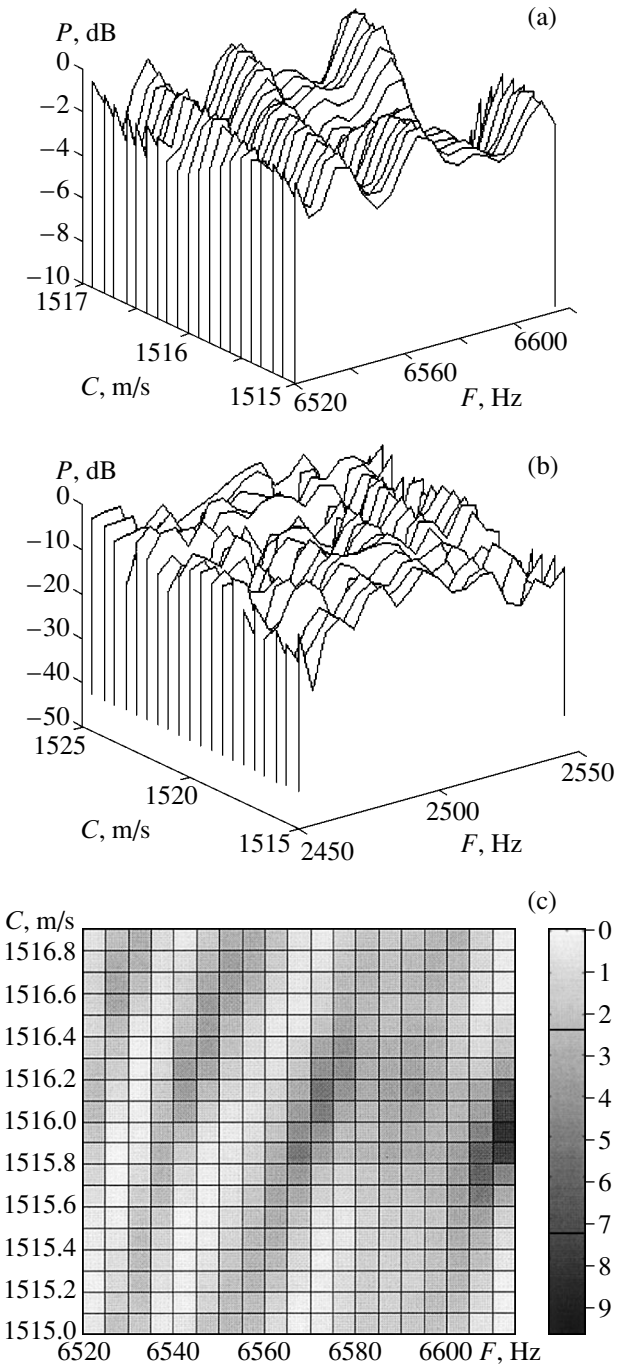

Fig. 2. Evolution of the pressure spectrum in the case of the surface heating: in the form of three-dimensional surfaces for the distances (a) 1 and (b) 5 km and (c) in the form of a tint pattern for the 1-km-long distance.

$M \geq 1$) occur at a frequency that is close to the interference maximum and determined by a set of rays with the phase condition governed by only one energy-dominant ray. A gain increase to $M \geq 1$ leads to the self-excitation of the oscillator. In this case, we obtain a monochromatic signal whose frequency responds to the changes in the propagation conditions on the path: a ship or a

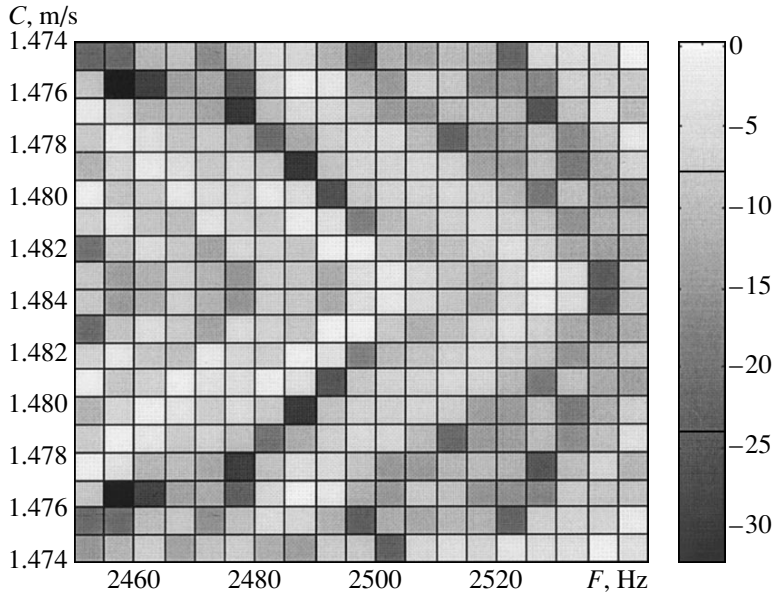

Fig. 3. Calculated evolution of the pressure spectrum in the case of sound velocity variation in the discontinuity layer within the internal wave period for the 5-km-long distance.

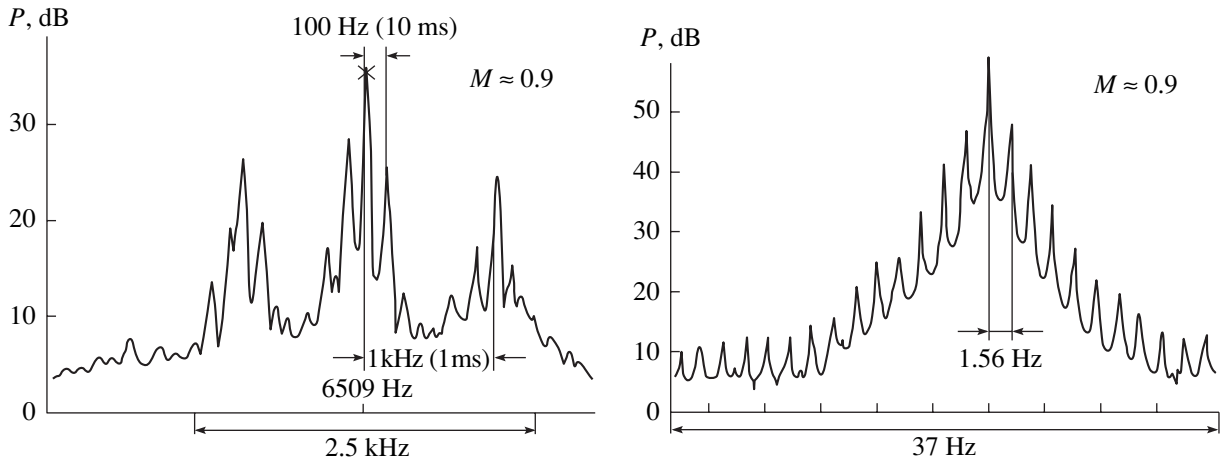

Fig. 4. Experimental testing of the regenerative circuit in the interference spectrum measuring mode.

fish shoal crossing the path, changes in the water temperature or currents, the passage of hydrographic inhomogeneities, etc.

ACKNOWLEDGMENTS

This work was supported by the Russian Foundation of Basic Research, project no. 00-05-64226.

REFERENCES

1. A. V. Furduev, in *Acoustics at the Threshold of the 21st Century* (Mosk. Gorn. Univ., Moscow, 1997), pp. 169–175.
2. A. V. Furduev and A. V. Agranovskiĭ, Patent of the Russian Federation No. 2134432 (10 August 1999).
3. A. V. Furduev, in *Acoustics of the Ocean* (GEOS, Moscow, 2000), pp. 25–29.
4. A. V. Furduev, Akust. Zh. **47**, 422 (2001) [Acoust. Phys. **47**, 361 (2001)].
5. V. V. Borodin and G. R. Minosyan, Akust. Zh. **41**, 34 (1995) [Acoust. Phys. **41**, 27 (1995)].
6. E. F. Orlov, in *Acoustics of the Ocean* (GEOS, Moscow, 2000), pp. 13–17.
7. P. Elisseeff, H. Schmidt, M. Jonson, *et al.*, J. Acoust. Soc. Am. **106** (1), 169 (1999).
8. O. C. Rodrígez and S. V. Jesús, J. Acoust. Soc. Am. **108**, 2816 (2000).

Translated by E. Golyamina

Acoustical Physics, Vol. 47, No. 5, 2001, pp. 507–510. Translated from Akusticheskiĭ Zhurnal, Vol. 47, No. 5, 2001, pp. 586–589.

A Theorem on the Representation of the Field of Forced Vibrations of a Composite Elastic System

Yu. I. Bobrovnitskiĭ

Blagonravov Institute of Mechanical Engineering, Russian Academy of Sciences, Malyĭ Khariton'evskiĭ per. 4, Moscow, 101990 Russia

e-mail: bobrovni@orc.ru

Received December 29, 2000

Abstract—A theorem on the representation of a vibration field of an elastic system comprising two subsystems is proved in a general form. It is assumed that the system is linear and the subsystems are rigidly connected and interact along a continuous surface *S*. According to the theorem, forced vibrations of the system can be represented in the form of the sum of two components, which are the solutions of two simpler auxiliary boundary-value problems. The first component is the field of vibrations of the isolated (separated or blocked along *S*) subsystems under the effect of preset external forces. The second component represents the forced vibrations of the junction of the subsystems, where the external forces are taken equal to zero and only the reaction forces obtained in solving the first auxiliary problem act at the surface *S*. The theorem is applied to the problem on the reflection and transmission of elastic waves through a junction of two media. It is demonstrated that the theorem utilization reduces the amount of calculations. Other applications are discussed. © *2001 MAIK "Nauka/Interperiodica".*

Forced vibrations of composite elastic systems are usually analyzed on the basis of the decomposition approach: a system is divided into several simpler subsystems and each subsystem is analyzed separately; then, partial solutions are combined into a general solution for the whole system. The SEA energy analysis [1], the methods of solving acoustoelastic problems [2, 3], the method of transfer functions [4], and many other techniques are grounded on this approach. The modification of this approach is also the replacement of a difficult boundary-value problem by a finite sequence of simpler problems. A classical example is the representation of a field by a sum of incident and scattered fields in the theory of wave diffraction [5]: the incident field is the solution to the problem on forced vibrations of a medium with preset sources but without a scatterer, and the scattered field is the solution to a problem on radiation by a scatterer into a medium without sources. Undoubtedly, each of these two auxiliary problems is simpler than the initial problem on forced vibrations of a medium with a scatterer. One of the extensions of this result of the diffraction theory to arbitrary linear oscillatory systems was given in our previous paper [6] without proof. Below, this extension is augmented and rigorously proved in the form of a theorem on the representation of a field of forced vibrations of a system consisting of two subsystems that are connected to each other along the surface *S*. The theorem states that the solution of the problem of forced vibrations of a system by external forces can be represented in the form of a sum of two components: the first component is the solution to the problem on forced vibrations of the isolated subsystems (separated or with a blocked contact surface *S*), and the second component represents the forced vibrations of the whole system under the action of simpler external forces (more precisely, the reaction forces at *S*, which were obtained in solving the first problem). The theorem is illustrated using an example of the elastic wave reflection and transmission through the junction of two media. It is demonstrated that the application of the theorem reduces the amount of calculations. Applications to other problems are discussed.

Let us consider an arbitrary oscillatory system, which can be presented as a combination of two subsystems *a* and *b* connected along a continuous surface *S* (see Fig. 1). We write down the oscillation equations and the boundary conditions for the system in the form

$$\begin{gathered} L_a u = \varphi_a \text{ in the region } V_a, \\ M_a u = \psi_a \text{ at the surface part } S_a, \\ L_b v = \varphi_b \text{ in the region } V_b, \\ M_b v = \psi_b \text{ at the surface part } S_b, \\ u = v, \quad f + g = 0 \text{ at the contact surface } S. \end{gathered} \tag{1}$$

Here, u and v are the displacement vectors of the subsystems *a* and *b*; $f = l_a u$ and $g = l_b v$ are the densities of the internal forces (stresses) acting upon the subsystems at the surface *S*; $L_{a,b}$, $M_{a,b}$, and $l_{a,b}$ are differential operators; and $\varphi_{a,b}$ and $\psi_{a,b}$ are the densities of the external bulk and surface forces. An inhomoge-

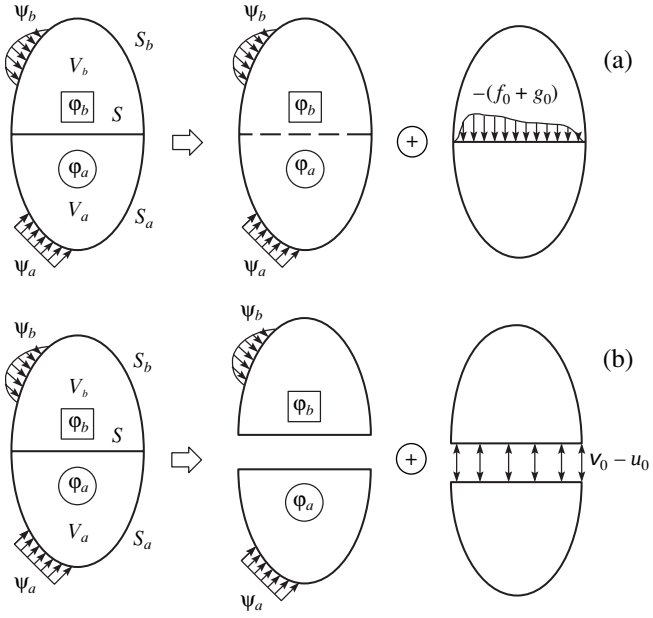

Fig. 1. The field of forced vibrations of a composite system is represented by a sum of two fields: (a) the field of forced vibrations of the subsystems with a stationary contact surface *S* and the field of the system vibrations under the action of force excitation at *S*; (b) the field of forced vibrations of separated subsystems and the vibration field of the system with a kinematic excitation.

neous boundary-value problem of mathematical physics is represented by Eqs. (1). This problem describes forced vibrations of all (known to the author) linear media and structures.

We seek the solution to problem (1) in the form of a sum of solutions of two simpler auxiliary problems:

$$u = u_0 + u_1, \quad v = v_0 + v_1. \tag{2}$$

Let the first auxiliary problem describe the forced vibrations u_0 and v_0 of isolated subsystems. The two field representations given below differ in the boundary conditions at the contact surface *S* of the first auxiliary problem: representation 1 corresponds to the blocked surface *S* and representation 2, to the surface *S* free of external loading. The second auxiliary problem for the determination of the terms u_1 and v_1 is formulated after the substitution of the solution given by Eqs. (2) into Eqs. (1). As it is shown below, the second auxiliary problems of these two representations also differ only in the boundary conditions at *S*. We treat each representation separately.

Representation 1. We assume that the displacements of both subsystems at the contact surface in the first auxiliary problem are equal to zero. This means that the functions u_0 and v_0 are solutions to the following two independent boundary-value problems for the subsystems *a* and *b*:

$$\begin{aligned} &L_a u_0 = \varphi_a \text{ in } V_a, \quad M_a u_0 = \psi_a \text{ at } S_a, \quad u_0 = 0 \text{ at } S; \\ &L_b v_0 = \varphi_b \text{ in } V_b, \quad M_b v_0 = \psi_b \text{ at } S_b, \quad v_0 = 0 \text{ at } S. \end{aligned} \tag{3}$$

In this case, the reaction forces acting upon both subsystems from the side of the stationary boundary *S* are equal to

$$f_0 = l_a u_0, \quad g_0 = l_b v_0. \tag{4}$$

Substituting Eqs. (2) into Eqs. (1) and taking into account Eqs. (3), we obtain the following equations for the determination of the components u_1 and v_1:

$$\begin{aligned} L_a u_1 &= 0 \text{ in } V_a, \quad M_a u_1 = 0 \text{ at } S_a, \\ L_b v_1 &= 0 \text{ in } V_b, \quad M_b v_1 = 0 \text{ at } S_b, \\ u_1 &= v_1, \quad l_a u_1 + l_b v_1 = -(f_0 + g_0) \text{ at } S. \end{aligned} \tag{5}$$

As one can see from these equations, the second auxiliary problem represents vibrations of the whole system with switched-off sources ($\varphi_{a,b} = \psi_{a,b} = 0$) under the action of the reaction forces (Eqs. (4)) applied to the contact surface *S*. Representation 1 is shown schematically in Fig. 1a.

Representation 2. Let the first terms in Eq. (2) be the fields in the subsystems separated along *S*. In this case, the first auxiliary problem has the form

$$\begin{aligned} &L_a u_0 = \varphi_a \text{ in } V_a, \ M_a u_0 = \psi_a \text{ at } S_a, \ l_a u_0 = 0 \text{ at } S; \\ &L_b v_0 = \varphi_b \text{ in } V_b, \ M_b v_0 = \psi_b \text{ at } S_b, \ l_b v_0 = 0 \text{ at } S. \end{aligned} \tag{6}$$

Substituting Eqs. (2) into the initial Eqs. (1) and taking into account Eqs (6), we obtain the following equations and boundary conditions for the second auxiliary problem:

$$\begin{aligned} L_a u_1 &= 0 \text{ in } V_a, \quad M_a u_1 = 0 \text{ at } S_a, \\ L_b v_1 &= 0 \text{ in } V_b, \quad M_b v_1 = 0 \text{ at } S_b, \\ u_1 - v_1 &= v_0 - u_0, \quad l_a u_1 + l_b v_1 = 0 \text{ at } S. \end{aligned} \tag{7}$$

The physical meaning of Eqs. (7) is as follows. They describe vibrations of the whole system without sources ($\varphi_{a,b} = \psi_{a,b} = 0$) under the action of a special load at the contact surface *S*. The load consists of two equal and opposite forces $l_a u_1$ and $l_b v_1$, which are applied to separate subsystems and have values such that the relative oscillatory displacement between the subsystems $u_1 - v_1$ is equal to the fixed value of $v_0 - u_0$ determined by the solution of the first auxiliary problem (Eqs. (6)). In practice, such an load can be realized, for example, by using piezoceramic plates inserted between the subsystems. Thus, the second auxiliary problem in representation 2 describes forced vibrations of the system without initial sources but with

a kinematic excitation at the contact surface S (see the schematic diagram in Fig. 1b).

As an illustration, let us demonstrate the results of the theorem application to some well-known problems of wave reflection. In the simplest case of reflection of plane waves from the plane boundary of two semi-infinite homogeneous liquid media with impedances Z_1 and Z_2, the solution is given by the Fresnel formulas for the reflection coefficient R and the coefficient of transmission T from the first medium to the second one:

$$R = (Z_2 - Z_1)/(Z_2 + Z_1), \quad T = 2Z_2/(Z_2 + Z_1). \quad (8)$$

According to the theorem given above, these coefficients can be represented as the sum of two components. Here, representation 1 (see Eqs. (2)–(5)) has the form

$$R = 1 - 2Z_1/(Z_2 + Z_1), \quad T = 0 + 2Z_2/(Z_2 + Z_1), \quad (9)$$

where the first terms (1 and 0, respectively) correspond to the incidence of a plane pressure wave with amplitude p_i on a stationary boundary and the second terms describe the vibrations of two media (without the incident wave) under the action of an external force distributed over the boundary with an amplitude $-2p_i$.

Representation 2 (see Eqs. (2), (6), and (7)) is written in the form

$$R = -1 + 2Z_2/(Z_2 + Z_1), \quad T = 0 + 2Z_2/(Z_2 + Z_1), \quad (10)$$

where the first terms (–1 and 0) correspond to the incidence of a plane wave on an absolutely soft boundary (the media are separated) and the second terms represent the media motion (without the incident wave) under the action of a distributed source located between the media; this source provides equal pressure at the boundaries of both media and maintains a fixed relative velocity with the amplitude $2p_i/Z_1$.

Here, the representations given by Eqs. (9) and (10) do not have any advantages over the Fresnel formulas (Eqs. (8)) in their structure or in the amount of calculation because of the simplicity of this example. The cases of more complex reflection problems are quite different. For example, let us consider the reflection and transmission of waves in the junction of two media or waveguides, where N normal modes can exist. The problem is to determine two $N \times N$ matrices of reflection and transmission coefficients. A direct solution of this problem leads to a system of $2N$ linear algebraic equations. At the same time, the application of the theorem proved above reduces the system to two systems of the Nth order. Since the amount of calculation necessary to solve a system is proportional to the cube of its order [7], the utilization of Eqs. (2) can provide a fourfold economy in calculation. This fact was verified in solving a problem on the wave reflection in a corner junction of two thin semiinfinite homogeneous straight rods (Fig. 2). In the case of rod vibrations in the corner plane, the number of normal modes is $N = 3$ (one longitudinal wave and two flexural waves, one of which is propagating and another is evanescent). A direct solution by sewing together the fields in the corner leads to a system of six algebraic equations [8, 9], whereas the utilization of representation 1 given in this paper (see Fig. 2) leads to a more than fourfold reduction in the amount of calculation, because longitudinal and flexural waves in separate rods are independent and the analytical solution of auxiliary problems is elementary in this case.

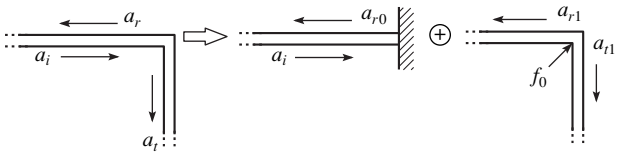

Fig. 2. The problem on the reflection and transmission of longitudinal and flexural waves in a corner junction of rods is equivalent to two auxiliary problems: the reflection from a stationary corner and forced vibrations under the action of a force concentrated in the corner.

In conclusion, we note that the most important applications of the theorem formulated in this paper should be expected in the case of solving the problems on forced vibrations of composite elastic systems with complex or unknown sources. A working machine can be an example: as it is impossible yet to describe the sources of vibrations inside a machine, the theorem (representation 2) provides an opportunity to move the sources to the machine support while staying within the framework of exact consideration (see also [10]). Another example of a problem of this type is sound transmission into an elastic shell from a propeller operating in a flow [2, 3]. The application of representation 1 provides an opportunity to separate the calculation of the external acoustic field of the propeller and the calculation of the shell vibrations together with the field of the inner acoustic volume and to simplify in such a way to the solution problem on the whole.

ACKNOWLEDGMENTS

This work was supported by the Russian Foundation for Basic Research, project no. 00-01-00577a.

REFERENCES

1. *Proceedings of IUTAM Symposium on Statistical Energy Analysis*, Ed. by F. J. Fahy and W. G. Price (Kluwer Academic, Dordrecht, 1999).
2. J. F. Wilby, J. Sound Vibr. **190**, 545 (1996).

3. J. S. Mixson and C. A. Powell, J. Aircr. **22**, 931 (1985).
4. T. C. Lim and J. Li, J. Sound Vibr. **231**, 1135 (2000).
5. M. A. Isakovich, *General Acoustics* (Nauka, Moscow, 1973).
6. Yu. I. Bobrovnitskiĭ, Dokl. Akad. Nauk SSSR **308** (5), 1061 (1989) [Sov. Phys. Dokl. **34** (10), 894 (1989)].
7. K. S. Godunov, A. G. Antonov, O. P. Kirilyuk, and V. I. Kostin, *Guaranteed Accuracy of Solving Systems of Linear Equations in Euclidean Spaces* (Nauka, Novosibirsk, 1988).
8. I. I. Artobolevskiĭ, Yu. I. Bobrovnitskiĭ, and M. D. Genkin, *Introduction to Acoustic Dynamics of Machines* (Nauka, Moscow, 1979).
9. B. M. Gibbs and S. D. Tattersall, Trans. ASME, J. Vib. Acoust. Stress **109** (4), 348 (1987).
10. V. I. Popkov, *Vibroacoustic Diagnostics and the Reduction of the Vibration Activity of Ship Mechanisms* (Sudostroenie, Leningrad, 1974).

Translated by M. Lyamshev

Acoustical Physics, Vol. 47, No. 5, 2001, pp. 511–516. Translated from Akusticheskiĭ Zhurnal, Vol. 47, No. 5, 2001, pp. 590–596.

Effect of the Sediment Layer on the Diffraction Focusing of an Acoustic Field in a Shallow Sea

E. L. Borodina and Yu. V. Petukhov

Institute of Applied Physics, Russian Academy of Sciences,
ul. Ul'yanova 46, Nizhni Novgorod, 603600 Russia
e-mail: petukhov@hydro.appl.sci-nnov.ru

Received May 10, 2000

Abstract—Features characterizing the formation of the spatial (in depth and horizontal distance) interference structure of an acoustic field generated by a point tone source or a vertically distributed tone source in a shallow-water oceanic waveguide are considered. The waveguide is modeled by a three-layered fluid medium. The main object of the study is the effect of the acoustic parameters of the sediment layer on the formation and structure of the spatial regions within which the diffraction focusing of the acoustic field takes place. © *2001 MAIK "Nauka/Interperiodica".*

The propagation of waves of different origin in the waveguide media can be accompanied by the diffraction focusing of the corresponding fields [1–12]. The name of this phenomenon was chosen by analogy with the formation of the diffraction images of periodic structures in optics [13–16]. The main features of diffraction focusing of acoustic fields in oceanic waveguides were considered in a number of publications [1–4, 8–12]. It was found (see [8–12]) that a rearrangement of the interference structure of the acoustic field occurs along an oceanic waveguide. This rearrangement is characterized by the minimal $R_{\min}$ and maximal $R_{\max}$ spatial periods and manifests itself as a partial repetition of the characteristic features observed for $0 \le r \ll R_{\min}$ in the spatial (in the depth z and in the horizontal distance r) distribution of the field intensity $J(r, z)$. Such a rearrangement of the interference structure leads to diffraction focusing of the acoustic field in the intervals of horizontal distances [8–12]

$$mR_{\min} \le r \le mR_{\max} \quad (m = 1, 2\ldots). \tag{1}$$

This phenomenon is the more pronounced the smaller the quantity

$$\Delta R = R_{\max} - R_{\min}. \tag{2}$$

Here,

$$\begin{aligned} R_{\min} &= \min\{R_g(l, l+1; l+1, l+2)\}, \\ R_{\max} &= \max\{R_g(l, l+1; l+1, l+2)\}, \end{aligned} \tag{3}$$

and the quantity

$$\begin{aligned} &R_g(l, l+1; l+1, l+2) \\ &= R_{l, l+1}R_{l+1, l+2}/|R_{l, l+1} - R_{l+1, l+2}|, \end{aligned} \tag{4}$$

where l is the mode number, corresponds to the period of the interference structure rearrangement of the field produced by adjacent pairs of modes with the corresponding interference periods

$$\begin{aligned} R_{l, l+1} &= 2\pi/(k_l - k_{l+1}), \\ R_{l+1, l+2} &= 2\pi/(k_{l+1} - k_{l+2}), \end{aligned} \tag{5}$$

and frequency dependences of the horizontal wave numbers k_l.

However, it should be noted that even in the case of a considerable difference between the values of $R_{\min}$ and $R_{\max}$ (Eqs. (3)) with the ratio $\Delta R/R_{\min} \approx 1$, diffraction focusing can manifest itself for certain groups of modes with relatively minimal variations of $R_g(l, l+1; l+1, l+2)$ (Eq. (4)) [10, 11]. Naturally, the greater the number of modes $L_m = l_b - l_s$ in each of these groups $l_s \le l \le l_b$ and the smaller the quantity $\Delta R_g = R_b - R_s$, the more pronounced the diffraction focusing of the acoustic field in the corresponding intervals of horizontal distances

$$mR_s \le r \le mR_b. \tag{6}$$

Here,

$$\begin{aligned} R_s &= \min\{R_g(l, l+1; l+1, l+2)\}, \\ R_b &= \max\{R_g(l, l+1; l+1, l+2)\}, \end{aligned} \quad (l_s \le l \le l_b) \tag{7}$$

and l_s and l_b are the boundary values of the mode numbers in a given group of modes.

For specific types of oceanic waveguides, the effect of the sound velocity stratification in the water column, as well as the effects of the radiation frequency and the source depth, on the spatial interference structure of the acoustic fields in the diffraction focusing zones was studied earlier [8–12]. However, the effect of the sediment layer on the formation of the diffraction focusing zones of acoustic fields was not investigated. The study

1063-7710/01/4705-0511$21.00

of this effect is fundamentally important for shallow-water oceanic waveguides, and it is the subject of this paper.

To solve the problem of interest, we use a relatively simple model of a shallow-water waveguide: an isovelocity water layer characterized by the depth H, the sound velocity C, and the density of the medium ρ overlying a homogeneous fluid sediment layer with the depth h, the sound velocity c_s, and the density ρ_s. The sediment layer in turn overlies a homogeneous fluid bottom with the corresponding acoustic characteristics c_b and ρ_b. We also assume that a point source generating a tone signal with the frequency ω is positioned in the water layer at the depth z_s. Then, in such a waveguide, the distribution of the sound field intensity in depth and horizontal distance in the water layer, $J_0(r, z) = rJ(r, z)$, will be described by the expression (the distribution is normalized to the geometric spread) [17]

$$J_0(r, z) = \left|\sum_{l=1}^{L} A_l(z_s, z, \omega)e^{ikr/u_l}\right|^2, \tag{8}$$

where $A_l(z_s, z, \omega)$ is the amplitude of the lth mode, $u_l = k/k_l$ is the normalized phase velocity of this mode, and $k = \omega/c$. Using the relationships presented in [17], we obtain the following expression for the lth mode amplitude:

$$A_l = 2\sqrt{2\pi k u_l}\frac{B_1(u_l)}{B_2(u_l)}\sin(kz_s\nu)\sin(kz\nu);$$

$$B_1(u_l) = \Pi_s\nu_s^2[\Pi\nu_b\cos(kh\nu_s) - \Pi_s\nu_s\sin(kh\nu_s)],$$

$$B_2(u_l) = \frac{\Pi_s}{2}\sin(2kh\nu)$$

$$\times\left[\Pi\cos(kh\nu_s)\left(\nu\nu_b - \nu_s^2\left(\frac{\nu}{\nu_b} + \frac{\nu_b}{\nu}\right)\right)\right.$$

$$\left. + \Pi_s\nu\nu_s\sin(kh\nu_s)\left(\frac{\nu_s^2}{\nu^2} - 2\right)\right] + \Pi_s kH\frac{\nu_s^2}{u_l} \tag{9}$$

$$\times\left[1 + \Pi_s\frac{h}{H}\left(\sin^2(kH\nu) + \frac{\nu^2}{\Pi_s^2\nu_s^2}\cos^2(kH\nu)\right)\right]$$

$$\times[\Pi\nu_b\cos(kh\nu_s) - \Pi_s\nu_s\sin(kh\nu_s)]$$

$$-\frac{\nu^2}{\nu_b}\cos^2(kH\nu)[\Pi\nu_s\sin(kh\nu_s) - \Pi_s\nu_b\cos(kh\nu_s)].$$

Here,

$$\Pi_s = \rho/\rho_s, \quad \Pi = \rho/\rho_b, \quad \nu = \sqrt{u_l^2 - 1}/u_l,$$
$$\nu_s = \sqrt{1 - b^2u_l^2}/u_l, \quad \nu_b = \sqrt{1 - a^2u_l^2}/u_l, \tag{10}$$
$$b = c/c_s, \quad a = c/c_b.$$

The normalized phase velocities of modes are determined from the dispersion equation characteristic of the given waveguide [17]

$$\tan(kH\nu)[\Pi_b\nu_b - \nu_s\tan(kh\nu_s)] = -\frac{\nu}{\Pi_s\nu_s}[\nu_s + \Pi_b\nu_b\tan(kh\nu_s)], \tag{11}$$

where

$$\Pi_b = \Pi/\Pi_s = \rho_s/\rho_b. \tag{12}$$

In the numerical calculations, as in [12], we used the following parameters of the sound radiation, the water layer, and the bottom: $f = \omega/2\pi = 300$ Hz, $z_s = 4.5$ m, $H = 300$ m, $c = 1.45$ km/s, $\rho = 10^3$ kg/m^3, $c_b = 1.7$ km/s, and $\rho_b = 1.6\rho$. In addition, we assumed that the sediment layer thickness was $h = 0.1H$, the density of this layer was $\rho_s = 1.4\rho$, and the sound velocity varied within natural limits $c \le c_s \le c_b$.

We numerically calculated the dependence of the quantity $|A_l(z_s, z, \omega)|$ determined by Eq. (9) on l at $z = z_s$ and the dependence of R_g (given by Eq. (4)) on l. The results of these calculations show that a decrease in the sound velocity in the sediment layer does not affect the dependence of the mode amplitude on the mode number (see [18]); in contrast, the dependence of the rearrangement period on the mode number exhibits not only quantitative but also fundamental qualitative changes in this case (Fig. 1). As c_s decreases (see Fig. 1), the range of values of R_g first slightly narrows for the low-number modes $1 \le l < 30$, which are responsible for the formation of the diffraction focusing zones [12]. Then, beginning from a certain value of c_s, the range of values of R_g for these modes noticeably widens with a simultaneous increase in R_g at $l = 1$. In addition, it should be noted that, at $c_s = c_b$, the dependence of R_g on l practically coincides with the corresponding dependence obtained in the absence of the sediment layer (at $h = 0$), whereas at $c_s = c$, it fundamentally differs from the latter dependence: it exhibits pronounced oscillations also for the lower mode numbers $1 \le l < 30$ (see Fig. 1).

From the behavior of the dependence of R_g on l described above, it follows that when the sound velocity in the sediment layer decreases to a certain value $c_s = c_0$, one should expect a slight narrowing of the spatial regions of the diffraction focusing while the diffraction focusing itself should be slightly enhanced. However, a further decrease in c_s should lead to a considerable widening and weakening of the zones of diffraction focusing down to their total disappearance. These conclusions are confirmed by the results of the numerical

calculations performed for the spatial distribution of the normalized intensity of the acoustic field, $J_0(r, z)$ (Eq. (8)). The calculated distributions are represented in Fig. 2 in the form of brightness pictures with a dynamic range of 18 dB. From the numerical simulation of the spatial distributions $J_0(r, z)$ in the waveguide under study, we also approximately determined the characteristic optimal value of the sound velocity in the sediment layer $c_s = c_0 \approx 1.55$ km/s, which corresponds to the formation of the diffraction focusing zones with maximal contrast (see Fig. 2).

The analysis of the results of numerical simulations (see Figs. 1, 2) suggests that as the difference in the sound velocities in the water and sediment layers decreases, the formation of the zones of diffraction focusing of the acoustic field is more and more strongly affected by the density stratification of the of the medium in the oceanic waveguide. Naturally, the value of c_0 will also depend on the density stratification of the medium in the waveguide, and to a greater extent it will depend on the density drop at the upper boundary of the sediment layer σ than on the density drop at its lower boundary δ:

$$\sigma = \frac{1}{\Pi_s} - 1, \quad \delta = \frac{1}{\Pi_b} - 1. \tag{13}$$

When $c_s \longrightarrow c$, the predominance of the effect of the parameter σ on the spatial structure of the diffraction focusing zones over the effect of δ should also manifest itself in the corresponding effects of these parameters on the phase velocities of the modes. Therefore, to determine the sensitivity of the quantity u_l to the variations in the parameters σ and δ, we analytically analyze the possible behavior of the solutions of the dispersion equation (11) for the particular cases $c_s = c$ and $c_s = c_b$.

At $c_s = c$, when $b = 1$ and $\nu = \nu_s$, Eq. (11) can be reduced to the form

$$P_1(u_l) = \sigma F_1(u_l), \tag{14}$$

where

$$\begin{aligned} P_1(u_l) &= \tan[k(H+h)\nu] + \frac{\nu}{\Pi\nu_b}, \\ F_1(u_l) &= \frac{1 + \dfrac{\nu(1+\delta)}{\nu_b}\tan(kH\nu)}{\tan(kH\nu)\tan(kh\nu) - 1}. \end{aligned} \tag{15}$$

From Eq. (14), it follows that as the density drop at the upper boundary of the sediment layer decreases ($\sigma \longrightarrow 0$), this equation tends to the dispersion equation $P_1(u_l) = 0$ characteristic of a Pekeris waveguide with the effective depth of the water layer being equal to $H + h$. However, even for small values of the parameter $\sigma \ll 1$ and for sufficiently high radiation frequencies $kh \gg 1$, the right-hand side of Eq. (14) will always differ from zero by a quantity of the same order of magnitude as σ. In fact, for modes with relatively low numbers, we have $u_l \longrightarrow 1$ for $kH \longrightarrow \infty$ and $l \longrightarrow 1$. Then, from Eq. (15), we obtain $F_1(u_l) \approx -1$. The latter means that at $c_s = c$, the effect of the parameter σ on the dependence of k_l on l and, hence, on the dependences $R_{l,l+1}(l)$ and $R_g(l)$ predominates over the effect of the parameter δ for the modes of relatively low numbers. Since it is these modes that determine the formation of the diffraction focusing zones, the spatial structure of the latter is also governed by a density drop at the upper boundary of the sediment layer.

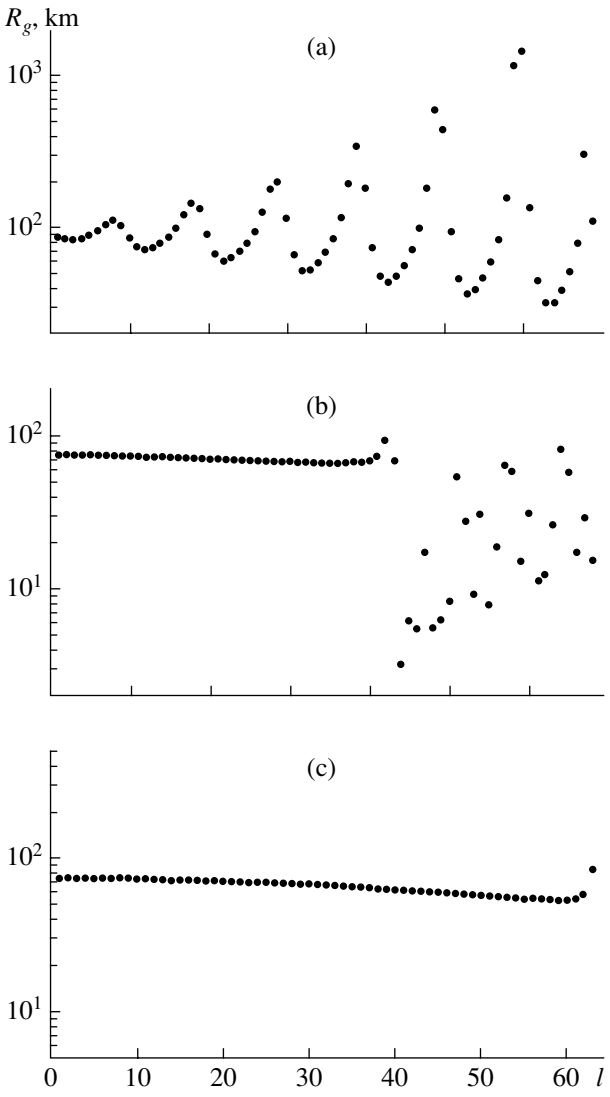

Fig. 1. Dependences of the spatial period R_g (Eq. (4)) on the mode number l for c_s = (a) 1.45, (b) 1.55, and (c) 1.7 km/s.

In the other limiting case, $c_s = c_b$, Eq. (11) at $b = a$ and $\nu_s = \nu_b$ is reduced to the form

$$P_2(u_l) = \delta F_2(u_l), \tag{16}$$

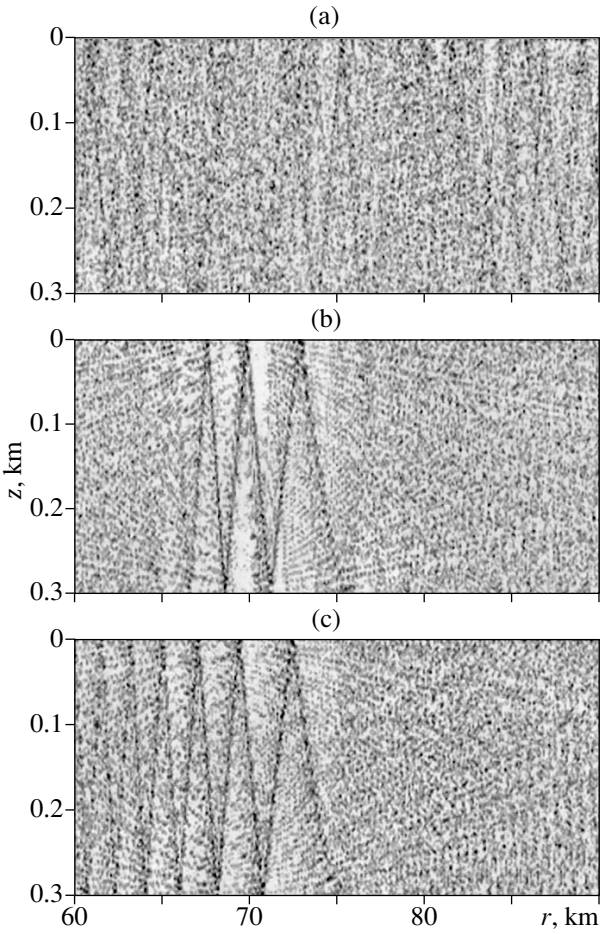

Fig. 2. Spatial dependences of the normalized intensity $J_0(r, z)$ for a point source at $z_s = 4.5$ m: c_s = (a) 1.45, (b) 1.55, and (c) 1.7 km/s.

where

$$P_2(u_l) = \tan(kHv) + \frac{v}{\Pi v_b},$$
$$F_2(u_l) = \frac{v}{\Pi v_b}\frac{\tanh(khv_b) - 1}{1 + (1+\sigma)\tanh(khv_b)} - \tan(kHv). \quad (17)$$

Naturally, as the density drop at the lower boundary of the sediment layer decreases ($\delta \longrightarrow 0$), Eq. (16) tends to the dispersion equation for a Pekeris waveguide $P_2(u_l) = 0$ with the depth H of the water layer.

From Eqs. (16) and (17), it follows that in the same high-frequency range $kh \gg 1$ for modes with relatively low numbers, we have $F_2(u_l) \longrightarrow 0$ for $kH \longrightarrow \infty$, because $u_l \longrightarrow 1$ when $kH \longrightarrow \infty$ and $l \longrightarrow 1$. Therefore, in the case under consideration, $c_s = c_b$, the effect of the variations of the parameter δ on the dependences $k_l(l)$, $R_{l,l+1}(l)$, and $R_g(l)$ for the low-number modes will be weaker than the effect of the variations of σ on the corresponding dependences in the case $c_s = c$.

The effect of the parameters σ and δ on the formation of the zones of the diffraction focusing of an acoustic field can be illustrated by using the source of radiation in the form of a continuous vertical antenna with aperture D and with the center at the depth $z_0 = H/2$. Then, assuming that the amplitude distribution of the excitation coefficient over the antenna aperture is constant and the corresponding phase distribution is absent, we obtain an expression for the mode amplitudes in the form of Eq. (9) with the factor $\sin(kz_s v)$ replaced by the quantity S_l:

$$S_l = \frac{1}{Dkv} \times \left\{\cos\left[kz_0 v\left(1 - \frac{D}{2z_0}\right)\right] - \cos\left[kz_0 v\left(1 + \frac{D}{2z_0}\right)\right]\right\}. \quad (18)$$

Naturally, in a free space, the direction of the major maximum of such an antenna should coincide with the direction of the r axis corresponding to the angle $\Theta = 0$. The width of this maximum can be estimated as $\Delta\Theta \approx 2\pi/kD \ll 1$.

The advantage of a vertical transmitting antenna over a point source in the waveguide under study consists in that it allows one to reduce the amplitudes of modes of relatively high numbers, which mask the effect of the diffraction focusing of the acoustic field [12]. For this purpose, it is necessary that the range of variation of the grazing angles $\Delta\Theta_l$ of the low-number modes, which determine the spatial structure of the diffraction focusing zones, be limited by the corresponding value of the quantity $\Delta\Theta$. The approximate equality expressing this condition,

$$\Delta\Theta_l \approx \Delta\Theta, \quad (19)$$

where

$$\Delta\Theta = 2\arcsin\{\sqrt{1 - (k_l/k)^2}\}, \quad (20)$$

makes it possible, at fixed values of l, to determine the optimal aperture size $D = D_{\text{opt}}$ for which the diffraction focusing of the acoustic field should be most pronounced.

For example, in the case of a homogeneous waveguide with a perfectly rigid bottom, from Eq. (19) we obtain an illustrative relationship for the antenna aperture

$$D_{\text{opt}} \approx \frac{H}{l - 1/2}, \quad (21)$$

which does not depend on the radiation frequency when $2\pi/kD_{\text{opt}} \ll 1$.

The approximate equality (21) also allows one to select an antenna aperture fairly close to the optimal one, D_{opt}, for the waveguide considered in this paper. This fact is quite important, because, when $D > D_{\text{opt}}$, the amplitudes of the low-number modes will noticeably decrease and, when $D < D_{\text{opt}}$, the modes with relatively

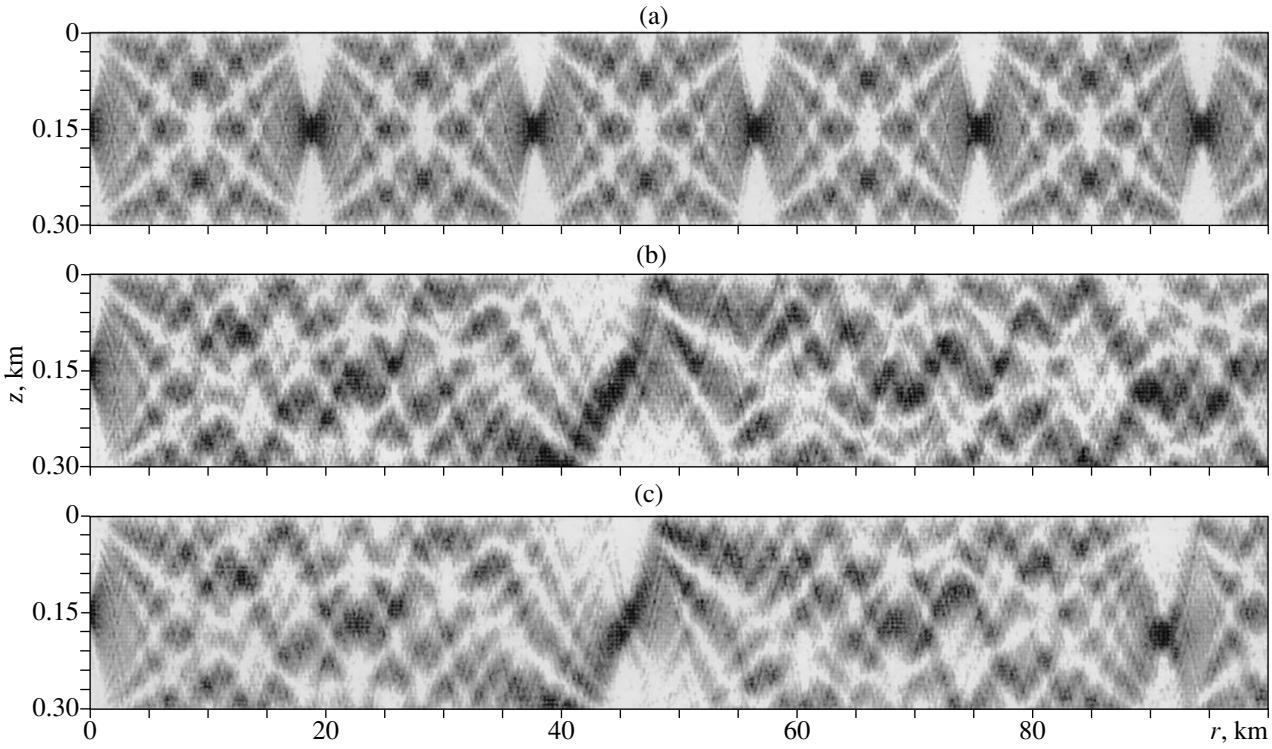

Fig. 3. Spatial dependences of the normalized intensity $J_0(r, z)$ for a vertical antenna at $z_0 = 150$ m: c_s = (a) 1.7 and (b, c) 1.45 km/s; ρ_s = (a, b) 1.4ρ and (c) 1.1ρ.

high numbers will make a substantial contribution to the total field, which will result in the suppression or masking of the effect of diffraction focusing, respectively.

With allowance for the aforesaid, the spatial distribution of the normalized intensity $J_0(r, z)$ of the acoustic field produced by a vertical transmitting antenna was numerically calculated with parameter values $2\pi/kD = 0.1$ and $z_0 = H/2$ that made it possible to illustrate more clearly both the diffraction focusing in the $z - r$ plane and its dependence on the density stratification of the medium in the oceanic waveguide. Here, it should be noted that the depth of the antenna center $z_0 = H/2$ was selected so that the diffraction could manifest itself with the spatial period $R = \frac{1}{4} R_{\max} \approx \frac{k}{2\pi} H^2$. Such a situation is characteristic of the case $c_s = c_b$ = 1.7 km/s (see Fig. 3a). In this case, the numerical calculations show (see also [18]) that the typical distribution $J_0(r, z)$ presented in Fig. 3a is practically independent of the density variations in the sediment layer on the condition that $\rho \le \rho_s \le \rho_b$. If the antenna is positioned closer to the surface ($z_0 < H/2$) or to the bottom ($z_0 > H/2$) of the oceanic waveguide, the diffraction focusing manifests itself clearly only with the maximal spatial period $R = R_{\max} \approx \frac{2k}{\pi} H^2$.

The spatial distributions $J_0(r, z)$ shown in Figs. 3b and 3c in the form of brightness pictures with a dynamic range of 18 dB confirm that a considerable effect of the density stratification of the medium on the formation of the diffraction focusing zones is observed only in the case of a very small difference between the sound velocities in the water and sediment layers of the oceanic waveguide.

In addition, the results shown in Fig. 3 offer another quite important conclusion. Since a vertical transmitting antenna allows one to make the diffraction focusing more prominent, the aforementioned features of this phenomenon can be used intentionally for focusing an acoustic radiation in an oceanic waveguide. For example, the positions of the diffraction focusing zones can be controlled along the horizontal direction by varying the radiation frequency and in the vertical direction by varying the antenna depth. Such an approach to focusing acoustic radiation in a shallow-water oceanic waveguide can in some conditions be preferable to the approach based on the phase conjugation method [19–23], which requires the use of an extended aperture with fairly complex amplitude and phase distributions of the excitation coefficients.

In closing, we briefly formulate the main results of this study.

It was shown that with a decrease in the difference between the sound velocities in the water and sediment isovelocity layers of an oceanic waveguide, the formation of the zones of diffraction focusing of the acoustic field is more and more strongly affected by the magni-

tude of the density drop between the corresponding media. Therefore, in certain conditions specified above, practically a complete spread of the diffraction focusing zones is possible in a shallow-water oceanic waveguide.

ACKNOWLEDGMENTS

This work was supported by the Russian Foundation for Basic Research, project nos. 98-05-64652 and 00-05-64604.

REFERENCES

1. A. B. Wood, J. Acoust. Soc. Am. **31**, 1213 (1959).
2. A. B. Wood, in *Underwater Acoustics*, Ed. by V. M. Alberts (Plenum, New York, 1963; Mir, Moscow, 1965).
3. D. E. Weston, J. Acoust. Soc. Am. **32**, 647 (1960).
4. D. E. Weston, J. Acoust. Soc. Am. **44**, 1706 (1968).
5. L. A. Rivlin and V. S. Shil'dyaev, Izv. Vyssh. Uchebn. Zaved., Radiofiz. **11**, 572 (1968).
6. L. A. Rivlin, Kvantovaya Elektron. (Moscow), No. 2, 46 (1972).
7. E. E. Grigor'eva and A. T. Semenov, Kvantovaya Elektron. (Moscow) **5** (9), 1877 (1978).
8. Yu. V. Petukhov, Akust. Zh. **42**, 401 (1996) [Acoust. Phys. **42**, 352 (1996)].
9. Yu. V. Petukhov, Akust. Zh. **42**, 688 (1996) [Acoust. Phys. **42**, 606 (1996)].
10. Yu. V. Petukhov, Preprint No. 443, NIRFI (Radiophysical Research Inst., Nizhni Novgorod State Univ., 1998); Akust. Zh. **46**, 384 (2000) [Acoust. Phys. **46**, 327 (2000)].
11. D. I. Abrosimov and Yu. V. Petukhov, Preprint No. 467, IPF RAN (Nizhni Novgorod, Inst. of Applied Physics, Russian Academy of Sciences, 1998); Akust. Zh. **46**, 149 (2000) [Acoust. Phys. **46**, 113 (2000)].
12. D. I. Abrosimov and Yu. V. Petukhov, Preprint No. 466, IPF RAN (Nizhni Novgorod, Inst. of Applied Physics, Russian Academy of Sciences, 1998); Akust. Zh. **46**, 5 (2000) [Acoust. Phys. **46**, 1 (2000)].
13. J. T. Winthrop and C. R. Worthington, J. Opt. Soc. Am. **55**, 373 (1965).
14. W. D. Montgomery, J. Opt. Soc. Am. **57**, 772 (1967).
15. R. F. Edgar, Opt. Acta **16**, 281 (1969).
16. Yu. I. Denisyuk, N. M. Ramishvili, and V. V. Chavchanidze, Opt. Spektrosk. **30**, 1130 (1971).
17. L. M. Brekhovskikh, *Waves in Layered Media* (Nauka, Moscow, 1957; Academic, New York, 1960).
18. E. L. Borodina and Yu. V. Petukhov, Preprint No. 529, IPF RAN (Nizhni Novgorod, Inst. of Applied Physics, Russian Academy of Sciences, 2000).
19. M. M. Dargeĭko, Yu. A. Kravtsov, V. G. Petnikov, *et al.*, Izv. Vyssh. Uchebn. Zaved., Radiofiz. **27** (6), 746 (1984).
20. F. M. Ismailov and Yu. A. Kravtsov, Akust. Zh. **37**, 294 (1991) [Sov. Phys. Acoust. **37**, 148 (1991)].
21. D. R. Dowling and D. R. Jackson, J. Acoust. Soc. Am. **89**, 171 (1991).
22. T. Akai, C. Ferla, W. S. Hodgkiss, *et al.*, J. Acoust. Soc. Am. **103**, 25 (1998).
23. T. Akai, C. Ferla, W. S. Hodgkiss, *et al.*, J. Acoust. Soc. Am. **105**, 1597 (1999).

Translated by E. Golyamina

Acoustical Physics, Vol. 47, No. 5, 2001, pp. 517–523. Translated from Akusticheskiĭ Zhurnal, Vol. 47, No. 5, 2001, pp. 597–604.

The Ray Approach for Analyzing the Modal Structure of the Sound Field in a Range-Dependent Waveguide

A. L. Virovlyanskiĭ, L. Ya. Lyubavin, and A. A. Stromkov

Institute of Applied Physics, Russian Academy of Sciences, ul. Ul'yanova 46, Nizhni Novgorod, 603600 Russia

e-mail: viro@hydro.appl.sci-nnov.ru

Received October 2, 2000

Abstract—Simple ray-approximation formulas are obtained for the mode amplitudes in a waveguide with range-dependent parameters. The idea of the proposed approach is based on the mode expansion of the complex field amplitude determined using the geometrical-optics approximation. A specific example of calculating mode amplitudes is analyzed for a deep-water sound channel with a sound speed profile nonadiabatically varying with distance. The results of the calculation are compared with the numerical solution obtained for the same problem by the parabolic equation method. © *2001 MAIK "Nauka/Interperiodica".*

INTRODUCTION

The WKB approximation is known to yield a simple analytical description of the field mode structure in both a planar stratified waveguide and a waveguide adiabatically varying along the path [1–3]. If the condition of adiabaticity is violated, i.e., the waveguide parameters change too quickly with distance, the mode amplitudes are usually calculated numerically [2, 4, 5]. The lack of analytical description hinders the study of the effects produced by varying parameters of the medium on the mode structure of the sound field. The greatest difficulties arise in solving inverse problems. That is why, in acoustic mode tomography, the sound field is often described in the framework of the adiabatic approximation [6], which is of limited validity in real conditions.

Here, we present an attempt to lift the aforementioned restrictions of the method of normal waves and to obtain analytical expressions that can be used for calculating the mode amplitudes in a range-dependent waveguide regardless of the validity of the adiabatic approximation. The idea consists in using the advantages of the ray approach, which, in contrast to the mode approach, does not loose its simplicity and physical clarity when the adiabatic approximation fails. The geometrical-optics formulas for the amplitude and the eikonal remain valid in a nonadiabatic waveguide.

We expand the geometrical-optics solution of the wave equation into normal waves and calculate the integrals by using the stationary phase method. The procedure results in relatively simple relations that express the mode amplitudes through the parameters of the ray trajectories. Earlier, we [7, 8] used a similar approach to study the variations in the mode structure of the sound field in response to a sound speed profile disturbance varying along the path (see also [9], where the approach was applied to the problems of quantum chaos). At each distance, the field was expanded into the modes of the undisturbed planar stratified waveguide, and simple ray formulas were found for the mode amplitudes. In practice, this approach works when the range-dependent waveguide only slightly differs from the planar stratified one. In underwater acoustics, especially in the problems of long-range sound propagation in the ocean, the waveguide parameters often change dramatically along the path and the proposed approach [7, 8] needs to be generalized.

Such a generalization is presented below. The formulas are obtained for the amplitudes of the so-called local modes or, in other words, for the modes of the reference waveguide [1]. In the considered approach, the refractive index is not broken into undisturbed and disturbed components. In the particular case of a two-layer waveguide whose thickness changes along the path, the results of this study coincide with the results obtained in [10].

We neglect the horizontal refraction of the waves and restrict ourselves to the cylindrically symmetric problem. Let us use a cylindrical coordinate system (r, ϑ, z) with the z axis oriented vertically downwards (the plane $z = 0$ coincides with the water surface). We assume that the sound speed c does not depend on the azimuthal angle ϑ. The complex amplitude of the monochromatic (cw) sound field $u(r, z)$ obeys the Helmholtz equation [1, 2]

$$\frac{\partial^2 u}{\partial r^2} + \frac{1}{r}\frac{\partial u}{\partial r} + \frac{\partial^2 u}{\partial z^2} + k^2 n^2(r, z)u = 0, \qquad n(r, z) = c_0/c(r, z), \tag{1}$$

where n is the refractive index, $k = 2\pi f/c_0$, f is the carrier frequency, and c_0 is constant.

In the small-angle approximation, a simplified description can be obtained by changing to a parabolic equation for the smooth envelope $v(r, z)$ of the wave field,

which is related to $u(r, z)$ by the expression $u(r, z) = v(r, z)\exp(ikv)/\sqrt{r}$. By substituting this expression into Eq. (1) and neglecting the second derivative with respect to the longitudinal coordinate r, we arrive at the parabolic equation [1, 2, 11]

$$2ik\frac{\partial v}{\partial r} + \frac{\partial^2 v}{\partial z^2} - 2k^2 U(r, z)v = 0,$$
$$U(r, z) = \frac{1}{2}(1 - n^2(r, z)). \tag{2}$$

We analyze the mode structure of the sound field for both Eqs. (1) and (2). For each equation, we consider the relationships that express the Hamiltonian formalism for calculating the ray pattern. In doing so, we use the same notations for the ray and mode parameters in both cases. (Identical notations cannot lead to confusion, because the solutions of the Helmholtz and the parabolic equations are considered in different sections of the paper.)

At first glance, one could restrict the consideration to analyzing only Eq. (1), especially because the small-angle approximation does not lead to any significant simplification. However, there are two reasons to consider Eq. (2). First, in contrast to Eq. (1), this equation can be simply solved by numerical means, even for a waveguide changing along the path. There are a number of accurate and fast computer codes that solve the parabolic equation, one of which (UMPE [13]) we used to quantitatively estimate the accuracy of approximate expressions. Such a comparison would be much more difficult for Eq. (1). The second reason is that parabolic equation (2) coincides with the Schröedinger equation in its form, and our results can be applied to quantum-mechanics problems for analyzing wave functions in potential wells whose parameters vary with time.

RAYS AND MODES IN THE APPROXIMATION OF A PARABOLIC EQUATION

Ray Representation for the Field

In the geometrical-optics approximation, the solution to Eq. (2) is represented in the form $v = A\exp(ikS)$, where A and S are the amplitude and eikonal for the ray, respectively. Before analyzing the explicit expressions for S and A [12], let us briefly consider the Hamiltonian formalism that will be used to describe the ray pattern of the field. According to this formalism, the ray trajectory is quite similar to a particle trajectory in classical mechanics, with the longitudinal coordinate r being the analog of time. For the mechanical momentum, its analog is the quantity $p = dz/dr = \tan\chi$, where χ is the grazing angle. The Hamiltonian is given by the following expression:

$$H = \frac{p^2}{2} + U(r, z). \tag{3}$$

In our case, the Hamilton equations that describe the motion of a mechanical particle [14] are the ray equations and have the form

$$\frac{\partial z}{\partial r} = \frac{\partial H}{\partial p}, \quad \frac{\partial p}{\partial r} = -\frac{\partial H}{\partial z}. \tag{4}$$

The eikonal S that serves as the analog of the mechanical action is expressed as

$$S = \int(pdz - Hdx), \tag{5}$$

where the integration is performed along the ray trajectory (the solution to the system of ray equations (4)). There are two formulas [14],

$$\frac{\partial S}{\partial z} = p, \quad \frac{\partial S}{\partial z_0} = -p_0, \tag{6}$$

which are well known in mechanics and useful to us. The eikonal S is assumed here to be a function of the starting depth z_0, the final depth z, and the range r.

The ray trajectories oscillate in a waveguide. Therefore, to describe them, it is convenient to complement the momentum–coordinate variables (p, z) with the action–angle variables related to (p, z) by the well-known canonical transformation [14]. In this paper, we need only the action variable (this quantity should not be confused with the eikonal S, which is the analog of the mechanical action). The action variable is introduced in the following way.

To begin with, we consider a planar stratified waveguide ($U = U(z)$) where the Hamiltonian does not change along the ray trajectory:

$$H = E = \text{const}. \tag{7}$$

In mechanics, Eq. (7) expresses the energy conservation law. In geometrical optics, it represents the Snell law in the small-angle approximation. The action variable I is given by the expression

$$I = \frac{1}{2\pi}\oint pdz = \frac{1}{\pi}\int_{z_{\min}}^{z_{\max}} dz\sqrt{2(E - U(z))}, \tag{8}$$

where $z_{\max}$ and $z_{\min}$ are the roots of the equation $U(z) = E$, which determine the turning horizons for the ray trajectory. In fact, Eq. (8) establishes the relation between the variables E and I, i.e., it determines the function $E(I)$, as well as its inverse function $I(E)$.

The following relation is well known from classical mechanics [14]:

$$\frac{dE}{dI} = \frac{2\pi}{D}, \tag{9}$$

where D is the cycle length for the ray (the trajectory period along the coordinate r).

In a waveguide varying along the path, the relation between E and I is specified by using the concept of a reference waveguide [1]. By this term, an imaginary

planar stratified waveguide is meant, whose vertical cross section coincides with that of the waveguide to be studied at the same distance. For a realistic range-dependent waveguide, an appropriate reference waveguide should be constructed at each distance. For all reference waveguides (at all distances r), Eq. (8), in general, determines different relations between the energy E and the action I with different functions $E(I)$ and $I(E)$. Thus, in a waveguide varying along the path, these functions are replaced by the functions $E(I, r)$ and $I(E, r)$. By specifying the distance, the additional variable r determines the parameters of the reference waveguide. Expressions (9) are still valid if the full derivative with respect to I is replaced by the partial derivative and D is treated as the length of the ray cycle in the reference waveguide.

The function $I(E, r)$ introduced in this way determines the action variable for the ray that carries the energy E at the distance r. Here, the range dependence of the waveguide parameters is not assumed to be smooth, and the well-known concept [14] of adiabatic invariance is not used for the action variable.

In conclusion for this subsection, we introduce the expression for the complex amplitude of the sound field of a point source [12], which is known from the geometrical-optics approximation. The field obeys Eq. (2) with the right-hand side in the form $2ik\delta(z - z_0)\delta(r)$. When $r \longrightarrow 0$, the solution coincides with the Green function for free space:

$$v = \sqrt{\frac{k}{2\pi i r}}\exp\left[i\frac{k(z-z_0)^2}{2r}\right]. \quad (10)$$

At an arbitrary distance from the source, the situation is typical with several rays arriving at the receiver. To find the total field, the contributions of all rays should be combined according to the formula [12]:

$$v = \sum_{\nu}\sqrt{\frac{k}{2\pi i\left|z^{\nu}_{p_0}\right|}}\exp[ikS^{\nu} - i\mu^{\nu}\pi/2], \quad (11)$$

where the superscript ν indicates the number of a received ray; μ^{ν} is the trajectory index for the νth ray, which is equal to the number of caustics touched by this ray on its way to the reception point (all caustics are assumed to be nonsingular); and the subscript p_0 denotes the partial derivative with respect to the starting value of the momentum.

Mode Representation for the Field

At each distance r, we expand the field in the modes of the reference waveguide, which are also called local modes. In this subsection, we present the main expressions for the eigenfunctions of a planar stratified waveguide in the WKB approximation [1]. By definition, every reference waveguide can be considered as a planar stratified waveguide. The eigenfunctions are the solutions to the equation

$$\frac{1}{2}\frac{d^2\varphi_m}{dz^2} + k^2(E_m - U)\varphi_m = 0$$

with the appropriate boundary conditions. The eigenvalues of the energy E_m are found from the relation $E_m = E(I_m)$ in view of the function $E(I)$ determined by Eq. (8) and the value of the action variable that corresponds to the mth mode determined by the Bohr–Sommerfeld quantization rule [1]:

$$kI_m = m - \frac{\phi_s + \phi_b}{2\pi}. \quad (12)$$

In this expression, ϕ_s and ϕ_b are the phases of the reflection coefficients in the upper (closest to the surface) and lower (closest to the bottom) turning points, respectively. If the turning point is within the water bulk, the phase of the reflection coefficient is $\phi = -\pi/2$. When the reflection occurs from a pressure-release surface, $\phi = \pi$, and in the case of the reflection from a perfectly rigid boundary, $\phi = 0$.

In the region between the turning points, the WKB approximation yields the following representation for the eigenfunction:

$$\varphi_m(z) = \varphi^{+}_m(z) + \varphi^{-}_m(z), \quad (13)$$

where

$$\varphi^{\pm}_m(z) = Q^{\pm}_m\exp[\pm i(kS_m(z) + \phi_s/2)], \quad (14)$$

$$S_m(z) = \int_{z_{\min}}^{z} dz\, p_m(z), \quad (15)$$

$$p_m(z) = \sqrt{2[E_m - U(z)]}, \quad (16)$$

$$D_m = 2E_m\int_{z_{\min}}^{z_{\max}}\frac{dz}{p_m(z)}, \quad (17)$$

$$Q^{\pm}_m = \sqrt{\frac{E_m}{p_m(z)D_m}}\exp(\pm i\phi_s/2). \quad (18)$$

In the WKB approximation, the eigenfunction is expressed through the parameters of the ray with the energy $E = E_m$. In particular, D_m is the cycle length of the ray, and $p_m(z)$ is the ray momentum at the depth z.

Expansion of Ray Representation of the Field in the Local Modes

For an inhomogeneous waveguide, the mode representation of the field has the form

$$v = \sum_m B_m(r)\varphi_m(r, z). \quad (19)$$

Here, we explicitly introduced the variable r for the local mode, which was omitted in the previous subsection. By using the orthogonality of the eigenfunctions of the local modes, we express the mode amplitude as follows:

$$B_m = \int dz\, v(r, z)\varphi_m(r, z). \tag{20}$$

In view of Eqs. (13) and (14), we break this amplitude into two components, B_m^+ and B_m^-, where

$$B_m^\sigma = \int dz\, v(r, z)\varphi_m^\sigma(r, z). \tag{21}$$

The parameter σ takes two values, +1 and –1, or simply a plus and a minus if it is used as a superscript.

To obtain explicit expressions for the mode amplitudes, we use the WKB approximation for the eigenfunctions and the ray representation of the field $v(r, z)$. Substituting Eqs. (11) and (14) into Eq. (21), we obtain the following integral:

$$B_m^\sigma = \int dz A Q^\sigma \exp[ik(S + \sigma S_m)]. \tag{22}$$

To calculate it, we use the stationary-phase method [1]. The stationary-phase point of the integrand

$$\Phi = k(S + \sigma S_m)$$

is determined by equating the derivative

$$\frac{\partial \Phi}{\partial z} = k(p + \sigma p_m). \tag{23}$$

to zero. Here, the derivative was calculated using Eqs. (6) and (15).

Formula (23) means that the main contribution to the field of the mth mode is made by the ray whose momentum meets the condition

$$p = -\sigma p_m(z).$$

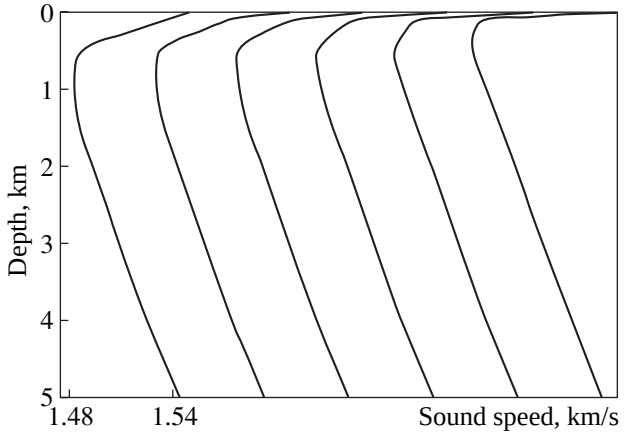

Fig. 1. Sound speed profiles in six vertical waveguide cross sections taken at six equidistant points of the path 141 km in length. On the left: profile at the reception point. On the right: profile at the maximal distance from the receiver.

This condition can be expressed in the form

$$I = I_m, \tag{24}$$

where I is the action variable for the ray that hits the stationary point.

For the rays that meet condition (24), we will use the term mode rays. Their number can be arbitrary [7, 8]. These rays determine the amplitude of the mode at a given distance. By evaluating integral (22) with the stationary phase method, we obtain the following expression for the contribution of a single mode ray:

$$B_m^\sigma = \sqrt{\frac{2\pi}{k\left|\frac{\partial^2 \Phi}{\partial z^2}\right|}} A Q^\sigma \exp(ik\Phi + i\gamma\pi/4), \tag{25}$$

where γ is the sign of the second derivative $\partial^2\Phi/\partial z^2$. To calculate this derivative, we differentiate Eq. (23) with respect to z. In doing so, we treat the momentum p on the right-hand side as a function of z and r. In other words, we interpret p as the momentum of the ray that hits a point z at a distance r. With the use of the relation

$$\frac{\partial p}{\partial z} = \frac{p_{p_0}}{z_{p_0}},$$

we find the value of the second derivative at the stationary point:

$$\frac{\partial^2 \Phi}{\partial z^2} = k\left(\frac{p_{p_0}}{z_{p_0}} - \sigma\frac{U_z}{p_m}\right) = -k\sigma\frac{E_{p_0}}{z_{p_0} p_m}. \tag{26}$$

Substituting this relation into Eq. (25), we obtain an explicit expression for the contribution of a single mode ray to the mode amplitude:

$$B_m^\sigma = \frac{1}{\sqrt{iD_m\left|\frac{\partial E}{\partial p_0}\right|}} \times \exp[ik(S + \sigma S_m) + i(\gamma - 2\mu)\pi/4 + i\sigma\phi_s/2]. \tag{27}$$

In view of Eq. (9), we represent this expression in the form

$$B_m^\sigma = \frac{1}{\sqrt{2\pi i\left|\frac{\partial I}{\partial p_0}\right|}} \times \exp[ik(S + \sigma S_m) + i(\gamma - 2\mu)\pi/4 + i\sigma\phi_s/2]. \tag{28}$$

To conclude with calculating the amplitude of the mth mode, all mode ray contributions given by Eqs. (27) or (28) should be combined.

Example of Calculating Mode Amplitudes

To illustrate the results obtained above, let us consider a deep-water acoustic waveguide that varies along the path. Figure 1 shows several sound speed profiles along a path 141 km in length. According to the plots,

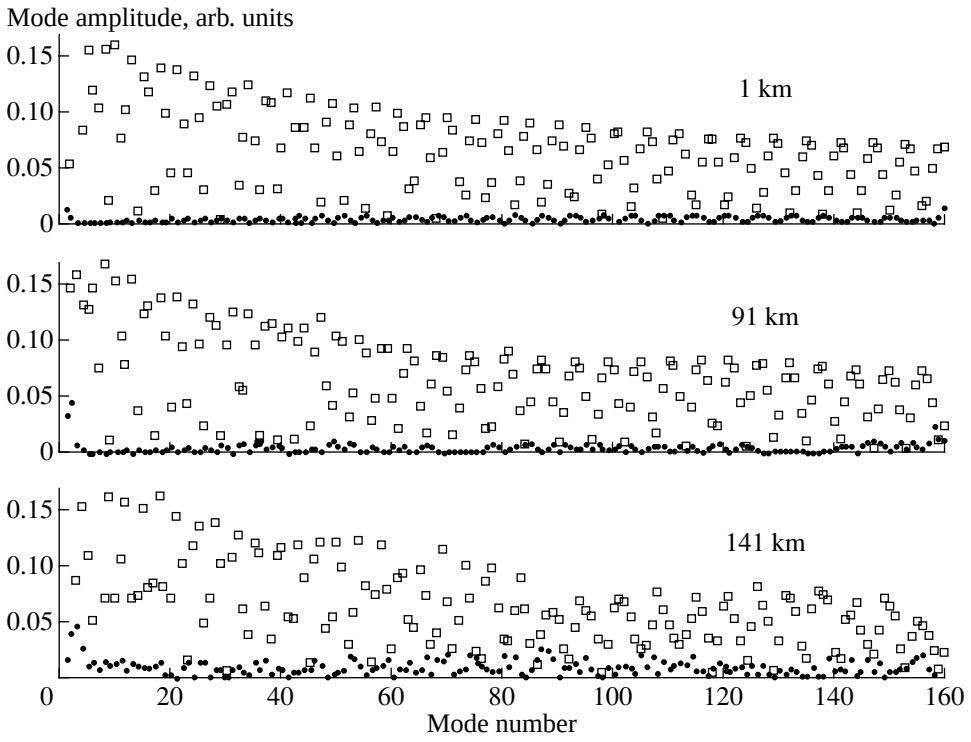

Fig. 2. Mode amplitudes (squares) at the distances 1 (top), 91 (middle), and 141 km (bottom), as calculated with the proposed ray formulas, and the depatures of these amplitudes (dots) from those calculated by the method of parabolic equation.

the profile considerably changes with distance. In particular, the channel axis rises from a depth of 915 km at $r = 0$ to 388 m at $r = 141$ km.

The point sound source (which is assumed to lie at the channel axis at $r = 0$) transmits a carrier frequency of 200 Hz. The sound field was calculated in the approximation of the parabolic equation by means of the UMPE program [13]. At chosen distances, vertical cross sections of the field were expanded in local modes, which were computed with the use of the WAN program [15]. The field amplitudes proved to significantly vary with distance; i.e., the adiabatic approximation was undoubtedly violated for the waveguide at hand.

In Fig. 2, the squares indicate the amplitudes of the first 160 propagating modes that are calculated according to Eq. (27) for three distances: 1, 91, and 141 km. At each distance, the amplitude of each mode was formed by the contributions of two eigenrays. The dots show the absolute values of the differences between the mode amplitudes found by the UMPE program and those calculated according to Eq. (27). The differences characterize the errors in estimating the amplitudes with our ray method. On average, these errors reach 6% (0.5 dB), 8% (0.7 dB), and 15% (1.4 dB) at the distances 1, 91, and 141 km, respectively. In parentheses, the differences in decibels are indicated between the exact and approximate values of the amplitude. At a distance of 1 km, the error is actually caused by the difference between the exact values of φ_m at the source depth, which determine the starting mode amplitudes, and the WKB-approximated values of these functions, which are used in our ray calculations.

RAYS AND MODES FOR THE FIELD SATISFYING THE HELMHOLTZ EQUATION

All results presented in the previous section can be easily generalized to the case when the field is governed by the Helmholtz equation (1) without assuming that the grazing angles of the propagating waves (and rays) are small. Here, we briefly consider the generalized formulas and make some relevant comments.

The complex field amplitude is again expressed through the amplitude A and the eikonal S of the ray:

$$u = \frac{A}{\sqrt{r}}\exp(ikS). \tag{29}$$

In turn, the quantities A and S can be expressed through the parameters of the ray trajectory. As above, the latter can be denoted as $z(r)$. Let us use the Hamiltonian formalism again. The ray equations have the form of the Hamilton equations (4), but the Hamiltonian itself now is given by the expression [16]

$$H = -\sqrt{n^2 - p^2} = -n\cos\chi. \tag{30}$$

The symbol χ stands for the grazing angle. The relation between the momentum and the velocity dz/dr now takes the form

$$p = n\frac{dz/dr}{\sqrt{1+(dz/dr)^2}} = n\sin\chi. \quad (31)$$

The expression for the eikonal is again specified by integral (5), but the new form of the Hamiltonian should be used in it. Formula (6) also remains valid.

For a planar stratified waveguide with $n = n(z)$, the analog of the energy conservation law, i.e., Snell's law [1], now takes the form

$$H = -n(z)\cos\chi = E. \quad (32)$$

The relation between the action variable and the energy is given by the integral that is similar to Eq. (8):

$$I = \frac{1}{2\pi}\oint p dz = \frac{1}{\pi}\int_{z_{\min}}^{z_{\max}} dz\sqrt{n^2(z)-E^2}. \quad (33)$$

The field produced by a point source is described by the Helmholtz equation (1) with the right-hand side $-\frac{2}{r}\delta(r)\delta(z-z_0)$. Transforming the well-known expression for the field of a point source [1] to our notation, we obtain an approximate solution for the Helmholtz equation:

$$u = \sum_{\nu}\frac{1}{\sqrt{r\left|E^{\nu}z^{\nu}_{p_0}\right|}}\exp[ikS^{\nu} - i\mu^{\nu}\pi/2], \quad (34)$$

where, as in Eq. (11), the superscript ν represents the numbers of all rays that hit the point (r, z).

Let us consider the mode representation of the field. The eigenfunctions of the planar stratified waveguide are the solutions to the equation

$$\frac{d^2\varphi_m}{dz^2} + k^2[n^2(z) - E_m^2]\varphi_m = 0$$

with the appropriate boundary conditions. The eigenvalues are again determined by the quantization rule given by Eq. (12), while the relation between I_m and E_m is now specified by Eq. (33).

Between the turning points, the eigenfunction is again represented as a sum of two components, according to Eqs. (13) and (14), whereas the explicit expressions for S_m, $Q_m^{\pm}$, and D_m now take the form

$$S_m(z) = \int_{z_{\min}}^{z} dz\, p_m(z), \quad (35)$$

$$p_m = \sqrt{n^2 - E_m^2}, \quad (36)$$

$$Q_m^{\pm} = \sqrt{\frac{E_m}{p_m(z)D_m}}\exp(\pm i\phi_s/2), \quad (37)$$

$$D_m = 2E_m\int_{z_{\min}}^{z_{\max}}\frac{dz}{p_m(z)}. \quad (38)$$

By analogy with the approximation of parabolic equation, the mode field representation has the form of a sum of local modes:

$$u(r) = \sum_m B_m(r)\varphi_m(r, z). \quad (39)$$

The next step consists in expanding the ray field representation given by Eq. (34) in the local modes. To do so, we follow the procedure described above. Namely, the mode amplitude B_m is again broken into two components, which are calculated by using the method of stationary phase. As a result, we arrive at expressions (19)–(24) in which (to be more specific, in Eqs. (19–(21)) ν is replaced by u.

An important fact should be mentioned: the mode amplitude is again formed by the contributions of the rays whose action variables satisfy Eq. (24).

The explicit expression for the second derivative of the phase with respect to the vertical coordinate is as follows:

$$\frac{\partial^2\Phi}{\partial z^2} = k\left(\frac{p_{p_0}}{z_{p_0}} + \frac{\sigma}{2}\frac{\partial n^2/\partial z}{p_m}\right) = \sigma\frac{k}{z_{p_0}p_m}EE_{p_0}.$$

The analogs of Eqs. (27) and (28) have the forms

$$B_m^{\sigma} = \sqrt{\frac{2\pi}{krn(r, z)\cos\chi D_m\left|H_{p_0}\right|}} \quad (40)$$

$$\times \exp[ik(S + \sigma S_m(z))]\exp[i(\gamma - 2\mu)\pi/4 + i\sigma\phi_s/2]$$

and

$$B_m^{\sigma} = \frac{1}{\sqrt{kr\left|EI_{p_0}\right|}} \quad (41)$$

$$\times \exp[ik(S + \sigma S_m(z))]\exp[i(\gamma - 2\mu)\pi/4 + i\sigma\phi_s/2].$$

As in the previous considerations, γ denotes the sign of the second derivative of the phase with respect to z at the stationary point.

CONCLUSIONS

The set of formulas presented above specifies the procedure of calculating the mode amplitudes for a waveguide varying along the path on the basis of solving ordinary ray equations. In many aspects, this procedure is similar to that of standard geometrical-optics calculations for the field amplitude at a given point. The procedure involves finding the mode rays that have the given value of the action variable at a given distance (the analog of the standard problem of targeting, i.e.,

finding the rays that hit a given spatial point) and calculating the parameters of the ray trajectories along with their derivatives with respect to the initial conditions. As in the expressions for the ray amplitudes (Eqs. (11) and (34)), in Eqs. (27), (28), (40), and (41) for the mode amplitudes, the denominators of the integrands can take zero values. Thus, there are analogs of caustics in this case (for more detail, see [8]). It is worth mentioning that the validity domain of proposed approach actually coincides with that of the ray approximation.

The results of this study provide a deeper understanding of the relationship between the mode and ray representations of the sound field in an inhomogeneous waveguide. An important conclusion from Eq. (24) is that, at a given distance, the main contribution to the field of the mth mode is made by the mode rays whose action variables are equal to the action variable of the given mode, I_m. In a planar stratified waveguide, there are two mode rays for each mode at each distance. They leave the source at the angles that are equal to the grazing angles of the Brillouin waves that form the mode. Along its mode rays, a mode in the planar stratified waveguide is combined in phase (constructively interferes) with adjacent modes [17, 18].

In a waveguide that changes along its path, an arbitrary number of mode rays can exist [8]. For the case of ray chaos, this number exponentially increases with distance, and the range dependence of the mode amplitude becomes irregular. The proposed approach establishes an unexpectedly simple relation between rays and modes for an inhomogeneous waveguide and allows one to understand how the chaotic behavior of ray trajectories manifests itself in the resulting wave pattern at a finite wavelength. This problem is central in studying wave chaos [16].

Another application of proposed approach can be the problem of the validity limits for the adiabatic approximation. On the basis of the analysis described above, we can indicate at least two mechanisms that violate this approximation. The first one consists in the nonconservation of the action variable along the mode ray. The second is related to the possibility of a multiplication of the mode rays. Both mechanisms can be studied with the proposed approach. In particular, the first mechanism was realized in the example considered in this paper. The second mechanism manifests itself in the example analyzed in [10].

ACKNOWLEDGMENTS

The authors are grateful to I.P. Smirnov who has developed the computer program used in our calculations of ray trajectories.

This work was supported by the Russian Foundation for Basic Research, project no. 00-02-17409.

REFERENCES

1. L. M. Brekhovskikh and Yu. P. Lysanov, *Fundamentals of Ocean Acoustics* (Gidrometeoizdat, Leningrad, 1982; Springer, New York, 1991).
2. F. B. Jensen, W. A. Kuperman, M. B. Porter, and H. Schmidt, *Computational Ocean Acoustics* (American Inst. of Physics, New York, 1994).
3. P. C. Mignerey, J. Acoust. Soc. Am. **107**, 1943 (2000).
4. J. A. Colosi and S. M. Flatte, J. Acoust. Soc. Am. **100**, 3607 (1996).
5. C. T. Tindle, L. M. O'Driscoll, and C. J. Higham, J. Acoust. Soc. Am. **108**, 76 (2000).
6. A. C. Voronovich and E. C. Shang, J. Acoust. Soc. Am. **101**, 2636 (1998).
7. A. L. Virovlyansky and G. M. Zaslavsky, Phys. Rev. E **59**, 1656 (1999).
8. A. L. Virovlyansky, J. Acoust. Soc. Am. **108**, 84 (2000).
9. G. P. Berman and G. M. Zaslavsky, Physica A (Amsterdam) **97**, 367 (1979).
10. A. L. Virovlyanskiĭ and O. V. Lebedev, Akust. Zh. **44**, 451 (1998) [Acoust. Phys. **44**, 384 (1998)].
11. F. D. Tappert, in *Wave Propagation and Underwater Acoustics*, Ed. by J. B. Keller and J. S. Papadakis (Springer, New York, 1977; Mir, Moscow, 1980).
12. V. P. Maslov and M. V. Fedoryuk, *Semi-Classical Approximation in Quantum Mechanics* (Nauka, Moscow, 1976; Reidel, Dordrecht, 1981).
13. K. B. Smith and F. D. Tappert, *UMPE: The University of Miami Parabolic Equation Model, Version 1.1*, Marine Physical Laboratory Technical Memo 432 (Scripps Inst. of Oceanography, San Diego, 1994).
14. L. D. Landau and E. M. Lifshits, *Mechanics*, 3rd ed. (Nauka, Moscow, 1973; Pergamon Press, Oxford, 1976).
15. I. A. Okomel'kova and I. A. Shereshevskiĭ, Preprint No. 235, IPF AN SSSR (Gorkiĭ Inst. of Applied Physics, USSR Academy of Sciences, 1989).
16. S. S. Abdullaev and G. M. Zaslavskiĭ, Usp. Fiz. Nauk **161** (8), 1 (1991) [Sov. Phys.–Usp. **34**, 645 (1991)].
17. C. T. Tindle and K. M. Guthrie, J. Sound. Vibr. **34**, 291 (1974).
18. L. B. Felsen, J. Acoust. Soc. Am. **69**, 352 (1981).

Translated by E. Kopyl

Acoustical Physics, Vol. 47, No. 5, 2001, pp. 524–528. Translated from Akusticheskiĭ Zhurnal, Vol. 47, No. 5, 2001, pp. 605–610.

Acoustic Mapping of the Ocean Bottom and Requirements of the Initial Data

V. I. Volovov, S. A. Vladimirov, V. I. Gel'fgat, A. I. Govorov, V. S. Gostev, and L. N. Nosova

Andreev Acoustics Institute, Russian Academy of Sciences, ul. Shvernika 4, Moscow, 117036 Russia

e-mail: bvp@akin.ru

Received December 22, 1999

Abstract—The amount and degree of detail of the initial information are analyzed as applied to the new method of ocean bottom mapping on the basis of the fine structure of the bottom-reflected sound field at normal incidence. For the mapping data obtained with a planar multielement receiving array, the distortions caused by insufficiently detailed information derived from discrete measurements of the bottom-reflected amplitude are considered. The relations between the number of receivers, the receiver spacing, the array aperture, and the horizontal correlation length of the sound field are determined. The problem is solved by computer simulation with the use of generalized quantitative data obtained in deep-water ocean experiments.

The sound field reflected by the bottom of the deep ocean at normal incidence is known to exhibit three spatial scales in the horizontal plane. Experiments show that, for each of these scales, the reflected field can be mapped. In other words, the field parameters (the amplitude, for instance) can be represented as a two-coordinate function in a relative fixed or (with the appropriate reference) geographic coordinate system [1–5]. The possibility of such mapping is very important, especially for the high-frequency scale of the field variability, because it opens up new possibilities for solving a number of practical problems, such as the independent determination of the parameters of motion for surface and underwater marine vehicles relative to the bottom, as well as other problems of navigation. The principle underlying such methods differs from the traditional ones [5–7] and seems to be highly promising [2–4]. However, the feasibility and quality of mapping is directly concerned with the time stability of the acquired data, i.e., with the data insensitivity to the real disturbing factors that change within the time interval required for solving a specific problem. In real conditions, these intervals vary over wide limits, from several seconds to the values characterizing the seasonal variability of the hydrological environment.

In our previous publication [8], we considered the effect of the disturbing factors on the stability of the acoustic maps. These factors included small-scale turbulent inhomogeneities of the ocean waters, fine-structure irregularities, lenses, and general changes in the sound speed profile. The analysis was applied to the highest-frequency variability scale (of the order of the sound wavelength) of the reflected field, because this variability governs the fine structure of the sound field, which has a phase nature and suffers from the disturbing factors to the maximal extent [2, 8]. In [8], we also specified when and what disturbing factors can be neglected, and in what cases preliminary estimates are needed to solve practical problems.

However, in practice, hydrological factors are not the only ones that influence the quality of the mapping data: disturbing factors of instrumental and methodical nature can be involved as well.

Let us consider the effect of the details of the initial data used for mapping on the resulting maps. The consideration is restricted to the aforementioned fine spatial structure of the reflected field. We use a computer simulation with the available generalized data of long-standing in-sea experiments on sound reflection from the ocean bottom [2].

The most advantageous way to obtain information on the fine spatial structure of the sound field reflected from the bottom of the deep ocean is to use horizontal multielement receiving antenna arrays. In this case, the data are collected from a finite number of discrete sound receivers distributed over the array aperture, with an independent and separate reception of the reflected signal by each receiving element. Then, by using purely computational procedures, one can construct a map for the parameter of interest, e.g., in a coordinate system whose axes are parallel to the mutually perpendicular array sides. To convert the discrete data to isolines, one can use standard computer software. By using a set of data obtained with the horizontal displacement of the array, provided that the apertures partially overlap at different array positions, an area can be covered that far exceeds that of the aperture. The latter fact was demonstrated in [4] for a coordinate system rigidly fixed to the bottom. It is worth mentioning that, nowadays, spatially

1063-7710/01/4705-0524$21.00

spaced arrays (with different data processing systems) are accepted [2, 4, 9, 10] as the most advantageous tools for receiving bottom-reflected (bottom-scattered) signals in various applications.

As for the required degree of detailing in the initial data, it is obvious that the spacing of the adjacent reception points should be sufficiently small, at least smaller than the horizontal correlation length of the reflected signal. On the other hand, the closer the reception points, the better the accuracy of mapping. However, starting from a certain spatial step, the information becomes excessive along with sharply increasing instrumental difficulties in the measuring procedure and with a rise in the cost of the bottom mapping.

To solve the problem of the effect of the spacing of the reception points on the quality of the collected data, a computer simulation is the most advantageous method. In the experiments, the receiving array is a solid structure with fixed receiving elements [2–4]. Then, with a constant array aperture, the only possibility to change the step of the data collection is a multiple-step decrease in the number of receivers along the array sides. One cannot thoroughly analyze the situation in this way. A computer simulation is free from such limitations, however, it requires the solution of the following problems:

(1) to obtain numerical realizations for the distribution of the amplitudes of the reflected signal over the array aperture for arbitrary spacings of the receivers in the rectangular coordinate system formed by the array sides at an arbitrary ratio of the correlation radius of the reflected amplitude to the receiver spacing ρ/d;

(2) to provide for the agreement between the generated realizations and the generalized experimental data (the Rayleigh and Rice laws for the amplitude probability density and the Gaussian form for the amplitude autocorrelation function [2]) for the given ratios ρ/d of the correlation radius to the minimal receiver spacing, and to permanently check that the obtained numerical data fit the corresponding characteristics;

(3) to calculate and reproduce the isolines of the measured parameter (the sound amplitude) for an arbitrary number and spacing of the curves;

(4) to select a quantitative criterion that characterizes the extent of map distortion caused by a change in the number of the receivers;

(5) to choose the necessary relations between the parameters of a rectangular array: the size (the aperture area), the number of receivers, and the correlation radius of the reflected signal.

The first three of these problems were solved with standard software. However, the case of an arbitrary number of receivers required a modification of the standard computer programs on the basis of the existing methods of interpolation.

Figure 1 shows maps of the same numerically modeled amplitude of the reflected signal, which correspond to different numbers of the reception points within the aperture of a square array, i.e., to different receiver spacings. As a basis for modeling (Fig. 1a), a situation was chosen that is characteristic for deep-water measurements with the GRANAT receiving system [2, 3]: 16×16 receivers, an array size of 4.2×4.2 m, and the frequency 10.0 kHz. The correlation radius ρ of the reflected amplitude was specified to be three times greater than the spacing d of the adjacent receivers. The isolines are represented in relative units that are common for all data with a step of 10 relative units. The isolines are numbered in order of increasing relative amplitudes. Note that in our computer simulation, the values of ρ and ρ/d are governed by the filtering of the sound field, which is initially specified as uncorrelated white noise with a Gaussian distribution of instant

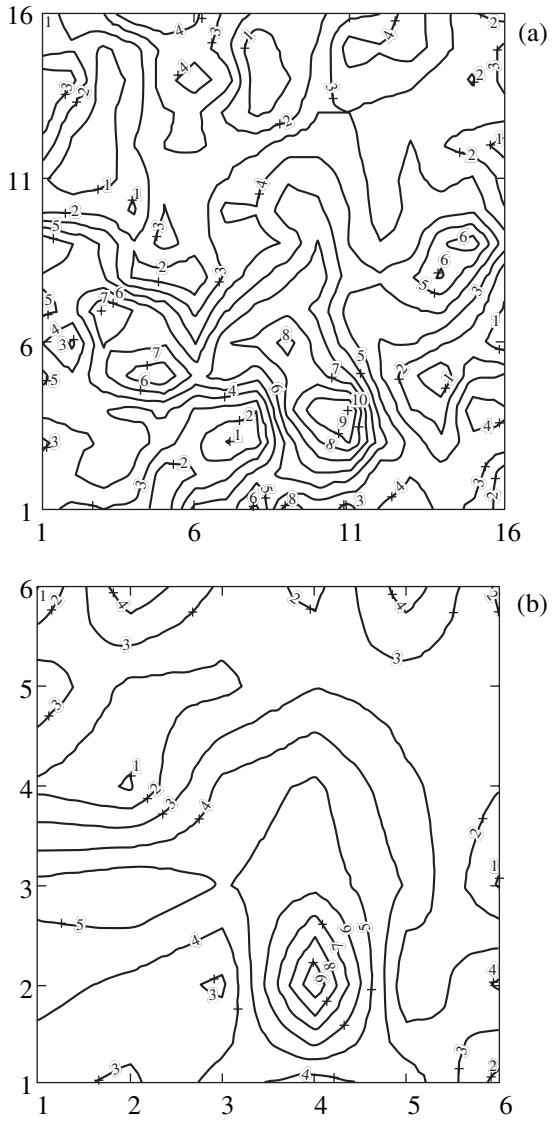

Fig. 1. Amplitude distributions of the reflected signals over the array aperture for different numbers of receivers: (a) 16×16 and (b) 6×6.

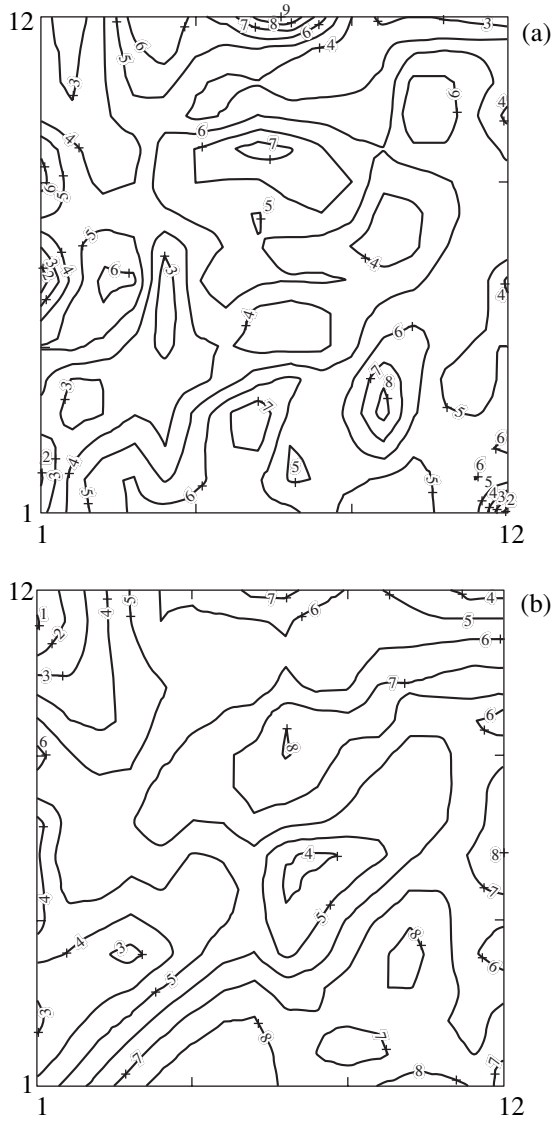

Fig. 2. Amplitude distributions of the reflected signals over the array aperture at a fixed number (12×12) of receivers for different extents of filtering of the initial signal: ρ/d = (a) 2 and (b) 4.

amplitudes and a Rayleigh distribution of envelope values.

The data presented show that an increase in the receiver spacing leads to a deformation of the signal pattern (though its general features remain unchanged): the number of isolines decreases, and their shapes are distorted. In other words, the quality of the mapping data decreases. However, this decrease depends not only on the number of receivers but also on the nature of the surface to be mapped: smoother surfaces can be satisfactorily represented by a smaller number of points than rougher surfaces. In our numerical simulation, this feature of the process is determined by the filtering band used for the generated data sequence and by the ratio of the correlation radius of the obtained realization to the minimal hydrophone spacing.

Figure 2 shows the maps obtained with a fixed number (12×12) of receivers for different ratios ρ/d. The data reveal an obvious tendency for simplification of the map structure with increasing correlation radius. According to the calculations, with a further increase in the correlation radius, the details in the map structure exhibit saturation. The latter fact evidences that, with the given number of receivers and the array size, the mapping resolution is exhausted.

A question arises about the quantitative criterion of the correctness of the obtained mapping data in the case of a varying number of receivers within the array aperture. A natural criterion is the correlation coefficient characterizing the relation between the centered values of the initial amplitude (16×16) and those formed at the same points with a decreased number of receivers.

Figure 3 presents the dependence of such a correlation coefficient on the number of receivers at each array side. The data correspond to several numerical realizations, which agree with the aforementioned average parameters and serve to illustrate the typical statistical spread of the chosen criterion. The low spread obtained for the data shown evidences the sufficient representativeness of the chosen realizations. The form of the dependence is quite understandable: as the number of the receivers increases, the correlation coefficient asymptotically tends to unity (the maps fully coincide); when the number of the receivers decreases to a certain value, the correlation sharply drops down to zero (the maps are different).

Figures 3a and 3b present the plots for two different values of ρ/d. As this ratio increases, the correlation coefficient decreases slower for a greater number of the receivers and more rapidly for a smaller number of them. An acceptable drop of the correlation coefficient, which is caused by a decrease in the number of the array receivers, is determined by the specific problem to be solved with the help of the map. If the problem of high-sensitivity positioning of a vessel relative to the bottom is to be solved, one should refer to special-purpose publications [2, 3, 9, 11] that analyze the errors of the positioning process.

In [12], a simplified situation of a piecewise linear vessel motion relative to the bottom is considered.[1] This simplification, which fully corresponds to the problem at hand, leads to the following estimate for the error in determining the vessel displacement relative to the bottom due to the disturbing factors:

$$\delta_{\text{random}} = \rho^2/(2\pi^{1/2}Lr), \qquad (1)$$

where ρ is the horizontal correlation radius of the amplitude of the reflected signal, L is the side length of

[1] A more complicated situation when, in addition to the translational motion, angular displacements of the array take place (the vessel yaws on the tack) is analyzed in [11].

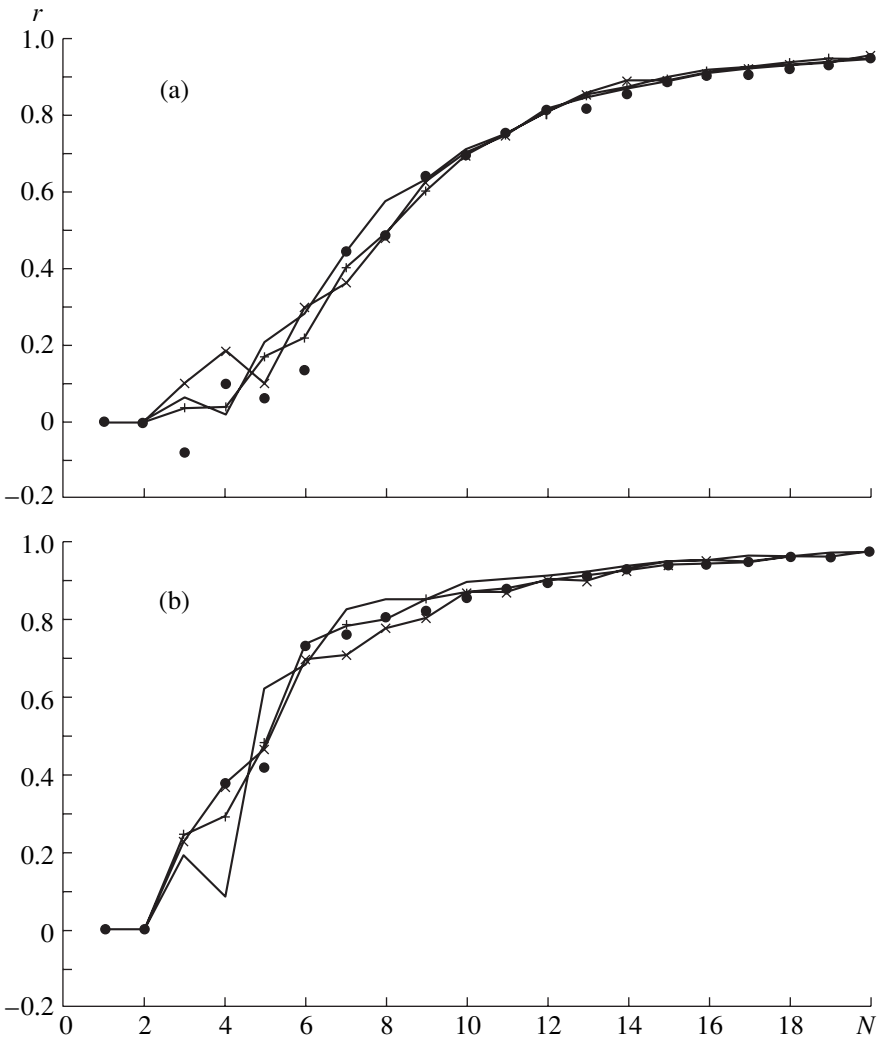

Fig. 3. Correlation coefficients versus the number of the array receivers for different ratios of the signal correlation radius to the receiver spacing (different realizations): ρ/d = (a) 2 and (b) 4.

the square receiving array, and r is correlation coefficient for two successive realizations of the signal received by the array. This formula is universal in the sense that it does not depend on the nature of the disturbing factors that lead to a decrease in the correlation coefficient. Such factors may include interfering noise, temporal fluctuations of the signal amplitudes received by separate hydrophones due to the processes of hydrological nature, offsets of the actual hydrophone positions from the horizontal plane, a spread in the transfer characteristics of separate receiving channels, etc. Earlier [12], we analyzed the effects of these factors and presented the corresponding explicit expressions and computational formulas. At the same time, Eq. (1) is quite adequate for our problem on the insufficient initial information, with the exception that this time there was no displacement of the realizations along the array sides.

With the introduced notations ρ/d and $L = d(N - 1)$, simple transformations lead to the result:

$$r_{\min} = \left(\frac{\rho}{d}\right)^2 \frac{d}{2\pi^{1/2}(N-1)\delta_{\text{random}}}. \qquad (2)$$

This expression determines the minimal acceptable value of the correlation coefficient for which the given error δ_{random} is provided in measuring the vessel displacement relative to the bottom. To find the required spacing of the receiving elements, one should use a set of plots similar to those shown in Fig. 3.

The estimates show that to obtain acceptable results in deep-ocean measurements with the GRANAT system (an accuracy of about several centimeters for a once measured vessel displacement), a decrease down to 0.7 in the correlation coefficient is allowed. The aforementioned considerations confirm that an array

whose parameters are close to those of the GRANAT system can be effectively used in all deep-water regions of the ocean.

ACKNOWLEDGMENTS

This work was supported by the Russian Foundation for Basic Research, project no. 98-05-65096.

REFERENCES

1. V. I. Volovov, Akust. Zh. **39**, 605 (1993) [Acoust. Phys. **39**, 317 (1993)].
2. V. I. Volovov, *Sound Reflection from the Ocean Bottom* (Nauka, Moscow, 1993).
3. V. I. Volovov, Akust. Zh. **40**, 142 (1994) [Acoust. Phys. **40**, 127 (1994)].
4. V. I. Volovov and A. I. Govorov, Akust. Zh. **43**, 476 (1997) [Acoust. Phys. **43**, 406 (1997)].
5. P. M. Cohen, Int. Hydr. Rev. **58** (1), 127 (1981).
6. P. H. Miln, Int. Hydr. Rev. **58** (1), 77 (1981).
7. B. S. McCartney, Int. Hydr. Rev. **58** (1), 91 (1981).
8. V. I. Volovov, A. I. Govorov, V. S. Gostev, and L. N. Nosova, Akust. Zh. **46**, 68 (2000) [Acoust. Phys. **46**, 56 (2000)].
9. F. R. Dickey and I. A. Edward, in *IEEE Plans Position Location Navigation Symposium Record* (San Diego, 1978), p. 255–271.
10. V. S. Riyait, M. A. Lawlor, A. E. Adams, *et al.*, Int. Hydr. Rev. **72** (1), 115 (1995).
11. V. I. Volovov and M. S. Klyuev, Akust. Zh. **40**, 571 (1994) [Acoust. Phys. **40**, 505 (1994)].
12. V. I. Volovov and M. S. Klyuev, Akust. Zh. **41**, 72 (1995) [Acoust. Phys. **41**, 62 (1995)].

Translated by E. Kopyl

Acoustical Physics, Vol. 47, No. 5, 2001, pp. 529–533. Translated from Akusticheskiĭ Zhurnal, Vol. 47, No. 5, 2001, pp. 611–615.

Acoustic Streaming with Resonance Gas Oscillations in a Cylindrical Tube

R. G. Galiullin, L. A. Timokhina, and S. E. Filipov

Kazan State University, ul. Kremlevskaya 18, Kazan, 420008 Russia

e-mail: elvira.galiullina@ksu.ru

Received May 12, 2000

Abstract—Acoustic streaming accompanying acoustic resonance oscillations of gas in a tube is considered. The effect of both the Prandtl number and the wall loss on the velocity of acoustic streaming in a viscous heat-conducting medium is investigated. Expressions for the longitudinal and transverse components of the flow velocity are obtained. © *2001 MAIK "Nauka/Interperiodica".*

Acoustic oscillations of gas in a channel give rise to stationary acoustic streaming, the study of which is important because of its role in the intensification of heat and mass transfer processes [1].

Rayleigh [2] was the first to consider the streaming that occurs in the case of the imposition of an acoustic field on a channel consisting of two plane-parallel plates. Later, acoustic streaming became the subject of numerous studies [3–7]. The limited validity of the theories developed in the cited publications is determined by the following facts: (a) the authors neglect the effects of the geometry of the volume and the way of excitation on the particle velocity in the flow core, where gas is assumed to be ideal [1–7]; (b) within the boundary layer, gas is assumed to possess a low viscosity and a zero heat conductivity [1–6]; and (c) the sound absorption by the walls is neglected.

The purpose of this paper is to study the effect of the Prandtl number on acoustic streaming in the case of oscillations of a real gas with absorption.

Oscillations excited in a long cylindrical tube ($L/R \gg 1$, where R is the radius of the tube and L is its length) by a piston performing harmonic oscillations with the amplitude $l_0 \ll L$ are characterized by the following parameters [8]:

$$M_p = \omega l_0/c_0, \quad \varepsilon = V/\omega L, \quad Sh = \omega R/V, \qquad H = R\sqrt{\omega/\nu}, \tag{1}$$

where c_0 is the sound velocity in an unperturbed gas, ν is the kinematic viscosity coefficient, V is the amplitude of the velocity oscillations at the open end, and ω is the cyclic frequency of oscillations. We assume that $H \gg 1$, $M_p \ll 1$, $\varepsilon \ll 1$, and $Sh \ll 1$. Then, instead of the full equations of motion, we can write the equations for the boundary layer, and, for $R/L \ll 1$, we also can neglect part of the terms in the energy equation. The solutions to the equations for $\varepsilon \ll 1$ can be sought in the form of a series expansion in the small parameter ε, where the subscript indicates the number of the approximation: 1 corresponds to the first (acoustic) approximation, 2 corresponds to the second approximation, etc.

The equations of the first approximation have the form

$$\rho_0 \frac{\partial u_1}{\partial t} + \frac{\partial p_1}{\partial x} = \frac{\mu}{r}\frac{\partial}{\partial r}\left(r\frac{\partial u_1}{\partial r}\right),$$

$$\frac{\partial \rho_1}{\partial t} + \frac{\rho_0}{r}\frac{\partial}{\partial r}(r v_1) + \rho_0 \frac{\partial u_1}{\partial x} = 0, \tag{2}$$

$$p_1 = \rho_0 R T_1 + R T_0 \rho_1,$$

$$\rho_0 C_p \frac{\partial T_1}{\partial t} = \frac{\partial p_1}{\partial t} + \frac{\lambda}{r}\frac{\partial}{\partial r}\left(r\frac{\partial T_1}{\partial r}\right),$$

where ρ is the density; p is the pressure; T is the temperature; R is the universal gas constant; C_p is the specific heat at constant pressure; μ is the dynamic viscosity coefficient; u and v are the axial and radial velocity components, respectively; x and r are the axial and radial coordinates; and t is time.

We consider the boundary conditions used in solving the equations of the first approximation. At the end at which the periodically oscillating piston is located, the condition considered in [9] is satisfied. In the case of a harmonically oscillating piston, the following relation is valid:

$$\tilde{u}_1(x = 0) = M_p \exp[i(\omega t - \pi/2)]. \tag{3}$$

At the open end, a nonlinear boundary condition is set [10]:

$$\tilde{p}_1(x = L) = m r_1 \tilde{u}_1(x = L), \tag{4}$$

where m is a constant, which can be calculated according to the method described in [10]. We consider the case of an isothermal wall with T_w = const.

1063-7710/01/4705-0529$21.00

The system of equations (2) describes the oscillatory motion in a narrow cylindrical tube and corresponds to the so-called case of a "low reduced frequency." The general solution to the equations of the first approximation is presented in [10]. When $H \gg 1$, this solution takes the form

$$\begin{aligned} p_1 &= \rho_0 c_0^2 r_1 \cos(kx + \alpha + i\beta)\exp[i(\omega t + \psi)], \\ u_1 &= r_1 c_0 \sin(kx + \alpha + i\beta) \\ &\times \exp[i(\omega t + \psi - \pi/2)](1 - e^{-(1+i)\eta}), \\ v_1 &= \frac{(1+i)\omega\delta}{2} r_1 \cos(kx + \alpha + i\beta) \\ &\times \left\{\left(1 + \frac{\kappa - 1}{\sqrt{\sigma}}\right)\frac{r}{R} - e^{-(1+i)\eta}\right. \\ &\left. - \frac{\kappa - 1}{\sqrt{\sigma}} e^{-(1+i)\eta\sqrt{\sigma}}\right\}\exp[i(\omega t + \psi)], \\ \rho_1 &= \rho_0 r_1 \cos(kx + \alpha + i\beta) \\ &\times \{1 + (\kappa - 1)e^{-(1+i)\eta\sqrt{\sigma}}\}\exp[i(\omega t + \psi)]. \end{aligned} \tag{5}$$

Here, r_1 and ψ are the magnitude and the principal value of the argument of the dimensionless oscillation amplitude; $k = k_0[(1 + \beta') + i\beta'']$, where $k_0 = \dfrac{\omega}{c_0}$, $\beta'' = -\beta' = -\dfrac{1}{2}\left(1 + \dfrac{\kappa - 1}{\sqrt{\sigma}}\right)\dfrac{r}{R}$, $\delta = \sqrt{\dfrac{2\nu}{\omega}}$, $\eta = \dfrac{R - r}{\delta}$; α and β are constants; σ is the Prandtl number; and $\kappa = C_p/C_v$, where C_v is the specific heat at constant volume.

To determine r_1, ψ, α, and β, it is necessary to average the second equation of Eqs. (5) over the tube cross-section [8]:

$$\begin{aligned} \tilde{p}_1 &= r_1 \cos(kx + \alpha + i\beta)\exp[i(\omega t + \psi)], \\ \tilde{u}_{1e} &= r_1 \mu_1 \sin(kx + \alpha + i\beta)\exp[i(\omega t + \psi + \varphi - \pi/2)], \end{aligned} \tag{6}$$

where μ_1 and φ are the magnitude and the principal value of the argument of the function $\Phi = \Phi(H)$ [8], $\tilde{p}_1 = p_1/\rho_0 c_0^2$, and $\tilde{u}_{1e} = u_{1e}/c_0$. For $H \gg 1$, we have $\mu_1 \approx 1$ and $\varphi \approx 0$. The substitution of Eqs. (6) in the boundary conditions (3) and (4) yields [10]

$$\begin{aligned} \alpha &= \frac{\pi}{2} - k_0 L(1 + \beta'), \quad \beta = k_0 L\beta' + m r_1, \\ r_1 &= \frac{1}{2m}\{[(k_0 L\beta')^2 + 4mM_p]^{1/2} - k_0 L\beta'\}. \end{aligned} \tag{7}$$

The equations of the second approximation describe the oscillatory motion with the frequency 2ω and the secondary stationary motion. To separate the latter, we average these equations over time:

$$\begin{aligned} &\frac{\partial\langle p_2\rangle}{\partial x} - \frac{\mu}{r}\frac{\partial}{\partial r}\left(r\frac{\partial\langle v_2\rangle}{\partial r}\right) \\ &= -\rho_0\left(\left\langle u_1\frac{\partial u_1}{\partial x}\right\rangle + \left\langle v_1\frac{\partial v_1}{\partial r}\right\rangle\right) - \left\langle \rho_1\frac{\partial u_1}{\partial t}\right\rangle, \\ &\rho_0\left[\frac{1}{r}\frac{\partial(r\langle v_2\rangle)}{\partial r} + \frac{\partial\langle u_2\rangle}{\partial x}\right] \\ &= -\left\langle v_1\frac{\partial\rho_1}{\partial r}\right\rangle - \left\langle u_2\frac{\partial\rho_1}{\partial x}\right\rangle + \left\langle\frac{\rho_1}{\rho_0}\frac{\partial\rho_1}{\partial t}\right\rangle. \end{aligned} \tag{8}$$

Here, the angular brackets denote the time averaging. We substitute Eqs. (5) in Eqs. (8) on their right-hand sides. In doing so, we take into account that, according to Eqs. (7), the quantity β is a first-order quantity. The resulting equations should be integrated with allowance for the boundary conditions

$$\begin{aligned} \langle u_2\rangle &= \frac{\partial\langle u_2\rangle}{\partial r} = 0, \quad r = 0, \\ \langle u_2\rangle &= \langle v_2\rangle = 0, \quad r = R. \end{aligned} \tag{9}$$

The integration of the first equation of Eqs. (8) yields

$$\langle u_2\rangle = C_1 r^2 + C_2 + \frac{c_0 r_1^2}{4} g_1(\eta, \sigma)\sin 2z, \tag{10}$$

$$\begin{aligned} g_1(\eta, \sigma) &= 3e^{-\eta}\sin\eta + \left(1 + \frac{\kappa - 1}{\sqrt{\sigma}}\right)e^{-\eta}\cos\eta \\ &+ \frac{1}{2}e^{-2\eta} - \frac{\kappa - 1}{\sqrt{\sigma}}e^{-\eta\sqrt{\sigma}}\sin\eta\sqrt{\sigma} \\ &- \frac{2(\kappa - 1)\sqrt{\sigma}}{(1 + \sigma)^2}e^{-(1+\sqrt{\sigma})\eta}\cos(1 - \sqrt{\sigma})\eta \\ &+ \frac{(\kappa - 1)(1 - \sigma)}{(1 + \sigma)^2}e^{-(1+\sqrt{\sigma})\eta}\sin(1 - \sqrt{\sigma})\eta, \end{aligned} \tag{11}$$

where $z = k_0 x(1 + \beta') + \alpha_0$.

To calculate $\langle v_2\rangle$, we differentiate Eq. (10) with respect to x, then substitute the result into the second equation of Eqs. (8) and integrate it once with respect to r with allowance for the fact that, near the wall, we have

$$\frac{1}{r}\frac{\partial\langle r v_2\rangle}{\partial r} = -\frac{1}{\delta}\frac{\partial\langle v_2\rangle}{\partial\eta}.$$

Then, for $\langle v_2\rangle$, we obtain

$$\begin{aligned} \langle v_2\rangle &= -C_1'\frac{r^3}{4} - C_2'\frac{r}{2} \\ &- \frac{\omega\delta r_1^2}{8}\{g_2(\eta, \sigma) + g_3(\eta, \sigma)\}, \end{aligned} \tag{12}$$

where

$$
\begin{aligned}
g_2(\eta,\sigma) &= -e^{-\eta}\cos\eta - e^{-\eta}\sin\eta - \frac{(\kappa-1)^2}{\sqrt{\sigma}}e^{-2\eta\sqrt{\sigma}} \\
&+ (\kappa-1)\left(1+\frac{\kappa-2}{\sqrt{\sigma}}\right)e^{-\eta\sqrt{\sigma}}\cos\eta\sqrt{\sigma} \\
&- (\kappa-1)\left(1+\frac{\kappa}{\sqrt{\sigma}}\right)e^{-\eta\sqrt{\sigma}}\sin\eta\sqrt{\sigma} \\
&- (\kappa-1)e^{-(1+\sqrt{\sigma})\eta}\cos(1-\sqrt{\sigma})\eta \\
&- (\kappa-1)e^{-(1+\sqrt{\sigma})\eta}\sin(1-\sqrt{\sigma})\eta, \\
g_3(\eta,\sigma) &= a_1 e^{-\eta}\cos\eta + b_1 e^{-\eta}\sin\eta \\
&+ a_2 e^{-\eta\sqrt{\sigma}}\cos\eta\sqrt{\sigma} + b_2 e^{-\eta\sqrt{\sigma}}\sin\eta\sqrt{\sigma} - \frac{(\kappa-1)^2}{\sqrt{\sigma}} \\
&\times e^{-2\eta\sqrt{\sigma}} + e^{-2\eta} + a_3 e^{-(1+\sqrt{\sigma})\eta}\cos(1+\sqrt{\sigma})\eta \\
&+ b_3 e^{-(1+\sqrt{\sigma})\eta}\sin(1-\sqrt{\sigma})\eta,
\end{aligned}
\tag{13}
$$

$$
a_1 = \left(9 - \frac{2(\kappa-1)}{\sqrt{\sigma}}\right),\quad a_2 = (\kappa-1)\left(1+\frac{\kappa-1}{\sqrt{\sigma}} - \frac{2-\sigma}{\sigma\sqrt{\sigma}}\right),
$$

$$
\begin{aligned}
a_3 &= -\frac{\kappa-1}{\sqrt{\sigma}(1+\sigma)^2}\{(1-\sigma)(1-\sqrt{\sigma})\sqrt{\sigma} \\
&- (\sigma^2+\sigma+2)(1+\sqrt{\sigma})\},
\end{aligned}
$$

$$
b_1 = 5 - \frac{2(\kappa-1)}{\sqrt{\sigma}},\quad b_2 = -(\kappa-1)\left(1+\frac{\kappa-1}{\sqrt{\sigma}} - \frac{2-\sigma}{\sigma\sqrt{\sigma}}\right),
$$

$$
\begin{aligned}
b_3 &= \frac{\kappa-1}{\sqrt{\sigma}(1+\sigma)^2}\{(\sigma^2+\sigma+2)(1-\sqrt{\sigma}) \\
&- (1-\sigma)(1+\sqrt{\sigma})\sqrt{\sigma}\}.
\end{aligned}
$$

The constants C_1 and C_2 are determined from the boundary conditions at the wall (Eqs. (9)). Finally, we obtain

$$
\begin{aligned}
\langle u_2\rangle &= \frac{c_0 r_1^2}{4}\left\{\left[g_1(0,\sigma)\left(1-\frac{2r^2}{R^2}\right) + g_1(\eta,\sigma)\right.\right. \\
&\left. - \frac{\delta}{R}g_3(0,\sigma)\left(1-\frac{2r^2}{R^2}\right)\right]\sin 2z \\
&\left. - \frac{2\omega x}{c_0}\frac{\delta}{R}g_2(0,\sigma)\left(1-\frac{r^2}{R^2}\right)\right\}, \\
\langle v_2\rangle &= \frac{\omega R r_1^2}{8}\left\{\left[2g_1(0,\sigma)\left(\frac{r^3}{R^3}-\frac{r}{R}\right) - \frac{\delta}{R}\left(g_3(0,\sigma)\right.\right.\right. \\
&\left.\times\left(\frac{r^3}{R^3}-\frac{2r}{R}\right) + g_3(\eta,\sigma)\right)\Big]\cos 2z \\
&\left. - \frac{\delta}{R}\left[g_2(0,\sigma)\left(\frac{r^3}{R^3}-\frac{2r}{R}\right) + g_2(\eta,\sigma)\right]\right\}.
\end{aligned}
\tag{14}
$$

Let us consider the behavior of acoustic streaming near the axis of the tube. We note that Eqs. (14) exactly satisfy the conditions set at the tube axis. According to the statement of the problem, we have $\delta/R \ll 1$ and, in addition, $g_1(\eta, \delta) \longrightarrow 0$. Therefore, without any considerable error, at the tube axis we have

$$
\langle u_2\rangle \approx \frac{c_0 r_1^2}{4}g_1(0,\sigma)\sin 2z,\quad \langle v_2\rangle = 0. \tag{15}
$$

In a liquid without heat conduction ($\sigma = \infty$), we have $g_1(0, \sigma) = 3/2$. In this case, we obtain a result that coincides with the result presented in [5]. Similarly, at $\sigma = 1$, we have $g_1(0, 1) = (2 + \kappa)/2$, and Eqs. (15) yield a result that agrees with [9].

Exactly at resonance, the maximum of $\sin 2z$ is in the middle of the tube, $x = 0.5L$. Then, at the tube axis, we obtain

$$
\begin{aligned}
\tilde{u}_{2m}^0 &= \frac{\langle u_{2m}^0\rangle}{c_0 r_1^2} \\
&= \frac{1}{4}\left\{g_1(0,\sigma) - \frac{\delta}{R}\left[g_3(0,\sigma) + \frac{\omega L}{c_0}g_2(0,\sigma)\right]\right\},
\end{aligned}
\tag{16}
$$

where the superscript 0 indicates the tube axis and the subscript m indicates the maximum corresponding to $x = 0.5L$.

The dependence of $\tilde{u}_{2m}^0$ on σ for the parameter of the setup described in [11] is shown in Fig. 1. One can see that a decrease in the Prandtl number leads to an increase in $\tilde{u}_{2m}^0$ and vice versa.

Figure 2 presents the dependences of $\tilde{u}_{2m}$ on the quantity $(R - r)/R$ for three values of σ (0.1, 0.7, and 1.0) in the flow core. One can see that a decrease in the

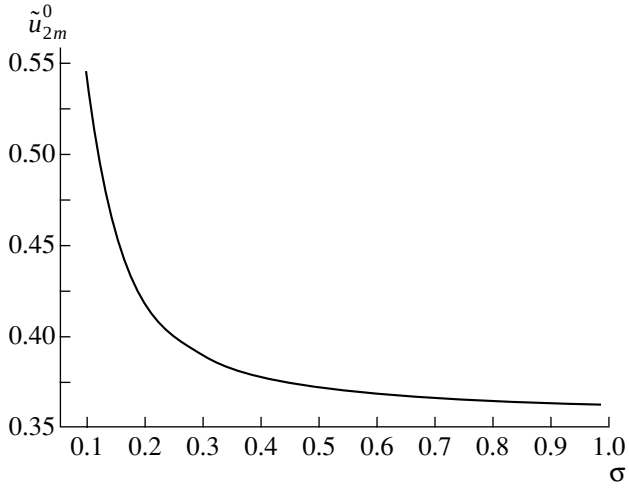

Fig. 1. Dependence of $\tilde{u}_{2m}^0$ on the Prandtl number σ for the parameter of the setup used in [11].

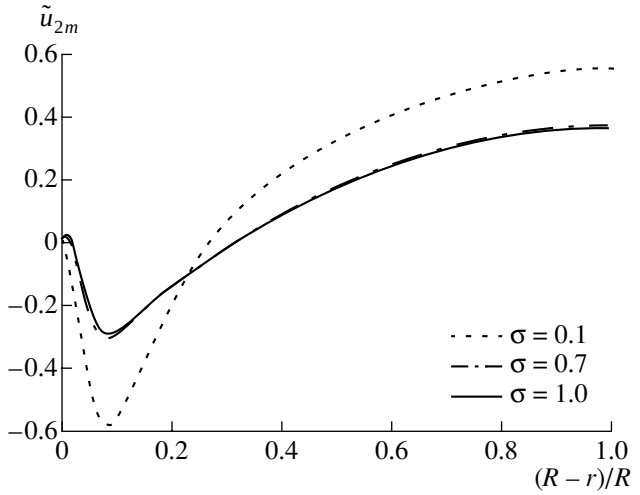

Fig. 2. Dependence of $\tilde{u}_{2m}$ on the dimensionless radial coordinate $(R - r)/R$ in the flow core at $x = L/2$ for $\sigma = 0.1$, 0.7, and 1.0.

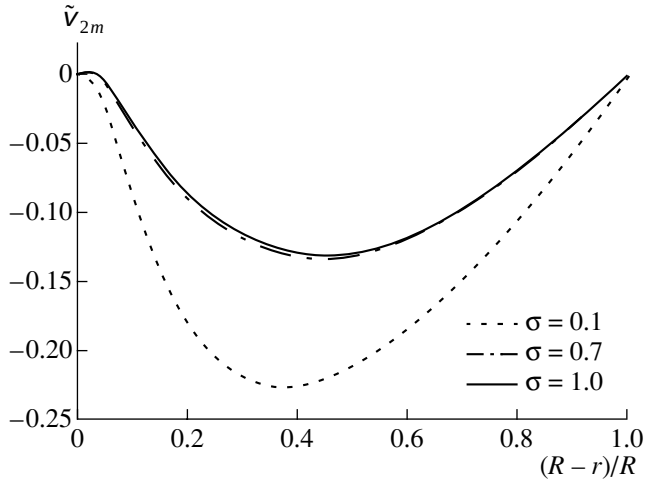

Fig. 3. Dependence of $\tilde{v}_{2m}$ on the dimensionless radial coordinate $(R - r)/R$ in the flow core at $x = 0$ for $\sigma = 0.1$, 0.7, and 1.0.

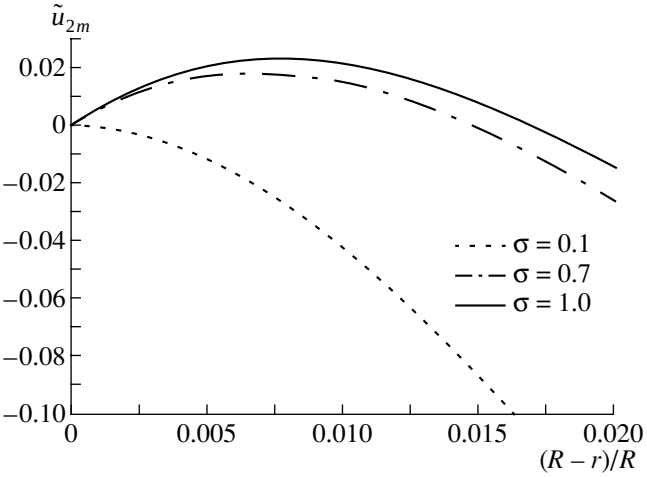

Fig. 4. Dependence of $\tilde{u}_{2m}$ on the dimensionless radial coordinate $(R - r)/R$ in the near-wall region at $x = L/2$ for $\sigma = 0.1$, 0.7, and 1.0.

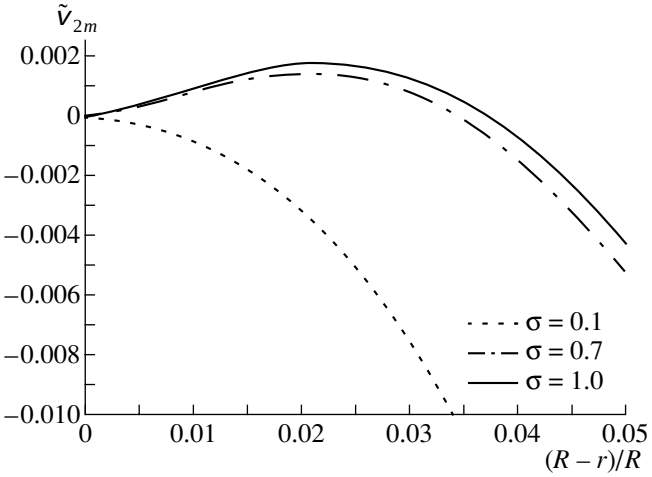

Fig. 5. Dependence of $\tilde{v}_{2m}$ on the dimensionless radial coordinate $(R - r)/R$ in the near-wall region at $x = 0$ for $\sigma = 0.1$, 0.7, and 1.0.

Prandtl number leads to a considerable (almost twofold) increase in the absolute value of $\tilde{u}_{2m}$ near the wall.

The maximums of $|\cos 2z|$ correspond to the ends of the tube, $x = 0$ and $x = L$. The dependence of $\tilde{v}_{2m}$ on $(R - r)/R$ in the flow core at $x = 0$ is shown in Fig. 3 for different Prandtl numbers ($\sigma = 0.1$, 0.7, and 1.0). One can see that a decrease in σ leads to an increase in the absolute value of $\tilde{v}_{2m}$ and a shift of the maximum of $\tilde{v}_{2m}$ toward the tube wall.

The dependence of $\tilde{u}_{2m}$ on the dimensionless radial coordinate $(R - r)/R$ for three values of σ (0.1, 0.7, and 1.0) in the near-wall region at $x = L/2$ is presented in Fig. 4. One can see that, in the near-wall vortex, which corresponds to the regions with $\tilde{u}_{2m} > 0$, the axial velocity component is much less than in the flow core. A decrease in the Prandtl number leads to a decrease in the size of the region occupied by the near-wall vortex, down to a total disappearance of the latter. The dependence of $\tilde{v}_{2m}$ on $(R - r)/R$ in the near-wall region at $x = 0$ is shown in Fig. 5 for three values of σ ($\sigma = 0.1$, 0.7, and 1.0). As one would expect, the size of the region occupied by the near-wall vortex decreases with decreasing σ. The distance within which $\tilde{v}_{2m}$ vanishes is approximately twice as long as the corresponding distance for $\tilde{u}_{2m}$.

The effect of the wall loss on the acoustic streaming can be revealed by considering the factor $c_0 r_1^2/4$ from Eqs. (14) to the piston velocity u_P. Taking into account Eqs. (7), we obtain

$$\frac{r_1^2}{4M_p} = \frac{1}{4m^2}[(N^2 + 4m)^{1/2} - N]^2, \qquad N = \frac{k_0 L \beta'}{\sqrt{M_p}}, \tag{17}$$

where m is a parameter, which in the conditions defined in [11] is equal to 0.346. One can see that the axial component of the velocity of acoustic streaming is determined by the parameter N: for the parameters of the setup described in [11], the variation of N from 0.309 to 0.715 leads to a decrease in $r_1^2/4M_p$ from 1.719 to 0.914.

Thus, it is evident that the flow velocity strongly depends on the Prandtl number and on the wall loss.

REFERENCES

1. R. G. Galiullin, V. B. Repin, and N. Kh. Khalitov, *Viscous Liquid Flow and the Heat Transfer between Bodies in a Sound Field* (Kazan. Gos. Univ., Kazan, 1978).
2. J. W. S. Rayleigh, *The Theory of Sound*, 2nd ed. (Macmillan, London, 1896; Gostekhizdat, Moscow, 1955), Vol. 2.
3. L. K. Zarembo and V. A. Krasil'nikov, *Introduction to Nonlinear Physical Acoustics* (Nauka, Moscow, 1966).
4. W. Nyborg, in *Physical Acoustics*, Ed. by W. Mason (Academic, New York, 1965; Mir, Moscow, 1966), Vol. 2, Part B.
5. O. V. Rudenko and S. I. Soluyan, *Theoretical Foundations of Nonlinear Acoustics* (Nauka, Moscow, 1975; Consultants Bureau, New York, 1977).
6. B. M. Galitseĭskiĭ, Yu. A. Ryzhov, and E. V. Yakush, *Thermal and Hydrodynamic Processes in Oscillating Flows* (Mashinostroenie, Moscow, 1977).
7. N. Rott, Z. Angew. Math. Phys. **25**, 417 (1975).
8. R. G. Galiullin, A. Z. Murzakhanova, and I. P. Revva, Akust. Zh. **36**, 973 (1990) [Sov. Phys. Acoust. **36**, 545 (1990)].
9. R. G. Galiullin, I. P. Revva, and G. G. Khalimov, *Theory of Thermal Self-Oscillations* (Kazan. Gos. Univ., Kazan, 1982).
10. R. G. Galiullin, E. R. Galiullina, and E. I. Permyakov, Akust. Zh. **42**, 769 (1996) [Acoust. Phys. **42**, 677 (1996)].
11. E. Stuhltrager and H. Thomann, Z. Angew. Math. Phys. **37**, 155 (1986).

Translated by E. Golyamina

Acoustical Physics, Vol. 47, No. 5, 2001, pp. 534–539. Translated from Akusticheskiĭ Zhurnal, Vol. 47, No. 5, 2001, pp. 616–622.

Spatial Correlation of the Sound Field in an Ocean Shelf Zone

O. P. Galkin, R. Yu. Popov, Yu. V. Semenov, and E. V. Simakina

Andreev Acoustics Institute, Russian Academy of Sciences, ul. Shvernika 4, Moscow, 117036 Russia

e-mail: bvp@akin.ru

Received December 26, 2000

Abstract—The spatial correlation of explosive signals received by hydrophones lying on the bottom of a shelf zone is studied as a function of the length of the propagation path. The correlation coefficient is found to exhibit quasi-periodic variations with increasing distance to the explosive source of sound. It is shown that the value of the correlation coefficient noticeably increases and its periodic variations practically disappear when the measurements are performed for the signals arriving by individual rays or narrow ray bundles. The low efficiency of a linear horizontal receiving array is pointed out. © *2001 MAIK "Nauka/Interperiodica".*

In recent years, the problems related to monitoring the ocean are often solved with the use of small self-contained sonar systems positioned in the sea away from the shore. However, because of the short lifetime and small detection range of such systems, a certain number of stationary zonal observation systems are also used for these purposes. The receiving arrays of such systems are placed in coastal waters, and the data received through the communication lines are supplied for further processing to computer systems installed at onshore laboratories. Since the construction of such sonar systems is quite expensive, it is important to have some justified predictions concerning the efficiency of their operation. Such predictions are impossible without considering the specific features of the sound field formation by signals and noise in the coastal wedge conditions. One of the important parameters of a sound field is the spatial correlation radius of the field and its variation with distance to the sound source.

Below, we describe the results obtained by studying the spatial correlation of the sound field in a coastal wedge of the Pacific coast of Kamchatka. The experiment was carried out in summer (in July). Figures 1 and 2 present the experimental site and the characteristics of the waveguide along the ~300-km-long propagation path used in the experiment. The conditions of the sound propagation varied along the path: the depth of the underwater sound channel axis was 100–105 m within the deep-water part of the path, decreased in the coastal wedge, and, finally, reached 60 m at the reception point. In addition, the sound velocity gradients above and below the sound channel axis differed greatly in the deep-water and shallow-water parts of the path.

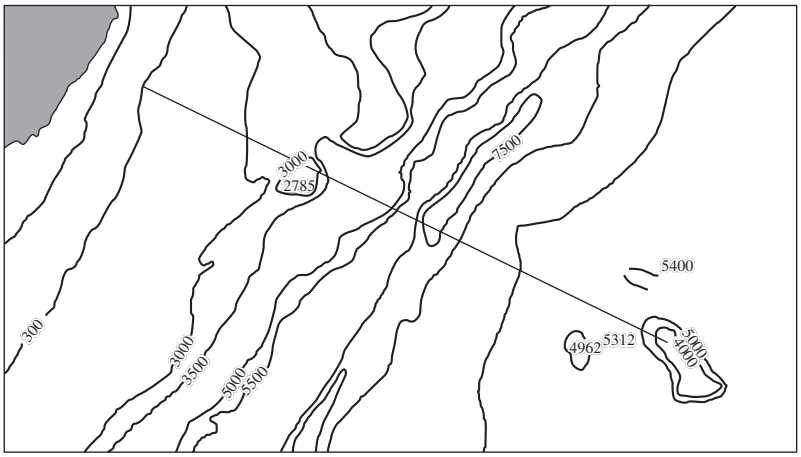

Fig. 1. Region of the experiment and the position of the acoustic propagation path.

1063-7710/01/4705-0534$21.00 © 2001 MAIK "Nauka/Interperiodica"

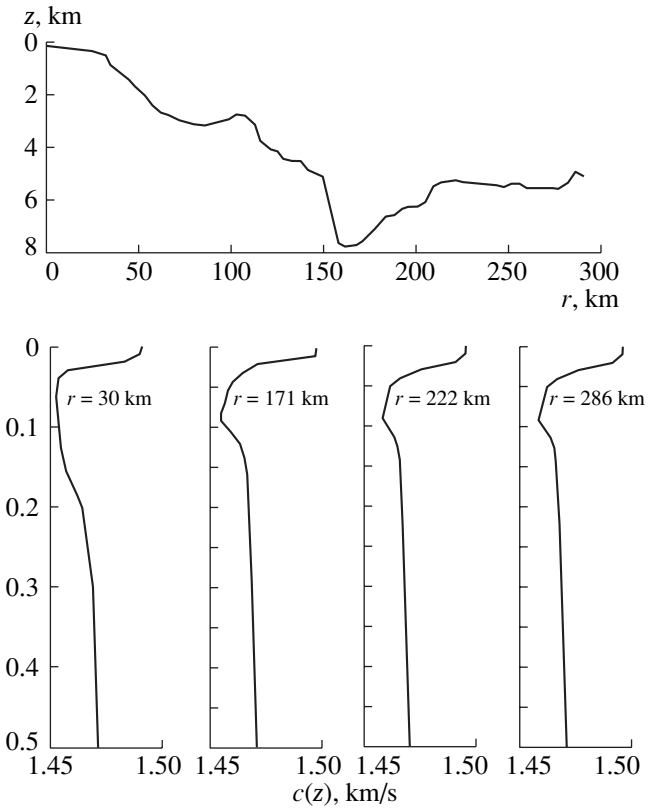

Fig. 2. Bottom profile along the path and the sound velocity c versus the depth z at four points of the path.

The propagation path was approximately perpendicular to the general isobath line. The angle made by the path with the normal to the receiving base was ~8°, and the point of intersection of the path with the line connecting the hydrophones was not at the center of the base, but away from it (at a distance of 4 km from the nearest hydrophone). The major part of the path ran through a deep-water region (where the ocean depth was greater than 2 km), and the rest of the path belonged to the continental slope and the shelf zone. The bottom slope angle varied from 5°–6° in the continental slope region to 0.5° near the hydrophones.

The sources of sound were explosive charges of mass ~300 g, which exploded at a depth of 150 ± 3 m. The charges were dropped into water from the board of a moving ship at 14-km intervals along the path. The explosion signals were received by two hydrophones positioned at the bottom along the 300-m isobath at a distance of ~6 km from each other. The signals received by the hydrophones were transmitted through radio channels (radio buoys) to a computer installed on a research ship. There, the structure of multiray signals was analyzed and the spatial correlation of the signals was studied as a function of the distance to the sound source. In particular, the cross-correlation coefficient was calculated for the signals received by the hydrophones in the frequency band 40–60 Hz.

Figure 3 shows the form of the signals received by one of the hydrophones (in a wide frequency band from ~20 to ~500 Hz) for different distances to the transmitting ship. From this figure, it follows that the duration of the signals received at long (greater than 100 km) and short (smaller than 30 km) distances exceeds the signal duration observed for the part of the path between 30 and 60 km. This occurs, because the variation of the time structure of a multiray signal with distance is governed by fundamentally different mechanisms within the deep-water and shallow-water parts of the path.

When the explosions occur near the hydrophones, i.e., in the shallow-water region, most signals experience

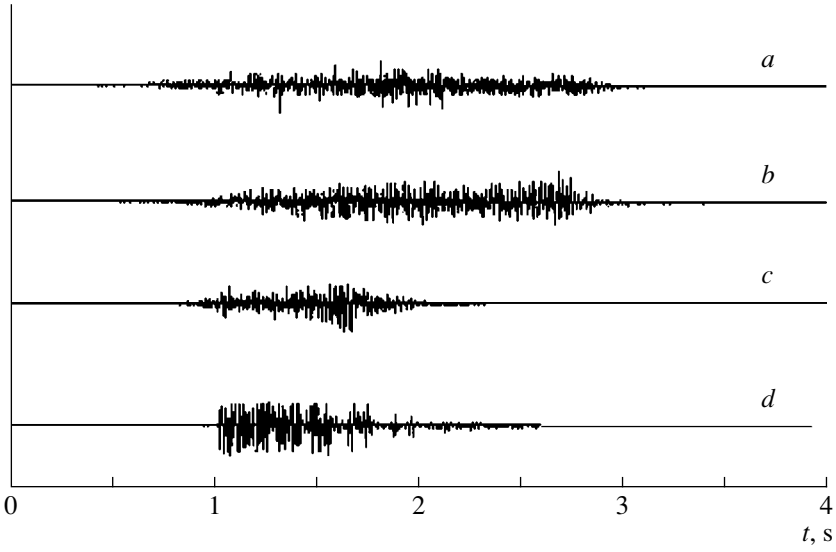

Fig. 3. Form of the received explosion signals for different distances to the explosion point: (*a*) 286, (*b*) 216, (*c*) 48, and (*d*) 6 km.

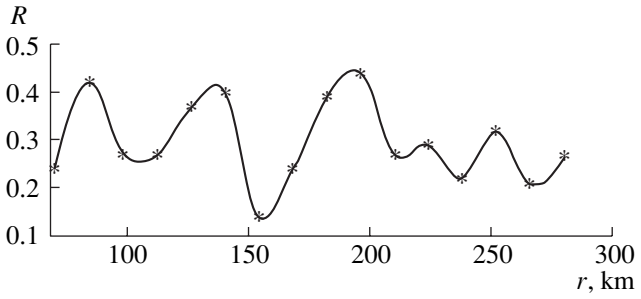

Fig. 4. Dependence of the cross-correlation coefficient R of the explosion signals received by two bottom-moored hydrophones on the distance to the explosion point. The averaging time T coincides with the signal spreading time ΔT.

bottom–surface reflections before they reach the hydrophones. The steeper the rays by which the explosion sound propagates, the greater the number of reflections experienced by the corresponding signal and the greater its delay time relative to the arrivals of signals propagating by less steep rays. As the distance from the hydrophones to the explosion points increases and the thickness of the water layer increases simultaneously; the number of signals that experience reflections from the boundaries of the water layer, as well as the number of reflections themselves, decreases, and the delays in the arrivals of these signals relative to the arrivals of signals propagating by the least steep rays decrease.

As the explosion points are shifted to the deep-water part of the path, the formation of the time structure of the received multiray signals becomes more strongly affected by the depth dependence of the sound velocity than by the boundaries of the water layer. In the hydrological conditions under consideration, most signals experience no reflections from the boundaries, and the sequence of the signal arrivals corresponds to the conditions of sound propagation in a deep ocean. In this case, the signals propagating by the water rays with maximal grazing angles arrive before the signals propagating by the rays with small grazing angles. In the experiment described in this paper, a distance to the explosion point of about 50 km corresponds to the distance at which the spreading of a multiray signal in the shallow-water and deep-water parts of the path compensate each other, and the resulting spreading time of the received multiray explosion signal is minimal.

Let us analyze the behavior of the cross-correlation coefficient R of the signals received by the bottom-moored hydrophones as a function of the distance to the point of explosion. Figure 4 presents the values of R versus the path length r (for the distances from 70 to 300 km). These data were obtained with the averaging time T equal to the spreading time of the explosion signal T, i.e., with allowance for all signals arriving to the spatially separated points of reception. The curve in Fig. 4 reveals the variations of R within 0.2–0.5 with a modulation depth of 0.15–0.20 and a period of about 50 km. The average value of R taken with allowance for the results of measurements on the whole path (from 6 to 300 km) is equal to 0.3 ± 0.1. Unfortunately, it was impossible in the experiment to repeat the measurements by passing along the path several times in order to obtain a more reliable average value.

Let us dwell on the explanation of the experimental results. The correlation of sound signals can be disturbed by a variety of factors. In the conditions under study, the main factors presumably are as follows: the uncorrelated signal fluctuations due to the inhomogeneities of the ocean medium and the boundaries of the water layer; the difference in the acoustogeological characteristics of the path near each of the hydrophones; and the multiray character of the sound propagation, which leads to a difference in the sound field structure at the spatially separated reception points and, hence, to the absence of a single phase front of the total arriving signal.

The quasi-periodic variations of R with increasing path length can hardly be explained by the phase fluctuations caused by random inhomogeneities of the medium, because the rms fluctuation of the propagation time of an individual signal monotonically increases with distance [1]. However, this process evidently makes some contribution to the decrease in the "smoothed" value of R with increasing distance. The difference in the acoustogeological characteristics in the region of reception are practically independent of distance for sufficiently large values of r ($r \gg l$, where $l = 6$ km is the distance between the hydrophones), and, hence, this difference also cannot explain the behavior of R shown in Fig. 4.

The variations of the angular (in the vertical plane) and time spectra of the signal at the hydrophone sites can be caused by the presence of the longitudinal component of the receiving base Δr and by the variations of the range of the vertical angles of signal arrivals by different rays because of the difference in the conditions of the signal entry into the coastal wedge for different distances r. We note that, even when $\Delta r = 0$, the variations observed in the angular spectrum of the received signals can be caused by an inaccurate positioning of the bottom-moored hydrophones in depth. In the case under consideration, Δr not only was nonzero, but also varied with the distance r, because the path ran on the side of the hydrophone base.

The geometry of the experiment determined first a monotone and fast decrease in Δr with increasing distance to the source (up to $r \approx 58$ km, where Δr is close to zero) and then a slow increase in Δr with a further increase in r. A change in Δr leads to a transformation of the interference structure of the field at the reception points. However, the periodicity of the interference transformations and the corresponding variations of R must depend on the distance r. Such a dependence is not observed for the variations of R shown in Fig. 4.

If a kind of zonal field structure exists in the deep ocean, the changes in the conditions of the signal entry into the coastal wedge should be almost periodic. To justify this statement, we calculated the field parameters in the region of reception for different distances to the point of explosion with allowance for the following data obtained in the course of the experiment: the sound velocity profiles $c(z)$ measured at six points along the path, the echo-sounding data on the bottom profile along the path, and the probability estimates made for the parameters of the ground on the basis of single measurements. The calculation showed that, as the distance to the source increases, considerable and almost periodic changes occur in both the range of the vertical angles of signal arrivals by different rays and the relative part of energy transferred along the water rays, i.e., rays that experience no bottom or surface reflections (we took into account the signals with the focusing factors no less than unity). As for the signals that experience bottom–surface reflections, their arrival times at the hydrophones are random to a considerable extent (specifically, the arrival time of such a signal depends on the parameters of the bottom roughness), and the corresponding part of the sound energy should be treated as a "signal" noise. One can plot an approximate dependence of the signal-to-"signal" noise ratio on the distance r and compare it with the curve $R(r)$.

Figure 5 presents the calculated ratio (in percent) of the energy E of the signals arriving by water rays to the total energy E_0 incident on a hydrophone versus the distance to the source r. The calculations were performed with a step of 14 km in distance, which corresponded to the experimental conditions. In terms of the periodicity of the process, the calculated curve agrees well with the dependence shown in Fig. 4. Thus, the main factor responsible for the specific features observed in the behavior of the function $R(r)$ is the multiray nature of the sound propagation in the ocean and the ensuing complex structure of the field at the reception points. However, the relatively large interval used for the field measurements in the experiment could prevent the detection of the details in the dependence of the spatial correlation coefficient on the distance to the sound source. To test this assumption, we calculated the field with a smaller step in distance (5 km). The analysis of the results of this calculation shows that the periodicity characterizing the variation of the conditions of the multiray signal entrance into the coastal wedge with distance (i.e., with r varying from 100 to 300 km) is about 25–30 km and is not observed in the experimental curve (Fig. 4) precisely because of the distance between the adjacent explosion points was too large.

The results presented above referred to the case when the signal averaging time T was equal to the whole length of the realization of the received explosion signal, i.e., was equal to the spreading time ΔT. There exists a possibility for a more detailed analysis of the changes that occur in the time structure of the received signals with distance from the source. The

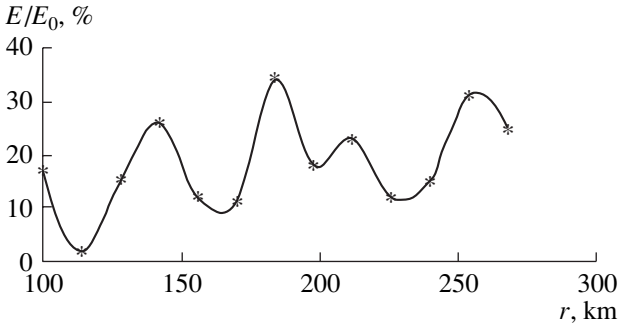

Fig. 5. Calculated ratio (percent) of the acoustic energy E arriving by the water rays to the total energy E_0 incident on a hydrophone as a function of the distance to the sound source r.

point is that the pulsed character of the transmitted signal makes it possible to resolve in time a major part of the signal arrivals by individual rays or narrow ray bundles. Then, by measuring the short-time correlation function $R^*(t)$ for t varying within the duration of the explosion signals received by the hydrophones ($t \le \Delta T$), it is possible to reveal the changes in the time structure of the signal within fractions of the period of the mean frequency of the analysis. The changes in the angular spectrum, which is usually related to the arrival times of signals propagating by the rays, can also be estimated to some extent. The technique used for such measurements is described in the literature [2, 3].

Figure 6 shows examples of the time dependence of the short-time correlation function R^* for different explosions. The delay time of the signal received by one of the hydrophones relative to the signal arriving at the other hydrophone is selected for the processing so as to obtain absolute maximums of the function $R^*(t)$ in this figure. The curves shown in Fig. 6 correspond to explosions fired at the following points: (*a*) at one of the end points of the path, (*d*) at a distance of ~48 km from the starting point of the path (this distance is close to the minimal value of Δr), and (*e*) in the vicinity of the 300-m isobath; (*b*, *c*) the remaining two curves correspond to intermediate path lengths. The averaging time T was chosen to be equal to one fourth of the spreading time ΔT. With such a choice of T, the analysis is possible at any distances within close angular ranges of the signal arrivals by individual rays. However, the accuracy of the estimates of $R^*(t)$, which is known to be proportional to $\sqrt{T}$, proves to be different for different parts of the path: the upper bound of the possible measurement error varies from 0.10–0.15 for the most distant explosions (T = 1 s) to ~0.6 for the distances that correspond to the minimal spreading time (T = 0.37 s).

A characteristic feature of the curves is the change of sign of the function $R^*(t)$ within the duration of each of the explosions under study. In a deep sea, such a change can be caused by either the vertical separation of the hydrophones Δh or their separation along the

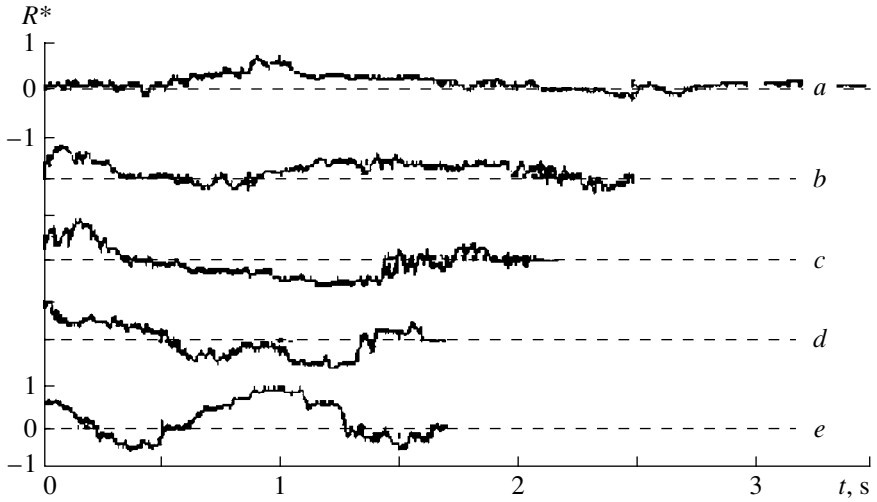

Fig. 6. Variation of the short-time correlation function R^* with time t for explosions fired at different distances from the hydrophones: (*a*) 286, (*b*) 216, (*c*) 160, (*d*) 48, and (*e*) 34 km.

path Δr. In the coastal wedge, a contributory factor can be the spatial variability of the parameters of the bottom at the reception site. In the measurements under consideration, the change of sign of the correlation function results from the combination of all three factors. The inaccuracy in positioning the bottom-moored hydrophones leads to a scatter in the reception depths and to the presence of a vertical component of the receiving base Δh [4].

Since the receiving base practically never coincided with the phase fronts of the arriving signal, the longitudinal component of this base Δr was always present. When the explosions occur at distant points of the path, Δr weakly depends on r. At the points belonging to the initial part of the path, i.e., in the coastal wedge, the variations of R^* with t become substantial (see curve *e* in Fig. 6), and noticeable changes in the behavior of the function $R^*(t)$ are observed even for adjacent explosion points. The latter fact is presumably related to the fast variation of Δr with r within this part of the path, as well as to the spatial variability of the parameters of the bottom at the reception site. The same is true for the variability of the range of the angular spectra of arriving signals. For example, for an explosion that occurs at a distance of ~28 km from the hydrophones, the range of arrival angles in the vertical plane is 13° (according to the calculation with allowance for only the rays whose focusing factor is no less than 0.5), whereas for the adjacent explosion (at r = 14 km), the corresponding angular range is 32°.

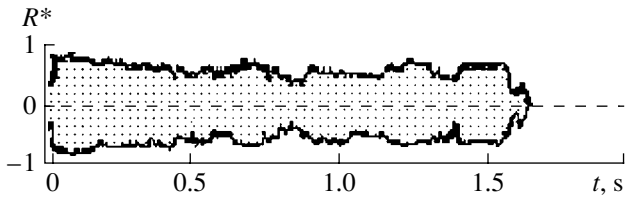

Fig. 7. Envelope of the curves $R^*(t)$ for τ varying within the period of the mean frequency of analysis. The path length is ~48 km.

The plots in Fig. 6 show that the peak value of $R^*(t)$ is within 0.8–0.9 for practically all distances. Therefore, one should expect that the spatial correlation coefficient of signals arriving by a narrow bundle of rays within any part of the range of vertical arrival angles will be sufficiently large for the corresponding values of the signal delay between the two hydrophones. To verify this statement, we consider the signals from an explosive source located at a distance of 48 km and obtain a set of curves $R^*(t)$ for different delays τ within the period of the mean frequency of analysis $\Delta\tau$ (curve *d* in Fig. 6 represents one of these curves for the delay τ_0 corresponding to the absolute maximum of the function $R^*(t)$). In the case under consideration, f_{av} = 50 Hz, and, hence, we have $\Delta\tau = 1/f_{av}$ = 20 ms $\{(\tau_0 - 10\ \text{ms}) \le \tau \le (\tau_0 + 10\ \text{ms})\}$. The envelope of these curves is shown in Fig. 7. One can see that, for the arrivals by a narrow bundle of rays (here, T = 0.37 s) at any possible vertical angles, the maximal values of $R^*(t)$ are no less than 0.8. Hence, the value of the spatial correlation coefficient obtained in the absence of the resolution of signal arrivals by individual rays (in our case, it is ten times smaller) does not reflect the potential coherence of the sound field. As one can see from Fig. 6, a substantial part of the signal proves to be negatively correlated at all distances. Therefore, the value of the correlation coefficient can be considerably smaller when the time of averaging coincides with the spreading time. For example, at the distance r = 48 km, the value of R at $T = \Delta T$ was as small as 0.08. In most practically important cases, when continuous signals are used rather than signals from a pulsed source, the length of the realization

to be analyzed and the corresponding averaging time T can noticeably exceed the spreading time in an oceanic waveguide. Therefore, the signals arriving by different rays cannot be resolved in time without special processing. In this case, the value of the spatial correlation coefficient of a multiray signal received by omnidirectional hydrophones proves to be much smaller than the corresponding values for the signals arriving by narrow ray bundles [5].

From the studies described above, we draw the following conclusions.

For explosive signals received by two omnidirectional hydrophones positioned at the bottom of a shelf zone at a distance of 6 km from each other, the cross-correlation coefficient, which was obtained with the averaging time equal to or greater than the spreading time of the multiray signals in the frequency band 40–60 Hz, exhibited amplitude variations within 0.08–0.45 with increasing distance to the explosion point (up to 300 km) with a period of about 50 km.

The sound field calculations corresponding to the experimental conditions showed that the main factor responsible for the amplitude variations of the spatial correlation coefficient is the almost periodic variation of the range of vertical angles of signal arrivals by different rays with increasing distance to the sound source. Simultaneously, the conditions of the signal entry into the coastal wedge and the relative amount of acoustic energy transferred by the water rays (without reflections) also vary. The period of these variations is about 20–25 km. The difference between the results of calculations and the experimental data is explained by the fact that, in the full-scale measurements, the distance between the adjacent explosion points was too large (14 km).

The short-time correlation coefficient of the received explosion signals (when the signals arriving by individual rays or narrow ray bundles are resolved in time) exhibits practically no amplitude variations, and its value obtained by the averaging time equal to one fourth of the signal spreading time in the frequency band 40–60 Hz is 0.8–0.9. The delay times, at which the aforementioned values of the correlation coefficient are observed, are different for different ray bundles.

The use of an extended horizontal cable-like array for monitoring ocean areas can be not very effective, because the spatial correlation of the sound field at the array aperture can be too low. In addition, the value of the correlation coefficient will vary with varying path length, and the period of such variations of the correlation coefficient will change with the source azimuth angle in different ways for different parts of the cable-like array. One of the possible methods to increase the efficiency of a receiving array is to develop it in the vertical plane, i.e., to use of a planar array. With the help of the latter, it is possible to obtain a directional pattern in the form of a vertical fan of narrow lobes. In this case, the value of the spatial correlation coefficient of the sound field can be high for each lobe, and, hence, its variations with distance from the source will be reduced.

ACKNOWLEDGMENTS

This work was supported by the Russian Foundation for Basic Research, project no. 00-02-17694.

REFERENCES

1. L. A. Chernov, *Wave Propagation in a Random Medium* (Akad. Nauk SSSR, Moscow, 1975; McGraw-Hill, New York, 1960).
2. O. P. Galkin, R. Yu. Popov, and E. V. Simakina, in *Acoustical Measurements: Methods and Means. The IV Session of the Russian Acoustical Society* (Moscow, 1995).
3. O. P. Galkin, A. V. Mikryukov, O. E. Popov, and R. Yu. Popov, Akust. Zh. **43**, 616 (1997) [Acoust. Phys. **43**, 529 (1997)].
4. Q. Wang and R. Zbang, J. Acoust. Soc. Am. **92**, 932 (1992).
5. P. F. Worcester, B. D. Comuelle, M. A. Dzieciuch, *et al.*, J. Acoust. Soc. Am. **105**, 3185 (1999).

Translated by E. Golyamina

Acoustical Physics, Vol. 47, No. 5, 2001, pp. 540–547. Translated from Akusticheskiĭ Zhurnal, Vol. 47, No. 5, 2001, pp. 623–631.

Regional Variability of the Phenomenon of Sound Penetration into Shadow Zones in the Ocean with Fine-Structure Stratification

V. S. Gostev and R. F. Shvachko

Andreev Acoustics Institute, Russian Academy of Sciences, ul. Shvernika 4, Moscow, 117036 Russia

e-mail: bvp@akin.ru

Received December 26, 2000

Abstract—The regional variability of the phenomenon of the shadow zone insonification in the ocean is manifested in the variability of the main parameters of the sound signals that penetrate into these zones because of the scattering by the fine-structure inhomogeneities of the refractive index. The intensity of the phenomenon is governed by a combination of the vertical distribution of intensity of the fine-structure inhomogeneities and the caustics that exist in the insonified domains, along with the caustic intensity and position, both of which depend on the mean sound speed profile and on the geometry of the experiment. For the chosen typical regions of the ocean, the characteristics of the fine structure are systematized, and the phenomenon under study is analyzed. The results obtained offer a justified approach to solving inverse problems and a way to perform practical-purpose studies aimed at improving the ultimate performance of underwater observation and monitoring systems.

Sharply anisotropic inhomogeneities of a fine structure can be treated as irregular (stochastic) in depth and regular (deterministic) in horizontal. These features lead to the Bragg scattering of sound and, hence, to such phenomena as sound penetration into shadow zones, prereverberation, and stochastic channeling. In other words, because of the sound reradiation by inhomogeneities, sound penetrates into domains (spatial, time, and angular ones) that are prohibited by the geometric acoustics. The intensity of insonification of the shadow zones depends both on the strength of the fine-structure inhomogeneities and on the presence and positions of caustics in the initial sound field, the caustics significantly enhancing the effect at hand. Therefore, to study the regional variability of the phenomenon of shadow-zone insonification, one should use the classification of ocean regions by both the vertical sound speed profiles and the fine-structure stratification.

The pattern of caustics in the initial sound field is governed by the sound speed profile and the depth of the source. The sound penetration into shadow zones has been successfully observed and studied many times in the tropical regions of the Indian and Pacific oceans and in the central region of the Atlantic Ocean [1–3]. In these regions, the vertical sound speed profiles are typical of tropical waters with a monotone decrease in the sound speed down to the depth of the sound channel axis and with a rather high gradient in the discontinuity layer. The phenomenon of sound penetration was most pronounced when the source was at depths of 0.2–0.3 km, while, for smaller source depths, the signals penetrating into the shadow zone became lower in their levels, nearly reaching the level of the ambient ocean noise.

We [4] have shown that, with certain assumptions, one can calculate the sound scattering by anisotropic fine-structure inhomogeneities from the only known characteristic: the one-dimensional vertical spectrum of sound speed fluctuations around the sound speed profile averaged over many realizations. In this case, the sound scattering by highly anisotropic, horizontally elongated inhomogeneities of the fine structure follows the Bragg diffraction law. A considerable level of scattering corresponds to the direction of specular reflection relative to the horizontal layered inhomogeneities. To calculate the squared pressure amplitude of the scattered wave, one can use the formula

$$P^2(r) = k^4 P_0^2 E_n(k_z) SV/2\pi r^2. \quad (1)$$

Here, k and P_0 are the wave number and pressure amplitude in the sound wave that is incident on the scattering structure, $E_n(k_z)$ is the vertical spatial spectrum of the fine-structure inhomogeinity, S is the area of the first Fresnel zone, V is the scattering volume, and r is the distance from it to the reception point. The argument of the vertical spectrum is taken to be equal in magnitude to the scattering vector, which, in the case of specular reflection, has only the vertical component: $k_z = 2k\sin\varphi$, where φ is the angle of the incidence direction relative to the horizon.

To estimate the expected intensity of the phenomenon, one should multiply the quantity $P^2(r)$ by the product of focusing factors F_s and F_I at the points of scatter-

1063-7710/01/4705-0540$21.00 © 2001 MAIK "Nauka/Interperiodica"

ing and reception. Then, for symmetric positions of the source and receiver, the received intensity can be calculated relative to the reference point that is located at a 1-km distance from the source (this procedure is considered in [1]). For the tropical region of the Indian Ocean, the intensity was experimentally measured with a sound source that was deployed to a depth of 0.2 km and emitted cw sound signals at frequencies from 0.63 to 3.15 kHz. For a distance of 10 km and a reception depth of 0.3 km, this relative intensity proved to be –40 to –50 dB, which agreed well with the calculated estimates.

The validity condition of the aforementioned approximation consists in the requirement for resonant inhomogeneity of the vertical scale $2\pi/k_z$ to horizontally extend for at least the length of the Fresnel zone [5]. For instance, in the case of backscattering at vertical incidence, the required value of the anisotropy ratio $\alpha = I_x/I_z$ can be found as $\alpha = 8(z/\lambda)^{1/2}$, where I_x and I_z are the horizontal and vertical scales of the inhomogeneities, respectively, and λ is the incident wavelength. For the frequency 1 kHz and depth z = 1 km, one obtains $\alpha \approx 2 \times 10^2$, this value being consistent with the anisotropy ratios for inhomogeneities observed in the ocean.

The fine-structure inhomogeneities manifest themselves in small deviations of the measured sound speed profiles from the general averaged one. The ocean medium is stratified in the form of more or less pronounced layers, 10 cm to 100 m thick, with lower vertical gradients of the thermohalinic parameters. These layers are separated by interlayers within which the vertical gradients can be much higher than the mean ones and have the same sign.

In addition, a situation is common (especially in the regions of thermohalinic fronts) when the fine-structure inhomogeneities are nearly compensated in the density field and inversion layers exist in the profiles $T(z)$ or $S(z)$ (or in both of them), where the gradients of T and S have the signs opposite to those of the mean gradients. According to [6], the first case corresponds to a stepped fine structure, while the second case is characteristic of a fine structure of intrusion type. These two types nearly exhaust the variety of the fine thermohalinic ocean structure, which, in turn, unambiguously determines the fine structure of the sound speed (of the refractive index).

In practice, a convenient way to describe the fine-structure inhomogeneities is to use statistical terms. With such a description, the sound speed field is broken into a large-scale deterministic component and a small-scale component of statistical nature. Garret and Munk [7] were the first to substantiate the possibility for the oceanic pycnocline to have a universal spectrum of the particle displacements ξ: $E_\xi(\kappa)$, where κ is the vertical wave number. On the background of the mean gradients of temperature, salinity, and sound speed, the field of internal waves, which has a universal space-time spectrum [7], must lead to universal spectra $E_T(\kappa)$ and $E_S(\kappa)$ that are equal to $E_\xi(\kappa)$ multiplied by the products of the corresponding gradients T_z and S_z. This statement has been experimentally confirmed [8–11] for the temperature spectra. Gregg [12] averaged 40 normalized spectra $E_{TN}(\kappa) = E_T(\kappa)/\overline{T}_z^2$ to construct the spectrum $\langle E_{TN}(\kappa)\rangle$ that corresponds to the model from [7] in its universality (for the wave numbers within $6 \times 10^{-4} \le \kappa \le 6 \times 10^{-2}$ cm^{-1}), but differs from this model in that it has two (rather than one) pronounced bands of wave numbers, which are separated by the scale $L_c = 2\pi/\kappa_c \approx 10$ m and has different exponents in the approximations $E_T(\kappa) \approx \kappa^{-\rho}$. According to [12], $\rho = 2$ for $\kappa \le \kappa_c$ and $\rho = 3$ for $\kappa \ge \kappa_c$ and $\rho = 3$ for $\kappa \ge \kappa_c$, while, according to [7], $\rho = 2.5$ for the entire range of κ and $\rho = 2$ in the latest modifications of the model [9, 10].

The fine-structure inhomogeneities of the sound speed or the refractive index, which are decisive for the acoustic models, have the same properties as the aforementioned temperature and salinity inhomogeneities. Small fluctuations n' of the refractive index can be estimated from the fluctuations of temperature T' as $n' = 2 \times 10^{-3} T'$.

We [4] directly measured the refractive index of the sea medium with the use of the cyclic velocitymeter that had a sensitivity of ~10^{-6} in units of the refractive index and a spatial resolution of approximately 1.5 m. We statistically processed the realizations of small disturbances $n'(z)$ in the vertical profile of the refractive index, which were obtained in different regions of the Atlantic and Indian oceans, down to a depth of about 3 km. The small-scale component was extracted by filtering with the cosine filter whose half-width was 30 m. The vertical spectra $E_n(\kappa_z)$ were calculated for the 300-m segments, which were sequentially shifted in depth. At all depths, the spectra obtained in this way exhibited approximately the same power-law dependence: $E_n(\kappa_z) = C_n \kappa_z^{-\rho}$ $(2 < \rho < 3)$, the value of ρ was equal to two in most cases. With $\rho = 2$, the experimental profiles of C_n were obtained that characterize the intensity of the fine-structure inhomogeneities of the refractive index at different depths in three typical ocean regions [4]: the tropical type (Figs. 1a and 1b) that is characteristic of the regions to the south from 20° N in the (a) Atlantic and (b) Indian oceans; the northern subtropical type (Fig. 1c) that is characteristic of the central region of the Atlantic Ocean (along the 30° W meridian, between 20° N and 40°–50° N, the warm half-year); and the Mediterranean type (Fig. 1d) that is characteristic of the ample area of the Mediterranean waters in the northern regions of the Atlantic Ocean (to the east of 30° W).

The experimental dependences presented in Fig. 1 offer the following quantitative conclusions:

(1) The fine structure of the sound speed (the refractive index) is most pronounced in the upper ocean layer,

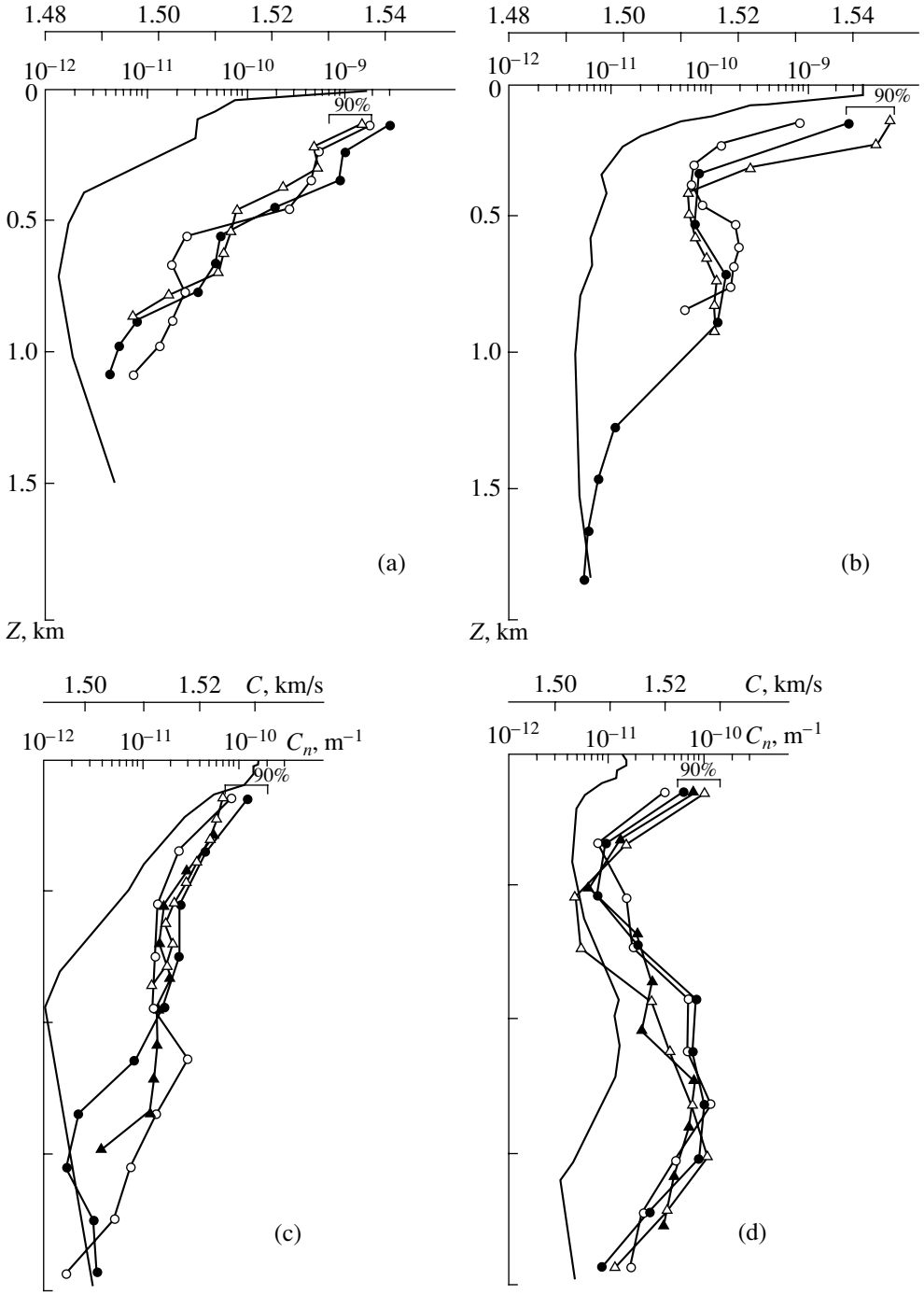

Fig. 1. Experimental profiles $C_n(z)$ for different ocean regions. At the left: average sound speed profiles.

down to the depth of the axis of the underwater sound channel (USC). At greater depths, the fine structure degenerates, and, in all regions, the value of C_n tends to 10^{-12} m^{-1}, which is of the order of the instrumental error.

(2) In the discontinuity layer, the quantity C_n depends on the vertical gradient of the refractive index: it reaches $(2–3) \times 10^{-9}$ m^{-1} in tropical regions with high gradients of the refractive index within the discontinuity layer, whereas, in subtropical regions, it is by an order of magnitude smaller.

(3) In the Mediterranean-type region of the Atlantic Ocean, at intermediate depths of 1.0–1.5 km, C_n increases up to the values typical of the discontinuity layer, which occurs because of the intense structuring processes in the water bulk and at the boundaries of the

core of Mediterranean waters entering the Atlantic Ocean.

(4) The depth dependences of C_n are monotone for the two other regions (Figs. 1a, 1c) of the Atlantic Ocean.

In our numerical calculations of the insonification of the shadow zones, we used a computer code [1] based on the ray approximation for the sound field. Most attention was paid to the calculation of caustic patterns. For this purpose, the calculation program was properly modified and supplied with additional tools of graphical representation of the computed data. An additional block of the software was developed to calculate and graphically represent the angular and time structures of the signals which, upon their specular reflection from the fine-structure inhomogeneities, arrive at a given point of the shadow zone. The modified software also allowed one to determine the positions of the domains from which the reflected signals originate. In the ray calculations of the initial sound field, we used different mean vertical profiles of the sound field, which provide a zonal structure of sound propagation with deep shadow zones. In view of the generalized experimental data on the vertical distribution of the fine structure, one can study the degree to which the shadow-zone insonification manifests itself.

To illustrate the above considerations, let us consider the shadow-zone insonification phenomenon for the subtropical region of the Central Atlantic (Fig. 1c). Figure 2a presents the vertical sound speed distribution down to a depth of 1 km, which governs the refraction of the channel-captured rays and the geometry of shadow zones. Figure 2b shows the arrival times for the signals propagating over the rays which leave the source (at a depth of 0.3 km) upwards and are specularly reflected by the horizontally elongated fine-structure layers presumably existing at all depths. These rays arrive at the given reception point, which lies in the shadow zone at the distance 15 km and at the depth 0.3 km, from above (curve *1*) and from below (curve *2*). The arrival times are plotted against the departure angle. In Fig. 2c, the depths of the specular reflections are presented for the rays that arrive at the receiver from above (curve *1*) and from below (curve *2*). According to Fig. 2b, both curve *1* and curve *2* have local extremums $S1'$, $S2'$, S, $S1$, and $S2$. These extremums correspond to the local extremums of Fig. 2c at certain departure angles. The latter extremums can be related to the caustics of the initial field, which are shown in Fig. 2d. For all rays that were uniformly emitted from the source upwards, the points were found (with a step of 0.02°) at which the ray was tangent to the caustic. As a result, we obtain a set of dots that represent the caustics of the initial field and illustrate the strength of the caustics in the form of the dot concentration. In addition, Fig. 2d shows two reference rays that demonstrate the refraction and zonal structure of the propagating sound field. The domains of specular reflection are shown as well for the extreme rays, which, according to Figs. 2b and 2c, hit the reception point. Figures 2e and 2f illustrate the focusing at the reception point for 1° wide bundles of rays that are specularly reflected from the surfaces S and $S2'$.

From the aforementioned data, it follows that, for the situation at hand, the reception point coincides with the crossing point of the caustics formed by the rays that are specularly reflected from the boundaries shown in Fig. 2c ($S1'$, $S2'$, S, $S1$, and $S2$). These domains make the major contribution to the resulting sound field in the shadow zone. The presented consideration explains the multiray character of signals in shadow zones, which was observed in ocean experiments [13]. It is also clear that the multiray pattern is governed by the complexity (the presence of caustics) of the initial field, and this complexity, in turn, is determined by the vertical distribution of the sound speed. In the case of a linear sound speed profile, the only depth of the boundary of the fine-structure inhomogeinity can be found for the rays that leave the source upwards and arrive at the receiver in the shadow zone, this boundary serving to reflect the rays that arrive at the receiver from below and form the caustic.

From the presented kinematic consideration, the conclusion can be drawn that, in a shadow zone, the sound field is formed by the signals that are reflected or scattered from the fine-structure inhomogeneities of the ocean water, which exist within local domains determined by the geometry of the experiment and by the vertical sound speed profile. Therefore, the degree to which the insonification phenomenon manifests itself depends on the intensity of the fine structure in these domains. Turning to Fig. 1c, one can see that, for the region at hand, the value of C_n is rather small in the upper layers and decreases to 10^{-11} m^{-1} at a depth of 0.5 km. According to Fig. 2, at distances of 15 km and more, the shadow-zone sound field is formed by the domains that are as deep as 0.5 km or more, and, without using more sophisticated techniques, one cannot observe more pronounced manifestations of the phenomenon against the background of the ambient noise. At shorter distances, the degree of insonification may increase. However, at such distances, the phenomenon can be masked with the initial field.

For the central region of the Indian Ocean (Fig. 1b), higher intensity of the fine structure is typical with C_n ranging within $(1 - 30) \times 10^{-10}$ m^{-1}, down to a depth of 1 km. According to Eq. (1), such an intensity can lead to 10–15 dB higher sound field levels in the shadow-zone, as compared to the aforementioned region. Figure 3 shows the vertical sound speed distributions (Fig. 3a) and the caustic patterns for the source depths 0.07, 0.2, and 0.3 km (Figs. 3b, 3c, and 3d, respectively). One can see that the caustics become smoother for deeper sources. For a source depth of 0.3 km, the caustics are at the depths of an intense fine structure, up to the distances 7–10 km from the source. Therefore,

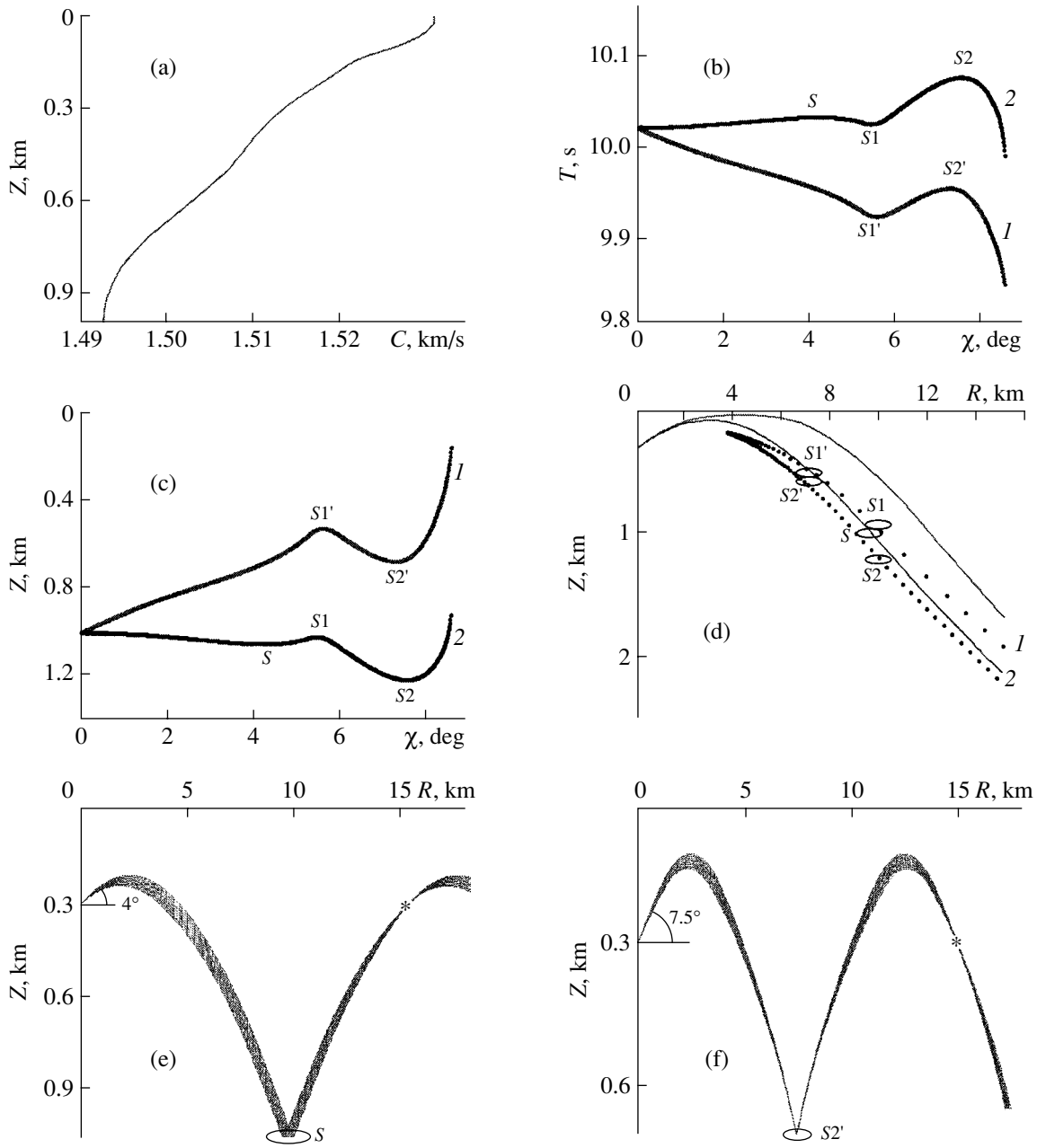

Fig. 2. Mechanism of sound penetration into a geometric shadow zone for the subtropical region of the Atlantic Ocean.

the phenomenon can be reliably measured at a reception depth of 0.3 km, up to the distances 20 km or more, which was confirmed in our experiments [1]. We numerically estimated the energy levels for the sound signals penetrating into the shadow zone in order to compare these levels with those measured experimentally. In the calculations, the value $C_n = 10^{-10}$ m^{-1} was specified. The complicated caustic pattern leads to several local domains that form the shadow-zone sound field and to a multiray structure of the received signal. These features were experimentally confirmed as well [13].

By applying the proposed approach to other regions, one can conclude that, for the tropical Atlantic regions, the high intensity of the fine structure is characteristic at small depths with a rapid intensity decrease at greater depths. This depth dependence can restrict the distances at which the phenomenon manifests itself, as compared to the considered central region of the Indian Ocean. In addition, the aforementioned features in the general sound speed profile (the uniform layer at the depths about 0.2 km, which is caused by the equatorial countercurrent) can mask the shadow zone insonification.

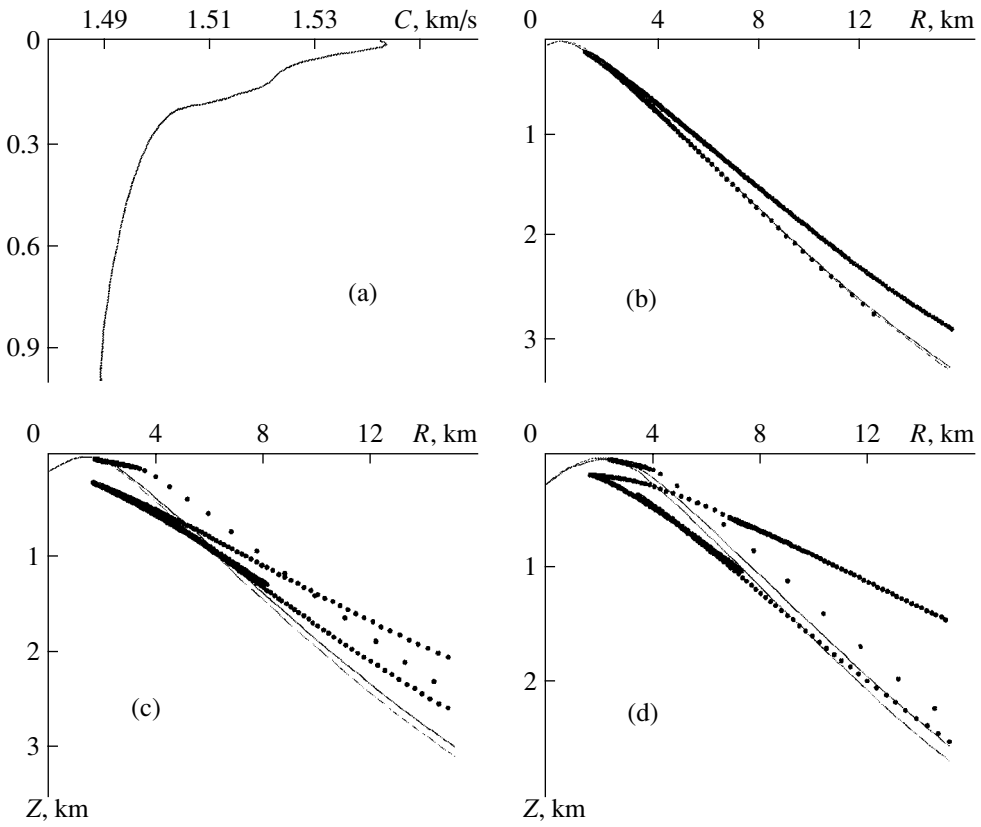

Fig. 3. Caustic patterns in the tropical region of the Indian Ocean for different source depths and (a) the average sound speed profile. The source depth is (b) 0.07; (c) 0.2; and (d) 0.3 km.

Finally, the large region of the Mediterranean waters in the Atlantic Ocean (Fig. 1d) can be studied to observe the fine-structure inhomogeneities in deeper ocean layers (depths of 1.0–1.5 km, $C_n = 10^{-10}$ m^{-1}). In addition, short shadow zones can exist in this region. Sound can penetrate in these zones through both the surface channel and microchannels in the water bulk. The separation of these two effects in the time domain can be impossible.

The combined analysis performed for the sound field and the fine-structure characteristics in different regions of the ocean show the variety of manifestations of the phenomenon of sound penetration into shadow zones. The tropical region of the Indian Ocean, among the others presented in Fig. 1, can be mentioned as the most advantageous for the observation and study of the phenomenon itself and for diagnosing the parameters and variability of the fine structure by means of the shadow zone insonification.

Another interesting ocean region should be mentioned. In Fig. 4, the fine structure of the sound speed profile is presented that was measured by us in the western region of the tropical Atlantic, at 10° N and 52° W (the region of the Guiana Hollow). Here, two types of the fine structure simultaneously occur: a pronounced stepped structure (depths of 0.2–0.4 km) and an intrusion-caused one (deeper than 0.5 km). The fine structure has high intensity and reaches the depth of the underwater sound channel whose axis is at a depth of 1.0 km. Many researchers [14] measured the fine structure in this region to study the mechanisms of its formation.

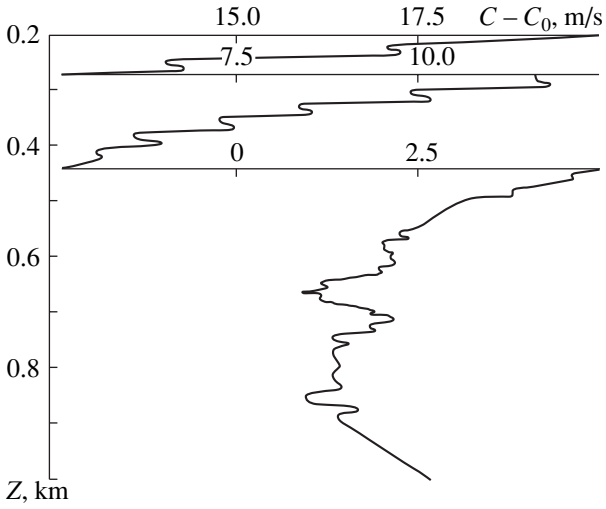

Fig. 4. Fine structure of the sound speed profile in the northwestern region of the tropical Atlantic Ocean.

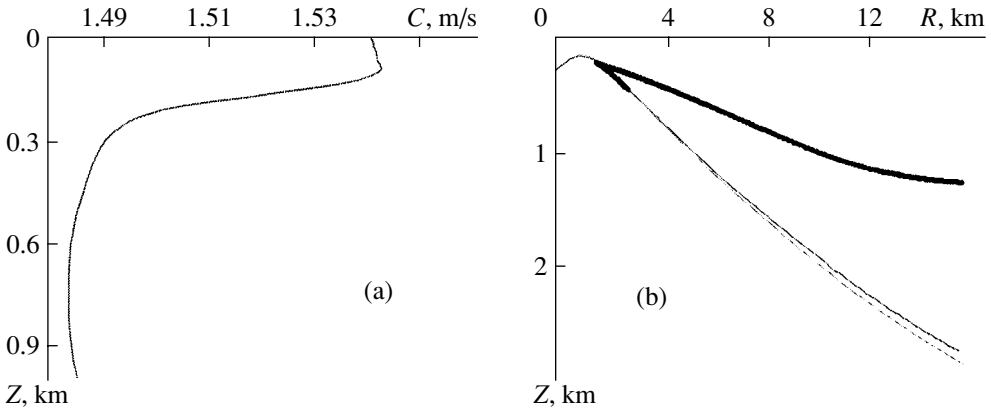

Fig. 5. (a) Averaged sound speed profile and (b) the caustic pattern in the north-western region of the tropical Atlantic Ocean for a source depth of 0.3 km.

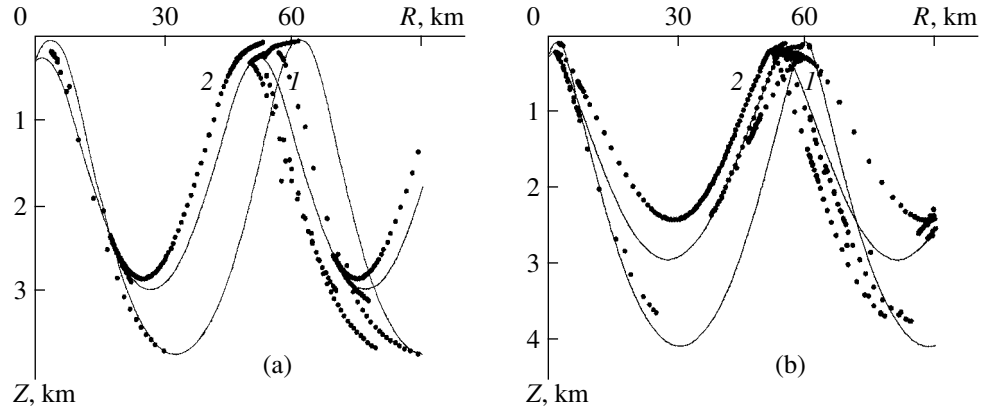

Fig. 6. Patterns of caustics in the near sound field and the convergence zones for (a) the tropical region of the Atlantic Ocean and (b) the subtropical region of the Indian Ocean. The source depth is 0.3 km. Points are indicated at which the rays are tangent to the caustics for the departure angles ranging (a) ±8.5° and (b) ±11° (at a step of 0.1°).

Figure 5a shows the average vertical distribution of the sound speed in this region. With this distribution, the pattern of caustics (Fig. 5b) was calculated for the source depth 0.3 km. The boundary of the shadow zone is produced by the powerful, nearly horizontal caustic that covers the depths where the fine structure exists, up to a distance of 15 km from the source. The existence of the fine structure and the caustic allows one to expect the insonification of the shadow zone in this region up to distances of 30 km or more. By using up-to-date experimental instruments like those described in [15] to obtain vertical or horizontal cross sections of the sound field in the shadow zone, one can extract the information on the fine-structure inhomogeneities for different depths at which the caustic exists from the analysis of the sound signals penetrating into the shadow zone. By long-term observations of the sound signals in the shadow zone at a fixed experimental geometry, one can observe the variability of the parameters of the fine-structure inhomogeneities within a fixed volume of the oceanic medium.

In the second shadow zone, the sound field is mainly formed by the caustic domains of the first convergence zone, the caustics of groups 1 and 2 (Figs. 6a, 6b) contributing to the sound field at the beginning and at the end of the shadow zone, respectively. From the comparison of the caustic patterns observed for the central regions of the Atlantic (Figs. 6a and 1c) and Indian (Figs. 6b and 1b) oceans, one can conclude that the concentration of caustics in the convergence zone is much lower in the first region than in the second one. In view of the low value of quantity C_n in the subtropical region (Fig. 1c), the sound penetration into the second shadow zone should be less pronounced, as compared to the tropical region (Fig. 1b) [2]. Nevertheless, in the second shadow zone of subtropics, the penetration phenomenon can be enhanced in comparison with the first zone, because, according to Fig. 6a, the convergence zone is enriched with caustics in the upper ocean layers, where C_n is at a level of 10^{-10} m^{-1}, which is sufficient for the phenomenon to be observed.

The presented study of the effect of sound penetration into the shadow zone, along with the established regional variability of this phenomenon, offers a justified approach to solving the inverse problems of determining the main fine-structure parameters. The results obtained above can also be used in the practical-purpose studies aimed at improving the ultimate performance of acoustic systems for underwater observation and monitoring [16, 17].

ACKNOWLEDGMENTS

This work was supported by the Russian Foundation for Basic Research, project no. 99-05-64379.

REFERENCES

1. V. S. Gostev and R. F. Shvachko, Dokl. Akad. Nauk SSSR **282**, 1082 (1985).
2. V. S. Gostev, L. N. Nosova, and R. F. Shvachko, Akust. Zh. **44**, 201 (1998) [Acoust. Phys. **44**, 162 (1998)].
3. S. V. Burenkov, V. S. Gostev, V. I. Neklyudov, *et al.*, Akust. Zh. **41**, 45 (1995) [Acoust. Phys. **41**, 37 (1995)].
4. V. S. Gostev and R. F. Shvachko, in *Problems of the Ocean Acoustics*, Ed. by L. M. Brekhovskikh and I. B. Andreeva (Nauka, Moscow, 1984), pp. 153–164.
5. S. N. Gurbatov and E. G. Shchemelev, Akust. Zh. **28**, 347 (1982) [Sov. Phys. Acoust. **28**, 205 (1982)].
6. V. M. Zhurbas and U. K. Lips, Okeanologiya (Moscow) **27** (4), 562 (1987).
7. C. J. Garret and W. H. Munk, J. Geophys. Res. **80**, 291 (1975).
8. A. S. Samodurov, Okeanologiya (Moscow) **22** (2), 182 (1982).
9. C. J. Garret and W. H. Munk, Annu. Rev. Fluid Mech. **11**, 339 (1979).
10. Y. G. F. Desaubies, J. Phys. Oceanogr. **6** (6), 976 (1976).
11. S. P. Hayes, T. M. Joyce, and R. S. Millard, J. Geophys. Res. **80**, 314 (1975).
12. M. C. Gregg, J. Phys. Oceanogr. **7** (3), 436 (1977).
13. S. V. Burenkov, V. S. Gostev, N. I. Knyazeva, *et al.*, Akust. Zh. **41**, 336 (1995) [Acoust. Phys. **41**, 293 (1995)].
14. V. M. Zhurbas and R. V. Ozmidov, Dokl. Akad. Nauk SSSR **290** (1), 220 (1986).
15. J. R. Potter, B. J. Uscinski, and T. Akal, Waves Random Media **10**, 199 (2000).
16. V. S. Gostev, L. N. Nosova, and R. F. Shvachko, Akust. Zh. **44**, 844 (1998) [Acoust. Phys. **44**, 736 (1998)].
17. V. S. Gostev and R. F. Shvachko, in *Proceedings of the Fifth International Conference on Applied Technologies in Hydroacoustics and Hydrophysics* (St. Petersburg, 2000), pp. 9–12.

Translated by E. Kopyl

Acoustical Physics, Vol. 47, No. 5, 2001, pp. 548–551. Translated from Akusticheskiĭ Zhurnal, Vol. 47, No. 5, 2001, pp. 632–636.

Elastic Properties of Dense Nanotube Layers

I. S. Grudzinskaya*, Z. Ya. Kosakovskaya, V. N. Reshetov***, and A. A. Chaban***

**Andreev Acoustics Institute, Russian Academy of Sciences,*
ul. Shvernika 4, Moscow, 117036 Russia
e-mail: chaban@akin.ru
***Institute of Radio Engineering and Electronics, Russian Academy of Sciences,*
ul. Mokhovaya 11, Moscow, 103907 Russia
****Moscow State Engineering Physics Institute, Kashirskoe sh. 31, Moscow, 115409 Russia*
Received December 29, 2000

Abstract—The Young modulus of a thin layer consisting of densely packed carbon nanotubes oriented normally to a substrate is measured using a scanning probe atomic force microscope. It is found that the adhesion of the film and the silicon substrate is not very strong, and, at certain conditions, this may lead to an intense energy dissipation in an oscillatory system loaded by the film. © *2001 MAIK "Nauka/Interperiodica".*

A great number of papers on the synthesis of carbon nanotubes and on the investigation of their physical properties were published after their discovery in 1991 [1, 2]. The interest to these objects is not incidental, since the prospects of their applications in technology are quite evident. Carbon nanotubes have unique electric, elastic, and mechanical properties; their cavities can be filled by atoms of various elements. For example, it was reported that an isolated nanotube can have a Young modulus along its axis greater than 1 TPa and a shear modulus of only 1 GPa simultaneously. The data reported by different authors strongly vary, which is most probably connected with the defects present in nanotubes. Now, it is possible to manufacture dense layers of nanotubes oriented normally to a substrate [3, 4]. Such layers proved to be effective cathodes for autoelectronic emission [5, 6]. At the same time, the investigation of the elastic and mechanical properties of dense layers of nanotubes is just at its starting point and is mainly of a theoretical character [7, 8]. In this paper, we report on the experimental studies of the elasticity of dense nanotube layers and the dissipation of the energy of elastic vibrations in them. First, we describe the results of measurements performed with the help of a scanning probe atomic force microscope and, then, the results of measurements of the Q factor of a macroscopic oscillating system loaded on a sample with a carbon nanotube film.

A nanotube layer with the thickness 142 nm was obtained by the deposition of carbon atoms on a silicon surface in the process of electron-beam evaporation of pure graphite in vacuum. The layer was a mixture of multilayer nanotubes with the diameters from 3 to 5 nm and single-layer tubes with the diameter of 1.1 nm. The tubes formed a fiber texture with the axis normal to the substrate surface.

A NanoScan measuring device was used in the studies by scanning probe microscopy. The device is described in detail in a review [9]. An oscillating system (a tuning fork) operating at a frequency of 20 kHz was loaded through a vibrating diamond stylus on various materials. The stylus pressing upon the substrate could be smoothly adjusted with the help of a piezoelectric control system. The displacement of the tuning fork reed, to which the stylus was fixed, was monitored with the precision up to 0.1 nm. The device could operate in two modes. In the first case, the shift of the resonance frequency in a self-oscillating system was measured. Here, the major contribution to the response (the frequency change) was provided by the elastic properties of the sample under test. Further, we will refer to this case as to the mode of "elasticity measurements." In the second case, the decrease that occurs in the vibration amplitude due to the contact with the substrate is measured. The dissipative processes are very important in this case, and, hence, it will be conditionally referred to as the mode of "viscosity measurements."

A stylus with a large enough curving radius was selected to measure the macroscopic characteristics of the sample by averaging over the area of tens of nanometers (this is important while working with nanotubes). The study of the surface relief showed that the surface of the nanotube film was smooth. There were single steps, protrusions, and indents with the height of several nanometers (Fig. 1). Small areas with special properties can sometimes be observed, which can be identified as the specks of the graphite phase.

The main results of the measurements are as follows. The dependences of the parameters of the oscillating system on the deformation (deepening of the stylus into the sample) were recorded. Generally speaking, the dependences of this type, which describe the response of various parameters of the system to the

change of conditions at contact are usually called the loading curves. (The most standard case of a loading curve is the dependence of the sample deformation on the load.) A diamond stylus was pressed into the sample under a smoothly varying external load and deformed it. In the mode of elasticity measurements, a smooth change of the resonance frequency f relative to the resonance frequency f_0 in air is observed in the process of stylus pressing. We proceed from the standard Hertz approximation [10]. We assume that the stylus point can be treated as a hemisphere with the radius R. We also assume that its Young modulus is greater than the corresponding moduli of the materials under test. In the case of a nanotube layer, this assumption is substantiated by [8]. Moreover, the validity of this assumption is substantiated by the results of measurements. Under these conditions, the frequency shift is equal to

$$f - f_0 = \frac{f_0}{k_0}\sqrt{R}\frac{E}{(1-\nu^2)}\sqrt{h}. \quad (1)$$

Here, k_0 is the elasticity coefficient of the oscillating system, E is the Young modulus of the tested sample, ν is the Poisson ratio of the sample, and h is the displacement of the tuning fork reed in the process of the stylus pressing.

Figure 2 presents the dependence of the quantity $(f-f_0)^2$ on the displacement of the tuning fork reed for three different samples. In the plot under consideration, this dependence for a homogeneous sample must be linear. In fact a dependence close to a linear one is observed for a (100)-cut silicon plate and glass. One has to keep in mind that the stylus point can be treated as a hemisphere only with a certain reservation. The relationship between the elastic constants, which is obtained from Eq. (1) and Fig. 2 for silicon and glass, agrees well with reference data. This allows one to conduct measurements on samples with unknown elastic moduli and determine their elastic parameters using Eq. (1) from the comparison with reference samples.

The properties of a nanotube layer deposited on silicon are of a major interest for us. In this case, a difficult problem that is not yet solved arises, namely, the problem of the relative contributions to the loading curve from the film and the substrate in the case of a layered system. We proceed from the fact that the penetration depth H of the deformation into a sample is about the radius of the contact area between the stylus and the sample in order of magnitude. Then, according to the Hertz theory, we have

$$H \approx \sqrt{Rh}. \quad (2)$$

When $H \le d$, where d is the film thickness, the behavior of the system is determined by the properties of the nanotube layer. When $H \gg d$, the system properties are governed by the substrate elasticity.

We observe this behavior in Fig. 2. The inclination angle of the loading curve for the layered structure is constant at small loads, and it is greater than the angle

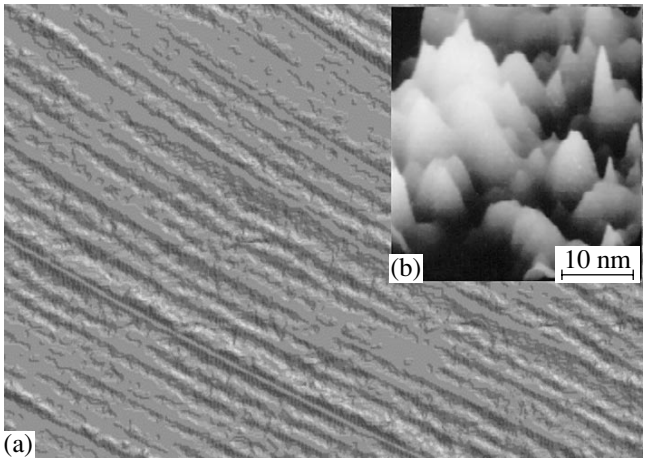

Fig. 1. (a) Surface relief of a carbon nanotube film observed by a scanning atomic force microscope. The area is $5 \times 7\ \mu m^2$, and the height difference is about 10 nm. (b) Surface relief of a carbon nanotube film observed by a scanning tunneling microscope with a resolution of 1 nm, which provides the observation of individual nanotubes.

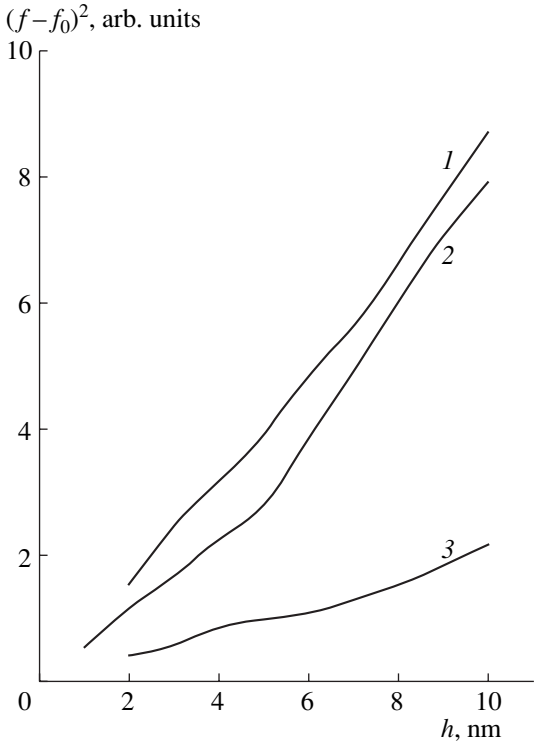

Fig. 2. Square of the frequency shift in an atomic force microscope versus the pressing depth for (*1*) silicon, (*2*) silicon with a nanotube layer, and (*3*) glass.

for glass but smaller than in the case of silicon. Only the elastic properties of the film are important in this region. In the case of large values of h, the inclination of the loading curve becomes the same as for silicon, and the elastic reaction of silicon becomes decisive.

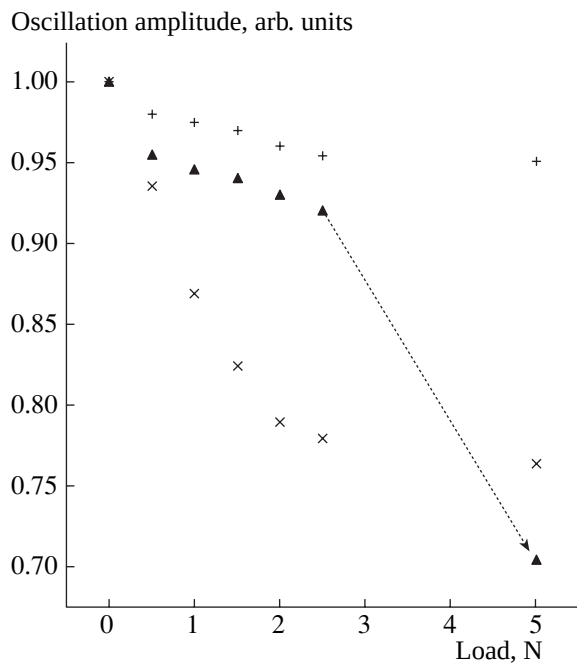

Fig. 3. Oscillation amplitude of a macroscopic oscillatory circuit versus the load: (+) silicon, (▲) silicon with a nanotube layer, and (×) plexiglas.

Using $h = 4$ nm as an approximate limiting point of the region where the role of the substrate is not yet significant, we can estimate the order of magnitude of the effective curving radius of our stylus from the condition $H \approx d$: $R \approx 5$ μm, which agrees qualitatively with our data on the stylus.

The comparison of the loading curve for silicon and the loading curve for the nanotube layer at small loads (when the role of the substrate is small) gives $E/(1 - \nu^2) \approx 140$ GPa for the nanotubes. According to the theoretical calculations [8], the Poisson ratio for a layer of nanotubes oriented normally to the surface, when the pressure is also normal to the surface, is small enough ($\nu \ll 1$). This means that it is possible to estimate $E \approx 140$ GPa. It is interesting to compare at least qualitatively this result with the theory. The Young modulus was calculated in [8], but it was obtained for a "crystal" of ideal single-layer nanotubes arranged in a triangular grid and oriented strictly parallel to each other. It turned out that, in the case of an experimental geometry analogous that used by us, the Young modulus along the axes of single-layer tubes 3 nm in diameter is close to 300 GPa, and, when the tube diameter is equal to 5 nm, the corresponding Young modulus is approximately 200 GPa. At the same time, the Young modulus across the tubes is as small as several gigapascals. Such a disagreement with our experiment is natural. Although the investigated film belongs to the best samples manufactured up to now, it consists of a mixture of multilayer tubes of different diameters with an admixture of single-layer tubes. Therefore, the tubes do not form an ideal triangular grid. Moreover, the stylus in the atomic force microscope is inclined to a certain extent with respect to the substrate plane, which introduces some distortions due to the strong asymmetry of the Young modulus.

It is necessary to note the excellent mechanical properties of the nanotube layer. Visible fracture of the film was observed only in the case of pressing of the stylus approximately to a depth of 100 nm, which was comparable with the film thickness.

Measurements of the oscillation amplitude as a function of the penetration of the stylus into the sample were also conducted. It is difficult here to obtain unambiguous information on the film properties. Several dissipation mechanisms come into play simultaneously (the adhesive friction, the water layer at the boundary, the viscoelasticity, etc.). In certain conditions, the processes caused not by the dissipation but by the equipment-related factors can also be partially responsible for the amplitude decrease in the atomic force microscope [11]. Here, we only note the following important fact. The amplitude decrease that occurred at the contact with the nanotube film turned out to be comparable to the decrease observed in the case of pure silicon. This means that we did not observe any unusually strong loss mechanisms by the atomic force microscopy.

We measured dissipative losses in a series of materials by a device that was a macroscopic analog of the probe of our microscope and that was developed much earlier under the name of a contact impedance meter [12]. An oscillatory circuit with the Q factor at least one order of magnitude higher than that of the atomic force microscope was loaded on a test sample through a steel ball. It was possible to detect the changes in both frequency and amplitude and to determine the elastic and dissipative parameters of the material. The region of deformation was greater than the film thickness because of the large diameter of the ball that was in contact with the sample (about 0.5 mm), and our oscillatory system was not suitable for the determination of the elastic constants of the layer. Therefore, the study was conducted only in the viscosity measurement mode (the measurement of the oscillation amplitude with the ball being pressed into the sample). The results are presented in Fig. 3. The load is plotted along the abscissa axis, and the oscillation amplitude reduced to the amplitude of the unloaded oscillatory system is plotted along the ordinate axis.

We stress that our device measured the dissipation in the sample rather than its elastic properties, and this fact was specially verified in our experiments. Figure 3 gives the data for silicon. However, they coincide within the precision of measurements with the data for the materials that are quite different in their elastic properties, such as glass, aluminum, and brass. It would be impossible to distinguish them in our plot. We took also viscoelastic materials for comparison. The data for plexiglas are given in Fig. 3 as an example.

Now let us consider the basic result, i.e., the measurements performed for a nanotube layer on silicon. In the case of a weak pressing, the dissipative losses are not large, though they are distinctly larger than for pure silicon. However, when the load increases, a sharp growth of losses was observed (a sharp decrease in amplitude is indicated by the line connecting neighboring points in the drop region). Regretfully, it was impossible to use loads greater than 2.5 N without taking the risk to smash the sample. It was possible only to use a load of 5 N with the application of a special gadget. That is why only a small number of points was obtained in the most interesting region.

Such a sharp growth of losses can be connected with the temporary local separation of the nanotube layer from the silicon substrate because of the insufficiently strong adhesion. The most probable reason for such separation is the presence of the tangential component in the forces caused by the ball pressure on the sample. Elastic vibrations of the system lead to a relative motion of the film and the substrate in the separation region and to energy losses due to the friction. Since the contact region is large in our case, the energy losses can be considerable. Moreover, the film separation from the substrate also leads to the displacement of nanotubes with respect to each other (the lower part of a tube is no more fixed to the substrate, and the bond between the tubes is fairly weak). We also cannot exclude the influence of this factor on the absorption of the elastic vibrations.

Qualitative estimates show that a sharp growth of losses occurs in our experiment when the tangential stresses at the film–substrate interface reach several tens of megapascals. In view of the high normal pressure applied at the symmetry axis of the system (up to several gigapascals), this result indicates a not very strong adhesion of the film and the substrate. Nevertheless, it is necessary to take into account that the separation can occur away from the symmetry axis, i.e., outside the region of the strongest pressing.

Performing repeated measurements, we obtained the same results as in the first measurement (for all values of the pressing force). If the film were unable to restore its initial bonds with the substrate, the subsequent measurements would differ from the initial ones. A good review of a very complex and interesting problem of adhesive friction, which may help to understand the problem, can be found in [13].

Measurements with a separated nanotube film of an analogous composition were also conducted. As expected, we observed a strong absorption, which far exceeded the absorption given in Fig. 3 already at small loads. This fact demonstrates once more that, if the separation were retained after the first measurement, the absorption in the repeated measurements would be greater.

It is important to note that, in some regions on the surface, no noticeable damping of vibrations could be observed at any applied loads. This is the evidence of a strong adhesion of the film and the substrate in these regions. Therefore, it is possible to obtain a strong adhesion of a nanotube film and a substrate with improved technology. The technique used in this study can be a good method of monitoring the film adhesion.

As a result of the investigation of a thin film of densely packed carbon nanotubes, it became possible to measure the Young modulus of the film, which is an important parameter from the point of view of future applications and which widely differs from the Young modulus of individual nanotubes and nanotube ropes [14, 15]. It was demonstrated that the adhesive bond between a film and a silicon substrate was not very strong for the major part of our sample. However, in some regions, this bond is strong enough, which means that it is possible to create layered structures with high mechanical stability by introducing the necessary improvements in the growth technology.

ACKNOWLEDGMENTS

This work was supported by the Russian Foundation for Basic Research, project nos. 00-02-16473 and 98-02-17130.

REFERENCES

1. R. Saito and M. S. Dresselhaus, *Physical Properties of Carbon Nanotubes* (Imperial College Press, London, 1998).
2. A. V. Eletskiĭ, Usp. Fiz. Nauk **167**, 945 (1997) [Phys.–Usp. **40**, 899 (1997)].
3. Z. Ya. Kosakovskaya, L. A. Chernozatonskiĭ, and V. A. Fedorov, Pis'ma Zh. Éksp. Teor. Fiz. **56** (1), 26 (1992) [JETP Lett. **56** (1), 26 (1992)].
4. J. S. Suh and J. S. Lee, Appl. Phys. Lett. **75**, 2047 (1999).
5. L. A. Chernozatonskii, Yu. V. Gulyaev, Z. Ya. Kosakovskaya, *et al.*, Chem. Phys. Lett. **233**, 63 (1995).
6. W. A. de Heer, A. Chatelain, and D. Ugarte, Science **270** (5239), 1179 (1995).
7. P. Calvert, Nature **399**, 210 (1999).
8. V. N. Popov, V. E. van Doren, and M. Balkanski, Solid State Commun. **114**, 395 (2000).
9. K. V. Gogolinskiĭ and V. N. Reshetov, Zavod. Lab. **64** (6), 30 (1998).
10. L. D. Landau and E. M. Lifshits, *Course of Theoretical Physics*, Vol. 7: *Theory of Elasticity*, 4th ed. (Nauka, Moscow, 1987; Pergamon, New York, 1986).
11. M. Gauthier and M. Tsukada, Phys. Rev. Lett. **85**, 5348 (2000).
12. C. Kleesattel and G. M. L. Gladwell, Ultrasonics **6**, 175 (1968).
13. G. V. Dudkov, Usp. Fiz. Nauk **170** (6), 585 (2000).
14. M. M. J. Treacy, T. W. Ebbesen, and J. M. Gibson, Nature **381**, 678 (1996).
15. J.-P. Salvetat, G. A. D. Briggs, J.-M. Bonard, *et al.*, Phys. Rev. Lett. **82**, 944 (1999).

Translated by M. Lyamshev

Acoustical Physics, Vol. 47, No. 5, 2001, pp. 552–555. Translated from Akusticheskiĭ Zhurnal, Vol. 47, No. 5, 2001, pp. 637–640.

Leaky Stoneley Waves at a Moving Interphase Boundary

Yu. V. Gulyaev* and N. S. Shevyakhov**

**Institute of Radio Engineering and Electronics, Russian Academy of Sciences, ul. Mokhovaya 11, Moscow, 103907 Russia*

***Institute of Radio Engineering and Electronics, Ul'yanovsk Branch, Russian Academy of Sciences, ul. Goncharova 48, Ul'yanovsk, 432011 Russia*

e-mail: ufire@mv.ru

Received July 25, 2000

Abstract—The possibility of the existence of a leaky Stoneley wave at a uniformly moving interphase boundary defined as a jump in the acoustic parameters of an isotropic elastic medium is discussed. It is shown that the motion of the interphase boundary exerts dissimilar effects on the orientation of the wave normals of partial waves forming the Stoneley wave, and this results in different Doppler shifts of the frequencies of the partial waves in the laboratory frame of reference. © *2001 MAIK "Nauka/Interperiodica".*

The parametric transformation of surface acoustic waves (SAWs) under the effect of a transverse motion of guiding boundaries was considered in earlier publications [1, 2] for the case of electroacoustic waves guided by 180° domain walls in ferroelectrics and by a step of the polarizing field in electrostrictive materials. The main result of these studies was the prediction of the "weathercock effect," that is, an acute-angle turn of the wave-front normal vector of an electroacoustic wave towards the direction of the boundary motion. The thus induced noncollinearity (more precisely, noncoplanarity) of the wave vector of an electroacoustic wave with the boundary does not affect the capability of this wave for an interfacial localization and a stationary (undamped) propagation along the boundary.

Now we consider the peculiarities of mode localization for other types of SAWs and for other types of moving boundaries in solids. The capability for a high-speed, self-sustained (in the autowave regime), or forced motion with Mach numbers $\beta < 10^{-1}$ ($\beta = V/c$, where V is the velocity of the boundary motion and c is the characteristic sound speed in the solid) is characteristic of, for example, the walls of elastic domains at martensite or ferroelastic phase transitions [3], an explosive crystallization front in an amorphous material [4], and the combustion surface of a nongasifiable solid explosive [5].

In most cases it is acceptable to ignore the details of a phase transition that is not accompanied by a change in aggregate state and to assume that the motion of the interphase boundary (IB) is predetermined and uniform. We use the model of a geometrically thin (on a wavelength scale) moving boundary between isotropic media, at which the elastic moduli and the density of the material undergo steplike changes. For example, if the IB in question is a plane front of explosive crystallization in an amorphous material [4], the elastic moduli and the density of the amorphous phase can be assumed to be lower than the respective values for the crystalline phase in view of the fact that the amorphous substance has an excessive free volume and that the crystallization leads to an increase in the average force of atomic interaction.

In the adopted model of a travelling step of acoustic parameters, it is the Stoneley waves [6] that are the alternative to electroacoustic waves [1, 2]; no special assumptions are being made concerning the nature of the boundary conditions at the moving IB.[1] As distinct from electroacoustic waves and Rayleigh SAWs, the Stoneley waves do not pertain to the category of unconditionally existing waves, and so their direct experimental observation is especially important (see [7, 8]).

We assume that the IB with the coordinate $z_s = Vt$ (t is time) separates the region $z < z_s$ occupied by the medium with the density ρ and the Lame coefficients λ and μ from the region $z > z_s$ characterized by the respective parameters ρ_0, λ_0, and μ_0. The Galilean relations between the laboratory reference coordinate system $x0yz$ and the rest system $\tilde{x}\,0\tilde{y}\,\tilde{z}$ allow us to write the

[1] For example, it appears that, in consequence of the dislocation mechanism of possible breaks of elastic bonds, the exclusion of slipping at the wall of elastic domains should be abolished, and the shearing stresses should be replaced by the effect of the frictional force at slipping.

1063-7710/01/4705-0552$21.00 © 2001 MAIK "Nauka/Interperiodica"

equations for the scalar potentials $\varphi(z < z_s)$, $\varphi_0(z > z_s)$ and the vector potentials $\psi(z < z_s)$, $\psi_0(z > z_s)$ in the form

$$\left[\left(\frac{\partial}{\partial\tilde{t}} - V\frac{\partial}{\partial\tilde{z}}\right)^2 - \begin{pmatrix} c_l^2 \\ c_{l_0}^2 \end{pmatrix}\tilde{\nabla}^2\right]\begin{pmatrix}\varphi\\ \varphi_0\end{pmatrix} = 0,$$
$$\left[\left(\frac{\partial}{\partial\tilde{t}} - V\frac{\partial}{\partial\tilde{z}}\right)^2 - \begin{pmatrix} c_l^2 \\ c_{l_0}^2 \end{pmatrix}\tilde{\nabla}^2\right]\begin{pmatrix}\psi\\ \psi_0\end{pmatrix} = 0, \quad (1)$$

where $\tilde{t}$ is time; $\tilde{\nabla}^2 = \partial^2/\partial\tilde{x}^2 + \partial^2/\partial\tilde{z}^2$; c_l and c_{l_0} are the velocities of longitudinal waves; and c_t and c_{t_0} are the velocities of transverse waves in the regions $z < z_s$ ($\tilde{z} < 0$) and $z > z_s$ ($\tilde{z} > 0$), respectively.

For the waves propagating along the IB in the direction of the $\tilde{x}$ axis, the solutions to Eqs. (1) have a common phase factor $\exp(i\phi)$. Here, $\phi = k\tilde{x} - \Omega\tilde{t}$, where k is the wave number and Ω is the frequency of a Stoneley wave in the rest system. Therefore, taking into account the requirement of finiteness of the potentials, we obtain

$$\begin{pmatrix}\varphi\\ \varphi_0\end{pmatrix} = \begin{pmatrix}F\\ F_0\end{pmatrix}e^{i\phi}\begin{pmatrix}\exp(q_l\tilde{z})\\ \exp(-q_{l_0}\tilde{z})\end{pmatrix},$$
$$\begin{pmatrix}\psi\\ \psi_0\end{pmatrix} = \begin{pmatrix}G\\ G_0\end{pmatrix}e^{i\phi}\begin{pmatrix}\exp(q_t\tilde{z})\\ \exp(-q_{t_0}\tilde{z})\end{pmatrix}. \quad (2)$$

The characteristic coefficients $q_{l,t}$ and q_{l_0,t_0} in Eqs. (2) are defined by the formula

$$q_s = (-1)^m i\frac{\beta_s}{1-\beta_s^2}k_s + \frac{1}{1-\beta_s^2}\sqrt{k^2(1-\beta_s^2) - k_s^2}, \quad (3)$$

where $k_s = \Omega/c_s$ are the wave numbers; $\beta_s = V/c_s$ are the Mach numbers of the partial waves with the index s taking on the values l, t, l_0, and t_0; and $m = 2$ for $s = l$, t and $m = 1$ for $s = l_0$, t_0.

The boundary conditions of continuity for the displacements and stresses, when expressed in a standard way in terms of potentials (see [6]), do not contain time derivatives and, hence, do not undergo any changes under the transformation from the laboratory reference system to the rest system. Substituting Eqs. (2) into these boundary conditions, we obtain a system of homogeneous algebraic equations, whose solvability condition yields the dispersion relation for the Stoneley wave at a moving boundary in the form of the determinant Δ_{ST} being equal to zero:

$$\Delta_{ST} = \frac{\mu}{\mu_0}(q_{l_0}q_{t_0} - k^2)\tilde{\Delta}_R + \frac{\mu_0}{\mu}(q_lq_t - k^2)\tilde{\Delta}_{R_0} + 2k^2[k_{t_0}^2 + 2(q_{l_0}q_{t_0} - k^2)][k_t^2 + 2(q_lq_t - k^2)] + k_{t_0}^2k_t^2(q_{l_0}q_t + q_lq_{t_0}) - \mathcal{D}(k, V) \equiv 0. \quad (4)$$

The quantities $\tilde{\Delta}_R$ and $\tilde{\Delta}_{R_0}$ in Eq. (4) are the Rayleigh determinants modified by the IB motion. Namely,

$$\begin{pmatrix}\tilde{\Delta}_R\\ \tilde{\Delta}_{R_0}\end{pmatrix} = \begin{pmatrix}\Delta_R\\ \Delta_{R_0}\end{pmatrix} + \begin{pmatrix}\frac{\lambda+2\mu}{\mu}\Gamma_l\Gamma_t\\ \frac{\lambda_0+2\mu_0}{\mu_0}\Gamma_{l_0}\Gamma_{t_0}\end{pmatrix} + \begin{pmatrix}\left[2k^2\left(1-\frac{\mu_0}{\mu}\right) - k_t^2\right]\left(\Gamma_t + \frac{\lambda+2\mu}{\mu}\Gamma_l\right)\\ \left[2k^2\left(1-\frac{\mu}{\mu_0}\right) - k_{t_0}^2\right]\left(\Gamma_{t_0} + \frac{\lambda_0+2\mu_0}{\mu_0}\Gamma_{l_0}\right)\end{pmatrix}, \quad (5)$$

where $\Delta_R = (2k^2 - k_t^2)^2 - 4k^2q_lq_t$ and $\Delta_{R_0} = (2k^2 - k_{t_0}^2)^2 - 4k^2q_{l_0}q_{t_0}$ are the common Rayleigh determinants [6]. The function $\mathcal{D}(k, V)$ is an additive correction to the Stoneley determinant because of the IB motion. This function is defined by the equation

$$\frac{\mathcal{D}(k,V)}{k^2 + q_{l_0}q_t} = \left[\frac{\lambda+2\mu}{\mu}(k_{t_0}^2 - \Gamma_{t_0})\Gamma_l + k_t^2\Gamma_{t_0}\right] + \frac{k^2 + q_lq_{t_0}}{k^2 + q_{l_0}q_t}\left[\frac{\lambda_0+2\mu_0}{\mu_0}(k_t^2 - \Gamma_t)\Gamma_{l_0} + k_{t_0}^2\Gamma_t\right]. \quad (6)$$

In Eqs. (5) and (6), $\Gamma_s = i\beta_sq_s(2k_s - i\beta_sq_s)$.

In spite of the cumbersome form, Eqs. (2)–(6) clearly show that, in the absence of the IB motion, when all the coefficients β_s and Γ_s are equal to zero, the constructed solution describes a classical Stoneley wave. Indeed, in this case $\tilde{\Delta}_{R,R_0} \longrightarrow \Delta_{R,R_0}$, $\mathcal{D}(k, V) \longrightarrow 0$, and Δ_{ST} takes the form of a standard Stoneley determinant [6] with positively defined characteristic coefficients (3), which take on the meaning of the amplitude decay coefficients of partial waves (2). It also follows from Eqs. (2) and (3) that, as in the case of electroacoustic waves guided by moving 180° domain walls in a ferroelectric [1, 2], the partial waves under the effect of the IB motion acquire corrections to the wave vectors, these corrections being oriented in the direction of the boundary motion. The corrections are determined by the imaginary parts of the characteristic coefficients and express the weathercock effect, which consists in the deflection of the wave-front normals of partial

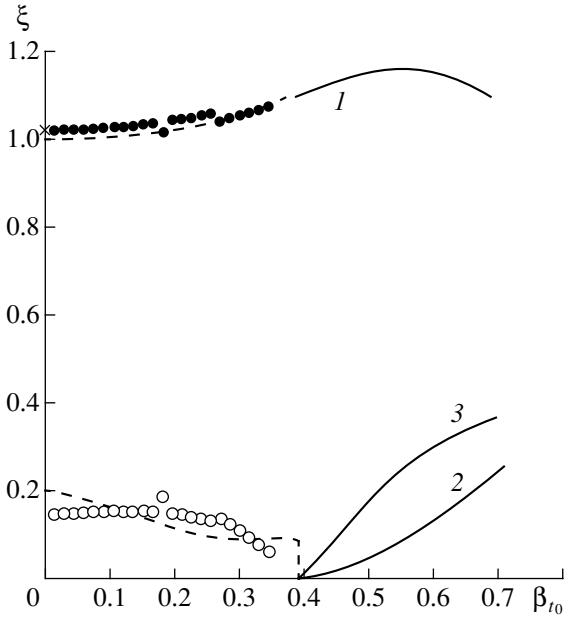

Parametric transformation of the spectrum of a leaky Stoneley wave at a moving interphase boundary in an isotropic solid.

waves from the boundary, i.e., from the line of intersection of the $x0z$ sagittal plane with the boundary plane. The resulting fan of wave vectors with a common projection on the boundary allows us to classify the Stoneley wave as a noncollinear boundary wave, which, in the general case, has a multicomponent spatial spectrum.

Due to the relativity of the spectral representation with respect to the observer's position, the single-frequency nature of the Stoneley wave spectrum disappears with the transformation to the laboratory reference system: the Ω spectral line undergoes Doppler splitting into the doublets $\omega_{l,t} = \Omega/(1 - \beta_{l,t}^2)$ and $\omega_{l_0,t_0} = \Omega/(1 - \beta_{l_0,t_0}^2)$. The presence of these doublets in the frequency spectrum of the recorded signal and their replacing one another with the IB crossing the receiver position appear to be decisive arguments for the identification of the Stoneley wave at a moving IB. The significance of similar Doppler effects was pointed out in the acoustic holography of flows with noise sources. The contrast of these sources considerably changes with the transformation to the coordinate system moving with the flow [9].

The common orientation of the z-components of the wave vectors of all partial waves (2) along the direction of IB motion allows one to consider the Stoneley wave as a combination of leaking-in ($\tilde{z} < 0$) and leaking-out waves ($\tilde{z} > 0$). Then, because of the difference between the wave vectors of identical partial waves on opposite sides of the IB, the time-average total energy fluxes p_+ and p_- directed towards the IB ($\tilde{z} < 0$) and away from it ($\tilde{z} > 0$), respectively, should be expected to be unbalanced. This implies the necessity of solving Eq. (4) in the complex plane $k = k' + ik''$ when the problem of numerical calculation is reduced to the standard procedure of searching for the zero minimum of $|\Delta_{ST}|$.

Depending on the ratio between p_+ and p_-, the following variants are possible: when $p_+ > p_-$ and $k'' < 0$, the Stoneley wave is amplified by the IB motion and belongs, on the whole, to the leaking-in type; when $p_+ < p_-$, and $k'' > 0$, the Stoneley wave attenuates due to the energy transfer to the IB and proves to be a leaky wave; if $p_+ \equiv p_-$ and $k'' \equiv 0$, it is a stationary Stoneley wave, similar in this quality to the electroacoustic wave on a moving 180° domain wall [1, 2].

The figure demonstrates the dependences of $\xi' = k'/k_{t_0}$ (curve *1*) and $\xi'' = k''/k_{t_0}$ (curve *2*) on β_{t_0}, which represent the results of a numerical solution of Eq. (4) by the method of descent by coordinates to the point of zero minimum of $|\Delta_{ST}|$ with the parameters $\rho/\rho_0 = 1.25$, $E/E_0 = 1.001$, $\sigma = 0.001$, and $\sigma_0 = 0.21$ (E and E_0 are Young's moduli and σ and σ_0 are Poisson's coefficients of the material for $\tilde{z} < 0$ and $\tilde{z} > 0$). This dependence permits the existence of a classical Stoneley wave on a stationary boundary (the corresponding value of ξ for $k > 0$ is marked by a cross). The correctness of the calculations was verified by checking the condition $\Delta_{ST} \approx 0$, which was satisfied with sufficient accuracy for $\beta_{t_0} > 0.4$. At smaller values of β_{t_0}, the equality $\xi'' = 0$ was always satisfied, which testifies to the existence of a stationary Stoneley wave in this region. However, in view of the noticeable inequality $\Delta_{ST} \neq 0$, which is revealed by the form of the dependences of Δ_{ST} on β_{t_0} (see the lower dashed curve for the ξ calculation by the descent method, or the succession of open points for the case of minimization of Δ_{ST} as a one-dimensional function, using the golden section scheme), the result of the solution cannot be considered as satisfactory (see the upper dashed curve, which is an extension of curve *1* to the region of small values of β_{t_0}, or the succession of bold points obtained by minimization of the one-dimensional function).

The correct form of the dependence $\xi' = \xi'(\beta_{t_0})$, $\xi'' = 0$ at $\beta_{t_0} < 0.4$ can be obtained by taking into account the additional stationarity relation for the Stoneley wave $p_+ = p_-$, which plays the role of a limiting condition typical of optimization problems [10] and is imposed on the objective function. A detailed consideration of this issue is beyond the limits of this publication.

Thus, the calculations described above testify to the existence of leaky Stoneley waves on moving IBs in solids. It is significant that the lower limit of the Mach number range, $\beta_{t_0} \approx 0.4$, at which the leaky Stoneley

wave is presumably transformed to a stationary Stoneley wave, proves to be the point of total delocalization of the leaking-in transverse partial wave. This is demonstrated by curve *3* of the dependence of the ratio $\mathrm{Re}(q_t)/k_{t_0}$ on β_{t_0}.

ACKNOWLEDGMENTS

This work was supported by the Federal Special-Purpose Program "Integratsiya," project no. A 0066.

REFERENCES

1. N. S. Shevyakhov, Akust. Zh. **45**, 570 (1999) [Acoust. Phys. **45**, 509 (1999)].
2. Yu. V. Gulyaev, O. Yu. El'meshkin, and N. S. Shevyakhov, Radiotekh. Elektron. (Moscow) **45** (3), 351 (2000).
3. V. S. Boĭko, A. M. Kosevich, and E. P. Fel'dman, Fiz. Tverd. Tela (Leningrad) **29** (1), 170 (1987).
4. V. A. Shklovskiĭ and V. M. Kuz'menko, Usp. Fiz. Nauk **157**, 311 (1989) [Sov. Phys.–Usp. **32**, 163 (1989)].
5. Ya. B. Zel'dovich, G. I. Barenblatt, V. B. Librovich, and G. M. Mikhviladze, *Mathematical Theory of Combustion and Explosion* (Nauka, Moscow, 1980).
6. S. V. Biryukov, Yu. V. Gulyaev, V. V. Krylov, and V. P. Plesskiĭ, *Surface Acoustic Waves in Inhomogeneous Media* (Nauka, Moscow, 1991).
7. Ch. Matteë, X. Jia, and G. Qentin, J. Acoust. Soc. Am. **102**, 1532 (1997).
8. C. Potel, S. Devolder, A. Ur Rehmann, *et al.*, J. Appl. Phys. **86**, 1128 (1999).
9. Soon-Hong Park and Yang-Hann Kim, J. Acoust. Soc. Am. **108**, 2719 (2000).
10. P. E. Gill, W. Murray, and M. H. Wright, *Practical Optimization* (Academic, London, 1981; Mir, Moscow, 1985).

Translated by A. Kruglov

Acoustical Physics, Vol. 47, No. 5, 2001, pp. 556–564. Translated from Akusticheskiĭ Zhurnal, Vol. 47, No. 5, 2001, pp. 641–649.

The Spatial Structure of the Acoustic Wave Field Generated in the Atmosphere by a Point Explosion

Ya. V. Drobzheva and V. M. Krasnov

Institute of Ionosphere, Ministry of Science and Higher Education of Kazakhstan, Kamenskoe Plato, Almaty, 480020 Kazakhstan

e-mail: jana@ionos.alma-ata.su

Received February 24, 1999

Abstract—The Mill Race experiment is used as an example to demonstrate the possibility of calculating the propagation characteristics of acoustic impulses generated by surface point explosions up to ionospheric heights with the use of the models that are based on the known exact solutions for homogeneous media with corrections for inhomogeneity. It is shown that, in the terrestrial atmosphere, the height where the amplitude of the particle velocity of an acoustic impulse reaches its maximum is independent of both the explosion power and the angle of departure of an acoustic ray. This height is about 120 km and depends mainly on the vertical atmospheric density profile. © *2001 MAIK "Nauka/Interperiodica".*

The knowledge of the laws governing the formation of the spatial structure of acoustic waves generated by different sources of natural and man-made origin is required for solving the problems of the energy transfer by these waves from the earth surface to space. From the applied point of view, the knowledge of the spatial structure of the field is required to choose the optimal conditions for radio sounding of the ionosphere in regions lying above acoustic energy sources (such as surface and underground explosions, missile launches, earthquakes, and volcano eruptions) with the aim of their remote control.

To date, no empirical relationship is known for describing the pattern of an acoustic field as a function of time and spatial coordinates from the earth surface to the ionospheric heights [1]. The only possibility of obtaining such a pattern of an acoustic field consists in using theoretical models whose development is the subject of a number of works (see, e.g., [2–7]). Considerable variations of the atmospheric characteristics with height and the large spatial scales require that the models take into account multiple factors, such as the inhomogeneity of the atmosphere, the nonlinear transformations of the impulse envelope during the propagation, the absorption and diffraction of waves, etc. Exact solutions to the equations of fluid dynamics with allowance for the above processes are hardly possible. For this reason, various approximations are used in deriving and in solving the wave equation. Specifically, Razin and Fridman [2] calculated the spatial structure of the acoustic field up to a height of 120 km without including the atmospheric absorption. Fitzgerald and Carlos [3] calculated the variations in the amplitude and length of an *N*-shaped acoustic impulse generated by an explosion with a trinitrotoluene charge of 500 kg to a height of 130 km without considering the height dependence of the sound velocity and the diffraction effects. Orlov and Uralov [4] described the spatial structure of the acoustic field for the heights 100–400 km; however, they considered the effect of atmospheric absorption on the acoustic impulse only in the first approximation, namely, they neglected the absorption for the propagation of an *N*-shaped impulse to ionospheric heights and then used a hyperbolic tangent function to smooth out the edges of the *N*-shaped impulse. Warshaw [5] derived the wave equation in the framework of the linear geometric acoustics and then extended this equation to the case of an acoustic impulse propagating along a ray path in a moving inhomogeneous absorbing medium with allowance for the nonlinear processes. Rudenko and Sukhorukova [6] obtained a modified Burgers-type equation that describes the evolution of an arbitrary impulse profile in an inhomogeneous absorbing medium. However, finding the solution to this equation in the general case remains a complicated problem despite the simplifications suggested in [6]. In the review devoted to nonlinear saw-tooth waves, Rudenko [7] outlined the difficulties encountered in solving the wave equation for inhomogeneous media and stated that specific solutions are few in number. It is obvious that the validity of solutions and models can be estimated only experimentally. Unfortunately, most publications contain either no correlation with the experiments or only qualitative estimates for a limited range of heights. In particular, only two height regions are usually considered for correlating the theoretical

1063-7710/01/4705-0556$21.00

and experimental data. The first region is located near the earth surface where the characteristics of the acoustic field can be measured directly, using sensors suspended, for example, on parachutes. The second region is the ionosphere whose response to the acoustic action can be observed using the Doppler sounding with radio signals. Both types of experiments are few in number, and the situations in which they are carried out simultaneously are much more rare. In this connection, the Mill Race experiment [8, 9] is unique. A point surface explosion of a chemical charge with a trinitrotoluene equivalent of 500 t was performed on September 16, 1981. During this experiment, acoustic measurements with probes suspended on four parachutes (heights about 10 km) and a Doppler sounding with radio signals of several frequencies were carried out simultaneously. Using the theory developed by Warshaw [5], Warshaw and Dubois [8] quantitatively correlated the response of the ionosphere to the acoustic impulse produced by this explosion with the results simulated for the heights 151, 221, and 262 km. Figure 1 illustrates this correlation: the circles correspond to the experiment and the crosses represent the simulations. For the height 151 km, the difference in duration is about 30% and the difference in the peak-to-peak amplitude is about 11%; for the height 221 km, these differences are 38 and 34%, respectively; and for the height 262 km, 36 and 5%, respectively. Such a difference between simulations and the experiment may be caused, among other factors, by the fact that simulations were performed using 1976 U.S. Standard Atmosphere, while the Mill Race experiment was carried out in the period of the high solar activity. In particular, on September 16 the solar activity index F10.7 was as high as 204.8, which resulted in a temperature profile essentially different from the standard profile above a height of 100 km (Fig. 2). In addition, Warshaw and Dubois [8] used the initial impulse in the form of the Reed impulse, which inadequately describes the rarefaction phase and must be modified for the Mill Race experiments (see Drobzheva and Krasnov [10]). To verify the results of the calculations performed by Warshaw and Dubois [8] with taking into account the above notes is a nontrivial problem. Warshaw [5] reported his final theoretical result in the form of a partial differential equation. The solution of this equation (as the solution of the generalized Burgers equation [6]) requires further simplifications or computations based on approximate numerical methods with the corresponding consideration for the solution stability. In this connection, it is of interest to consider the possibility of interpreting the Mill Race experiment using the known exact solutions for a homogeneous atmosphere (Rudenko and Soluyan [11]) with corrections for the inhomogeneity and, if this approach appears to fit the experiment, to determine the laws governing the signature of the acoustic field.

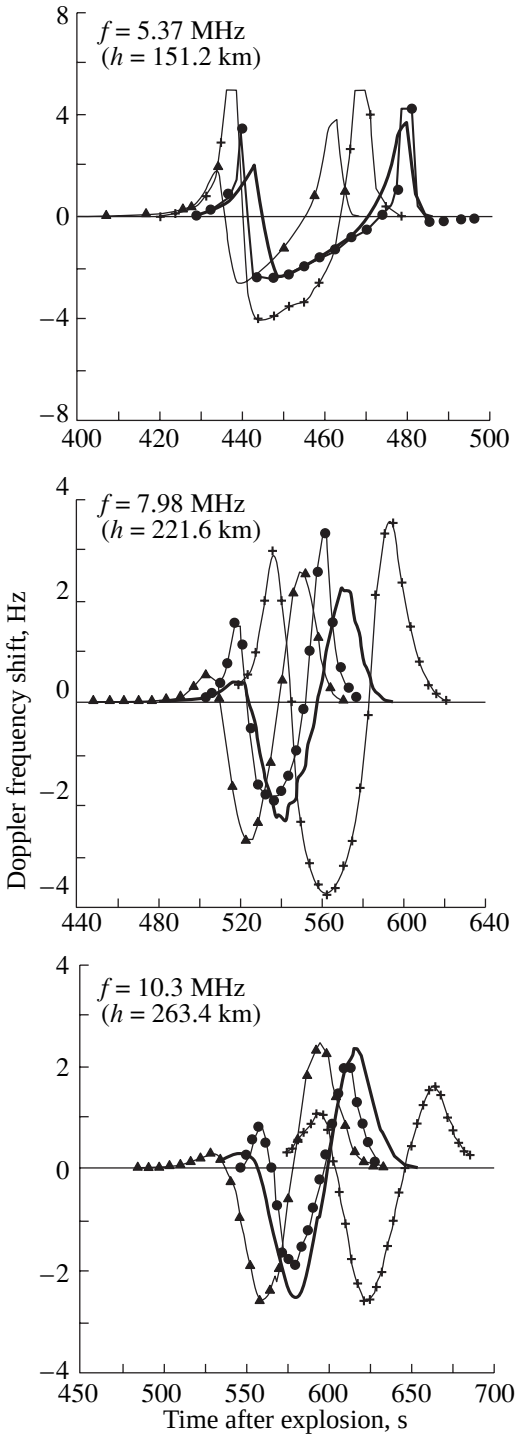

Fig. 1. Doppler frequency response of the radio-sounding signal to an acoustic impulse: the experimental data (circles), the calculations by Warshow and Dubois [8] (crosses), our calculations for the initial temperature profile (triangles), and our calculations for the corrected profile (the solid line).

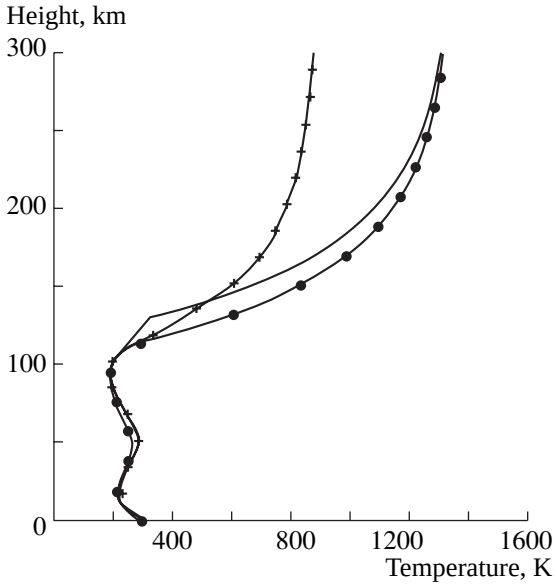

Fig. 2. Temperature profiles: the profile calculated by the MSIS model (circles), the profile calculated from the sound speed profile given by Warshaw and Dubois [8] for the standard atmosphere (crosses), and the corrected profile (the solid line).

We will use the initial acoustic impulse in the form of the modified Reed impulse that was empirically determined in [10]:

$$\begin{cases} p(t) = \Delta p(1 - t/t_+)(1 - t/\tau_g)(1 - (t/\tau_g)^2) \\ \longrightarrow 0 \le t \le 0.4\tau_g \\ p(t) = kt + d \longrightarrow 0.4\tau_g \le t \le \tau_s \\ p(t) = 0 \longrightarrow t > \tau_s, \end{cases}$$

where p is the pressure disturbance, Δp is the peak value of the shock wave, τ_g is the total duration of the Reed impulse, t_+ is the duration of the compression phase, t is the time variable, τ_s is the time instant for which the area of the wave in the rarefaction phase is equal to the area of the wave in the compression phase, $d = p(0.4\tau_g) - 0.4k\tau_g$, and $k = \partial p/\partial t$ for $t = 0.4\tau_g$.

Describing the propagation of acoustic waves in the atmosphere, we used the following approximations. We calculated the acoustic field along acoustic rays whose trajectories were obtained taking into account inhomogeneity of the atmosphere and the ray deformation. In so doing, we considered the wave as a plane one for every small ray segment located at a sufficiently large distance from the source. We assumed that the atmosphere is inhomogeneous only in the vertical direction. In the calculations, we used two models. The first model is described in detail in [10]. It includes the nonlinear effects, the spherical divergence of rays, and the corrections for the inhomogeneity. We used this model for calculating the initial signatures of impulses and their subsequent propagation to heights of about 10 km (i.e., to heights for which the acoustic field was measured with parachute probes during the Mill Race experiment). We approximated the vertical profiles of atmospheric parameters by stepped functions; i.e., the atmosphere was considered as homogeneous for each layer. The correlation with the parachute experiment showed (see [10]) that the height of an atmospheric layer equal to 0.1 km is a proper choice for which the experimental and theoretical results for acoustic impulses coincide within several percent in both duration and amplitude.

The second model was used for interpreting the Doppler shift measured during the Mill Race experiment for the ionospheric heights. In contrast to the first model, it takes into account the absorption and is developed on the basis of the Burgers equation [11],

$$\frac{\partial V}{\partial s} - \frac{\varepsilon}{c^2} V \frac{\partial V}{\partial \tau} - \frac{b}{2\rho c^3} \frac{\partial^2 V}{\partial \tau^2} = 0,$$

where V is the velocity of hydrodynamic particles, ρ is the density of the atmosphere, c is the velocity of sound, $\varepsilon = (\gamma + 1)/2$, γ is the ratio of specific heat at constant pressure (c_p) to specific heat at constant volume (c_v), $b = \left(\zeta + \frac{4}{3}\eta\right) + \left(\frac{1}{c_v} - \frac{1}{c_p}\right)\chi$; ζ and η are the bulk and shear viscosity coefficients, χ is the heat conductivity coefficient, the s axis is directed along the ray, and $\tau = t - s/c$.

With the substitution

$$V = \frac{b}{\varepsilon c \rho} \frac{\partial}{\partial \tau} (\ln U), \tag{1}$$

the Burgers equation is reduced to the equation $\frac{\partial U}{\partial s} = \frac{b}{2c^3\rho} \frac{\partial^2 U}{\partial \tau^2}$ whose solution is [11]

$$U = \frac{1}{\sqrt{4\pi a s}} \int_{-\infty}^{+\infty} U(\tau') \exp\left[-\frac{(\tau' - \tau)^2}{4as}\right] d\tau', \tag{2}$$

where $a = b/2c^3\rho$.

In numerical simulations, we first used Eq. (2) to obtain the function U and then we used substitution (1) to calculate the function $V(\tau)$. When a ray passed from one atmospheric layer to another, we introduced a correction in $V(\tau)$ to take into account the spherical divergence of the ray and the inhomogeneity of the atmosphere in the vertical direction. This correction was calculated using the results reported in [10] where the following expression was obtained with consideration for the area of the positive or negative unit acoustic impulse $I_v = \int_0^T V \partial \tau$ as a function of the parameters of

the atmospheric inhomogeneity for a spherically divergent wave:

$$I_v = I_{v*}\left(\frac{\rho_*}{\rho}\right)^{1/2}\frac{c_* L_*}{cL}. \quad (3)$$

Here, T is the duration of the acoustic impulse and L is the distance along the ray from the point of explosion to the observation point; the quantities with the asterisk correspond to the initial front of the acoustic wave and the quantities without asterisk correspond to an arbitrary point on the ray.

We used this formula to calculate the area of the impulse in the compression phase (the area of the impulse in the rarefaction phase is assumed to be equal to the area of the impulse in the compression phase by virtue of the momentum conservation). Then, we calculated the area of the impulse in the compression phase P_1 by integrating the solution $V(\tau)$ from Eq. (1). From these data, we determined the correction factor for $V(\tau)$ as $k = I_v/P_1$. This correction to the quantity $V(\tau)$ was introduced for every passage from one layer to another; in particular, we multiplied the velocity profile $V(\tau)$ by k at the upper boundary of each layer. It is obvious that such multiplication at the layer boundaries modifies only the impulse amplitude, and not the impulse duration. However, substitution (1) shows that this multiplication results in the corresponding correction to the amplitude of the function $U(t)$. In turn, the time interval essential for convolution (2) calculated for the subsequent layer depends on the amplitude of the function $U(t)$, so that the variation of this amplitude changes the impulse duration in comparison with the case of $k = 1$. Thus, we took into account the inhomogeneity of the atmosphere by the correction factor k for the passages from one layer to another and by the use of actual height-dependent atmospheric parameters at the lower boundary of each layer. The correlation with the experiment showed that 1 km is a proper choice for the height of an atmospheric layer in this case. To calculate the vertical profiles $\rho(z)$, $c(z)$, $b(z)$, $\gamma(z)$, $c_p(z)$, and $c_v(z)$, we used the MSIS-90 model [12] of the neutral atmosphere for the following parameters: the explosion date was September 16, 1981; the explosion time was 12:45:40 LT; the explosion coordinates were 33.62° N, 253.53° E; the solar activity index averaged over three months was F10.7 = 190.2; the solar activity index for the day preceding the explosion was F10.7 = 207.4; and the index of geomagnetic activity was $A_p = 7$. The coefficients of heat conductivity and shear viscosity were set according to the formulas [13]: $\chi = k_0 T^{3/2}/M$ and $\eta = \frac{4k_0}{(9\gamma - 5)c_v}$, where $k_0 = 0.015$ J K^{-1} m^{-1} s^{-1}, T is the temperature, and M is the molecular weight. The bulk viscosity was set as $\zeta = 2/3\eta$ [14].

To determine the effect of the acoustic wave on the ionosphere and, correspondingly, on the Doppler frequency of the sounding radio signal, we used the expression derived in [15]

$$f_d(t) = -\frac{f}{c_r}\int_T^R \frac{dl}{nN_f}$$
$$\times\left[N\left(\frac{V}{L}\sin^2\theta + \frac{\partial V}{\partial s}\cos^2\theta\right) + V\frac{dN}{dz}\cos\theta\cos\psi\right],$$

where f_d is the Doppler frequency, c_r is the speed of light, the integration is carried out over the ray trajectory from the transmitter T to the receiver R, n is the refraction index of radio waves, N_f is the ionosphere electron concentration such as to reflect a wave of frequency f incident on the ionosphere in the vertical direction, N is the electron concentration along the radio ray trajectory, θ is the angle between the direction of the geomagnetic field and the direction of the acoustic ray, and ψ is the angle between the direction of the geomagnetic field and the z axis.

This expression was derived in the geometrical optics approximation, and, for this reason, it fails in the region where radio waves are reflected. Near the reflection point, we used the linear approximation for the height-dependent electron concentration, which allowed us to obtain rigorous expressions. As a result, we obtained the following formula for the Doppler frequency shift near the reflection point of radio waves:

$$f_d(t) = -\frac{4f}{3c_r}(z_r - z_b)\cos\varphi$$
$$\times\left(\frac{V}{L}\sin^2\theta + \frac{\partial V}{\partial s}\cos^2\theta + \frac{V}{N_d}\frac{dN_d}{dz}\cos\theta\cos\psi\right),$$

where z_r is the height of reflection of the radio wave, z_b is the height within which the calculations according to geometrical optics formulas are adequate, φ is the angle of incidence of the radio wave on the ionospheric layer at a point z_b, and $N_d = N(z_r) - N(z_b)$. In the calculations, the values of V and $\partial V/\partial s$ were averaged over the heights from z_b to z_r.

We calculated the profile of the electron concentration in the ionosphere from an ionogram recorded in the region of the Mill Race explosion. The radio wave trajectories for the vertical sounding of the ionosphere at the frequencies 5.37, 7.98, and 10.3 MHz were calculated by taking into account the geomagnetic field. The corresponding heights of reflection of the radio waves appeared to be equal to 151, 222, and 263 km.

The calculated values of $f_d(t)$ are shown in Fig. 1 by triangles. As can be seen, the curves calculated for the heights 222 and 263 km are closer to the experimental curves than the curves by Warshaw and Dubois [8]; at the same time, for the height 151 km, our results, as the results of Warshaw and Dubois [8], significantly differ from the experiment in impulse duration. It can be

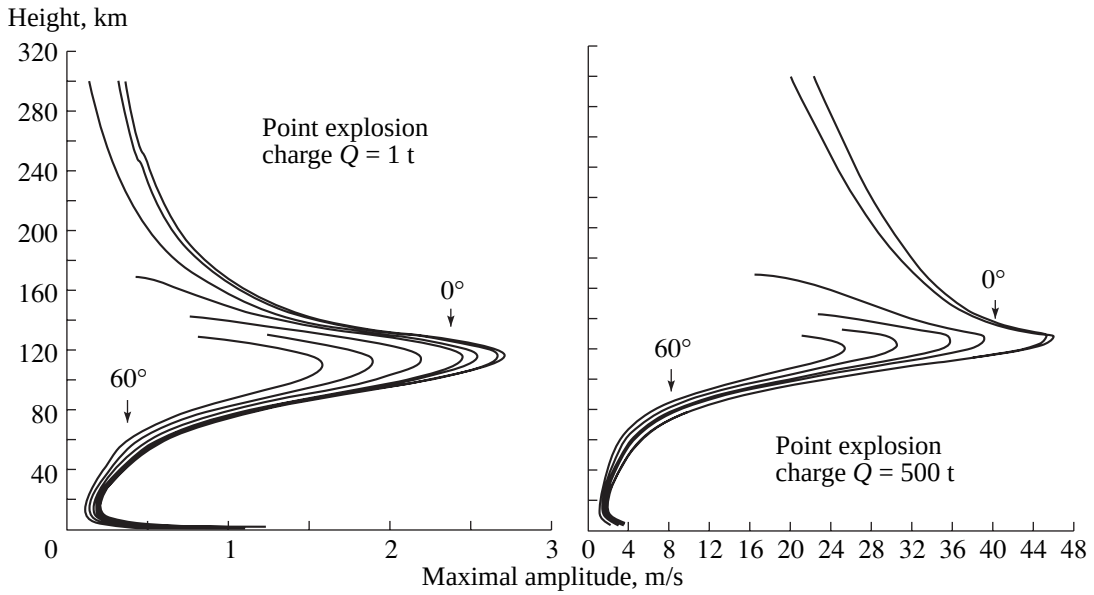

Fig. 3. Simulated maximal amplitude of the particle velocity of the acoustic impulse (V_{max}) versus the height for explosions with the equivalent trinitrotoluene charge of 1 and 500 t and for the zenith angles of ray departure 0°, 10°, 20°, 30°, 40°, 50°, and 60° (the upper end of the curves in the interval 120–170 km corresponds to the ray reflection height).

shown that these differences in duration can be reduced by decreasing the velocity of the acoustic wave (or the temperature) for the heights above 100 km. Figure 2 shows the temperature profile constructed by the MSIS-90 model and the corrected profile that goes slightly above the initial curve. The curve for $f_d(t)$ calculated for the corrected profile is shown in Fig. 1 by the solid line. The coincidence of the calculated curves with the experimental ones has become better for all three heights. An interesting point is that a considerable increase in the duration of the disturbance at the height of 151 km only slightly changes the duration for the heights of 222 and 263 km. A possible explanation is as follows. The duration of the disturbance in $f_d(t)$ is governed by the spatial size of the acoustic impulse and its velocity near the height of reflection of the radio wave. The height of 151 km lies in the region of a high temperature gradient (see Fig. 2), and a slight upward displacement of the curve considerably decreases the temperature and, correspondingly, the velocity of sound. For the heights of 222 and 263 km, the temperature gradient is small and the upward shift of the curve only slightly affects the velocity of sound.

Thus, using the models based on the known exact solutions for the homogeneous atmosphere with corrections for inhomogeneity [10, 11], the MSIS-90 atmosphere model, and the initial impulse in the form of the modified Reed impulse, we obtained a better agreement between the theoretical and experimental results, as compared to the calculations by Warshaw [5]. For this reason, the models suggested here are preferable for studying the formation of the spatial structure of an actual acoustic field in the atmosphere. The calculated acoustic fields are shown in Figs. 3 and 4. In particular, we calculated the height-dependent amplitude of the particle velocity for the acoustic impulses generated by explosions with equivalent trinitrotoluene charges of 1, 4, 20, 100, and 500 t for different zenith angles of ray departure. As an example, Fig. 3 shows the results calculated for the explosions with equivalent charges of 1 and 500 t. As seen from this figure, an acoustic impulse generated by a surface explosion and characterized by the initial amplitude of the particle velocity exceeding fractions of meter per second can penetrate the whole thickness of the atmosphere and ionosphere with significant velocity values. Simulations show that this fact follows primarily from the decrease in the atmosphere density with height and from the momentum conservation law (Eq. (3)). An increase in the amplitude of the particle velocity of an acoustic impulse with height is a feature favorable for a remote control of acoustic sources by the Doppler radio sounding of the ionosphere.

The above calculations offer an important conclusion: the height where the amplitude of the particle velocity of an acoustic impulse reaches its maximum is independent of the angle of ray departure and the equivalent explosion charge and lies at a height of about 120 km. Let us consider the factors that govern the formation of the velocity maximum at just these heights. Differentiating Eq. (1) and determining the velocity V at the instant τ_m corresponding to the positive maximum of the impulse,

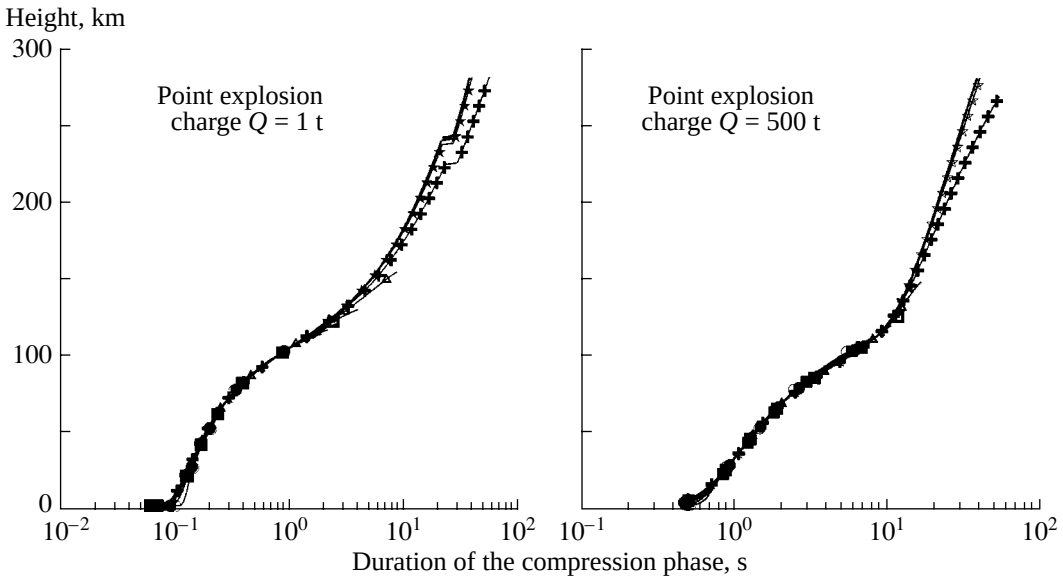

Fig. 4. Duration of the compression phase of the acoustic impulse versus the height for explosions with the equivalent charge of 1 and 500 t and for the zenith angles of ray departure 0° (the solid line), 10° (asterisks), 20° (crosses), 30° (triangles), 40° (squares), 50° (full triangles), and 60° (full circles). The duration was determined at a level of 0.1 of V_{max}.

one can obtain the relationship $V_m = k_1k_2k_3$, where $k_1 = \frac{c^2}{\varepsilon s}$, $k_2 = \int_{-\infty}^{+\infty} U(\tau')\exp\left[-\frac{(\tau' - \tau_m)^2}{4as}\right](\tau' - \tau_m)d\tau'$, and $k_3 = 1/\int_{-\infty}^{+\infty} U(\tau')\exp\left[-\frac{(\tau' - \tau_m)^2}{4as}\right]d\tau'$.

The numerical analysis of the height dependence of these coefficients shows that the coefficient k_1 is minimal near the height 100 km and then monotonically increases, while the coefficients k_2 and k_3 are maximal for the heights 110–120 km. This means that the height of the maximum of the acoustic impulse is mainly governed by coefficients k_2 and k_3. Both these coefficients are calculated by the convolution of the function $U(\tau')$ with the respective time windows $O_2 = \exp\left[-\frac{(\tau' - \tau_m)^2}{4as}\right](\tau' - \tau_m)$ and $O_3 = \exp\left[-\frac{(\tau' - \tau_m)^2}{4as}\right]$ at the instant τ_m. The function $U(\tau')$ is a positive function that monotonically increases from zero to a maximum during the compression phase of the impulse $V(t)$ and then, during the rarefaction phase, monotonically decreases to zero. The window O_3 is a bell-shaped impulse with a unit maximum, and the window O_2 is an impulse with a negative peak followed by a positive one. The amplitude of the window O_2 increases with the quantity as. Both windows are of infinite duration; however, one can select significant intervals that yield the dominant contributions to the integrals. The effective duration of these windows is proportional to the quantity $\tau_0 = \sqrt{4as}$. Using the coefficient k_2 as an example, let us consider in detail how the convolution is performed. In the general case, the window O_2 moves along the function $U(\tau')$; in the course of this motion, the window is multiplied by $U(\tau')$ and the result is integrated over the window duration. In this process, the segment where $U(\tau')$ increases determines the positive phase of the acoustic signal, and the segment where $U(\tau')$ decreases determines the negative phase; as a result, the impulse duration increases. Let us determine the instant corresponding to the maximum in the impulse $V(t)$. In the course of the integration, the terms corresponding to the positive and negative phases of the window O_2 are, clearly, subtracted. Hence, we can expect that the integral for k_2 will be maximal at the instant when the difference between the positive and negative terms in the integral will be maximal. It appears that this situation is realized when the positive portion of the window O_2 totally overlaps the function $U(\tau')$. With increasing height, the parameter as increases and, correspondingly, an increase occurs in the magnitude and duration of the positive peak in the window O_2. As a result, the area of integration increases, and the coefficient k_2 grows. Along with this effect, the opposite process can affect the coefficient k_2 with increasing height. Since the amplitude of the window is less than unity and the window is composed of positive and negative segments, the convolution procedure decreases the amplitude of the curve $U(\tau')$, which eventually results in an absorption of the acoustic impulse. An important point is that going from one layer to another can be accompanied by an increase in the integration area and, correspondingly, in the impulse amplitude, if the effect of the increase in the window duration and magnitude will exceed the effect

of the decay of the function $U(\tau')$. A similar consideration can be easily carried out for the coefficient k_3.

The existence of the maxima in the height-dependent coefficients k_2 and k_3 for heights of about 120 km indicates that the decrease in the function $U(\tau')$ mitigates the tendency of the impulse amplitude to increase with increasing parameter as. Now, we determine what atmospheric parameter plays the key role in this process. For simplicity, we consider the case of equithick atmospheric layers and an acoustic ray propagating in the vertical direction. In this case, the quantity s has a fixed value for all layers, and all height-dependent variations of the coefficients k_2 and k_3 depend only on the height dependence of the parameter a. In addition, the propagation path of the acoustic impulse will grow proportionally to the layer number.

An analysis of the height dependence of the parameter $a = b/(2c^3\rho)$ shows that all its variations are predominantly related to the variations in the atmospheric density (because the density varies according to an exponential law, while the velocity of sound $c(z)$ and the quantity $b(z)$ are relatively slow functions); the height dependence of the velocity $c(z)$ appreciably affects the profile $a(z)$ beginning from a height of about 100 km where a high positive gradient of the velocity of sound occurs (see Fig. 2). The effect of the height-dependent quantity $b(z)$ on the gradient of $a(z)$ is even smaller. It is known (see [12]) that temporal and spatial variations in the vertical profile of the atmospheric density are less prominent than those in the temperature profile. In addition, the rate of the decrease in the atmospheric density begins to decrease appreciably for heights of about 120 km. Correspondingly, smaller height-dependent variations in the density cause a smaller increase in the parameter a, which, as was shown above, reduces the factors governing the increase in the coefficients k_2 and k_3.

In line with this effect, the function $U(\tau')$ continues to decay from one layer to another along the acoustic ray despite a certain decrease in the decay rate. As a result, this factor acquires an increasing role in the process of the impulse formation. It can be easily seen that an increase in the gradient of the velocity of sound near a height of 100 km has similar consequences. Indeed, an increase in the velocity of sound with height causes a decrease in the parameter a, whereas a decrease in the density increases this parameter; in other words, the decrease in the sound velocity slows down the increase in the parameter a due to the decrease in the atmospheric density with height. Therefore, we can expect that an increase in the sound velocity will reduce the impulse amplitude and slightly (since the profile $c(z)$, unlike $\rho(z)$, only slightly affects the behavior of $a(z)$) reduce the height of the maximum in comparison with the case of the absence of this gradient at a height of 100 km. Determine now the role played in this process by the coefficient $k_1 = c^2/\varepsilon s$. In contrast to the above consideration, an increase in the velocity of sound should increase the impulse amplitude. However, simulations show that the effect of an increase in the velocity of sound on the amplitude is caused predominantly by the parameter a, because it strongly depends on the variations in the velocity profile c and appears in the exponent. Therefore, an increase in the velocity of sound causes the impulse amplitude to decrease.

Now, we consider the effect of the explosion power on the impulse amplitude and on the height corresponding to its maximum. An increase in the explosion charge increases the initial amplitude and duration of the impulse and, correspondingly, the amplitude and duration of the initial function $U(\tau')$, which leads to an increase in the area of significant values of the integrand in the convolution integral and an increase in the impulse amplitude for greater heights, all other factors being the same. However, the increase in the integration area and the impulse decay with height depend predominantly on the exponential behavior of the parameter a. For explosions with equivalent trinitrotoluene charges from 1 to 500 t, the increase in the integration area appeared to be a small additive that only slightly affects the position of the amplitude maximum. However, as we noted above, the rate of increase in the parameter a considerably decreases for heights above 120 km, and this additive begins to play an increasingly important role. As a result, the impulse decay becomes slower, which is shown in Fig. 3 with the simulated results.

The effect of the angle of departure of the acoustic ray on the impulse magnitude (Fig. 3) can be explained by the behavior of the height-dependent parameter s, which determines the length of the ray path in the layer as a function of the angle of wave incidence α, $s = \Delta z/\cos\alpha$, where Δz is the thickness of the layer. Considering the angles $\alpha \neq 0$ and taking into account the fact that a sharp increase in the gradient of the velocity of sound near a height of 100 km results in a faster decrease in the refraction coefficient and, consequently, in a faster increase in the angle α along with the fact that the angle α and the parameter s are related through a nonlinear relationship, we find that the ray path length in the layer becomes appreciably longer. As a result, the absorption of the impulse increases from one layer to another along the ray, and a clearly pronounced dependence of the amplitude on the initial angle of ray departure is observed in the region of the maximum (Fig. 3).

Thus, we can conclude that, for the considered explosions with the equivalent trinitrotoluene charges from 1 to 500 t, the height dependence of the density in an inhomogeneous atmosphere is the key factor that predominantly determines the height-dependent behavior of an acoustic impulse and the formation of its maximum at a height of about 120 km. On the one hand, the decreased density of the atmosphere results, according

to the momentum conservation law, in an increase in the amplitude of the acoustic impulse. On the other hand, the decay of the impulse mitigates this increase near a height of 120 km. As a result, a maximum is formed in the amplitude $V(t)$. The effect of the sharp increase in the sound velocity at heights above 100 km is reduced to a decrease in the impulse amplitude and a small shift of the amplitude maximum in the downward direction. This result differs qualitatively from the result of Orlov and Uralov [4] who reported that the height of the maximal amplitude strongly depends on the angle of the ray departure and varies from 300 to 150 km for angles of departure from 0° to 25°, respectively. In addition, these authors also noted that the height of the maximum is independent of the explosion power; however, they presented only the result for the zero angle of departure and obtained a value of 300 km for the height of the amplitude maximum.

As for the fact that, for a fixed height of the point of observation, the field amplitude is independent of the angle of ray departure from the point source (this phenomenon was revealed by Razin and Fridman [2]), our study demonstrated that, with the inclusion of the atmospheric absorption, this statement holds only for heights below 80–100 km (Fig. 3). Above this region, the amplitude of the impulse depends on the angle of ray departure. The weak dependence of the impulse amplitude on the angle of ray departure that occurs for heights below 80–100 km can serve as an indicator of a chemical point explosion.

Figure 4 shows the duration of the compression phase of the acoustic impulse versus the height for explosions with equivalent trinitrotoluene charges of 1 and 500 t and for different angles of ray departure. It can be seen that the duration of the compression phase increases with height and, to a height of about 120 km, is almost independent of the initial angle of ray departure. As was shown earlier, the height-dependent parameter as varies predominantly due to the variations in the atmospheric density, which causes a nearly exponential increase in the parameter as and, correspondingly, in the amplitude of the window O_2 and the duration of the windows O_2 and O_3. As a result, both the area significant for integrating in the convolution and the impulse duration increase according to an exponential law. The rate of variation of the compression phase appreciably increases for the heights 80–120 km. This increase is caused, primarily, by the fact that, for these heights, the variation of the atmospheric density is characterized by a higher rate. For heights above 120 km, the rate of variation of the density decreases and, correspondingly, the rate of the increase in the duration of the impulse compression phase also decreases with increasing height. The stronger dependence of the impulse duration on the angle of ray departure for heights above 120 km is caused by the same reason as the increase in the impulse amplitude, namely, by a faster increase in the parameter s with height.

Let us consider the effect of the absorption coefficient b on the impulse duration. It is clear that an increase in b with height, as well as a decrease in ρ with increasing height, will increase parameter a. However, in the case of increasing absorption, the parameter a varies much slower than in the case of decreasing density. As a result, the windows O_2 and O_3 only slightly increase in their durations, whereas the function $U(\tau')$ continues to decay from one layer to another. Consequently, calculating the convolution, we obtain a slower rate of increase in the impulse duration with increasing height. The highest positive gradient of the absorption coefficient $b(z)$ occurs near a height of 120 km with a following monotonic increase. In this connection, the increase in the absorption coefficient b is an additional factor that slows down the growth of the impulse duration at heights above 120 km (Fig. 4).

As seen from Fig. 4, for a fixed height, the impulse duration in the case of the explosion with the charge of 500 t appears to be longer than in the case of a charge of 1 t. This fact is primarily related to the longer initial duration of the impulse in the first case and to the rates of the following increase in the durations of both impulses. Nevertheless, it is seen that the impulse produced by the powerful explosion is generally characterized by a slower increase in its duration. This fact can be explained as follows. Relationship (3) shows that the increase in the impulse area with height is independent of its initial area. At the same time, the amplitude of the impulse produced by the more powerful explosion, as we showed earlier, decreases slower with increasing height. Consequently, its duration should increase slower to conserve the impulse area for a fixed height.

The increase in the impulse duration at a fixed height with increasing charge of explosion qualitatively confirms the results obtained in [4]. This result makes it possible to determine the explosion power from the impulse duration measured at ionospheric heights. In addition, the fact that, as was shown above, the duration of the compression phase only weakly depends on the angle of ray departure offers an opportunity to omit the angle of departure in the calculations and, hence, to simplify the procedure of determining the explosion charge.

ACKNOWLEDGMENTS

We are grateful to the anonymous reviewer for helpful remarks, to G. Gordienko for calculating the profiles of electron concentration from the ionogram, to V. Vodyannikov for the program for calculating the paths of radio rays, and to A.E. Hedin for the program of the MSIS-90 model.

This work was supported by University of California, Lawrence Livermore National Laboratory, Livermore, California, USA, under the contract to the US Department of Energy and the Science Foundation of the Republic of Kazakhstan, project no. 89-98.

REFERENCES

1. O. A. Pokhotelov, M. Parrot, E. N. Fedorov, *et al.*, Ann. Geophys. (France) **13**, 1197 (1995).
2. A. V. Razin and V. E. Fridman, Akust. Zh. **41**, 281 (1995) [Acoust. Phys. **41**, 242 (1995)].
3. T. J. Fitzgerald and R. C. Carlos, Radio Sci. **32** (1), 169 (1997).
4. V. V. Orlov and A. M. Uralov, Izv. Akad. Nauk SSSR, Fiz. Atmos. Okeana 20 (6), 476 (1984).
5. S. I. Warshaw, *On a Finite Amplitude Extension of Geometric Acoustic in a Moving, Inhomogeneous Atmosphere* (Lawrence Livermore National Lab., USA, 1980).
6. O. V. Rudenko and A. K. Sukhorukova, Akust. Zh. **37**, 753 (1991) [Sov. Phys. Acoust. **37**, 392 (1991)].
7. O. V. Rudenko, Usp. Fiz. Nauk **165** (9), 1011 (1995) [Phys.–Usp. **38**, 965 (1995)].
8. S. I. Warshaw and P. F. Dubois, *Preliminary Theoretical Acoustic and RF Sounding Calculation for Mill Race* (USA, 1981), Report 550.
9. J. R. Banister and W. V. Hereford, J. Geophys. Res. D **96**, 5185 (1991).
10. Ya. V. Drobzheva and V. M. Krasnov, Akust. Zh. **45**, 213 (1999) [Acoust. Phys. **45**, 190 (1999)].
11. O. V. Rudenko and S. I. Soluyan, *Theoretical Foundations of Nonlinear Acoustics* (Nauka, Moscow, 1975; Consultants Bureau, New York, 1977).
12. A. E. Hedin, J. Geophys. Res. A **96**, 1159 (1991).
13. J. M. Forbes and H. B. Garrett, Rev. Geophys. Space Phys. **17** (8), 1951 (1979).
14. A. Ivanovskiĭ, A. Repnev, and E. Shvidkovskiĭ, *Kinetic Theory of the Upper Atmosphere* (Gidrometeoizdat, Leningrad, 1967).
15. V. M. Krasnov, G. M. Pelenitsyn, O. E. Ryaskov, and N. M. Salikhov, Vestn. Akad. Nauk Kaz. SSR, No. 8, 44 (1991).

Translated by A. Vinogradov

Acoustical Physics, Vol. 47, No. 5, 2001, pp. 565–571. Translated from Akusticheskiĭ Zhurnal, Vol. 47, No. 5, 2001, pp. 650–656.

Employment of the Scattering Amplitude in Solving the Diffraction Problems for Waves in a Halfspace

A. V. Zatserkovnyĭ, V. A. Sergeev, and B. P. Sharfarets

Institute of Applied Mathematics, Far East Division, Russian Academy of Sciences, ul. Radio 3, Vladivostok, 690007 Russia

Kuznetsov Naval Academy, Vyborgskaya nab. 73/1, St. Petersburg, 197045 Russia

e-mail: sharg@mail.rcom.ru

Received October 27, 1997

Abstract—The problem on the diffraction of an acoustic wave by a finite-size scatterer (inclusion) located in a halfspace is considered. The method of solving this problem is based on the use of the scattering amplitude of the inclusion. A formula analogous to the Green formula is presented. It allows one to determine the scattering amplitude of the inclusion for an arbitrary incident wave (determined by the directional pattern of the source of primary waves) from the scattering amplitude corresponding to plane incident waves. The algorithm is presented for solving the problem on the operation of an acoustically opaque radiator in a halfspace whose boundary is characterized by an arbitrary reflection coefficient. As an example, the problem is solved on the generation of low-frequency oscillations by a sphere with an acoustically soft boundary near an acoustically hard or soft boundary of the halfspace. *© 2001 MAIK "Nauka/Interperiodica".*

The literature on the scattering problems is quite extensive. Here, we only mention some publications that are concerned with the problems of the sound scattering in acoustic waveguides [1–7] and that describe numerical or asymptotic methods for their solution. A two-dimensional acoustic scattering problem formulated in terms of regular integral equations was solved by Yang [17]. Ochmann [18] studied a two-dimensional problem on the scattering by an arbitrary body located near an impedance boundary. This problem was solved by the boundary-element method. Bishop [19] obtained a three-dimensional solution to the problem on the scattering by elastic bodies located near a boundary between two homogeneous halfspaces one of which was assumed to be liquid and the other elastic. The problem was solved by the T-matrix method, which was cumbersome, yet approximate. In this paper, for solving the problems on the scattering in bounded media, we use an extension of the domain of definition of the scattering amplitude to the whole complex plane of the angles of incidence. The technique used to realize this approach is described in, e.g., [8–10]. We obtain an expression that is similar to the Green formula and that allows one to determine the scattering amplitude of an inclusion for an arbitrary incident wave (given by the directional pattern of the source of primary waves) from the scattering amplitude corresponding to plane incident waves.

We present the algorithm for solving the problem on the operation of an acoustically opaque source in a halfspace whose boundary is characterized by an arbitrary reflection coefficient. As an example, we solve the problem on the generation of low-frequency oscillations by a sphere with an acoustically soft surface near an acoustically hard or soft boundary of the halfspace.

Let us consider the problems of steady-state scattering from a volume scatterer and a surface scatterer in R^3. We consider a bounded region $E \in R^3$ with the boundary $\partial E = S$. The volume scatterer is determined by the perturbation of the refraction index in the region E (for simplicity, we assume that the density of the medium in E is constant and coincides with the density of the medium in the surrounding homogeneous space R^3). The surface scatterer is characterized by the boundary conditions at the surface S.

The total field U can be represented in the form of a sum of the incident U_0 and scattered U_S fields. The source of the incident field can be either a radiator concentrated in a region B, which in the general case does not coincide with the region E, or a plane wave arriving from infinity [11, 12]. For example, in the case of a volume scatterer when the source of the incident field is a radiator with a volume density F, $\mathrm{supp}F = B$, the following expression is valid (when $F = 0$, the source of the incident field is a plane wave arriving from infinity):

$$\Delta U + k^2 U = -V(\mathbf{x})U + F, \quad \mathbf{x} \in R^3, \qquad \mathrm{supp}V = E, \quad \mathrm{supp}F = B, \tag{1}$$

$$U_S(\mathbf{x}) = O(|\mathbf{x}|^{-1}), \qquad \frac{\partial U_S}{\partial |\mathbf{x}|} - jkU_S = o(|\mathbf{x}|^{-1}) \ \text{ for } \ |\mathbf{x}| \longrightarrow \infty. \tag{2}$$

Here, $V(\mathbf{x}) = k^2(n^2 - 1)$, where n is the refraction index in the region E; in the region $R^3 \backslash E$, $n(\mathbf{x}) \equiv 1$; and k is the wave number.

The incident field U_0 must not necessarily satisfy conditions (2) (e.g., in the case of a plane incident wave). Analogously, for a surface scatterer, when the source of the incident field is a plane wave arriving from infinity, we have

$$\Delta U + k^2 U = 0, \quad \mathbf{x} \in R^3 \backslash E, \tag{3}$$

$$\frac{\partial U}{\partial \mathbf{n}} = \alpha(\mathbf{x}); \quad U(\mathbf{x}) = \beta(\mathbf{x}); \quad \mathbf{x} \in S, \tag{4}$$

where U_S again satisfies conditions (2). Here, the functions $\alpha(\mathbf{x})$ and $\beta(\mathbf{x})$ are related by an integral equation following from the Kirchhoff formula [11]:

$$\beta(\mathbf{x}) = \int_S G(\mathbf{x}, \mathbf{y})\alpha(\mathbf{y}) - \beta(\mathbf{y})\frac{\partial G(\mathbf{x}, \mathbf{y})}{\partial n(\mathbf{y})} dS(\mathbf{y}),$$

$$\mathbf{x}, \mathbf{y} \in S,$$

where the function G is defined below.

The solution to the problem given by Eqs. (1) and (2) at $F \equiv 0$ can be represented (using the Green formula) in the form

$$U(\mathbf{x}) = U_0(\mathbf{x}) + \int_E V(\mathbf{y})G(\mathbf{x}, \mathbf{y})U(\mathbf{y})dy, \quad \mathbf{x} \in R^3 \tag{5}$$

(see, e.g., [11]). The solution to the problem given by Eqs. (3), (4), and (2) can be represented as follows:

$$U(\mathbf{x}) = U_0\mathbf{x}$$

$$+ \int_S \left[G(\mathbf{x}, \mathbf{y})\frac{\partial U(\mathbf{y})}{\partial \mathbf{n}} - U(\mathbf{y})\frac{\partial G(\mathbf{x}, \mathbf{y})}{\partial n(\mathbf{y})} \right] dS(\mathbf{y}), \quad \mathbf{x} \notin E \tag{6}$$

(see [11]).

In Eqs. (5) and (6), $G(\mathbf{x}, \mathbf{y}) = \exp(jk|\mathbf{x} - \mathbf{y}|)/(4\pi|\mathbf{x} - \mathbf{y}|)$ and n is the inner normal to S. Expressions (5) and (6) are integral equations for the determination of the resulting field $U(\mathbf{x})$.

Using Eqs. (5) and (6) and the technique described in [8], we can express the scattering field through the function T_i:

$$U_S^i(\mathbf{x}) = \frac{j}{2\pi}\int_{R^2} \frac{T_i(\boldsymbol{\xi})}{\alpha(\boldsymbol{\xi})}\exp(j\mathbf{k}_i\mathbf{x})d\xi, \quad i = 1, 2. \tag{7}$$

Here, $i = 1$ and 2 for the upper and lower halfspaces, respectively; $\boldsymbol{\xi} = (k_x, k_y) \in R^2$; $\mathbf{k}_i = (k_x, k_y, (-1)^i\alpha(k_x, k_y))$; $d\xi = dk_x dk_y$; and $\alpha(k_x, k_y) = \sqrt{k^2 - k_x^2 - k_y^2}$, where we consider the branch of the root with $\mathrm{Re}(\alpha) \geq 0$. The quantity T_i can be determined by the formulas

$$T_i(\boldsymbol{\xi}) = \frac{1}{4\pi}\int_E V(\mathbf{x})U(\mathbf{x})\exp(-j(\mathbf{k}_i\mathbf{x}))d\mathbf{x}, \tag{8}$$

$$T_i(\boldsymbol{\xi}) = \frac{1}{4\pi}\int_S \left[\frac{\partial U(\mathbf{y})}{\partial \mathbf{n}} + j(\mathbf{k}_i\mathbf{n})U(\mathbf{y}) \right] \times \exp(-j(\mathbf{k}_i\mathbf{y})dS(\mathbf{x}), \text{ where } \mathbf{y} \in S \tag{9}$$

for the volume and surface scatterers, respectively.

In the theory of scattering, the function T_i defined in the region $|\boldsymbol{\xi}| \in [0, k]$ (the so-called visible region where the angle of incidence is $\theta \in [0, \pi]$) is called the scattering amplitude or the scattering diagram (see, e.g., [11, 12]). For the function T_i defined in the region $|\boldsymbol{\xi}| \in [0, \infty)$ (the angle of incidence is $\theta \in [0, \frac{\pi}{2} - j\infty)$), we will also use the term *scattering amplitude*. The necessity to extend the domain of definition of this function follows from Eq. (7). For a correct description of the scattering field by Eq. (7), the domain of definition of the scattering amplitude of a scatterer should be extended to the region $|\boldsymbol{\xi}| \in [0, \infty)$, which is equivalent to the region $\theta \in [0, \frac{\pi}{2} - j\infty)$, $\varphi \in [0, 2\pi]$ in the polar coordinate system. Naturally, T_i depends on the incident wave. In view of this, the scattering amplitude corresponding to a plane incident wave is of particular interest, because the scattering amplitude corresponding to an arbitrary incident wave can be expressed through the directivity pattern of the incident wave and the scattering amplitude of the scatterer for plane incident waves. To prove this statement, we consider an incident wave $U_0 = \exp(j(\mathbf{k}_{pm}\mathbf{x}))$ (this is the amplitude of a plane wave with the wave front normal to the vector $\mathbf{k}_{pm}$). Here, the subscript p indicates that it is an incident wave and the subscript m corresponds to the propagation direction of this wave relative to the Oz axis: $m = 1$ when the plane wave propagates in the direction of increasing z, and $m = 2$ when it propagates in the opposite direction. Evidently, we have $\mathbf{k}_{p1} = (\boldsymbol{\xi}_p, \alpha_p)$ and $\mathbf{k}_{p2} = (\boldsymbol{\xi}_p, -\alpha_p)$. Thus, the wave U_0 characterized by the vector $\mathbf{k}_{p1}$ is incident on the scatterer from above (the Oz axis is directed downward), and the wave with the vector $\mathbf{k}_{p2}$ is incident from below.

We denote the scattering amplitude corresponding to the wave U_0 by $T_i^m(\boldsymbol{\xi}_p, \boldsymbol{\xi}_s)$ (in quantum mechanics, a similar function is called the scattering matrix (see p. 893 in [13])). Hence, $T_i^m(\boldsymbol{\xi}_p, \boldsymbol{\xi}_s)$ is the scattering amplitude in the following case: the incident wave is characterized by the vector $\mathbf{k}_{pm}$ and the scattered wave is considered in the halfspace lying above ($i = 1$) or below ($i = 2$) the scatterer in R^3. The scattered plane waves are characterized by the vectors $\mathbf{k}_{s1} = (\boldsymbol{\xi}_s, -\alpha_s)$ and $\mathbf{k}_{s2} = (\boldsymbol{\xi}_s, \alpha_s)$ for the upper and lower (relative to the scatterer) halfspaces in R^3, respectively (note that precisely these vectors are involved Eq. (8)).

From the physical point of view, the meaning of the function T_i^m is as follows: when a wave with the vector

$\mathbf{k}_p$ arrives at the input of the system, a sum of plane waves with the vectors $\mathbf{k}_s$ is formed at its output.

We express the arbitrary incident field of a source located at the origin of coordinates through the directional pattern of the source [8]:

$$U_{0m}(\mathbf{x}) = \frac{j}{2\pi}\int_{R^2}\frac{D_m(\boldsymbol{\xi})}{\alpha(\boldsymbol{\xi})}\exp(j(\mathbf{k}_m\mathbf{x}))d\boldsymbol{\xi}, \quad m = 1, 2. \tag{10}$$

We introduce the operators

$$A^v U = \int_E V(\mathbf{y})G(\mathbf{x}, \mathbf{y})U(\mathbf{y})d\mathbf{y},$$

$$A^s U = \int_S\left[\frac{\partial U(\mathbf{y})}{\partial n(\mathbf{y})}G(\mathbf{x}, \mathbf{y}) - U(\mathbf{y})\frac{\partial G(\mathbf{x}, \mathbf{y})}{\partial n(\mathbf{y})}\right]ds(\mathbf{y}),$$

$$B_i^v U = \frac{1}{4\pi}\int_E V(\mathbf{y})U(\mathbf{y})\exp(-j(\mathbf{k}_i\mathbf{y}))d\mathbf{y},$$

$$B_i^s U = \frac{1}{4\pi}\int_S\left[\frac{\partial U(\mathbf{y})}{\partial n(\mathbf{y})} + j(\mathbf{k}_i\mathbf{n}(\mathbf{y})U(\mathbf{y}))\right]\exp(-j(\mathbf{k}_i\mathbf{y}))ds(\mathbf{y}).$$

The superscripts v and s indicate the type of scattering—the volume and surface scattering, respectively. From Eqs. (5) and (6), we obtain (the superscripts v and s are omitted): $(I - A)U = U_0$ and $U = (I - A)^{-1}U_0$, where the operator $(I - A)^{-1}$ is an integral one and the properties of its kernel allow subsequent operations. Expressions (8) and (9) yield

$$T_i = B_i U = B_i(I - A)^{-1}U_0. \tag{11}$$

Now, using representation (10) for U_0, we derive

$$T_i(\boldsymbol{\xi}_s) = \frac{j}{2\pi}\int_{R^2}\frac{D_m(\boldsymbol{\xi}_p)}{\alpha(\boldsymbol{\xi}_p)}B_i(I - A)^{-1}\exp(j\mathbf{k}_{pm}\mathbf{x})d\boldsymbol{\xi}_p.$$

At the same time, from Eq. (11), it follows that $T_p^m(\boldsymbol{\xi}_p, \boldsymbol{\xi}_s) = B_i(I - A)^{-1}\exp(j\mathbf{k}_{pm}\mathbf{x})$, and, hence, we have

$$T_i(\boldsymbol{\xi}_s) = \frac{j}{2\pi}\int_{R^2}\frac{D_m(\boldsymbol{\xi}_p)}{\alpha(\boldsymbol{\xi}_p)}T_i^m(\boldsymbol{\xi}_p, \boldsymbol{\xi}_s)d\boldsymbol{\xi}_p, \quad i, m = 1, 2. \tag{12}$$

This means that the scattering matrix in the theory of scattering has the same meaning as the Green function in the theory of boundary-value problems. The Green function represents the field of point sources and allows one to reconstruct the field of an arbitrary source, whereas the scattering matrix represents the scattering amplitude of a scatterer in the case of plane incident waves and allows one to determine the scattering amplitude for an arbitrary incident wave.

After the scattering amplitude of the scatterer for a given incident wave is determined, the scattering field can be obtained from Eq. (7). However, a more simple way is to use the field expansion in powers of $1/kR$ (see [9]):

$$U_s(\mathbf{x}) = \frac{\exp(jkR)}{R}\sum_{n=0}^{\infty}\frac{T_n'(\vartheta, \varphi)}{(kR)^n}, \tag{13}$$

where

$$\left.\begin{aligned} T_0'(\pi - \vartheta, \varphi) &= T_1(\boldsymbol{\xi}) \\ T_0'(\vartheta, \varphi) &= T_2(\boldsymbol{\xi}) \end{aligned}\right\} \quad \begin{aligned} \boldsymbol{\xi} &= (k\sin\vartheta\cos\varphi, k\sin\vartheta\sin\varphi), \\ \vartheta &\in [0, \pi/2 - j\infty], \quad \varphi \in [0, 2\pi], \end{aligned} \tag{14}$$

and the quantities T_n' for $n > 0$ are obtained from T_0' using the recurrence relation (see [9]).

Let us use the technique considered above for solving the following problem: an acoustically opaque radiator determined by the region E, the directional pattern $D_i(\boldsymbol{\xi})$, and the scattering matrix $T_i^m(\boldsymbol{\xi}_p, \boldsymbol{\xi}_S)$ is placed in a homogeneous halfspace. The reflecting boundary $z = 0$ is characterized by the reflection coefficient $V(\boldsymbol{\xi})$. The source E generates a wave U_0. We denote the contraction of U_0^i in Ω_i ($i = 1, 2$) ($\Omega_1 = \{(\mathbf{x}, \mathbf{y}) \in R^2, z \le z_0\}$, $\Omega_2 = \{(\mathbf{x}, \mathbf{y}) \in R^2, z \ge z_0\}$, where z_0 is the ordinate of the radiator center) by U_0^i. The quantity U_0^i can be expressed through $D_i(\boldsymbol{\xi})$ (see [11]):

$$U_0^i(\mathbf{x}) = \frac{j}{2\pi}\int_{R^2}\frac{D_i(\boldsymbol{\xi})\exp(j(-1)^i\alpha(\xi)(z - z_0))}{\alpha(\xi)}\exp(j\xi r)d\xi. \tag{15}$$

Here, $\mathbf{x}_0 = (0, 0, z_0)$. The phase additive $\exp[j(-1)^i\alpha(\xi)(z - z_0)]$ is caused by the fact that D_i is calculated for the radiator position with the origin of coordinates at $\mathbf{x}_0 = (0, 0, z_0)$ (see [8]). The direct wave U_0^2 produces no scattering wave, because it propagates from the source directly into the lower halfspace Ω_2.

The wave U_0^1 behaves in a different way. It reaches the boundary $z = 0$ where it is reflected and propagates

downward into Ω_2 giving rise to waves scattered by E, which propagate upward (into Ω_1) and downward (into Ω_2). The primary wave scattered upward is reflected from the boundary $z = 0$, then it propagates downward causing secondary scattering in the upward and downward directions, and so on. To determine the field in Ω_i ($i = 1, 2$), it is necessary to combine all waves multiply scattered from E and reflected from the boundary.

We introduce the operators

$$A_2^i[D_1](\boldsymbol{\xi}_s) = \int_{R^2} T_2^i(\boldsymbol{\xi}_p, \boldsymbol{\xi}_s)\exp[2j\alpha(\boldsymbol{\xi}_p)z_0]V(\boldsymbol{\xi}_p)\frac{D_1(\boldsymbol{\xi}_p)}{\alpha(\boldsymbol{\xi}_p)}d\xi_p. \quad (16)$$

Here, $T_2^i(\boldsymbol{\xi}_p, \boldsymbol{\xi}_s)$ is the scattering matrix of the radiator E when the plane wave is incident on E from above and is scattered upward ($i = 1$) or downward ($i = 2$). Combining all multiply scattered waves, we obtain the resulting field in Ω_i in the form

$$U^1(\mathbf{x}) = \frac{j}{2\pi}\int_{R^2}\sum_{n=0}^{\infty}(A_2^1)^n[D_1](\boldsymbol{\xi}_s)[\exp(-j(z-z_0)\alpha(\boldsymbol{\xi}_s)) + V(\boldsymbol{\xi}_S)\exp(j(z+z_0)\alpha(\boldsymbol{\xi}_S))]\frac{\exp(j\boldsymbol{\xi}_S\mathbf{r})}{\alpha(\boldsymbol{\xi}_S)}d\xi_S, \quad (17)$$

$$\mathbf{x} \in \Omega_1$$

$$U^2(\mathbf{x}) = \frac{j}{2\pi}\int_{R^2}\left[\sum_{n=0}^{\infty}(A_2^1)^n[D_1](\boldsymbol{\xi}_s)V(\boldsymbol{\xi}_s) \times \exp(j(z+z_0)\alpha(\boldsymbol{\xi}_s)) + \left[\sum_{n=0}^{\infty}A_2^2(A_2^1)^n[D_1](\boldsymbol{\xi}_S) + D_2(\boldsymbol{\xi}_S)\right]\right. \quad (18)$$

$$\left.\times \exp(j(z-z_0)\alpha(\boldsymbol{\xi}_S))\right]\frac{\exp(j\boldsymbol{\xi}_S\mathbf{r})}{\alpha(\boldsymbol{\xi}_S)}d\xi_S,$$

$$\mathbf{x} \in \Omega_2.$$

The operator series in Eqs. (17) and (18) converge, if the norm of the operator A_2^1 is less than unity. The latter can be easily proved using the energy considerations. We introduce the notation

$$\tilde{T}_1(\boldsymbol{\xi}) = \sum_{n=0}^{\infty}(A_2^1)^n[D_1](\boldsymbol{\xi}), \quad \tilde{T}_2(\boldsymbol{\xi}) = A_2^2[\tilde{T}_1](\boldsymbol{\xi}). \quad (19)$$

Convolving the Neumann operator series in Eq. (19), we obtain

$$\tilde{T}_1(\boldsymbol{\xi}) = (I - A_2^1)^{-1}[D_1](\boldsymbol{\xi}). \quad (20)$$

Inverting Eq. (20), we obtain a Fredholm integral equation of the second kind

$$(I - A_2^1)[\tilde{T}_1](\boldsymbol{\xi}) = D_1(\boldsymbol{\xi}), \quad (21)$$

which can be solved by conventional means. With allowance for Eq. (19), we represent Eqs. (17) and (18) in a compact form

$$U^1(\mathbf{x}) = \frac{j}{2\pi}\int_{R^2}\tilde{T}_1(\boldsymbol{\xi}_s)[\exp(-j(z-z_0)\alpha(\boldsymbol{\xi}_s)) + V(\boldsymbol{\xi}_s)\exp(j(z+z_0)\alpha(\boldsymbol{\xi}_s))]\frac{\exp(j\boldsymbol{\xi}_s\mathbf{r})}{\alpha(\boldsymbol{\xi}_s)}d\xi_s, \quad (22)$$

$$U^2(\mathbf{x}) = \frac{j}{2\pi}\int_{R^2}\tilde{T}_1(\boldsymbol{\xi}_s)V(\boldsymbol{\xi}_s)[\exp(j(z+z_0)\alpha(\boldsymbol{\xi}_s)) + [\tilde{T}_2(\boldsymbol{\xi}_S) + D_2(\boldsymbol{\xi}_S)]\exp(j(z-z_0)\alpha(\boldsymbol{\xi}_S))] \times \frac{\exp(j\boldsymbol{\xi}_S\mathbf{r})}{\alpha(\boldsymbol{\xi}_S)}d\xi_S. \quad (23)$$

As one can see from Eqs. (22) and (23), the functions T_i can be interpreted as the directional diagram of some transparent radiator that is equivalent to the given radiator. The structure of expressions (22) and (23) shows that the field is formed by a real and an imaginary source. The coincidence with the classical form will be complete, if in a particular case we take $D_1 \equiv D_2$ and $A_2^2 = A_2^1$. Then, as one can see form Eq. (18), the pre-exponential of $\exp(j(z-z_0)\alpha)$ will transform to T_1. Constructing the series of type (13) by the method described in [9], we obtain the field in the halfspace under consideration in the form

$$U_s(\mathbf{x}) = \frac{\exp(jkR)}{R}\sum_{n=0}^{\infty}\frac{D_{1n}(\vartheta, \varphi)}{(kR)^n} + \frac{\exp(jkR')}{R'}\sum_{n=0}^{\infty}\frac{D_{2n}(\vartheta', \varphi')}{(kR')^n}. \quad (24)$$

Here,

$$\left.\begin{aligned} D_{1,0}(\pi - \vartheta, \varphi) &= \tilde{T}_1(\boldsymbol{\xi}) \\ D_{1,0}(\vartheta, \varphi) &= \tilde{T}_2(\boldsymbol{\xi}) + D_2(\boldsymbol{\xi}) \\ D_{2,0}(\vartheta, \varphi) &= \tilde{T}_1(\boldsymbol{\xi})V(\boldsymbol{\xi}) \end{aligned}\right\} \quad \vartheta, \vartheta' \in \left[0, \frac{\pi}{2} - j'\infty\right], \quad \varphi \in [0, 2\pi].$$

The leading terms are determined from the recurrence relation [10]

$$D_{1,n+1}(\vartheta, \varphi) = \frac{\Delta_{\vartheta,\varphi} + n(n+1)}{2j(n+1)}D_{1,n}(\vartheta, \varphi),$$

$$\Delta_{\vartheta\varphi} = \frac{1}{\sin\vartheta}\left(\frac{\partial}{\partial\vartheta}\left[\sin\vartheta\frac{\partial}{\partial\vartheta}\right] + \frac{1}{\sin\vartheta}\frac{\partial^2}{\partial\varphi^2}\right).$$

The coordinates (R, ϑ, φ) and $(R', \vartheta', \varphi)$ characterize the position $\mathbf{x}$ relative to the real and the imaginary sources.

Let us calculate the field in the following simple case.

We consider a sphere, which has a radius R_0 and its center at the point $\mathbf{x}_0 = (0, 0, z_0)$, in a homogeneous half-space with a plane boundary characterized by the reflection coefficient $V(\xi) \equiv 1$ (a hard boundary) or $V(\xi) \equiv -1$ (a soft boundary). We assume that the Dirichlet condition is satisfied at the sphere surface. In addition, the density of the sound sources uniformly distributed over the sphere surface satisfies the condition $D_1 = D_2 \equiv 1$. In the low-frequency approximation (correct to $O(k^3)$), the scattering matrix of such a sphere has the following form in polar coordinates (see p. 86 in [11]):

$$\begin{aligned} T(\vartheta, \varphi, \vartheta_0, \varphi_0) &= A + B\cos\vartheta\cos\vartheta_0 \\ &+ \sin\vartheta\sin\vartheta_0\cos(\varphi - \varphi_0), \\ A &= -R_0 + \frac{2}{3}k^2R_0^3 + jkR_0^2, \quad B = -k^2R_0^3. \end{aligned} \tag{25}$$

Substituting Eq. (16) in Eq. (21) and changing to the spherical coordinate system, we arrive at the integral equation

$$\begin{aligned} &\tilde{T}_1(\vartheta, \varphi) \\ &\mp k\int_0^{2\pi}\int_0^{\frac{\pi}{2}-j\infty} [A + B(-\cos\vartheta\cos\vartheta_0 + \sin\vartheta\sin\vartheta_0) \\ &\times \cos(\varphi - \varphi_0)]\exp(j2k\cos\vartheta_0 z_0) \\ &\times \sin\vartheta_0\tilde{T}_1(\vartheta_0, \varphi_0)d\vartheta_0 d\varphi_0 = 1. \end{aligned} \tag{26}$$

Here, the minus sign before $\cos\vartheta$ indicates that we consider the scattering matrix T_2^1, and the sign $\mp$ selected before the integral means that the minus sign is taken in the case of a hard bottom and the plus sign in the case of a soft bottom. We note that Eq. (26) is an integral equation with a degenerate kernel. Hence, the solutions should be sought in the form [12]

$$\begin{aligned} \tilde{T}_1(0, \varphi) &= 1 + a_1 + a_2\cos\vartheta \\ &+ a_3\sin\vartheta\cos\varphi + a_4\sin\vartheta\sin\varphi, \end{aligned} \tag{27}$$

$$\begin{aligned} \tilde{T}_1(0, \varphi) &= 1 - c_1 - c_2\cos\vartheta \\ &- c_3\sin\vartheta\cos\varphi - c_4\sin\vartheta\sin\varphi. \end{aligned} \tag{27'}$$

Here, $a_i(c_i)$ characterize a hard (soft) boundary. The coefficients a_i and c_i with $i = 1, 4$ are determined from the system of linear algebraic equations obtained from Eq. (26) by a standard procedure. The resulting solution has the form

$$\begin{aligned} a_1(c_1) &= \frac{\frac{2\pi kA}{\alpha}e^{\alpha} \pm \frac{(2\pi k)^2}{\alpha^4}ABe^{2\alpha}}{1 \mp \frac{2\pi k}{\alpha}Ae^{\alpha} \pm \frac{2\pi kB}{\alpha^3}e^{\alpha}(\alpha^2 - 2\alpha + 2) - \frac{(2\pi k)^2}{\alpha^4}ABe^{2\alpha}}, \\ a_2(c_2) &= \frac{\frac{2\pi k}{\alpha^2}Be^{\alpha}(1 - \alpha)}{1 \mp \frac{2\pi k}{\alpha}Ae^{\alpha} \pm \frac{2\pi kB}{\alpha^3}e^{\alpha}(\alpha^2 - 2\alpha + 2) - \frac{(2\pi k)^2}{\alpha^4}ABe^{2\alpha}}, \\ a_3 &= c_3 = a_4 = c_4 = 0; \quad \alpha = j2kz_0. \end{aligned} \tag{28}$$

Here, the upper (lower) signs correspond to a hard (soft) bottom. The coefficients a_3, c_3, a_4, and c_4 are exactly zero, which is a consequence of the azimuthal symmetry of the problem.

Substituting the expressions for a_1, a_2, c_1, and c_2 in Eq. (27), we derive the low-frequency approximation for the scattering amplitude $\tilde{T}_1$; the function $\tilde{T}_2$ can be calculated from Eqs. (19) through $\tilde{T}_1$ in the following way:

$$\begin{aligned} \tilde{T}_2(\vartheta) &= 2\pi k\int_0^{\frac{\pi}{2}-j\infty} (A + B\cos\vartheta\cos\vartheta_0) \\ &\times \exp(\alpha\cos\vartheta_0)\sin\vartheta_0\tilde{T}_1(\vartheta_0)d\vartheta_0. \end{aligned} \tag{29}$$

Here, all terms containing the angle φ are zero (as above) because of the azimuthal symmetry of the

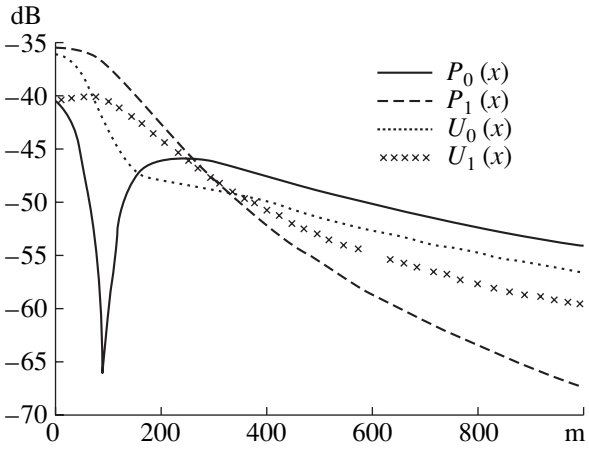

Fig. 1. Sound field amplitude versus the distance with and without allowance for the scattering; $R_0 = 4$ m and $Z_0 = 5$ m.

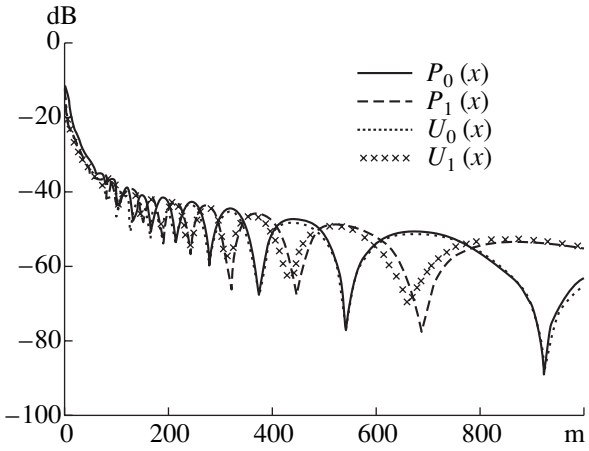

Fig. 2. Sound field amplitude versus the distance with and without allowance for the scattering; $R_0 = 4$ m and $Z_0 = 100$ m.

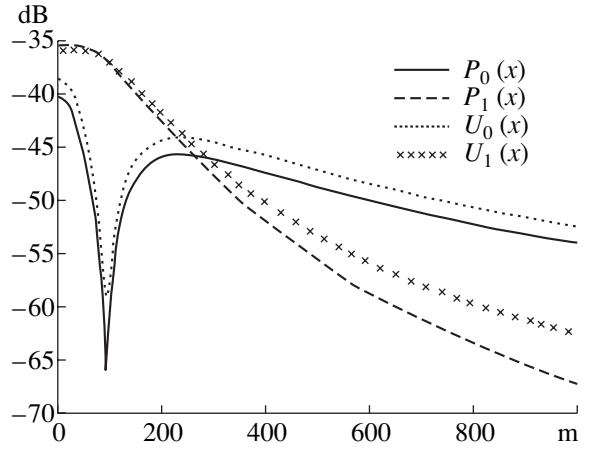

Fig. 3. Sound field amplitude versus the distance with and without allowance for the scattering; $R_0 = 0.4$ m and $Z_0 = 5$ m.

problem. The calculation by Eq. (29) yields the expressions

$$\tilde{T}_2(\vartheta) = 2\pi k\left\{A(1+a_1)\frac{e^{\alpha}}{\alpha} + [Aa_2 + B(1+a_1)\cos\vartheta] \times \frac{e^{\alpha}}{\alpha^2}(\alpha-1) + Ba_2\cos\vartheta\frac{e^{\alpha}}{\alpha^3}(\alpha^2-2\alpha+2)\right\} \quad (30)$$

for a hard and a soft bottom, respectively.

Substituting Eqs. (27) and (30) with allowance for Eqs. (28) in Eq. (24), we obtain the total field. In these calculations, it is necessary to take into account the relations

$$\tilde{T}_2(\vartheta) = 2\pi k\left\{A(1-c_1)\frac{e^{\alpha}}{\alpha} + [A(-c_2) + B(1-c_1)\cos\vartheta] \times \frac{e^{\alpha}}{\alpha^2}(\alpha-1) + B(-c_2)\cos\vartheta\frac{e^{\alpha}}{\alpha^3}(\alpha^2-2\alpha+2)\right\}, \quad (30')$$

$$\left.\begin{aligned} D_{1,0}(\pi-\vartheta) &= \tilde{T}_1(\vartheta) \\ D_{1,0}(\vartheta) &= \tilde{T}_2(\vartheta) + 1 \\ D_{2,0}(\vartheta) &= \tilde{T}_1(\vartheta)V(\vartheta) \end{aligned}\right\} \quad \vartheta \in [0, \pi/2], \quad (31)$$

where $V(\vartheta) \equiv 1$ in the case of a perfectly hard boundary and $V(\vartheta) \equiv -1$ in the case of a soft boundary.

Figures 1–3 present the results of the calculations for the amplitude of the sound field U with allowance for the scattering; the plots are presented for different depths of the source (scatterer) and also for different values of the scatterer radius. The independent variable in the plots is the horizontal distance between the source and the receiver. The field was calculated by Eq. (24) with allowance for only the leading terms of the series (with $n = 0$). The current values of the angles ϑ and ϑ' were determined from the geometry of the problem.

The corresponding values of $D_{1,0}(\vartheta)$ and $D_{2,0}(\vartheta')$ were calculated from Eqs. (31), (27), and (30). The subscript 0 corresponds to a hard boundary, and the subscript 1, to a soft boundary.

For comparison, the same figures present similar dependences $P(x)$ obtained by the method of imaginary sources (without taking into account the scattering). All calculations were performed for a frequency of 100 Hz and a receiver depth of 105 m. The values along the ordinate axis are normalized by the field amplitude of the same source at a unit distance in a homogeneous unbounded space.

The analysis of the plots shows that the field scattering from the source considerably affects the total sound field, and this effect is most pronounced when the

dimensions of the source are comparable with the depth of its immersion.

We note that the latter problem formulated in a similar way was considered in a number of publications (e.g., [14–16]). The problem on the scattering by two spheres was considered in application to electrodynamics [14]. The resulting scattering diagram of the two spheres was calculated. The scattering field of a sphere with a perfectly hard surface in a homogeneous halfspace was studied in [15, 16]. In this case, the scattering gives rise to a plane incident wave.

In the example considered above, we used the scattering matrix calculated approximately. In the two-dimensional case, the scattering matrix can be calculated exactly for a large class of scatterers by the Wiener–Hopf method, because this matrix represents the Fourier transform of the scattering field of a plane incident wave. In more complex cases, it is necessary to use numerical methods for both the determination of the scattering matrix and the solution of the integral equation (21). The method described in this paper can be also used in solving scattering problems in a plane-layered waveguide.

REFERENCES

1. A. A. Kleshchev, Akust. Zh. **23**, 404 (1977) [Sov. Phys. Acoust. **23**, 225 (1977)].
2. E. A. Krasil'nikov, Dokl. Akad. Nauk SSSR **263** (3), 556 (1982) [Sov. Phys. Dokl. **27**, 192 (1982)].
3. V. N. Nemtsova and M. V. Fedoryuk, Akust. Zh. **32**, 131 (1986) [Sov. Phys. Acoust. **32**, 81 (1986)].
4. Yu. A. Kravtsov, V. M. Kuz'kin, and V. G. Petnikov, Akust. Zh. **30**, 339 (1984) [Sov. Phys. Acoust. **30**, 199 (1984)].
5. A. M. Karnovskiĭ, A. G. Leĭko, and A. D. Suprun, Akust. Zh. **36**, 880 (1990) [Sov. Phys. Acoust. **36**, 491 (1990)].
6. V. E. Belov, S. M. Gorskiĭ, A. Yu. Zinov'ev, and A. I. Khil'ko, Akust. Zh. **40**, 548 (1994) [Acoust. Phys. **40**, 485 (1994)].
7. V. A. Eliseevnin and Yu. I. Tuzhilkin, Akust. Zh. **41**, 249 (1995) [Acoust. Phys. **41**, 214 (1995)].
8. B. P. Sharfarets, Akust. Zh. **31**, 119 (1985) [Sov. Phys. Acoust. **31**, 68 (1985)].
9. B. P. Sharfarets, Akust. Zh. **35**, 738 (1989) [Sov. Phys. Acoust. **35**, 426 (1989)].
10. B. A. Kosyrev and B. P. Sharfarets, Preprint, TOI DVO AN SSSR (Vladivostok Pacific Inst. of Oceanology, Far East Division, Russian Academy of Sciences, 1991).
11. P. M. Morse and H. Feshbach, *Methods of Theoretical Physics* (McGraw-Hill, New York, 1953; Inostrannaya Literatura, Moscow, 1960), Vol. 2.
12. V. S. Vladimirov, *Equations of Mathematical Physics*, 4th ed. (Nauka, Moscow, 1981; Dekker, New York, 1971).
13. *Encyclopedia of Mathematics* (Sovetskaya Entsiklopediya, Moscow, 1984), Vol. 4.
14. E. A. Ivanov, *Diffraction by Two Bodies* (Nauka i Tekhnika, Minsk, 1968).
15. J. C. Gaunaurd and H. Huang, J. Acoust. Soc. Am. **96**, 2526 (1994).
16. J. C. Gaunaurd and H. Haung, IEEE Trans. Ultrason. Ferroelectr. Freq. Control **43**, 690 (1996).
17. S. A. Yang, J. Acoust. Soc. Am. **105**, 93 (1999).
18. Martin Ochmann, J. Acoust. Soc. Am. **105**, 2574 (1999).
19. G. C. Bishop, J. Acoust. Soc. Am. **105**, 130 (1999).

Translated by E. Golyamina

Acoustical Physics, Vol. 47, No. 5, 2001, pp. 572–577. Translated from Akusticheskiĭ Zhurnal, Vol. 47, No. 5, 2001, pp. 657–663.

Potentialities of Cepstral Analysis in Refining the Reciprocal Delays and Amplitudes of Signals

V. A. Zverev and A. A. Stromkov

Applied Physics Institute, Russian Academy of Sciences, ul. Ul'yanova 46, Nizhni Novgorod, 603600 Russia

e-mail: zverev@hydro.appl.sci-nnov.ru

Received July 10, 2000

Abstract—It is demonstrated that the determination of the relative positions of two signals on the time axis with the help of cepstral analysis is characterized by higher immunity to signal fluctuations than a direct measurement of their positions. The theory of the cepstral approach and the results of numerical calculations that demonstrate its potentialities are presented. The cepstral analysis is applied to the processing of signals obtained in a full-scale tomographic experiment in the Mediterranean Sea in 1994. Refined values of the time intervals between the arrivals of signals transmitted through a 200-km-long propagation path are determined. It is demonstrated that the method used for the determination of the signal propagation times is immune to noise associated with the distortions of the signal wave form. © *2001 MAIK "Nauka/Interperiodica".*

Acoustic methods are successfully used for the determination of many oceanological parameters. Fluctuations that occur in wave propagation because of the internal waves in the ocean, as well as the effect of the gradients of sound velocity on this phenomenon, were studied in [1]. Today, the most well known and complex problem of the determination of oceanic parameters is the program of acoustic thermometry (ATOC). The determination of the propagation times of pulses also forms the basis of the ocean tomography [2]. The range of problems that can be solved by the determination of the propagation time of an acoustic signal essentially depends on the precision of its measurement. Inaccuracies caused by the multipath character of an acoustic channel were considered in [3]. In order to avoid the errors caused by the multipath propagation, it is proposed to increase the time resolution of signals by broadening the effective frequency range of the measurements. The optimal (from the point of view of precision) degree of smoothing of the signal frequency characteristic is determined by taking into account additive noise.

This paper (as in [3]) is devoted to the problem of increasing the precision of the estimates of the pulse propagation time in a sound channel characterized by multipath propagation. We consider the case of a very high signal-to-noise ratio, which allows one to determine the pulse propagation time with a precision better than within the inverse width of the pulse spectrum, as was obtained in [4]. A large excess of a signal over the noise level provides an opportunity to estimate the positions of the signal maximum with the precision better than within the interval of the signal discretization in time. The last condition excludes the possibility of increasing the time resolution of the received signals. Therefore, not only does the problem of controlling the multipath character of the channel become important, but also does the problem of finding a way to reduce the errors in the determination of a pulse position in the conditions of multipath propagation. The major source of such errors is the change in the pulse form due to small fluctuations of the pulse propagation time along different ray paths of interfering signals. The purpose of this work is the investigation of the possibility of eliminating the errors caused by the fluctuations of the pulse form by transferring the measurements from the time domain to the spectral one. In the absence of fluctuations (the source of errors lies not in the presence of multipath propagation, but in the fluctuations), the time-domain and spectral-domain determinations of the signal propagation time are fully equivalent. In the conditions of a multipath channel, the situation is different. By processing the experimental data with these two techniques (in the time domain and in the spectral domain), we obtained a difference in the determination of the pulse propagation time, and this difference far exceeded the error due to additive noise. The difference is a consequence of the error obtained with the time-domain technique. On the basis of the theoretical considerations and numerical estimates relying on the experimental data, it is demonstrated that the spectral method of the determination of the pulse propagation time is much less sensitive (by several orders of magnitude) to the fluctuations of pulse form.

Let us explain the essence of the spectral method. Consider two almost identical signals "*a*" and "*b*" delayed with respect to each other. The signal spectrum taken within the interval including both signals can be represented as

$$G_y(\omega) = G_a(\omega)\exp(i\omega\tau_a) + G_b(\omega)\exp(i\omega\tau_b). \quad (1)$$

1063-7710/01/4705-0572$21.00 © 2001 MAIK "Nauka/Interperiodica"

Here, $G_{a,b}(\omega)$ are the spectra of each of the signals taken within the same interval as their summary spectrum; the position of each signal is indicated on the time axis $\tau_{a,b}$ in these spectra.

Let us transform Eq. (1) by factoring out the parameters of the signal "*a*." We obtain

$$G_y(\omega) = G_a(\omega)\exp(i\omega\tau_a)\{1 + \alpha\exp[i\omega(\tau_b - \tau_a)], \quad (2)$$

where

$$\alpha = G_b(\omega)/G_a(\omega). \quad (3)$$

It follows from Eq. (2) that, in the case of spectrum measurement, the difference in the forms of the signals "*a*" and "*b*" (more precisely, their spectra) affects only the coefficient α that characterizes such changes and does not contain any information on the delay of the signals. More precisely, the change of spectra can lead to a difference in the measured signal delay from $\tau = (\tau_b - \tau_a)$ only if an imaginary part proportional to ω is present in α. The presence of such a term in α is not a disadvantage but a consequence of the fluctuations of the signal position, which must be taken into account. If we measure the time position of a signal according to the position of its maximum, there will be no guarantee that it will not change in the case of a small random deformation of the signal form.

In order to use the advantage of the separation of the amplitude and time factors in Eq. (2), it is necessary to use this relation as the basis of the method of measurement of the quantity $\tau = (\tau_b - \tau_a)$. Such a method is the cepstral analysis [5]. Let us write down the logarithm of the modulus of Eq. (2):

$$\ln[|G_y(\omega)|] = \ln[|G_a(\omega)|] + \ln[|1 + \alpha\exp(i\omega\tau)|]. \quad (4)$$

It follows from Eq. (4) that the logarithm of the spectrum modulus contains two terms. The first one is the logarithm of the modulus of the spectrum of one pulse with the Fourier transform consisting of almost only low-frequency components. The spectrum of the second term contains harmonic terms with the frequencies being multiples of τ. Thus, the Fourier transform of Eq. (4) (the cepstrum) contains low-frequency components and a harmonic series with the period τ. The delay between the pulses is determined according to the position of the first harmonic of this series. The spectral analysis must be performed for a sufficiently long frequency interval. The larger the window of the spectral analysis, the more reliable the separation of the frequency (quefrency) τ in the cepstrum (4). In order to determine the value of τ with the precision better than within the signal quantization interval, the function given by Eq. (4) must be supplemented by zeros before taking the spectrum (cepstrum) from it.

Supplementing the function spectrum by zeros does not increase the resolution of the method. In this sense, this operation is useless. This is just a necessary procedure for the numerical calculation. The point is that, in the case of numerical calculations, the axis of delays consists of a series of discrete values. The discretization interval is the limit of the time resolution. However, in the case of large signal-to-noise ratios, the time position of a pulse (without application of any special techniques) is obtained with a much higher precision. In order to use this opportunity, it is necessary to increase the number of points on the delay axis. This can be achieved by supplementing the function by zeros. It is necessary to note that supplementing the function by zeros smoothes the differences that occur between the numerically obtained cepstra with an integral or nonintegral number of the function periods constituting the interval of the function setting.

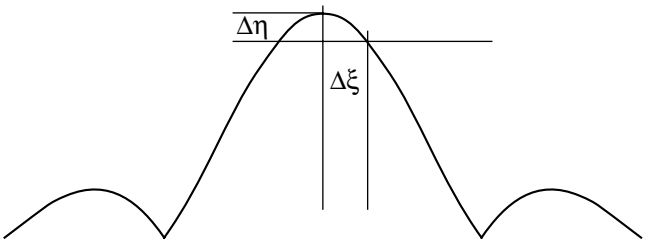

Fig. 1. Form of the cepstrum for two pulses separated in time, at the delay quefrency.

The form of the cepstrum obtained in this case is given in Fig. 1. If Eq. (4) is not supplemented with zeros, the distance between the reading points of the function cepstrum in Fig. 1 corresponds to the distance between the readings of this function. As a result, it is possible to measure the value of τ only with the error equal to the quantization period of the pulses being investigated. Supplementing Eq. (4) with zeros, we introduce additional readings into the cepstrum. Their number is proportional to the supplemented number of zeros. It is pointless to infinitely increase the number of supplemented zeros. The precise determination of the maximum of the function given in Fig. 1 is impeded by additive noise in the function given by Eq. (4). One can see from Fig. 1 that the lower the noise level shown in Fig. 1 by the segment $\Delta\eta$, the higher the precision in the determination of the position of the maximum $\Delta\xi$. The value of $\Delta\xi$ determines the expedient number of zeros that should be introduced into Eq. (4). Proceeding from the fact that the plot in Fig. 1 in the vicinity of the maximum has the form $\sin(x)/x$, we give in Fig. 2 the plot of the ratio of the number of expediently supplemented zeros to the length of the initial spectrum depending on the noise level in Eq. (4). This noise level is given in decibels relative to the modulus of α with allowance for the gain in the case of the spectral analysis of 1024 points of the spectrum (30 dB). One can see from the plot that it is expedient to increase the spectrum length by a factor of 16, supplementing it with zeros when the pulse already exceeds the noise level by 20 dB or more. This means that such an important parameter as the pulse

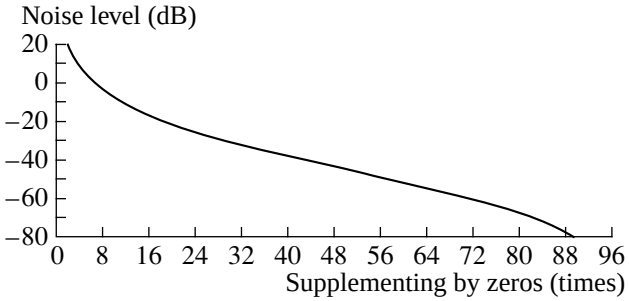

Fig. 2. Ratio of the number of possible zeros to the length of the initial spectrum versus the noise level in Eq. (4). The noise level is given in decibels relative to the modulus of α with allowance for the gain in the case of the spectral analysis of 1024 points of the spectrum (30 dB).

position with respect to the reference pulse can be determined to within 1/16 of the distance between the reading points on the time axis. The distance between the reading points is usually much smaller than the interval of the signal resolution, which is determined as the inverse value of the signal bandwidth. Here and below, we discuss the problem of increasing the resolution relative to the time interval of signal quantization and not to the inverse value of the signal spectrum.

Let us indicate two important points. First, we do not suggest any superhigh resolution. It is necessary to supplement the signal spectrum not with zeros but with the values of its real spectrum obtained by estimating it in a sophisticated way [6] to obtain a superhigh resolution. Instead of superhigh resolution, we use a more accurate determination of the position of the cepstrum maximum obtained in a common way, as it is shown in Fig. 1. Second, Fig. 1 and the plot presented in Fig. 2 are only an illustration of the possibilities rather than the basis for their realization. The feasibility of the technique used here becomes clear directly in the process of its realization, on the basis of the form of spectrum (4) (cepstrum) observed in reality. The technique is feasible if the cepstrum form is smooth in the vicinity of the maximum and close to the form shown in Fig. 1.

The complex coefficient α is estimated on the basis of the already determined value of τ. We present two such ways as examples.

For the first way, let us write a relation containing both α and τ:

$$M(t) = S(t) - kS(t-\tau), \tag{5}$$

where $S(t)$ is the form of the initial signal containing both signals "*a*" and "*b*" and k is the yet arbitrary complex factor. Both pulses are superposed in Eq. (5) at a certain instant: the direct pulse multiplied by k and the delayed one. It is possible to observe their interference. The minimum amplitude of the combined pulse is observed under the condition

$$k = \alpha. \tag{6}$$

Proceeding from this condition, the real and imaginary parts of α are determined at the minimum of the combined pulse.

Now, for the second way, let us write down the following relation:

$$G_M(\omega) = \frac{G_y(\omega)}{1 + k\exp(i\omega\tau)}. \tag{7}$$

If the condition given by Eq. (6) is valid, Eq. (7) transforms into

$$G_M(\omega) = G_a(\omega). \tag{8}$$

Therefore, the spectrum given by Eq. (7) (the cepstrum of $S(t)$) reaches its minimum at the quefrency τ under the condition given by Eq. (6). This technique is integral. It should be preferred if one wants to exclude or reduce the influence of local changes of the signal form. It is valid on the condition that the denominator in Eq. (7) is never equal to zero. If this happens, it is necessary to exclude these points from the consideration.

We used the technique described above for processing the data of a full-scale hydroacoustic experiment to demonstrate its applicability to hydroacoustic measurements.

The experiment was conducted under the program of the THETIS-II international tomographic experiment in the Mediterranean Sea, in the summer of 1994.

Phase-manipulated pulses with phase manipulation according to a pseudo random law (an M-sequence) were studied in the course of this experiment. The results of processing the signals from one of the sources that operated at a carrier frequency of 400 Hz are given below. The length of the phase-modulating pseudo-random sequence was equal to 511 units (5.11 s), each unit containing four periods of the carrier frequency (0.01 s). A series of 40 identical pulses were emitted several times a day. The total length of each series was 204.4 s.

The signals were received by a vertical array of omnidirectional hydrophones submerged from a drifting research vessel *Akademik Sergeĭ Vavilov.* The receiving ship was positioned at a distance of about 200 km from the emission point.

The compression of the received pulses by their correlation with the copy of the initially emitted signal was conducted in the course of the preliminary processing. The idea of this standard procedure, which is also called matched filtering, is based on the fact that the effective width of the autocorrelation function of the emitted signal is equal to the length of the unit of the pseudo-random sequence modulating the phase (0.01 s in our case). Therefore, by virtue of the problem linearity, a compressed signal is equivalent to the signal that was received after the emission of a short pulse with the form of the autocorrelation function of the signal emitted in reality. Thus, at the correlator output, we obtained a sequence of pulses with the time distribution corre-

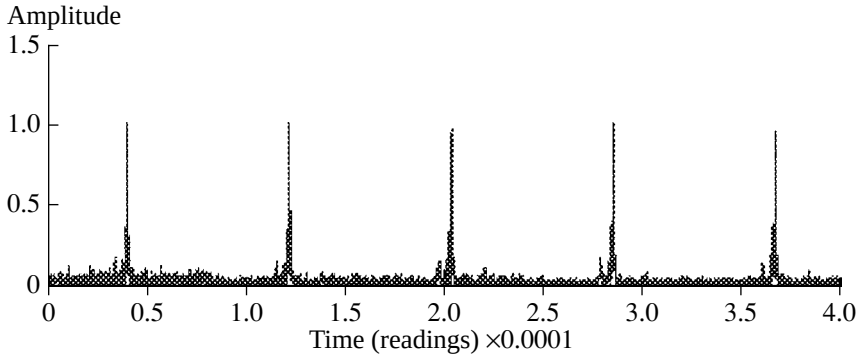

Fig. 3. Form of the processed sequence of pulses. Time (in reading points) is represented by the horizontal axis, and the vertical axis represents the pulse amplitude on a linear scale.

sponding to the distribution of arrival times of short pulses propagating along different ray paths. These pulses we call ray pulses. The distribution of the arrival times of rays and the parameters of the emitted signal are such that the ray pulses can be resolved either completely, or partially, or not resolved at all.

The special feature of the preliminary processing in this case was the transformation of the time scale due to the Doppler effect caused by the drift of the vessel. Since the ambiguity function of an emitted signal in the delay–Doppler shift coordinates has a so called needle shape, the reference signal used for matched filtering must be transformed according to the Doppler change. The autocorrelation of the received signal was used to evaluate the real transformation of the signal, and the average change of the period and the corresponding Doppler distortion was evaluated from the first significant maximum at the nonzero delay (close to the period of the M-sequences). It is evident that, in real conditions, the drift velocity of the hydrophones of the array can change even during the time of a single session. Moreover, there is a series of physical processes in the ocean that lead to analogous changes of the propagation time, e.g., internal waves. The measurement of the exact value of the propagation time fluctuations is important. The used technique has good prospects for such estimations.

The conditions of the signal reception from a drifting ship make it impossible to conduct a full-scale tomographic experiment. In the case under consideration, this test was used only to adjust the technique of such experiments.

We used five groups of pulses from the correlator output, produced by five sequences following each other. The fixed velocity of the receiver motion was used to partly compensate for the Doppler distortions. The signal was received by one of the hydrophones of the vertical array. The above example was given in order to demonstrate the possibilities for refining the pulse repetition period using the described technique.

The processing was as follows. We conducted the spectral analysis of the signal realization including two pulses (Fig. 3). After that, we took the logarithm of the modulus of the obtained spectrum. We roughly evaluated (with the precision up to one reading point) the delay with respect to the cepstrum maximum by the spectrum of this modulus (the cepstrum). After that, the coordinate of the cepstrum maximum was refined by either adding zeros to the spectrum modulus, or in another way. We performed the common Fourier transformation with respect to a small number of points (sixteen) in the vicinity of the maximum. In this case, the points were taken with the interval of one thousandth of the quantization interval. Then, we determined the relative amplitude of pulses by applying it to Eqs. (5) or (7) according to Eq. (6) up to the point of minimization of the second pulse in Eq. (5) or in the spectrum given by Eq. (7). In this way, we determined the delays and the relative amplitude values for the neighboring pairs of the pulses shown in Fig. 3.

The results obtained in this study are presented in the table and illustrated by the figures.

The first column of the table indicates the numbers of the intervals between the pulses from the sequence used for processing. The plot of this pulse sequence is given in Fig. 3. The next column of the table shows the difference between the values of the pulse spacing, which were determined with the precision of one thousandth of the quantization period, and the value 8176 (the repetition period of the M-sequences) determined within one quantization unit. The third column of the table presents the values of the relative pulse amplitude in the sequence. It is necessary to note that the form of compressed pulses was close to a triangle with a base of 32 quantization units.

Figures 4–6 illustrate the basic stages of the signal processing for the full-scale experiment. Figures 4 and 5 show the determination of the relative amplitudes of pulses by the technique utilizing the subtraction of a signal and its delayed copy according to Eq. (5). The form of the function $M(t)$ is shown in Figs. 4a and 5a, and Figs. 4b and 5b show the form of the function $S(t)$ involved in Eq. (5).

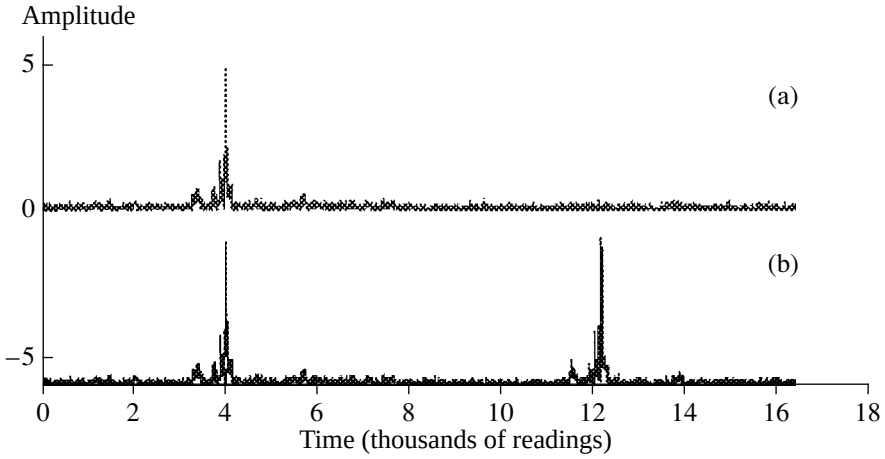

Fig. 4. Determination of the relative pulse amplitude. (a) The difference $M(t)$ (Eq. (5)) in the case of validity of Eq. (6); (b) $S(t)$, one of the terms of this sum. The horizontal axis represents time in thousands of reading points.

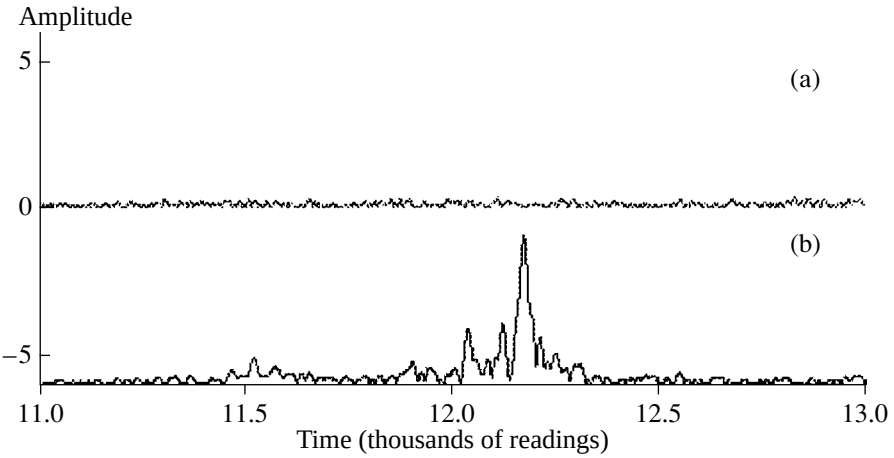

Fig. 5. Same as in Fig. 4, but on a different time scale.

Figure 6 demonstrates the determination of the refined value of the delay between the pulses. Sixteen values of the cepstrum (the spectrum given by Eq. (4)) taken per one thousandth of the quantization interval in the vicinity of the maximum of the modulus of this function are given in this figure. A smooth regular shape of this curve shows that noise practically does not affect the result of the determination of the maximum position.

Table

Number of interval between pulses	Deviation of interval length	Relative amplitude
1	0.092	1.08
2	0.242	1.13
3	0.119	1.06
4	−0.105	0.95

We compared the technique used by us with the method of the delay determination by the maximum of a correlation function (see, e.g., [4]). The relative delay in the second pair of pulses was measured according to the difference of the positions of the maximums of correlation functions, which were measured up to several thousandths of the resolution interval. This value differs by 0.311 of the quantization interval from the value given in the table.

The correctness of the result given in the table is verified by a numerical experiment utilizing the full-scale initial data. A fluctuation of the pulse amplitude near the maximum was simulated. This was done by multiplying (multiplicative noise was simulated) the signal by 1.001 at two points near the maximum of one of the correlation functions, the time interval between which was to be evaluated. Figure 7a shows the form of the

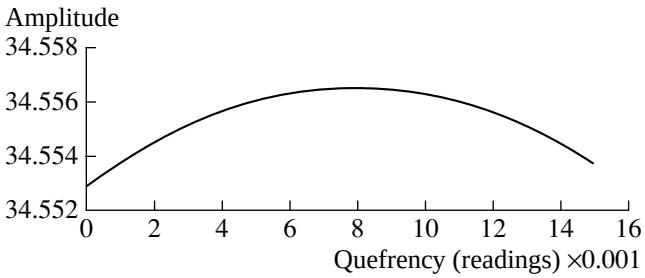

Fig. 6. Oscillogram of the cepstrum of Eq. (4) in the vicinity of the maximum. The horizontal axis represents τ in 0.001 of a reading point.

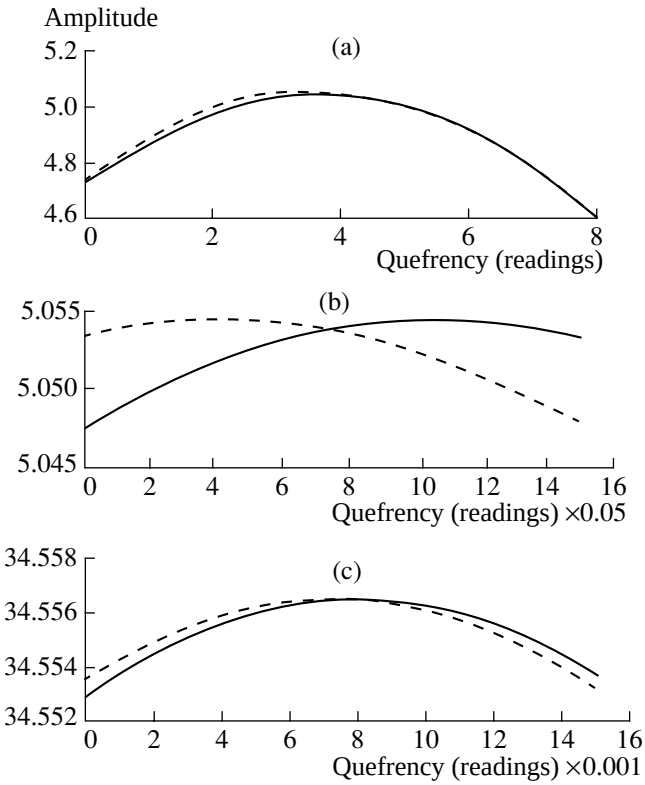

Fig. 7. Result of the simulation of a real signal fluctuation. The solid line shows the unperturbed signal in the vicinity of its maximum, and the dashed line shows its fluctuation. (a) The signal oscillogram at reading points; (b) the signal oscillogram at 0.05 of a reading point; (c) the oscillogram of the cepstrum of Eq. (4) taken at 0.001 of a reading point.

correlation function portion close to the maximum with the curve, which contained the aforementioned changes, superimposed upon it. Figure 7b demonstrates the same portion on the scale increased by a factor of 20. As the result of the introduction of the fluctuation, the position of the maximum of the correlation function, as determined on the basis of the shape of the correlation curve peak (this is the common procedure), was shifted by approximately 0.34 of the resolution interval. A part of the cepstrum of the same function is shown in Fig. 7c on an even more extended (by a factor of 1000) scale. In this case, the delay measured using the spectral method described above and determined within 0.001 of the quantization unit did not change. This demonstrates the immunity of the spectral method to pulse form fluctuations caused by the multipath propagation.

ACKNOWLEDGMENTS

We are grateful to the reviewer for useful comments, which allowed us to make the essence of our paper more evident.

The work was supported by the Russian Foundation for Basic Research, project nos. 00-15-96741, 00-02-17409, and 99-02-16401.

REFERENCES

1. S. M. Flatte and R. B. Stoughton, J. Geophys. Res. C **91**, 7709 (1986).
2. W. Munk and C. Wunsh, Deep-Sea Res., Part A **26** (2), 123 (1979).
3. J. E. Ehrenberg, T. E. Ewart, and R. D. Morris, J. Acoust. Soc. Am. **63**, 1861 (1978).
4. A. N. Guthrie, R. M. Fitzgerald, D. A. Nutile, and J. D. Shaffer, J. Acoust. Soc. Am. **56**, 58 (1974).
5. A. V. Oppenheim, R. W. Schafer, and T. G. Stockham, IEEE Trans. Audio Electroacoust. **AU-16** (3) (1968).
6. S. J. Kung, D. V. Bhaskar Rao, and K. S. Arun, in *VLSI and Modern Signal Processing*, Ed. by S. J. Kung, H. J. Whitehouse, and T. Kailath (Prentice-Hall, Englewood Cliffs, NJ, 1985; Radio i Svyaz', Moscow, 1989).

Translated by M. Lyamshev

Acoustical Physics, Vol. 47, No. 5, 2001, pp. 578–584. Translated from Akusticheskiĭ Zhurnal, Vol. 47, No. 5, 2001, pp. 664–670.

Visualization of Blood Flow by Ultrasound Speckle Interferometry

N. V. Zuĭkova, T. V. Kondrat'eva, and V. D. Svet

Andreev Acoustics Institute, Russian Academy of Sciences, ul. Shvernika 4, Moscow, 117036 Russia

e-mail: bvp@akin.ru

Received December 22, 1999

Abstract—A new method for the visualization of flowing liquids is suggested. The method makes it possible to obtain images of dynamic objects located in an inhomogeneous medium. The main requirement for the realization of this method is the stability of the field during two successive measurements. The dimensions of the irradiating beam depend on the value of the spatial correlation interval characterizing the inhomogeneities of the medium, while the amplitude distribution in the beam can be arbitrary. A numerical modeling of the method is performed, and images of the models of blood vessels lying under an inhomogeneous layer are presented. © *2001 MAIK "Nauka/Interperiodica".*

INTRODUCTION

Ultrasound diagnostics is now the most common method of blood vessel examination. The main advantages of the ultrasound method, compared to X-ray examination, are the noninvasivenessvity, the absolute safety, and the portability of the ultrasonic equipment. Unlike the X-ray examination, ultrasound makes it possible to obtain information on the structure of external and internal vessel walls and on the parameters of the blood flow. There are two ways of gaining information on blood vessels by using ultrasound. The first is based on estimating the blood flow parameters (integral and local ones) by the Doppler method. This method provides no direct image of the blood flow but allows one to make only indirect judgments by the form and some parameters of the spectrum of scattered signals. Therefore, in many cases this method is subjective and the quality of the diagnostics depends on the experience of the physician performing the examination. The second method, which received the names of "B-Flow" or "Speckle Tracking" in American literature [1, 2], makes it possible to obtain a dynamic ultrasonic image of the blood flow due to the scattering of ultrasonic signals by erythrocytes or an echo contrast liquid injected into an artery. This method is based on the well-known algorithm of alternate-period subtraction of signals at every element of the spatial resolution of the antenna. In this case, the ultrasonic images of stationary structures are subtracted, whereas the images of moving scatterers are not subtracted or are compensated only partially, which makes it possible to obtain the image of the blood flow. This subtraction is necessary, because the signals reflected from the walls of vessels are many times greater than the echo signals from erythrocytes and, in a conventional processing, the weak signals will be suppressed by the responses from strong echo signals and by their side lobes. The mentioned methods of ultrasound diagnosis are successfully used for examining the so-called "open" organs, when blood vessels are located in the medium that can be considered as an analog of free space and the distortions of the wave fronts of the propagating signals due to inhomogeneities of the biological medium are insignificant. Therefore, for phasing ultrasonic antenna arrays, the conventional methods of focused processing are used.

However, for examining the blood vessels of brain, today's possibilities of ultrasound diagnosis are very limited because of the presence of thick skull bones which greatly distort the sounding and echo signals and, in addition, introduce a high attenuation. For these reasons, transcranial ultrasound diagnostics is performed only through the so-called "windows of acoustic transparency," that is, through such parts of the skull where the bones are either thin (the temple area) or are lacking (the eye-socket and the large occipital opening). However, the anatomical location of these windows does not make it possible to obtain detailed ultrasonic images of deep brain vessels.

In papers [3, 4], a method of ultrasonic visualization of brain vessels through thick skull bones was developed and experimentally tested. This method is based on the use of complex superwideband signals (to compensate the attenuation) and on the spatial processing matched with the medium for the compensation of the distorting effect of the skull bone.

In this paper, we consider a new possibility of obtaining ultrasonic images of blood flow by echolocation through such inhomogeneous media on the basis of the methods of acoustic speckle interferometry [5–9].

1063-7710/01/4705-0578$21.00

ALGORITHM OF THE IMAGE RECONSTRUCTION

In the previous papers [5–7], it was shown that the methods of acoustic speckle interferometry allows one to reconstruct the image of a point source, moving or stationary, through a layered inhomogeneous or strongly scattering medium without using the matched-field processing. To be more specific, it is not the point source function, which is reconstructed in the conventional method of a wave front inversion in a homogeneous medium, but a certain functional of this function, and, in the strict sense, this functional is not the image of the point source. In particular, it was shown that by using the method of the correlation speckle interferometry it is possible to reconstruct the autocorrelation function of a point source, the angular dimensions of which practically coincide with the angular dimensions of the response of the antenna array to a plane or spherical wave [5].

A key property of the methods of speckle interferometry is that they do not require any detailed mathematical description (or measurement) of the parameters of the inhomogeneous and scattering medium, which, in view of the considered problem, is the determining factor.

Below we will show that, using the ideas of speckle interferometry, it is possible, under certain conditions, to produce ultrasonic images of blood flow with the elimination or minimization of the effect of the layered inhomogeneous medium (such as the bone tissues and internal structures of the brain). In this respect, the proposed method of obtaining ultrasonic images can be considered as a full analog of X-ray angiography, since only the blood flow is visualized.

Let us now turn to the formulation of the problem: the blood moves with a certain velocity along a vessel of an arbitrary shape and, possibly, of varying diameter. The vessel is located in an acoustically inhomogeneous medium: the outer layer is a bone tissue and then come the soft structures of brain in which the blood vessel is located (Fig. 1). On the surface of the bone, a linear multielement array and an ultrasonic radiator are placed (they may be combined or separated).

The signals transmitted through the inhomogeneous medium and reflected from the blood flow pass through the inhomogeneous medium once more and then arrive at the receiving array. We *a priori* consider the medium to be random and unknown. Therefore, the ultrasonic field received by the array receivers has a random spatial distribution of amplitude and phase. Since the inhomogeneous medium is stationary, the received random amplitude–phase distribution is stable: for the same radiated signal and constant positions of the receiver and radiator, we will obtain the same random distribution of the field over the array.

Blood is an essentially inhomogeneous liquid consisting of plasma (a water solution of salts) and, mainly, erythrocytes, which are randomly oriented in plasma.

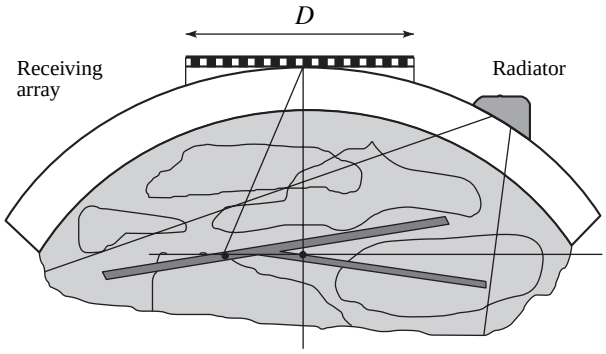

Fig. 1. Arrangement of sensors and vessels.

The erythrocytes are similar to biconcave disks with a mean diameter of the order of 7 μm and a thickness of 1 μm at the center and 2 μm at the periphery. Thus, from the acoustic point of view, blood can be considered as a liquid filled with random scatterers, the sizes of which are small compared to the wavelength of ultrasound. Since this liquid moves, the ultrasonic field scattered by the erythrocytes is a random function not only of spatial coordinates but also of time, and the interval of time correlation of the scattered field fluctuations depends on the velocity of the liquid motion. This property is used in the suggested method of visualization: in the field received by the array, two spatial interference structures are present, namely, a constant structure formed by the stationary inhomogeneous layer and a time-variable structure formed by the signals scattered by the moving blood. The speckle-interferometric processing selects only the dynamic part of the spatial interference structure, which makes it possible to eliminate the distortions introduced by the inhomogeneous layer.

We consider now in more detail how this method can be realized by the example of a harmonic signal. Suppose we have recorded a complex instantaneous distribution of the ultrasonic field over the receiving antenna at some instant of time. We designate this distribution as

$$P(x, t) = A(x)\cos[\omega t + \phi(x)], \qquad (1)$$

where x is the coordinate of the array (the number of receiver), $A(x)$ is the amplitude distribution, $\phi(x)$ is the phase distribution, and ω is the angular frequency of the signal. Let us determine the amplitudes and phases of the signals separately. It can be done in various ways, for instance, the desired phase distribution $\phi(x)$, $x \in (0, D)$, can be obtained by the Fourier transform of $P(x, t)$ with respect to time at every receiver of the array. Then, its real part $\mathrm{Re}P(x, t)$ is equal to

$$A(x)\cos\phi(x) = \int_0^{\tau/n} P(x, t)\cos\omega t dt \qquad (2)$$

and its imaginary part $\mathrm{Im}P(x, t)$ is equal to

$$A(x)\sin\phi(x) = \int_0^{\tau/n} P(x, t)\sin\omega t dt, \tag{3}$$

where n is an integer.

The time interval τ should be less or equal to the phase correlation interval of signals at their reflection from the flow. The medium should be stable at least during the double interval 2τ.

Then the amplitude and phase of the field are found from the known relations

$$A(x) = \sqrt{\mathrm{Re}^2 P(x) + \mathrm{Im}^2 P(x)},$$
$$\phi(x) = \arctan\frac{\mathrm{Im}P(x)}{\mathrm{Re}P(x)}. \tag{4}$$

Now we describe the algorithm of the signal processing. Let us record the distribution $\Phi_1(x)$ at the moment t_1 and store it. The next measurement will be made after a time interval $t_2 - t_1 = \tau$, and its result will be denoted as $\Phi_2(x)$. These two phase distributions differ from each other, because, in the field scattered from a certain part of the vessel, which is divided into the elements of the angular resolution of the receiving array, the signal phases will change completely within the time τ, and $\Phi_2(x)$ will be an entirely different phase distribution. We will form the new function

$$\Delta\Phi(x) = \Phi_1(x) - \Phi_2(x) \tag{5}$$

and invert the wave front according to function (5). The reconstructed image, if we use a holographic analogy, will be the image reconstructed from the phase hologram (or "bleached" hologram) where only the phase information is retained and the amplitude information is ignored. In our case, this is necessary because our goal is to obtain the image of a dynamic object located under a stationary layer of inhomogeneities and to eliminate the distortions introduced by this layer. Since this layer introduces multiplicative distortions into the spatial distribution of the signal, the operation $[\Phi_1(x) - \Phi_2(x)]$ subtracts all constant phase shifts gained by the signal during its propagation through the inhomogeneous layer, while the amplitude distortions $A_{sl}(x)$ introduced by the layer under the operation of division of signals $P1(x)/P2(x)$, which yields the distribution $\Delta\Phi(x) = \Phi_1(x) - \Phi_2(x)$, cancel each other

$$\frac{A_1(x)A_{sl}(x)}{A_2(x)A_{sl}(x)} = \frac{A_1(x)}{A_2(x)}. \tag{6}$$

Note that the considered method of processing, from the point of view of using the operation of subtraction, looks like the B-Flow method [1, 2]. However, the latter does not work in an inhomogeneous medium, because the whole temporal compensation is performed after the formation of the ultrasonic image, that is, after the formation of directional patterns (the spatial processing). When there is an inhomogeneous interfering layer between the array and the vessel, its high-quality image cannot be formed and, consequently, the image of the blood flow cannot be obtained. As is known, the images reconstructed by using phase holograms almost do not differ from the images reconstructed by using amplitude–phase holograms.

The information on the position of an object in the plane of image is retained owing to the two nonlinear operations given by Eqs. (4).

If now we try to reconstruct the image by using the distribution $\Delta\Phi(x)$, it will not correspond to the vessel image (in this case, to its one-dimensional cross section, because we consider a one-dimensional case). The reconstructed image will consist of separate peaks with random positions and random amplitudes, and the number of these peaks will also be random. The most important fact is that the peaks will be located only in the area determined by the blood flow cross section, or by the internal diameter of the vessel. Therefore, if we periodically repeat these measurements and average (combine) the resulting images, the pattern of the peaks will smooth out. The peaks will appear at random places and will fill the whole area where the scatterers occur, that is, the cross section of the vessel interior. As a result, after a certain number of cycles of averaging and the following square-law detection, we will obtain the image of an envelope whose width will be equal to the cross section of the blood flow, or to the internal diameter of the vessel. This image is the image of the blood flow. In spite of the fact that, in a classical sense, the described procedure is not the procedure of the image reconstruction in a homogeneous space, the resulting ultrasonic image of the envelope is completely analogous to an X-ray angiographic image: only the blood flow is visualized and other (stationary) structures are absent in the image.

We note that, if we use pulsed signals, or wide-band signals with subsequent compression (similar to B-scanning), or a two-dimensional array, then, using a similar procedure, we will obtain two-dimensional $\{I(x, R), I(x, y)\}$ and, in the general case, three-dimensional $\{I(x, y, R)\}$ images of vessels by combining a two-dimensional receiving array and a pulsed signal.

The algorithm of reconstruction or the wave front inversion according to the function $\Delta\Phi(x)$ can be realized on the basis of the Fourier–Fresnel transforms. For the case of a far-field zone of the array, when the condition $R_0 \gg D^2/\lambda$ is satisfied, where R_0 is the distance to the vessel and D is the size of the receiving array, the algorithm of reconstruction can be represented as follows:

$$I(\xi) = \left|F_\xi[\phi_1(x) - \phi_2(x)]\right|^2, \tag{7}$$

where F is the Fourier operator and the variable ξ is the coordinate of the axis in the plane of the image of the vessel, which in this case is parallel to the x axis.

If the vessel is located in the Fresnel zone of the receiving array, then either the Fresnel transform is performed or the exact wave front inversion is carried out according to the expression

$$I(\xi) = \left| \int_0^D \{\phi_1(x) - \phi_2(x)\} \exp(ikR)\, dx \right|^2. \quad (8)$$

Here, $k = 2\pi/\lambda$ is the wave number, and the distance R to every element of the ξ axis is calculated by the formula

$$R = \sqrt{R_0^2 + (\xi - x)^2}.$$

Below, in the numerical modeling of the considered method of visualization, the field was calculated by taking the sign of the second exponential function in Eq. (9) to be opposite to the sign of the exponential function in Eq. (8):

$$P(x) = \sum_{m=0}^{K} A_m(\xi_m) \exp\{i\varphi_m \xi_m\} \times \exp\{-ik\sqrt{R_0^2 + (\xi_m - x)^2}\}. \quad (9)$$

Here, A_m is the amplitude of the signal reflected from the mth element of the scattering volume of the vessel and φ_m is the phase shift of the signal at its reflection from the mth element. The amplitude coefficient $1/R$ multiplying $\exp(-ikR)$ is omitted.

THE RELATION BETWEEN THE PARAMETERS OF THE ARRAY, THE INHOMOGENEOUS LAYER, AND THE VESSEL

Consider now for what relative positions of the inhomogeneous layer, the vessel, and the receiving array is the suggested algorithm, which actually subtracts the distortions introduced by the inhomogeneous layer into the image, valid.

Let the length of the vessel consist of K elements of the array resolution, the length of these elements being equal to $\lambda R/D = \Delta\xi$ (Fig. 2).

We will take into account only the direct rays transmitted through the layer and acquiring a phase shift $\Delta\varphi_i$ at the ith receiver of the array. If the distance from the array to the lower boundary of the layer is R_s (see Fig. 2), all the rays forming the shift $\Delta\varphi_i$ at the ith receiver should pass through the same portion of the layer, otherwise the subtraction will not occur—this is the main condition. In other words, the interval of correlation of the layer inhomogeneities should be no less than a certain quantity, which we designate by Δs. If this condition fails, then, with the change of the initial phases at every mth element of the object, the total field from all K elements of resolution of the vessel at the ith receiver will not have the form of the product

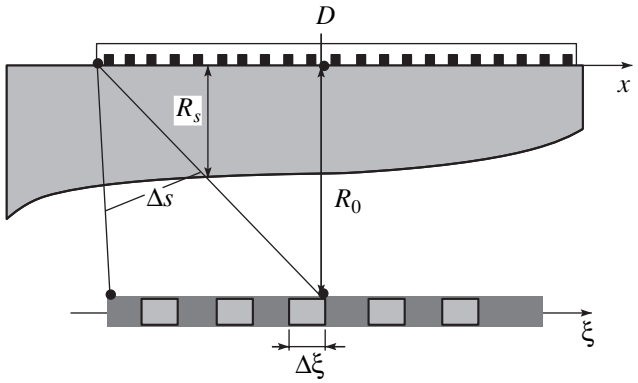

Fig. 2. Position of a vessel under an inhomogeneous layer.

$$P(x_i) A_{sl}(x) e^{i\Delta\varphi_i},$$

where $P(x_i)$ is the field at the ith receiver in the absence of the inhomogeneous layer, since the cosines of the phase shifts for every ray are combined, and this operation is nonlinear by itself. So, we can formulate the following condition

$$\Delta\xi K/R_0 = \Delta s/R_s$$

or

$$\Delta s = R_s(\lambda/D)K. \quad (10)$$

For the vessel length equal to $g = \Delta\xi K$, the condition for the interval of correlation of the inhomogeneities is as follows:

$$\rho_{sl} \geq \Delta s = g\frac{R_s}{R_0}. \quad (11)$$

This relation is more valid, the less the length of the observed part of the vessel. It is desirable that the correlation interval of inhomogeneities be as large as possible (in this case, the layer smoothly changes its parameters) and the distance from the array to the lower boundary of the layer R_s be as short as possible, compared to the distance to the vessel R_0. The best situation is when the layer is close to the array and has a small thickness. In this case, all rays arriving at one receiver at various paired instants will pass through the same element of the layer Δs. Evidently, this is a limiting situation, when $\Delta s = \lambda/2$ is the minimal interval of correlation and $R_s = \lambda/2$. In this case, the possible size of the observed part of the vessel is $g \approx R_0$, and $K = N/2$, where N is the number of receivers in the array.

If the stated conditions are not satisfied, the output image component that is determined by the uncompensated signals transmitted through different regions of the inhomogeneous medium will grow.

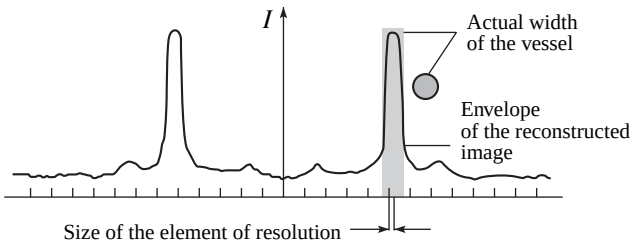

Fig. 3. Reconstructed image of a vessel in the far-field zone. The inhomogeneous layer is absent. The width of the vessel is equal to five elements of the array resolution.

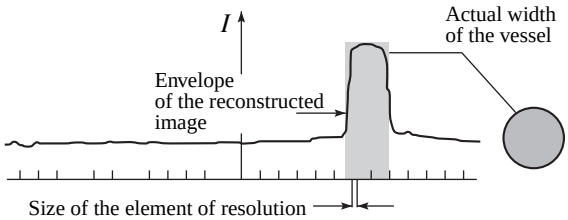

Fig. 4. Reconstructed image of a vessel in the near-field zone of the array; the image is averaged over 100 exposures. The inhomogeneous layer is absent. The width of vessel is equal to nine elements of resolution.

TEMPORAL RELATIONS

We consider two limiting cases: (i) the vessel is oriented along the ξ axis parallel to the array, which extends along the x axis (Fig. 1), and (ii) the vessel is perpendicular to the ξ axis.

In the first case, the information carried by the amplitudes and phases of signals reflected from the blood flow changes with the velocity of the blood flow transporting the erythrocytes, from which the incident ultrasonic wave is scattered. We assume that the information is completely renewed when the blood flow is displaced by one element of resolution of the array. We designate the corresponding time interval by τ. If the element of the linear resolution of the array equals $\Delta\xi = \lambda R_0/D$ and the velocity of the blood flow is V, we have the first case:

$$\tau_{\Rightarrow} = \frac{\Delta\xi}{\vartheta_{\Rightarrow}} = \frac{\lambda R_0}{D\vartheta_{\Rightarrow}}. \tag{12}$$

The time τ found in this way is the minimal required time interval between two phase measurements $\Phi_1(x, t)$ and $\Phi_2(x, t + \tau)$. This interval determines the necessary operation speed of the system. However, the time during which the distribution of the signal phase over the array must be measured with sufficient accuracy should be n times shorter. For example, $n = 10$ for the calculations to be made with reliably stable signals.

In the second case, when the flow is perpendicular to the array, the information changes instantaneously on the whole length of the vessel (and over its whole cross section), this length consisting of several elements of resolution. The directional pattern of single receivers of ultrasonic antenna arrays is usually sufficiently wide. We assume that the main energy arrives from the angular sector of more than 60°, or from the part of a tube of length R_0. Then, the time during which the blood flow travels the distance R_0 is $\tau = R_0/V$, and it determines the interval between adjacent samples for measuring $\Phi_1(x, t)$ and $\Phi_2(x, t + \tau)$.

RESULTS OF NUMERICAL MODELING

Numerical modeling of the suggested method was performed on the basis of Eq. (9). In this equation, the amplitudes $A_m(\xi_m)$ and phases $\varphi_m(\xi_m)$ of the signals scattered by the mth element of the vessel were set as an amplitude–phase distribution of secondary sources. The amplitudes $A_m(\xi_m, t)$ and phases $\varphi_m(\xi_m, t)$ form random time sequences of numbers, which change from one sample to another. First of all, the distributions of the phase fields over the array were calculated by Eqs. (5) and (6) for two samples of random quantities $\{A_m(\xi_m, t), \varphi_m(\xi_m, t)\}_{1,2}$, and then the wave front inversion was performed by Eqs. (7) or (8), depending on the type of the wave zone of the array. The final expression for the averaged image was written as

$$\sum_{l=1}^{L} I_l(\xi) = \sum_{l=1}^{L}\left|\sum_{i=1}^{N}\{\phi_{1l}(x_i) - \phi_{2l}(x_i)\}\exp\left[ik\sqrt{R_0^2 + (\xi - x_i)^2}\right]\right|^2 \tag{13}$$

for $2L$ realizations of the random quantities $A_m(\xi_m)$, $\varphi_m(\xi_m)$. In all examples, the linear array consisted of 128 receivers located at half-wave intervals $\lambda/2$.

Figure 3 shows the reconstructed image of a vessel whose size was equal to five elements of the array resolution. The number of averaged exposures was $L = 100$, and the vessel was located in the Fraunhofer zone of the array. The image is symmetric about the axis, since the amplitude of the Fourier transform of the real function $\{\Phi_1(x) - \Phi_2(x)\}$ is an even function. It is most convenient to place the object at the center of the angular field of view of the receiving array. For the case of the far-field, we consider the angular field of view as the N angles of resolution of the array α ($\alpha = \lambda/D = \lambda/(\lambda/2*N) = 2/N$), which are measured relative to the axis perpendicular to the array and passing through its center. The position of the object in the middle of the field clears the image from additional images appearing as diffraction orders with the period equal to the distance between the object and the central axis.

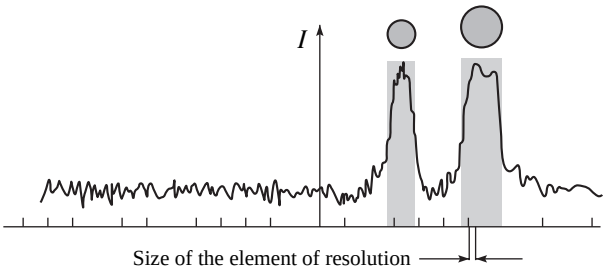

Fig. 5. Reconstructed image of two vessels in the near-field zone; the image is obtained through a random inhomogeneous layer. Averaging is performed over 50 exposures.

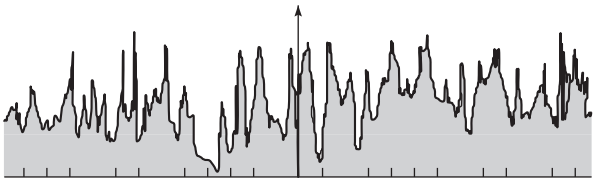

Fig. 6. Image of the same vessels as in Fig. 5; the image is obtained through an inhomogeneous layer with a standard focusing of the array in the Fresnel zone. The image cannot be reconstructed.

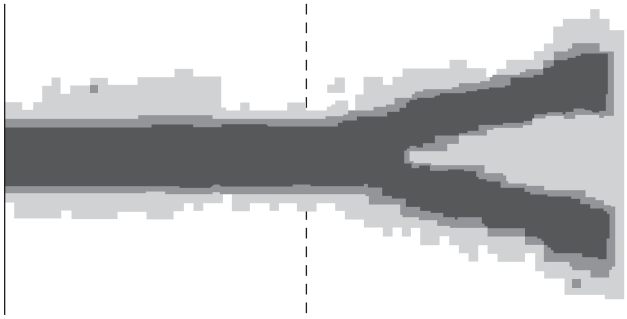

Fig. 7. Two-dimensional image of the cross section of a model of a vessel with bifurcation; the image is obtained through an inhomogeneous layer by the method of speckle interferometry in the near-field zone. Averaging is performed over 100 exposures.

In the near-field, the real and imaginary images are not separated on the sides of the traverse of the array. Their positions are symmetric with respect to the array, and the divergent beam of rays from the imaginary image somewhat increases (compared to Fig. 3) the background pedestal (Fig. 4).

Figure 5 shows the reconstructed image of the cross sections of vessels located in the near-field zone for $R_0 = 66\lambda$ and $D = 64\lambda$, for the case when the array and the vessels were separated by an inhomogeneous layer whose parameters smoothly varied introducing random phase shifts from 0 to 2π into the scattered signals. The layer was at a distance of 25λ from the receiving array. Two vessels were modeled with the cross section diameter of one of them being equal to five elements of resolution and the corresponding diameter of the other being equal to seven elements of resolution. The distance between the vessels was chosen to be equal to 10λ. For comparison of the efficiency of the suggested method of visualization with the conventional (classical) methods of image reconstruction, Fig. 6 displays the image of the same vessels reconstructed by using conventional echo sounding through an inhomogeneous layer, when a sample of the field is subjected to the Fresnel transform. As could be expected, no image can be obtained in this case.

In conclusion, we present the results of the reconstruction of a two-dimensional image of the blood flow for a model of a vessel with bifurcation (Fig. 7). The averaging was made over 100 exposures. It is seen that the shape of the inner walls of the vessel is visualized with a sufficiently high quality. The irregularities of the contour are of the size of one quantization element of the image, which is equal to $\lambda/2$, whereas the element of resolution of the array is equal to λ.

CONCLUSIONS

1. The numerical modeling described above showed that the suggested new method of ultrasonic visualization makes it possible to obtain the images of blood flow through an inhomogeneous medium, which allows one to visualize the internal structure of blood vessels. Since this method provides the image only of flowing blood, there is a good reason to consider it as an analogue of X-ray angiography, i.e., as an ultrasound angiography.

2. The influence of the inhomogeneous medium on the image of the blood flow appears as an additive to the steady component, and the greater its magnitude is, the more condition (11) for the interval of spatial correlation of the field scattered by the blood flow is violated.

3. The spatial (angular) resolution of the method is the same as the resolution of a conventional antenna array, and, therefore, the receiving array must have sufficiently large wave dimensions, so that the required minimal diameter of the vessel be equal to several elements of spatial resolution. This requirement is the same as for the conventional B-type ultrasound systems.

4. The quality of the image can be considerably enhanced by using irradiation with a wideband signal. In this case, narrowband filtering is carried out beforehand, the reconstruction of images is performed at separate frequencies, and, then, the resulting images are incoherently combined.

5. The suggested method permits the use of two-dimensional arrays and the irradiation by pulsed signals, which, in principle, offers a possibility for reconstructing three-dimensional images.

6. In view of the relatively low velocities of the blood flow and with the temporal relations obtained for

the maximal frequency of sampling, the requirements imposed on the speed of operation do not go beyond the possibilities of parallel signal processing with today's ultrasonic diagnostic equipment operating in the range of several megahertz.

REFERENCES

1. *B-Flow. New Way of Visualizing Blood Flow. Ultrasound Technology*, Preprint (GE Ultrasound Europe, 1999).
2. L. N. Bohs *et al.*, in *Acoustical Imaging* (Plenum, New York, 1994), Vol. 21.
3. V. Svet, A. Molotilov, *et al.*, in *Proceedings of 25th International Symposium on Acoustical Imaging* (Bristol, UK, 2000).
4. V. Svet, S. Baykov, A. Molotilov, *et al.*, in *Proceedings of 25th International Symposium on Acoustical Imaging* (Bristol, UK, 2000).
5. V. D. Svet, T. V. Kondratieva, and N. V. Zuikova, Akust. Zh. **42**, 225 (1996) [Acoust. Phys. **42**, 196 (1996)].
6. V. D. Svet, T. V. Kondratieva, and N. V. Zuikova, in *Acoustical Imaging* (Plenum, New York, 1997), Vol. 23, pp. 555–562.
7. N. V. Zuĭkova, T. V. Kondrat'eva, and V. D. Svet, Akust. Zh. **44**, 220 (1998) [Acoust. Phys. **44**, 180 (1998)].
8. N. V. Zuĭkova, T. V. Kondrat'eva, and V. D. Svet, Akust. Zh. **44**, 779 (1998) [Acoust. Phys. **44**, 678 (1998)].
9. V. D. Svet, T. V. Kondratieva, and N. V. Zuikova, in *Proceedings of 25th International Symposium on Acoustical Imaging* (Bristol, UK, 2000).

Translated by A. Svechnikov

Acoustical Physics, Vol. 47, No. 5, 2001, pp. 585–590. Translated from Akusticheskiĭ Zhurnal, Vol. 47, No. 5, 2001, pp. 671–677.

Analytical Representations for the Transient Admittance of a Plate Vibrating in a Medium

M. B. Korotyaev and D. P. Kouzov

St. Petersburg State Marine Technical University, ul. Lotsmanskaya 3, St. Petersburg, 190008 Russia

e-mail: kouzov@ipme.ru

Received November 2, 2000

Abstract—Flexural vibrations of a plate contacting on one side with an ideal compressible liquid are considered. The plate is driven by a harmonic force uniformly distributed along a straight line. The transient admittance of the plate as a function of the distance from the line of the force application is shown to be representable as a sum of an integer function and an integer function multiplied by a logarithmic function. A procedure for determining the power series expansions of these functions is described, and the initial terms of the expansions are derived. The approximations formed by these initial terms and the asymptotic expansion at infinity are compared with the results of numerical calculations for several particular values of the parameters. Vibrations of a liquid with an impedance load at its surface are considered as an auxiliary problem, and, in the framework of this problem, the initial terms of the power series expansions of the integer functions, which appear in the expression for the transient admittance, are determined. The expansions obtained make it possible to raise the speed of the admittance calculations near the points of application of the driving force. *© 2001 MAIK "Nauka/Interperiodica".*

INTRODUCTION

The input and transient admittance of a plate contacting with an acoustic medium on one or two sides and driven by a harmonic force distributed along a straight line were first calculated in connection with the study of the external acoustic field of a homogeneous plate [1–3]. Later on, interest in these quantities was mainly concerned with studying the external acoustic fields of plates whose elastic properties were disturbed (by cracks, supports, stiffening ribs, etc.) along a straight line or a set of straight lines [4–6]. Here, we mentioned only the first papers whose authors used exact analytical representations for the input and transient admittances of the plate vibrating in a medium. The literature on the second of these two objects is quite extensive, and the main body of works falls within 1970s to 1980s. However, this topic remains urgent [7–12]. In what follows, we restrict our consideration to the case of a plate whose one side is in contact with a liquid, and we consider only flexural motions of the plate by using the Kirchhoff equation. A two-side contact can be considered in a similar manner; the final results will differ from the results given below by a factor of two for certain parameters. Note that the procedure suggested for obtaining the power series expansions is applicable to a fairly wide variety of problems. In particular, it is applicable to any known model of plate vibrations, including the models taking into account the longitudinal motions.

Figure 1 schematically illustrates the model. An integral representation for the velocity of flexural displacements of a plate is well known and can be easily obtained using the Fourier transform [13]:

$$v(x) = F_0 A(x),$$

where the quantity

$$A(x) = -\frac{i\omega}{2\pi B}\int_{-\infty}^{\infty}\frac{\gamma(\lambda)\exp(i\lambda x)}{(\lambda^4 - k_p^4)\gamma(\lambda) - \mu k_p^4}d\lambda \qquad (1)$$

is the transient admittance of the plate vibrating in a medium. Here, m is the plate surface density, B is the flexural rigidity of the plate, $\mu = \rho/m$, ρ is the density of the medium, $k_p = (m\omega^2/B)^{1/4}$, $\gamma(\lambda) = \sqrt{\lambda^2 - k_0^2}$, and k_0 is the acoustic wave number. The radical is assumed to take on arithmetic values for $\lambda > k_0$ and $\lambda < -k_0$, and its other values are determined using its analytical extension in λ. The time dependence in the form $\exp(-i\omega t)$ will be omitted in the following calculations. The inte-

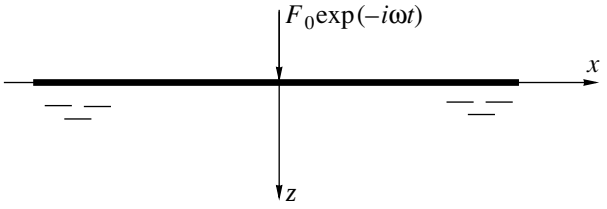

Fig. 1. Schematic representation of the model.

1063-7710/01/4705-0585$21.00

gration is carried out along the real axis; in accordance with the limiting absorption principle, the integrand singularities corresponding to the negative part of the real axis are bypassed from above and the singularities corresponding to the positive part are bypassed from below. For reasons of convenience, we use the exponent in Eq. (1) with the sign opposite to that used in [13]. This change of sign is possible since the function $A(x)$ is an even function.

From Eq. (1) it follows that a successive differentiation of the integral appearing on the right-hand side with respect to x yields a divergent integral. This means that the standard approach used for constructing power expansions is inapplicable in the case of a transient admittance near the zero point, and this is the reason why its analytical properties in the vicinity of zero have been poorly understood. Some progress in studying the analytical properties of the transient admittance of a plate as a function of the distance from the line of application of a harmonic force was achieved by Crighton [13] who showed that the asymptotic representation of this admittance for small distances from the source contains power and logarithmic terms. Crighton described a factorization-based procedure for obtaining the initial terms of the asymptotic series. However, he obtained the numerical values only for the expansion coefficients that could be evaluated from elementary considerations (see the discussion in [14, 15]). Below, we show that the series suggested by Crighton are not only asymptotic ones. They converge for arbitrary argument values, which means that the transient admittance of a plate as a function of distance from the line of application of a disturbing force is a sum of an integer function and an integer function multiplied by a logarithmic function.

VIBRATIONS OF A LIQUID WITH AN IMPEDANCE LOAD ON ITS SURFACE

We consider vibrations of a liquid loaded by an impedance on its surface and assume that the driving force is a time-harmonic force distributed along a straight line. Namely, we assume that the driving force is distributed along the Oz axis and has a linear density F_0. In this case, the transient admittance has the form

$$A_0(x) = \int_{-\infty}^{\infty} \frac{\gamma(\lambda)\exp(i\lambda x)}{\gamma(\lambda) - \alpha} d\lambda, \quad \alpha \in C. \tag{2}$$

If the distributed mass of density μ is responsible for the impedance on the surface, as it was the case in [13], we have $\alpha = -\mu$. In the following section, we will show that studying the properties of the transient admittance of a plate can be reduced to analyzing the integrals of this type. In what follows, we will consider only positive values of the x coordinate, because $A_0(x) = A_0(|x|)$ by virtue of the symmetry of the problem under consideration.

Following [13], we represent integral (2) as a sum of three terms

$$\int_{-\infty}^{\infty} \exp(i\lambda x) d\lambda + \alpha^2 \int_{-\infty}^{\infty} \frac{\exp(i\lambda x)}{\lambda^2 - (k_0^2 + \alpha^2)} d\lambda + \alpha \int_{-\infty}^{\infty} \frac{\gamma(\lambda)\exp(i\lambda x)}{\lambda^2 - (k_0^2 + \alpha^2)} d\lambda = I_1 + I_2 + I_3, \tag{3}$$

where

$$I_1 = 2\pi\delta(x),$$

$$I_2 = i\pi\alpha^2 \frac{\exp(iax)}{a}.$$

Here, a is the value of $\sqrt{k_0^2 + \alpha^2}$ belonging to set C_+ that is a subset of points in the complex plane C determined as the upper half-plane $\mathrm{Im}\,\lambda > 0$ united with the positive part of the real axis.

For I_3 in Eq. (3), we have

$$I_3 = \alpha \int_{-\infty}^{\infty} \frac{\gamma(\lambda)\exp(i\lambda x)}{\lambda^2 - a^2} d\lambda = \alpha \int_{-\infty}^{\infty} \frac{\exp(i\lambda x)}{\gamma(\lambda)} d\lambda + \alpha^3 \int_{-\infty}^{\infty} \frac{\exp(i\lambda x)}{(\lambda^2 - a^2)\gamma(\lambda)} d\lambda = i\alpha\pi H_0^{(1)}(k_0 x) + \alpha^3 i\pi \frac{\exp(iax)}{a\sqrt{\alpha^2}} + 2\alpha^3 u(x), \quad \alpha \in C, \quad \mathrm{Re}\sqrt{\alpha^2} > 0,$$

where

$$u(x) = \int_{k_0}^{k_0 + i\infty} \frac{\exp(i\lambda x)}{(\lambda^2 - a^2)\gamma(\lambda)} d\lambda. \tag{4}$$

Similar to the integral on the right-hand side of Eq. (1), the function $u(x)$ has no power series expansion in the vicinity of zero, because the integral in Eq. (4) becomes divergent after being twice differentiated.

In order to investigate the function $u(x)$ in more detail, we consider its analytical extension to the complex half-plane $\mathrm{Re}\,z > 0$.

For large arguments, an asymptotic expansion of the obtained function can be found using the Watson lemma. The first three terms of this expansion are as follows:

$$u(z) = -\frac{\exp\left(i\frac{5i}{4}\right)\sqrt{\pi}}{2a\sqrt{2k_0}} \frac{\exp(ik_0 z)}{\sqrt{z}} \times \left\{ -\frac{2ai}{\alpha^2} + \frac{(8k_0^2 - \alpha^2)a}{4k_0\alpha^4 z} \right. \tag{5}$$

$$+\frac{3ai}{64k_0^2\alpha^6}(128k_0^4+16k_0^2\alpha^2+3\alpha^4)\frac{1}{z^2}+O\left(\frac{1}{z^3}\right)\Bigg\}.$$

To determine the behavior of the function $u(z)$ in the near zone, we consider its variation in bypassing the point $z = 0$ along a closed contour. As $\arg z$ varies from 0 to 2π, the direction of the fastest decrease of the integrand in the expression for $u(z)$ varies from $\pi/2$ to $-3\pi/2$. This issue was considered in [16]; later, it was studied it in more detail in [17]. As a result, we have

$$u(z\exp(2\pi i)) = u(z) + u_0(z),$$

where

$$u_0(z) = \oint_L \frac{\exp(i\lambda z)}{(\lambda^2-a^2)\gamma(\lambda)}d\lambda \tag{6}$$

and L is the closed contour passing clockwise around the branch points and both poles of the integrand.

Thus, we have

$$u(z) = u_1(z) - \frac{i}{2\pi}u_0(z)\ln\frac{zk_0}{2}.$$

In this formula, $u_1(z)$ is an integer function of the argument z and $u_0(z)$ determined by Eq. (6) is also an integer function of z. One can easily show that $u_0(0) = u_0'(0) = 0$.

For the function $u(z)$, we can write a differential equation:

$$\frac{d^2u}{dz^2}+a^2u = -\frac{i\pi}{2}H_0^{(1)}(k_0z). \tag{7}$$

Complementing this equation with two obvious initial conditions,

$$\begin{cases} u(0) = \displaystyle\int_{k_0}^{k_0+i\infty}\frac{d\lambda}{(\lambda^2-a^2)\gamma(\lambda)} \\ u(0) = \displaystyle\int_{k_0}^{k_0+i\infty}\frac{i\lambda d\lambda}{(\lambda^2-a^2)\gamma(\lambda)}, \end{cases} \tag{8}$$

we obtain a closed problem for the function $u(z)$.

We will use the method of undetermined coefficients to seek the function $u(z)$ in the form

$$u(z) = \sum_{k=0}^{\infty}c_k'z^k - \frac{i}{2\pi}\sum_{k=2}^{\infty}c_k''z^k\ln\frac{zk_0}{2}, \tag{9}$$

where c_k' and c_k'' are the undetermined coefficients to be found. Substituting Eq. (9) into Eqs. (7) and (8), we obtain the following expressions for the initial terms of the expansion:

$$c_0' = -\frac{i\pi}{2a\sqrt{\alpha^2}} - \frac{\sinh^{-1}(\sqrt{\alpha^2}/k_0)}{a\sqrt{\alpha^2}},$$

$$c_1' = \begin{cases} \dfrac{\pi}{2\sqrt{\alpha^2}}, & \alpha^2 \in C_+ \\ -\dfrac{\pi}{2\sqrt{\alpha^2}}, & \alpha^2 \notin C_+, \end{cases}$$

$$c_2' = \frac{1}{2}\left(-\frac{i\pi}{2}+c-\frac{3}{2}-a^2c_0'\right),$$

$$c_2'' = i\pi, \quad c_4'' = -\frac{i\pi}{24}(k_0^2+2a^2).$$

The subsequent terms can be found using the recursion relations

$$c_{2n+1}'(2n+1)2n + a^2c_{2n-1}' = 0,$$

$$c_{2n+2}'(2n+2)(2n+1) + a^2c_{2n}' - \frac{i}{2\pi}c_{2n+2}''(4n+3)$$

$$= \frac{(-1)^nk_0^{2n}}{((2n)!!)^2}\left[-\frac{i\pi}{2}+c-S_n\right]$$

$$(n = 1, 2, \ldots),$$

$$S_n = \sum_{k=1}^{n}\frac{1}{k}, \quad c = 0.5772\text{—the Euler constant}, \tag{10}$$

$$c_{2n+1}'' = 0,$$

$$c_{2n+2}''(2n+2)(2n+1) + a^2c_{2n}'' = 2\pi\frac{(-1)^nk_0^{2n}}{((2n)!!)^2}i$$

$$(n = 1, 2, \ldots).$$

The coefficients c_{2n}'' can be also found immediately from Eq. (6) by evaluating the residue of the integrand at infinity:

$$u_0(z) = \oint_L \frac{\exp(i\lambda z)}{(\lambda^2-a^2)\gamma(\lambda)}d\lambda$$

$$= 2\pi i\operatorname*{Res}_{\lambda=\infty}\frac{\exp(i\lambda z)}{(\lambda^2-a^2)\sqrt{\lambda^2-k_0^2}}$$

$$= 2\pi i\operatorname*{Res}_{\lambda=\infty}\frac{1}{\lambda^3}\left(\sum_{k=0}^{\infty}\frac{(i\lambda z)^k}{k!}\right)\left(\sum_{n=0}^{\infty}\frac{S_{2n}}{\lambda^{2n}}\right)$$

$$= -2\pi i\sum_{n=1}^{\infty}\frac{(-1)^nS_{2n-2}}{(2n)!}z^{2n}.$$

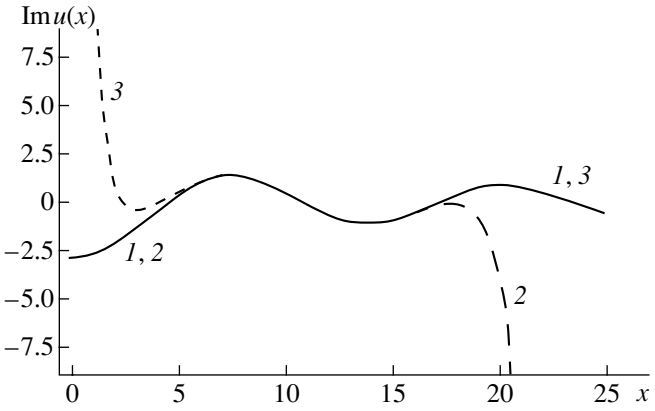

Fig. 2. Curve Im $u(x)$.

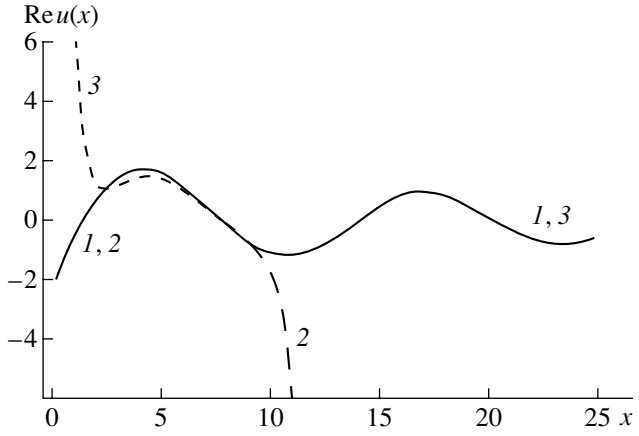

Fig. 3. Curve Re $u(x)$.

Here,

$$S_0 = 1,$$

$$S_{2n} = a^{2n} + \sum_{l=1}^{n} \frac{(-1)^{l-1} a^{2(n-l)} (2l-1)!! k_0^{2l}}{l! 2^l}.$$

Returning to Eq. (2), in view of Eqs. (10), we obtain $A_0(x)$ in the form

$$A_0(x) = \frac{i}{2\pi m\omega}[2\pi\delta(x) - i\pi\mu H_0^{(1)}(k_0 x) - 2\mu^3 u(x)] = \frac{i\delta(x)}{m\omega} - \frac{i}{m\omega}[A\ln x + B + Cx + Dx^2 + Ex^2\ln x] + O(x^3),$$

where

$$A = -\mu/\pi,$$

$$B = -\frac{\mu}{\pi}\left(\ln\frac{k_0}{2} + c\right) + \frac{i\mu}{2} - \frac{\mu^2 i}{2a} - \frac{\mu^2}{a\pi}\sinh^{-1}\frac{\mu}{k_0},$$

$$C = \mu^2/2,$$

$$D = \frac{1}{2\pi}\left[\frac{\mu(2\mu^2 + k_0)}{2}\ln\frac{k_0}{2} + \frac{k_0^2\mu}{4}(2(c-1) - i\pi) + \mu^3\left(-\frac{i\pi}{2} + c - \frac{3}{2} - a^2\left[\frac{i\pi}{2a\mu} + \frac{1}{2a\mu}\sinh^{-1}(\mu/k_0)\right]\right)\right],$$

$$E = \frac{\mu}{2\pi}\frac{2\mu^2 + k_0^2}{2}.$$

The first three coefficients were obtained by Crighton [13] as the coefficients of the asymptotic representation at $x \longrightarrow 0$.

As follows from the above consideration, the transient admittance is representable in this case as a combination of the Hankel function and the function $u(x)$ (the exponential terms are canceled). The curves given in Figs. 2 and 3 make it possible to visually estimate the region of applicability of the obtained exact expansion of the function $u(x)$, as well as the region where this expansion transforms to an asymptotic one at certain, arbitrarily chosen values of the impedance ($m = 1500$) and frequency ($\omega = 500$) for vibrations propagating in water. Here and below, index *1* labels the result computed using the integral representation, index *2* corresponds to the result computed using the above series, and index *3* corresponds to the result computed using the asymptotic expansion. The data given in Tables 1 and 2 demonstrate that the first terms of the constructed series taken for the same parameter values ensure a sufficient accuracy. Despite the fact that the rate of convergence of the constructed expansions rapidly decreases with increasing distance from zero (in constructing the curves and calculating the data for the tables, we used the first 40 terms), the suggested series appear to be useful. First, they allow one to avoid cumbersome calculations of the oscillating integrals appearing in the integral expression (1). Second, even a short initial segment of the series ensures a good approximation for the admittance near the excitation line. Third, these series make computations faster when the admittance is calculated for several points of a plate, because the expan-

Table 1

Im $u(x)$	$x = 0.1$	$x = 1.0$	$x = 2.0$	$x = 5.0$	$x = 7.0$	$x = 10.0$	$x = 12.0$	$x = 20.0$	$x = 50.0$
1	−2.82547	−2.63424	−2.09152	0.41195	1.34888	0.50509	−0.60165	0.87032	−0.3496
2	−2.82547	−2.63424	−2.09152	0.41195	1.34888	0.50509	−0.60171	−3.52011	−1.3E+09
3	4519.57	14.0254	0.89774	0.51416	1.31221	0.47557	−0.60881	0.86953	−0.3497

Table 2

Re$u(x)$	$x = 0.1$	$x = 1.0$	$x = 2.0$	$x = 5.0$	$x = 7.0$	$x = 10.0$	$x = 12.0$	$x = 20.0$	$x = 50.0$
1	−1.75833	−0.2978	0.80858	1.58732	0.47096	−1.1126	−0.9498	0.148829	−0.44131
2	−1.75833	−0.2979	0.80856	1.58731	0.47052	−1.9149	−36.178	−1.4E+06	−2.2E+14
3	4237.597	7.75179	1.06703	1.37286	0.39003	−1.1062	−0.9342	0.145603	−0.44120

sion coefficients are calculated only once, whereas the use of representation (1) requires a recalculation of integrals at every point.

TRANSIENT ADMITTANCE OF A PLATE

Now, we return to the consideration of vibrations of a plate. If we represent the denominator in Eq. (1) as a fifth-order polynomial in γ, factorize this polynomial, and then decompose the integrand into partial fractions, then Eq. (1) takes the form

$$A(x) = -\frac{i\omega}{2\pi B}\sum_{n=1}^{5} A_n \int_{-\infty}^{\infty} \frac{\gamma(\lambda)\exp(-i\lambda x)}{\gamma(\lambda)-\alpha_n} d\lambda, \qquad (11)$$

where

$$A_n = 1/\prod_{j\neq n}(\alpha_n - \alpha_j)$$

and α_n are the roots of the denominator in the integrand of Eq. (1).

It is obvious that the integrals on the right-hand side of Eq. (11) are the integrals of the same type as in Eq. (2); consequently, they can be expanded into series described in the previous section. Carrying out formal transformations, we obtain

$$A(x) = -\frac{i\omega}{B}\delta(x)\sum_{n=1}^{5} A_n + \frac{\omega}{2B}H_0^{(1)}(k_0 x)\sum_{n=1}^{5} A_n\alpha_n + \frac{\omega}{B}\sum_{\alpha_n\in C_+} A_n\alpha_n^2\frac{\exp(ia_n x)}{a_n} - \frac{i\omega}{\pi B}U(x), \qquad (12)$$

where

$$a_n = \sqrt{k_0^2+\alpha_n^2}, \quad \text{and} \quad U(x) = \sum_{n=1}^{5} A_n\alpha_n^3 u_n(x).$$

In the expression for $U(x)$, the functions $u_n(x)$ are determined by Eq. (4), where α_n is substituted for α.

Taking into account the equalities

$$\sum_{n=1}^{5} A_n = 0 \quad \text{and} \quad \sum_{n=1}^{5} A_n\alpha_n = 0,$$

Eq. (12) can be simplified and finally takes the form:

$$A(x) = \frac{\omega}{B}\sum_{\alpha_n\in C_+} A_n\alpha_n^2\frac{\exp(ia_n x)}{a_n} - \frac{i\omega}{\pi B}U(x). \qquad (13)$$

The last term in Eq. (13) is obviously of greatest interest. Using the method described in the previous section, it can be represented as a sum of an integer function and an integer function multiplied by a logarithmic function and find the coefficients in the power series expansions of these functions.

Figures 4 and 5 show the curves for the function $A(x)$. These curves make it possible to estimate the region where the approximation of the function $U(x)$ with the initial terms of the constructed expansions (again, we consider the first 40 terms) is applicable for

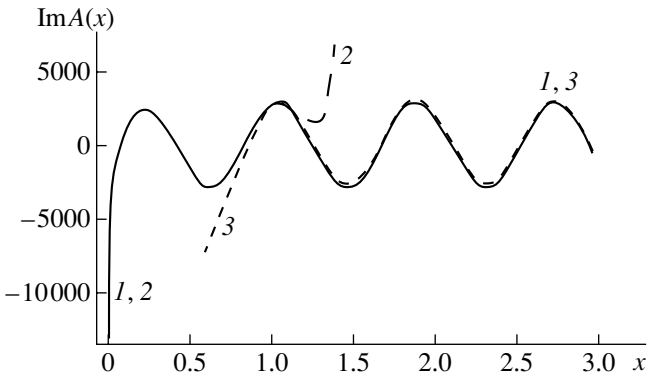

Fig. 4. Curve Im$A(x)$.

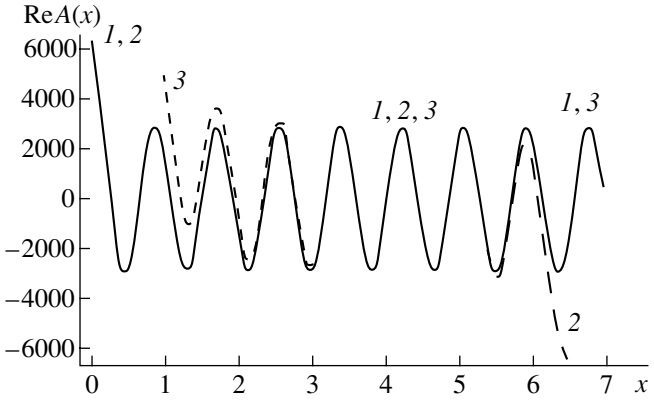

Fig. 5. Curve Re$A(x)$.

Table 3

Im$A(x)$	x = 0.01	x = 0.1	x = 1.0	x = 2.0	x = 3.0	x = 4.0	x = 5.0	x = 6.0	x = 7.0
1	–5945.74	818.933	2576.65	2310.95	–409.465	–2684.32	–2047.58	810.1223	2789.075
2	–5945.74	818.932	2581.54	1.5E+07	6.4E+10	2.4E+13	2.4E+15	1.1E+17	2.6E+18
3	–3.0E+08	–859.587	2349.92	2561.08	–273.825	–2615.82	–2013.82	825.7273	2795.145

Table 4

Re$A(x)$	x = 0.01	x = 0.1	x = 1.0	x = 2.0	x = 3.0	x = 4.0	x = 5.0	x = 6.0	x = 7.0
1	6121.326	4066.22	1312.24	–1650.6	–2808.3	–921.19	1965.10	2719.90	524.462
2	6121.326	4066.22	1312.24	–1650.6	–2808.3	–921.59	1938.34	1799.774	–18839.3
3	3.1E+08	1.0E+06	4942.61	–1177.1	–2714.4	–909.85	1956.39	2707.974	514.1173

the case of vibrations of a steel plate on the water surface (the cyclic frequency is $\omega = 500$ and the plate thickness is $h = 0.01$ m). The data given in Tables 3 and 4 allow one to judge the accuracy of the approximations under consideration. For the case of such a plate, Nayak [18] reported the values of the input admittance computed for a fairly wide range of cyclic frequencies.

It should be noted that, in calculating the data given in the tables and curves, we evaluated the first term in Eq. (13) using standard methods characterized by a very high accuracy; for this reason, the only errors were those caused by the approximations of the function $U(x)$.

CONCLUSION

To conclude, we note the essential similarity between the behavior of the considered transient admittance and the behavior of cylindrical functions (the Hankel functions, primarily). Clearly, this similarity is explained not only by the formal fact that the Hankel function appears on the right-hand side of the linear differential equation (7) for the function $u(x)$, but also by the similarity of the physical situations in which they appear in the theoretical consideration.

As can be seen from the study described in this paper, the well-known computational procedures for obtaining numerical values of cylindrical functions (an exact series for the near field and an asymptotic expansion for the far field, both coinciding in the intermediate zone) can also be used for calculating the transient admittance of a plate.

REFERENCES

1. M. Heckl, Acustica **9**, 371 (1959).
2. L. Ya. Gutin, Akust. Zh. **10**, 431 (1964) [Sov. Phys. Acoust. **10**, 369 (1964)].
3. G. Maidanik, J. Sound Vibr. **3**, 289 (1966).
4. D. P. Kouzov, Prikl. Mat. Mekh. **27**, 1037 (1963).
5. D. P. Kouzov, Prikl. Mat. Mekh. **28**, 409 (1964).
6. I. P. Konovalyuk and V. N. Krasil'nikov, in *Diffraction and Measurement of Waves* (Leningr. Gos. Univ., Leningrad, 1965), Issue 4, pp. 149–165.
7. V. N. Romanov, Akust. Zh. **44**, 407 (1998) [Acoust. Phys. **44**, 346 (1998)].
8. I. V. Andronov and B. P. Belinskiy, J. Acoust. Soc. Am. **103**, 673 (1998).
9. R. M. Grise and R. J. Pinnington, J. Sound Vibr. **230**, 825 (2000).
10. R. M. Grise and R. J. Pinnington, J. Sound Vibr. **230**, 851 (2000).
11. R. V. Craster and D. P. Williams, J. Sound Vibr. **235**, 655 (2000).
12. N. J. Kessissoglou and J. Pan, Int. J. Acoust. Vibr. **5**, 15 (2000).
13. D. G. Crighton, J. Sound Vibr. **20**, 209 (1972).
14. G. W. Bentien, M. A. González, and J. W. Young, J. Sound Vibr. **47**, 136 (1976).
15. D. G. Crighton, J. Sound Vibr. **47**, 137 (1976).
16. D. P. Kouzov, in *Proceedings of International Seminar Day on Diffraction'97* (St. Petersburg, 1997), p. 22.
17. D. P. Kouzov, Zap. Nauchn. Semin. POMI **257** (1997); Mat. Vopr. Teor. Rasprostr. Voln, No. 28, 116 (1997).
18. P. R. Nayak, J. Acoust. Soc. Am. **47**, 191 (1970).

Translated by A. Vinogradov

Acoustical Physics, Vol. 47, No. 5, 2001, pp. 591–597. Translated from Akusticheskiĭ Zhurnal, Vol. 47, No. 5, 2001, pp. 678–684.

Radiation and Scattering of Sound Waves in Oceanic Waveguides

V. M. Kuz'kin

Wave Research Center, General Physics Institute, Russian Academy of Sciences, ul. Vavilova 38, Moscow, 117942 Russia

e-mail: gera@kapella.gpi.ru

Received January 22, 2001

Abstract—The applicability conditions for the concept of a directivity pattern (a scattering amplitude) in the problems of waveguide propagation are formulated. The consideration is based on the solution of the Sturm–Liouville problem. The results of the comparison between these conditions and the analogous conditions obtained earlier in the ray approximation are discussed. The expression for the scattering matrix of waveguide modes is modified on the basis of the suggested conditions in such a way that it involves only the quantities determined from the solution of the Schrödinger equation. This makes it possible to perform numerical calculations by using the results of numerous studies of the propagation in inhomogeneous waveguides and the diffraction by complex-structured bodies in free space. © *2001 MAIK "Nauka/Interperiodica".*

A tendency to extend customary concepts and methods beyond their lawful domain of applicability is often observed in science and, especially, in practical engineering. Hence, it is no wonder that in considering such problems as the sound radiation by extended arrays and the scattering of sound by bodies in oceanic waveguides many authors try to describe these phenomena within the framework of customary ideas that are conventional for free space. Since it was clear from the beginning that the concept of a directivity pattern (a scattering amplitude) in waveguides has a restricted domain of applicability, the efforts were directed at solving the problem approximately and determining the limits of applicability of the corresponding approximations. Such a problem was considered earlier [1–3] in the framework of the WKB approximation.

This paper is a further development of the aforementioned studies. The applicability conditions for the concept of a locally homogeneous medium in a multimode plane-layered waveguide are discussed on the basis of the solution to the Sturm–Liouville problem. The term "locally homogeneous medium with the characteristic dimension ρ" will be understood as an inhomogeneous medium where normal waves can be considered as quasi-plane within a layer with the thickness ρ. If the array aperture or the vertical dimension of a body does not exceed the thickness of such a quasi-homogeneous layer, the directivity pattern (the scattering amplitude) is an adequate characteristic of radiation (scattering) in the stratified waveguide. These conditions are compared with the analogous conditions obtained earlier using the ray approximation. On the basis of these conditions, a modified expression, which contains only the values determined by solving the Sturm–Liouville problem, is suggested for the scattering matrix of waveguide modes.

First of all, we consider the applicability conditions for the concept of a locally homogeneous medium within the framework of the ray approximation. Let a vertical linear array with the length l be positioned between the levels $z_1 = z_0 - l/2$ and $z_2 = z_0 + l/2$, where z_0 is the coordinate of the array center. In the WKB approximation, which is one of the forms of the geometric acoustics approximation, the mode amplitudes in an inhomogeneous waveguide are represented with the help of a directivity pattern in the case of validity of the following inequalities:

$$l^2 \ll l_1^2 = 4\lambda L_n \sin\beta_m(z_0)/\pi n_0^2, \quad (1)$$

$$l \ll l_2 = 4L_n \sin^2\beta_m(z_0)/n_0^2, \quad (2)$$

$$l^6 \ll l_3^6 = 6.57 \times 10^{-2}\lambda^4 L_n^2/n_0^4, \quad (3)$$

where $n_0 = n(z_0)$ is the refraction index of the medium at the level $z = z_0$; λ is the sound wavelength; $L_n = n_0/|\nabla_z n(z_0)|$ is the characteristic vertical scale of the inhomogeneity variation in the medium; and $\beta_m(z)$ is the grazing angle of the Brillouin ray corresponding to the mth mode [1, 2]. The first inequality (1) corresponds to the condition of smallness of the nonlinear phase variations of normal modes in depth within the aperture, and the second inequality (2) corresponds to the smallness of the amplitude variations [1]. Inequalities (1) and (2) are equivalent to the requirement that normal modes be treated as quasi-plane waves within a layer with the vertical dimension l; i.e., one can ignore the amplitude variations and the nonlinear phase changes in such a layer. It should be noted that, as a rule, in estimating the array fields in oceanic waveguides, one can

1063-7710/01/4705-0591$21.00 © 2001 MAIK "Nauka/Interperiodica"

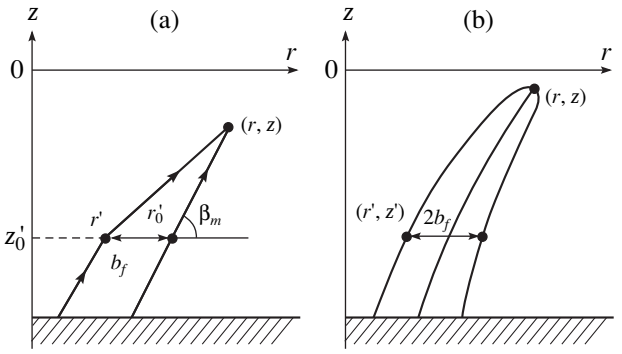

Fig. 1. Schematic diagram of the Fresnel volume.

ignore the amplitude variations of normal modes [4]. The only exclusion is the case when the turning point corresponding to the *m*th mode falls within an array and the WKB approximation becomes invalid. Inequality (3) can be interpreted as the condition at which the normal modes excited within the angular width of the major lobe of the directivity pattern can be considered as quasi-plane [2]. Condition (3) is a consequence of inequalities (1) and (2), but it is more illustrative and convenient in the case of the determination of the applicability limits for the concept of a locally inhomogeneous medium when the major part of radiation energy is concentrated within the major lobe of the directivity pattern; therefore, this condition is important by itself. In the particular case of a homogeneous waveguide ($n(z)$ = const), we have $L_n = \infty$, and normal waves are plane within the entire depth of the waveguide.

The quantity l_1 has the meaning of the vertical dimension d_{Fr} of the Fresnel volume of the Brillouin ray, and condition (1) can also be interpreted as the criterion of the far wave field of an array in a layered inhomogeneous medium. Indeed, the horizontal dimension of the Fresnel volume of a ray is equal to (see [5])

$$b_{\mathrm{Fr}} = |r - r'_0| = \left\{\lambda \frac{d}{da_m}\int_{z'}^{z} \frac{a_m}{\sqrt{n^2(z) - a_m^2}}dz\right\}^{1/2}, \qquad (4)$$

where (r, z) is the observation point, (r', z') is the current point of the boundary of the Fresnel volume, and r'_0 is the coordinate of the point of intersection of the "reference" ray with the plane z'_0 = const; $a_m = n(z'_0)\cos\beta_m$ is the parameter characterizing the ray; and β_m is the angle between the ray and the horizontal axis r'_0 (Fig. 1a). The general view of the Fresnel volume of the ray is shown in Fig. 1b. We write Eq. (4) in the form $b_{\mathrm{Fr}} = \{\lambda(dr/da_m)\}^{1/2}$. Representing the derivative dr/da_m as $dr/da_m = (dr/dz)(dz/da_m)$ and taking into account that $da_m/dz = n(z'_0)\sin\beta_m(d\beta_m/dz)$ and $dr/dz = \cot\beta_m$, we arrive at the expression for the quantity b_{Fr}:

$$b_{\mathrm{Fr}} = \left[\lambda\cos\beta_m/n(z'_0)\sin^2\beta_m\frac{d\beta_m}{dz}\right]^{1/2}.$$

It is clear from geometric reasons (Fig. 1a) that the projections of the Fresnel volume onto the *z* and *r* axes are interrelated by the dependence $d_{\mathrm{Fr}} = b_{\mathrm{Fr}}\tan\beta_m$. In this case, from the expression obtained for the vertical dimension d_{Fr}, we easily derive

$$d_{\mathrm{Fr}} = [\lambda L_n \sin\beta_m/n(z'_0)]^{1/2}. \qquad (5)$$

Equation (5) agrees well with condition (1) for l_1.

Now, let us formulate the applicability conditions for the concept of a locally homogeneous medium in a multimode plane-layered waveguide without using the WKB asymptotics of eigenfunctions in the vicinity of the array. We represent the field of a linear array as a sum of normal modes

$$u(r, z) = \frac{i}{4}\sum_m c_m(z_0)\psi_m(z)H_0^{(1)}(h_m r),$$

where

$$c_m(z_0) = \int_{z_1}^{z_2} E(z - z_0)\psi_m(z)dz \qquad (6)$$

is the amplitude of the *m*th mode, $E(z)$ is the distribution of the particle velocity over the aperture, and $H_0^{(1)}(x)$ is the zero-order Hankel function of the first kind. Following [1], we determine the conditions at which the amplitude c_m is expressed with the help of the directivity pattern of the array.

The orthonormal eigenfunctions $\psi_m(z)$ (see Eq. (6)) of the Sturm–Liouville problem, which correspond to the spectrum of the propagation constants h_m, satisfy the Schrödinger equation

$$\left[\frac{d^2}{dz^2} + (k^2(z) - h_m^2)\right]\psi_m(z) = 0 \qquad (7)$$

with the appropriate boundary conditions at the bottom and the surface [6]. If we use the analogy between oscillatory and wave processes [7], it is possible to treat the waveguide as a linear filter transmitting a discrete set of frequencies. The spectrum of the signal transmitted through the filter is equal to the product of the filter spectra (the frequency response) and the initial signal. In the considered case, the spatial spectrum of eigenfunctions determines the transmission of the spatial spectral components of the field of a directional radia-

tor. According to the known theorem on the spectrum of the integral $\int_{-\infty}^{+\infty} x_1^*(\theta)x_2(\theta-\tau)d\theta$ [7], we have

$$\int_{-\infty}^{\infty} E(z-z_0)\psi_m(z)dz = 2\pi\int_{-\infty}^{\infty} E(\gamma)\psi_m(\gamma)\exp(i\gamma z_0)d\gamma, \quad (8)$$

where $E(\gamma)$) and $\psi_m(\gamma)$ are the Fourier transforms of the functions $E(z)$ and $\psi_m(z)$:

$$E(\gamma) = \frac{1}{2\pi}\int_{-\infty}^{\infty} E(z)e^{-i\gamma z}dz,$$

$$\psi_m(\gamma) = \frac{1}{2\pi}\int_{-\infty}^{\infty} \psi_m(z)e^{-i\gamma z}dz.$$

It is rather difficult to determine the spectrum of eigenfunctions in a general case. Therefore, we proceed as follows. We compare the function $\psi_m(z)$ to the function $\phi_m(z)$, which is its approximation for a homogeneous medium and for which it is easy to determine the Fourier transform. In a homogeneous layer ($n(z) = n_0 =$ const), Eq. (7) is a differential equation with constant coefficients $k_0^2 - h_m^2 = \gamma_m^2$ and $k_0 = k(z_0)$:

$$\left[\frac{d^2}{dz^2} + \gamma_m^2\right]\phi_m(z) = 0 \quad (9)$$

and with a known solution [6]:

$$\phi_m(z) = a_m^+\exp(i\gamma_m z) + a_m^-\exp(-i\gamma_m z). \quad (10)$$

We require that the functions $\psi_m(z)$ and $\phi_m(z)$ be close to each other within such a homogeneous layer whose thickness can be as small as desired. We determine the constants $a_m^\pm$ from the initial conditions that the values of these functions and their first derivatives at the point $z = z_0$ are equal to

$$\phi_m(z_0) = \psi_m(z_0), \quad \left.\frac{d\phi_m(z)}{dz}\right|_{z=z_0} = \left.\frac{d\psi_m(z)}{dz}\right|_{z=z_0}. \quad (11)$$

As a result, we obtain

$$a_m^+ = \frac{1}{2i\gamma_m}[i\gamma_m\psi_m(z_0) + \psi_m'(z_0)]\exp(-i\gamma_m z_0),$$
$$a_m^- = \frac{1}{2i\gamma_m}[i\gamma_m\psi_m(z_0) - \psi_m'(z_0)]\exp(i\gamma_m z_0), \quad (12)$$

where $\psi_m'(z_0) = \left.\frac{d\psi_m(z)}{dz}\right|_{z=z_0}$. It should be noted that the constants $a_m^\pm$ (Eq. (12)) can be determined not only from the initial conditions (Eq. (11)), but also in some other ways. For example, in inequalities (1)–(3), the sum of two linearly independent solutions (Eq. (7)) in the WKB approximation of two quasi-plane waves at the point z_0 was used as the function $\psi_m(z)$ [1, 2]. The Fourier transform of $\phi_m(z)$ is equal to

$$\phi_m(\gamma) = a_m^+\delta(\gamma-\gamma_m) + a_m^-\delta(\gamma+\gamma_m), \quad (13)$$

where $\delta(x)$ is the Dirac delta-function. In Eq. (13), the representation of the function $\delta(x)$ by the Fourier integral [2] was used:

$$\delta(x-y) = (1/2\pi)\int_{-\infty}^{\infty}\exp[i\omega(x-y)]d\omega.$$

We write Eq. (6) in the form of two terms

$$c_m(z_0) = c_m^{(0)}(z_0) + c_m^{(1)}(z_0), \quad (14)$$

where

$$c_m^{(0)}(z_0) = \int_{-\infty}^{\infty} E(z-z_0)\phi_m(z)dz, \quad (15)$$

$$c_m^{(1)}(z_0) = \int_{-\infty}^{\infty} E(z-z_0)[\psi_m(z) - \phi_m(z)]dz \quad (16)$$

is the correction to the amplitude of the mth mode that is caused by the inhomogeneity of the medium. The integration limits in Eqs. (15) and (16) are extended in comparison with Eq. (6) up to infinity, which does not change the integral values, because, outside the array aperture, $E(z) = 0$. Using Eq. (8), we represent Eq. (15) in the form

$$c_m^{(0)}(z_0) = 2\pi\int_{-\infty}^{\infty} E(\gamma)\phi_m(\gamma)\exp(i\gamma z_0)d\gamma. \quad (17)$$

Applying Eq. (10) to Eq. (17), with allowance for Eqs. (12) we obtain

$$c_m^{(0)}(z_0) = 2\pi[E(\gamma_m)a_m^+\exp(i\gamma_m z_0) + E(-\gamma_m)a_m^-\exp(-i\gamma_m z_0)]. \quad (18)$$

As is known [7], the Fourier transform $E(\gamma)$ is proportional to the directivity pattern of the array $D(\beta)$ in the far wave field:

$$E(\gamma) \sim \begin{cases} D(\beta), & |\gamma| \le k_0, \quad \beta = \arcsin(\gamma/k_0) \\ 0, & |\gamma| > k_0. \end{cases}$$

Thus, the first term $c_m^{(0)}$ (Eq. (18)) in Eq. (14) is determined by the directivity pattern of the array in the homogeneous medium and by the eigenfunctions and their derivatives at the array aperture. The second term $c_m^{(1)}$ (Eq. (16)) is determined by the difference between

the eigenfunctions $\psi_m(z)$ and $\phi_m(z)$ weighted with the distribution $E(z - z_0)$ within the array aperture.

Let us estimate the accuracy of the field representation in an inhomogeneous waveguide with the help of the array directivity pattern in a homogeneous medium. For this purpose, we expand the difference $\vartheta_m(z) = \psi_m(z) - \phi_m(z)$ into the Taylor series in the vicinity of the array center $z = z_0$:

$$\vartheta_m(z) = b_0 + b_1(z - z_0) + b_2\frac{(z - z_0)^2}{2} + b_3\frac{(z - z_0)^3}{6} + \dots, \quad (19)$$

where

$$b_0 = \psi_m(z_0) - \phi_m(z_0), \quad b_1 = \psi'_m(z_0) - \phi'_m(z_0),$$
$$b_2 = \psi''_m(z_0) - \phi''_m(z_0), \quad b_3 = \psi'''_m(z_0) - \phi'''_m(z_0). \quad (20)$$

It follows immediately from the initial conditions (11) that $b_0 = b_1 = 0$. From Eqs. (7), (9), and (11), we obtain $b_2 = 0$. Finally, we obtain for $\vartheta_m(z)$ (Eq. (19)):

$$\vartheta_m(z) = b_3\frac{(z - z_0)^3}{6} + \dots. \quad (21)$$

Let us determine the value of b_3. The third derivatives of the functions $\psi_m(z)$ and $\phi_m(z)$ can be determined by differentiating Eqs. (7) and (9) with respect to z, which yields

$$b_3 = -2(k_0)^2(n_0^2/L_n)\phi_m(z_0).$$

Now, if we expand $\phi_m(z)$ into the Taylor series in the vicinity of the array center $z = z_0$ and take into account the fact that, according to Eq. (10), $\phi''_m(z) = -\gamma^2\phi_m(z)$ and $\phi'''_m(z) = -\gamma^2\phi'_m(z)$, the expression for the amplitude of the mth mode (Eq. (14)) in the approximation of the third-order correction will have the form

$$c_m(z_0) = \int_{z_1}^{z_2} E(z - z_0) \times \left\{\phi_m(z_0)\left[1 - \frac{\gamma_m^2(z - z_0)^2}{2} - \frac{k_0^2 n_0^2(z - z_0)^3}{3L_n} + \dots\right]\right. \quad (22)$$
$$\left. + \phi'_m(z_0)\left[(z - z_0) - \frac{\gamma_m^2(z - z_0)^3}{6} + \dots\right]\right\} dz.$$

We can preset, for example, a certain form of the distribution of the initial field $E(z)$ and consider in such a way the influence of the correction term due to the inhomogeneity of the oceanic medium. However, it is possible to proceed in a different way without losing the generality. If $\gamma_m l < 1$, the terms of the series (22) decrease rapidly with their number, and we can restrict ourselves to the first terms only. In this case, in order to make valid the condition of smallness of the correction $c_m^{(1)}(z_0)$ (Eq. (16)) relative to $c_m^{(0)}$ (Eq. (15)), it is enough to require the validity of the inequality

$$l^3 \ll 0.61\lambda^2 L_n/n_0^2, \quad (23)$$

which is close to inequality (3). When $\gamma_m l > 1$, the series (22) converges slowly and, in order to use the approximation of smallness of the quantity $c_m^{(1)}(z_0)$, it is necessary for the correction term to be much smaller than its closest neighbor on the left [8]. This requirement leads to the inequality

$$l \ll 3L_n \sin^2\beta_m(z_0)/n_0^2, \quad (24)$$

which differs from condition (2) only by a factor of 1.3. Here, $\beta_m(z_0) = \arcsin[\gamma_m(z_0)/k_0]$ is the grazing angle of the Brillouin ray of the mth mode at the level $z = z_0$. The validity of this inequality guarantees that the correction term will always be smaller than any predominant term of the sequence given by Eq. (22). When $\gamma_m l > 1$, it is necessary in the general case to take into account the terms of higher orders in Eq. (22). However, if the inequalities

$$1 \gg n'(z_0) \gg n''(z_0) \gg n'''(z_0) \gg \dots \quad (25)$$

are satisfied, the inclusion of additional terms in the expansion (22) does not change the estimate given by Eq. (24). Thus, if conditions (23) and (24) are satisfied, the directivity pattern adequately describes the angular distribution of the radiated power in an inhomogeneous waveguide. However, in a locally homogeneous medium these inequalities must be complemented with the condition of smallness of the directivity pattern variations due to the variations of the phase of normal modes over the whole aperture. The restrictions imposed on the array length in this case can be estimated as follows.

Let us expand the exponent $\gamma_m(z)$ of the Fourier transform $E(\gamma_m)$ into the Taylor series in the powers of the distance $\xi = z - z_0$ from the array center by taking into account only the linear term

$$\gamma_m(z) = \gamma_m(z_0) + \frac{d\gamma_m(z_0)}{dz}\xi + 0(\xi^2),$$

where $d\gamma_m(z_0)/dz = k_0 n_0^2/L_n \sin\beta_m(z_0)$. The angular displacement $\delta\beta_m(l)$ of the directivity pattern as a whole, because of the variations of $\gamma_m(z)$ at the aperture, $\delta\gamma_m(l) = \gamma_m(l/2) - \gamma_m(-l/2)$, is estimated as $\delta\beta_m(l) \approx n_0^2/L_n \sin\beta_m(z_0)$. For the field variations to be small, the angular distance must be much smaller than the width of the directivity pattern λ/l, $\delta\beta_m(l) \ll \lambda/l$. Finally, we obtain

$$l^2 \ll \lambda L_n \sin\beta_m(z_0)/n_0^2. \quad (26)$$

Table

Correspondence table

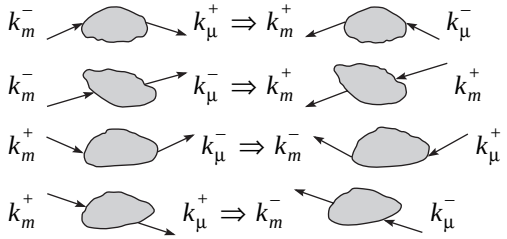	$F(k_m^-, k_\mu^+) \Rightarrow F(k_\mu^-, k_m^+)$
	$F(k_m^-, k_\mu^-) \Rightarrow F(k_\mu^+, k_m^+)$
	$F(k_m^+, k_\mu^-) \Rightarrow F(k_\mu^+, k_m^-)$
	$F(k_m^+, k_\mu^+) \Rightarrow F(k_\mu^+, k_m^-)$

Inequality (26), which plays the role of the condition of the far wave field of the array in a layered inhomogeneous medium (see Eq. (5)), coincides with condition (1).

Thus, the restrictions expressed by inequalities (1)–(3) and obtained earlier within the framework of the ray theory are of a diffractive on nature. This result is evident, because, in solving the differential equation (6), it was assumed that Eq. (25) is valid, which is in fact the condition of applicability of the WKB asymptotics of eigenfunctions in the vicinity of the array center in an inhomogeneous medium.

Now let us consider the scattering matrix of waveguide modes. We assume that the following conditions are satisfied:

(i) The effects of multiple scattering are small, i.e., we can ignore the fields that are scattered by a body after their reflection from the waveguide walls. As the analysis of numerical calculations [9] and the analytical estimates [10] show, the condition of smallness of repeatedly scattered fields is satisfied for bodies located at distances greater than their equivalent radii from the waveguide boundaries. In this case, the intensity of multiply scattered fields does not exceed 10% of the total energy of the perturbed field. For example, in the case of a reflecting sphere, the equivalent radius coincides with the radius of a large circle, and, in the case of a spheroid extended in the horizontal plane, it is the minimal radius of a circle circumscribed around the spheroid in the direction of the wave incidence.

(ii) Normal modes are quasi-plane within the vertical dimension of the scatterer, which means that inequalities (1)–(3) or (23), (24), and (26) are satisfied.

According to [3], the expression for the scattering matrix of waveguide modes, $S_{\mu m}$, in the framework of these approximations has the form

$$\begin{aligned} S_{\mu m} = \frac{1}{4\sin\varphi_m \sin\varphi_\mu}\{ & F(\mathbf{k}_m^+, \mathbf{k}_\mu^+)\exp[i(\varphi_m - \varphi_\mu)] \\ & + F(\mathbf{k}_m^-, \mathbf{k}_\mu^-)\exp[i(\varphi_\mu - \varphi_m)] \\ & - F(\mathbf{k}_m^+, \mathbf{k}_\mu^-)\exp[i(\varphi_m + \varphi_\mu)] \\ & - F(\mathbf{k}_m^-, \mathbf{k}_\mu^+)\exp[-i(\varphi_m + \varphi_\mu)]\}, \end{aligned} \quad (27)$$

where

$$\varphi_m(z_0) = \int_{z_0}^{\bar{z}_m} \gamma_m(z')dz' + \delta_m.$$

Here, $\mathbf{k}_m^\pm = (h_m \pm \gamma_m)$ are the local wave vectors of the Brillouin ray with the horizontal h_m and vertical γ_m components corresponding to the mth mode; $\bar{z}_m$ is the turning point that can lie at the waveguide boundary; δ_m is the caustic phase shift; z_0 is the depth of the scatterer center; $F(\mathbf{k}_m^\pm, \mathbf{k}_\mu^\pm)$ is the scattering amplitude in a homogeneous medium, which describes the amplitude and phase of a scattered wave in the far wave field in the $\mathbf{k}_\mu^\pm$ direction on condition that a plane wave propagating in the $\mathbf{k}_m^\pm$ direction is incident on the body. Equation (27) for the scattering matrix is modified to some extent for convenience, as compared to the initial expression [3]. The scattering matrix in the new formulation, as well as the scattering amplitude, is measured in meters, which is more adequate in terms of the physical meaning. As one can see, Eq. (27) is symmetric with respect to the interchange of indices, $S_{\mu m} = S_{m\mu}$, which agrees with the reciprocity theorem for waveguides [11]. Examining the reciprocity properties, one has to take into account the equality

$$F(\mathbf{k}_m^\alpha, \mathbf{k}_\mu^\beta) = F(\mathbf{k}_\mu^{-\beta}, \mathbf{k}_m^{-\alpha}),$$

where the indices α and β can take the values +1 and –1. All four possible combinations of indices are shown in the table. Thus, the matrix S' transposed with respect to the scattering matrix S is equal to the matrix S, $S' = S$. In the case of an isotropic scattering ($F(\mathbf{k}_m^\pm, \mathbf{k}_\mu^\pm) = F_0 = \text{const}$), the value of $S_{\mu m}$ is equal to the scattering amplitude F_0, $S_{\mu m} = F_0$, as it should be expected.

Equation (27) is obtained using the WKB asymptotics of eigenfunctions in the vicinity of the scatterer position [3], which is inconvenient for numerical calculations. It is desirable that any code developed for calculating the sound field in a waveguide on the basis of the mode approach (i.e., calculating the eigenfunctions

and eigenvalues of the Sturm–Liouville problem for an unperturbed waveguide) could be included as a part into a code for calculating the sound diffraction by bodies in a waveguide. For this purpose, it is necessary to recast Eq. (27) for the scattering matrix S in such a way that it contain only the necessary quantities. This can be performed in various ways. One of the methods based on solving the Schrödinger equation is given in [12]. Another method is described below.

As it was demonstrated earlier, the restrictions for the vertical dimension of an array (a body), at which the use of a directivity pattern (a scattering amplitude) is possible in the problems on the waveguide propagation and which are obtained in the WKB approximation (inequalities (1)–(3)) and on the basis of the solution of the Sturm–Liouville problem (inequalities (23), (24), and (26)) are equivalent. From the results obtained above, it follows that it is possible to proceed from the ray representation of S-matrix to the mode representation, if in Eq. (27) we formally change from the WKB asymptotics of the eigenfunctions to their mode representation. According to [6], in the WKB approximation the eigenfunctions $\psi_m(z)$ are determined by the relation

$$\psi_m(z) = \sin\varphi_m(z)/\sqrt{s_m(z)N_m}, \tag{28}$$

where

$$s_m(z) = \gamma_m(z)/k_0 = \sqrt{(k_0^2 n^2(z) - h_m^2)/k_0},$$

$$N_m = \int_{-H}^{0} s_m^{-1}(z)\sin^2\varphi_m(z)dz.$$

Here, H is the waveguide depth. Now, if we ignore the weak dependence $s_m(z)$ as compared to $\sin\varphi_m(z)$, which is quite admissible, Eq. (27) can be represented in the form

$$\begin{aligned} S_{\mu m}(z_0) &= p_m^+ p_\mu^+ F(\mathbf{k}_m^+, \mathbf{k}_\mu^-) + p_m^- p_\mu^- F(\mathbf{k}_m^-, \mathbf{k}_\mu^+) \\ &+ p_m^+ p_\mu^- F(\mathbf{k}_m^+, \mathbf{k}_\mu^+) + p_m^- p_\mu^+ F(\mathbf{k}_m^-, \mathbf{k}_\mu^-), \end{aligned} \tag{29}$$

where

$$p_{m,\mu}^{\pm}(z_0) = \frac{1}{2} \pm \frac{\psi'_{m,\mu}(z_0)}{2i\gamma_{m,\mu}(z_0)\psi_{m,\mu}(z_0)}.$$

This result coincides with the modified expression for the scattering matrix S obtained in [12]. If a symmetry of the scattering amplitude takes place (e.g., in the case of a body of revolution),

$$F(\mathbf{k}_m^+, \mathbf{k}_\mu^+) = F(\mathbf{k}_m^-, \mathbf{k}_\mu^-), \quad F(\mathbf{k}_m^+, \mathbf{k}_\mu^-) = F(\mathbf{k}_m^-, \mathbf{k}_\mu^+),$$

we can reduce Eq. (29) to the form

$$S_{\mu m}(z_0) = P_{\mu m}^+ F(\mathbf{k}_m^+, \mathbf{k}_\mu^+) + P_{\mu m}^- F(\mathbf{k}_m^+, \mathbf{k}_\mu^-),$$

where

$$P_{\mu m}^{\pm}(z_0) = \frac{1}{2} \pm \frac{\psi'_m(z_0)\psi'_\mu(z_0)}{2\gamma_m(z_0)\gamma_\mu(z_0)\psi_m(z_0)\psi_\mu(z_0)}.$$

Thus, the coefficients $p_{m,\mu}^{\pm}$ or $P_{\mu m}^{\pm}$ determining the scattering matrix are formulated directly for the quantities to be calculated, such as the eigenfunctions, their derivatives, and the eigenvalues. This allows one to match the codes for numerical calculation of the wave fields and diffraction by bodies in a waveguide. However, it is necessary to keep in mind that, within the framework of the considered approach [3], Eqs. (27) and (29) are equivalent and differ only in notation. This is caused by the fact that the representation of the S-matrix with the help of the scattering amplitude is one of the necessary conditions of applicability of the WKB asymptotics of eigenfunctions in the vicinity of the scatterer. Therefore, if a body is located in the region of shadow of the incident or (and) scattered modes, such modes are excluded from consideration.

Thus, the applicability conditions for the concept of a locally homogeneous medium in the problems of waveguide propagation are obtained on the basis of the solution of the Sturm–Liouville problem. It is demonstrated that they are close to the analogous conditions obtained earlier in the WKB approximation. Depending on the character of the inhomogeneity variation in the water medium, the sound wavelength, and the mode number, these conditions impose certain restrictions upon the thickness of the water layer within which the normal modes can be considered as quasi-plane. It is convenient to analyze the wave pattern of the field with the help of these conditions, because a directivity pattern (a scattering amplitude) is an adequate characteristic of radiation (scattering) within such a quasi-homogeneous layer.

A new formulation for the scattering matrix of waveguide modes, which contains only the quantities (and their derivatives) calculated by solving the Schrödinger equation, is proposed. It provides an opportunity not only to adequately calculate the mode components of the scattered fields, but also to use the results of numerous studies of the diffraction by bodies in a free space.

ACKNOWLEDGMENTS

This work was supported by the Russian Foundation for Basic Research, project no. 99-02-17671.

REFERENCES

1. Yu. A. Kravtsov and V. M. Kuz'kin, Akust. Zh. **33** (1), 49 (1987) [Sov. Phys. Acoust. **33** (1), 28 (1987)].
2. V. M. Kuz'kin and T. A. Frolova, Akust. Zh. **34**, 891 (1988) [Sov. Phys. Acoust. **34**, 515 (1988)].
3. Yu. A. Kravtsov, V. M. Kuz'kin, and V. G. Petnikov, Akust. Zh. **30**, 339 (1984) [Sov. Phys. Acoust. **30**, 199 (1984)].

4. Yu. A. Kravtsov and V. M. Kuz'kin, Akust. Zh. **33**, 49 (1987) [Sov. Phys. Acoust. **33**, 28 (1987)].
5. Yu. A. Kravtsov and Yu. I. Orlov, *Geometric Optics of Inhomogeneous Media* (Nauka, Moscow, 1980).
6. D. S. Ahluwalia and J. B. Keller, in *Wave Propagation and Underwater Acoustics*, Ed. by J. B. Keller and J. S. Papadakis (Springer, New York, 1977; Mir, Moscow, 1980).
7. V. A. Zverev, *Radiooptics* (Sov. Radio, Moscow, 1975).
8. F. W. J. Olver, *Asymptotics and Special Functions* (Academic, New York, 1974; Nauka, Moscow, 1990).
9. V. V. Varadan and V. K. Varadan, J. Acoust. Soc. Am. **70**, 213 (1981).
10. N. K. Uzunoglu and J. G. Fikioris, J. Acoust. Soc. Am. **72**, 628 (1982).
11. Young-Chung Cho, J. Acoust. Soc. Am. **67**, 1421 (1980).
12. V. A. Grigoriev, B. G. Katsnelson, V. M. Kuz'kin, and V. G. Petnikov, Phys. Vibr. **7** (3), 185 (1999).

Translated by M. Lyamshev

Acoustical Physics, Vol. 47, No. 5, 2001, pp. 598–606. Translated from Akusticheskiĭ Zhurnal, Vol. 47, No. 5, 2001, pp. 685–693.

A Nonlinear Granular Medium with Particle Rotation: A One-Dimensional Model

S. A. Lisina*, A. I. Potapov*, and V. F. Nesterenko**

**Blagonravov Institute of Mechanical Engineering, Nizhni Novgorod Branch, Russian Academy of Sciences, ul. Belinskogo 85, Nizhni Novgorod, 603024 Russia*

e-mail: apotapov@sandy.ru

***University of California, San Diego, Dept. of AMES UCSD, La Jolla 92093-0411, USA*

Received October 19, 2000

Abstract—Equations of nonlinear acoustics are derived from the micromechanical representation of a granular medium as a system of elastically interacting particles possessing translational and rotational degrees of freedom. The structure of the equations is invariant with respect to the shape and size of the particles. The changes in the latter affect only the coefficients in the equations. The inclusion of microrotations and moment interactions of particles leads to the formation of a new type of waves in the medium—microrotational waves. Their dispersion properties are similar to those of spin waves propagating in a magnetoelastic medium. In the low-frequency approximation, the microrotational waves disappear, and the equation describing the transverse waves acquires a term with quadratic nonlinearity. The latter provides an explanation for the generation of the second shear harmonic that is observed in real solids contrary to the predictions of the nonlinear theory of elasticity, which prohibits such phenomena. © *2001 MAIK "Nauka/Interperiodica"*.

INTRODUCTION

In recent years, the micromechanics of granular media has been rapidly developed in connection with the numerous technological applications of composite and polymer materials [1–4]. The structure of the medium and, specifically, the grain size is one of the most important characteristics of the material quality that immediately affects the strength and the viscoelastic properties of the material [5–7]. In many cases, the dynamic behavior of such media at high rates of deformation cannot be explained in terms of the classical mechanics of deformed solids. Therefore, new approaches have been proposed for the development of the theories to describe granular and structure-sensitive materials with allowance for the discrete medium structure, the additional internal degrees of freedom, and the nonlocal and nonlinear character of particle interactions [6–12].

The continuum theory proceeds from the assumption that a continuous medium can be represented as a system of material particles. However, the relation between the continuous models and a system of material particles is still not fully understood. In the classical limit, which originates from the works of O. Cauchy, a material particle is represented as a material point. However, this representation does not always fit the reality. The classical model contains no spatial scales, and, therefore, it cannot describe the effects related to the dispersion of elastic waves. In this model, the only internal interactions are the forces of the contact character. A real material usually has a hierarchically organized complex structure, which evolves in different ways under external actions. For an adequate description of the dynamic processes in a structurally inhomogeneous material, it is necessary to consider at least the micro-, meso-, and macrostructural levels, which continuously interact with each other due to the internal constraints [1, 3, 4]. At the microstructural level, the deformation of individual fragments of the structure is considered. At the mesostructural level, the presence of structural formations such as grains, domains, and blocks is taken into account and the dynamic behavior of the medium is described with allowance for their force and moment interactions. At the macrostructural level, the properties of the medium are "homogenized."

The mechanical properties of a granular medium, like ground or ceramic material, depend on the geometry of microparticles, their arrangement, and the interaction forces acting between them. In the mathematical modeling of such media, one of the main problems is the derivation of the equations of motion and equations of state that can adequately describe the discrete character of the medium. In this connection, a series of studies were performed to describe the dynamic behavior of granular media with regular and random packings without taking into account the rotation of particles [10, 12–16]. The models of granular media that included particle rotation were considered in [6–9, 17, 18]. In the general case, the field of displacements and the field of microrotations are related to each other. If this relation

is determined by the dynamic equations of the field theory, the corresponding model is called a micropolar model [2, 3, 7, 11], and its structure is close to the Cosserat micropolar continuum.

Discrete and continuous variable systems are related to each other by the Taylor expansions that establish the correspondence between the functions given at discrete points and their power-series approximations. When the number of the expansion terms is sufficiently large, a continuum can reflect the properties of a discrete system with an accuracy sufficient for practical applications. Such are the so-called weakly-nonlocal (gradient or moment) models [2, 5, 8, 12]. The classical theory operates with the continuous-medium models in which the expression for the internal energy involves only the first-order gradients of the displacement field. If the internal energy depends on the second-order or higher-order gradients, one obtains the gradient models of the second order, fourth order, etc. [5, 8]. The presence of higher gradients in a mathematical model means that scales with the length dimension occur in the medium. A theoretical description of a medium with internal structure can be based on the following types of models: a complex crystal lattice [5, 11, 18], a continuum of solid particles–bodies [6–8], a generalization of the latter to a continuum consisting of deformed particles [3, 15–17], or statistical models of microinhomogeneous media [19]. Each of the aforementioned approaches has its own advantages and disadvantages.

In this paper, which is an extended version of our earlier publication [18], the granular material is considered as a set of particles interacting with each other through elastic contacts [6, 7]. The rigidity of the particles far exceeds that of the contacts, and the particles can be considered as perfectly rigid bodies separated by elastic layers through which the force and moment actions are transmitted. The motion of each particle consists of the displacements of its center of mass and rotations about the center of mass. Hence, in the general case, a particle has six degrees of freedom: three translational and three angular. In the case of two-dimensional motions, the number of degrees of freedom is reduced to three: two translational and one angular. When the particles move relative to each other, forces transmitted through the contacts act along both the normal and the tangent to the contact plane. These forces can be modeled by elastic springs transmitting the forces and the moments.

The analysis of the theoretical and experimental studies carried out in this field of research shows that, despite the variety of theories developed for describing complexly structured media, there is a need for new models to describe the dynamic behavior of granular media. These models must satisfy the following conditions:

(i) They must use minimal generalizations that lead to new qualitative consequences. The number of new parameters included in a model must be as small as possible.

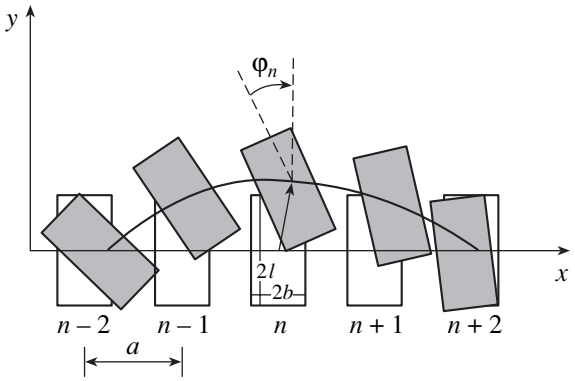

Fig. 1. Functional diagram of a granular medium.

(ii) The relation between the parameters of a micromodel and the basic physical-mechanical characteristics of the medium (such as density, porosity, elastic moduli, etc.) should be clearly defined.

(iii) In the limiting cases, a new model should as a rule pass into the known classical theories of solids.

Below, we discuss a one-dimensional model of a granular medium that satisfies the aforementioned requirements.

DISCRETE MODEL

We consider a one-dimensional chain formed by rectangular grains with the dimensions $2l \times 2b$. In the initial state, the distance between the centers of mass of the particles is equal to a ($a > 2b$). Each particle has three degrees of freedom: displacements of the center of mass of a particle along the x and y axes (the translational degrees of freedom u_n and w_n) and rotation about the center of mass (the rotational degree of freedom φ_n) (Figs. 1, 2).

The central springs have a rigidity k_0, and the upper and lower horizontal springs have a rigidity $k_1/2$. Together, they determine the force interactions in the material under compression and tension, and the springs $k_1/2$ provide the transfer of moments in the case of the particle rotations. The diagonal springs with a rigidity $k_2/2$ characterize the force interactions of particles in the case of shear deformations of the material (Fig. 2). The elongations of the springs D_j are determined by the relative variations of the distances between the corresponding points of the bodies–particles:

$$\begin{aligned} D_0 &= a^{-1}\sqrt{(x_{n+1}-x_n)^2 + (y_{n+1}-y_n)^2} - 1, \\ D_1 &= \delta^{-1}\sqrt{(x_D-x_A)^2 + (y_D-y_A)^2} - 1, \\ D_2 &= \delta^{-1}\sqrt{(x_C-x_B)^2 + (y_C-y_B)^2} - 1, \\ D_3 &= \delta_1^{-1}\sqrt{(x_D-x_B)^2 + (y_D-y_B)^2} - 1, \\ D_4 &= \delta_1^{-1}\sqrt{(x_C-x_A)^2 + (y_C-y_A)^2} - 1, \end{aligned} \qquad (1)$$

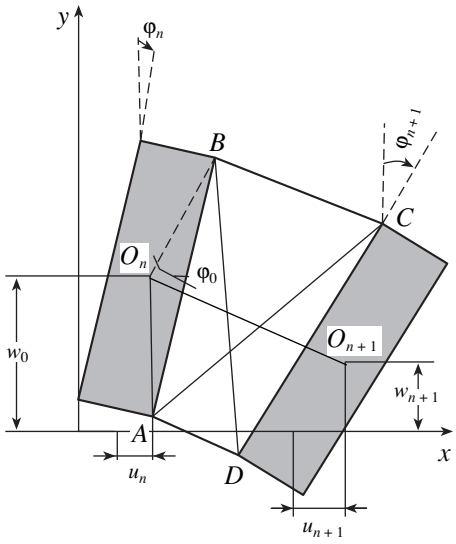

Fig. 2. Schematic representation of the force interaction of particles.

where $\delta = a - 2b$ is the gap between the particles, which is equal to the initial length of the horizontal springs; $\delta_1 = \sqrt{\delta^2 + 4l^2}$ is the initial length of the diagonal springs; and the coordinates of the points *A*, *B*, *C*, and *D* are determined through the displacements and rotations of the particles:

$$\begin{gathered} x_{on} = na + u_n, \quad x_{on+1} = (n+1)a + u_{n+1}, \\ y_{on} = w_n, \quad y_{on+1} = w_{n+1}, \\ x_B = u_n + d\sin(\varphi_n + \varphi_0) = x_A + 2l\sin\varphi_n, \\ y_B = w_n + d\cos(\varphi_n + \varphi_0) = y_A + 2l\cos\varphi_n, \\ x_C = u_{n+1} + d\sin(\varphi_{n+1} - \varphi_0) + a = x_D + 2l\sin\varphi_{n+1}, \\ y_C = w_{n+1} + d\cos(\varphi_{n+1} - \varphi_0) = y_D + 2l\cos\varphi_{n+1}. \end{gathered} \tag{2}$$

Here, $d = \sqrt{b^2 + l^2}$ is the characteristic size of a particle, which is equal to half of the length of its diagonal, and the parameter $l/b = \tan\varphi_0$ characterizes the shape of the particle (the ratio of its dimensions in two orthogonal directions).

Substituting Eqs. (2) in Eqs. (1) and expanding the radicals into power series in the small quantities $\Delta u_n = (u_{n+1} - u_n)/a \sim \Delta w_n = (w_{n+1} - w_n)/a \sim \varepsilon \ll 1$ and $\Phi_n = (\varphi_{n+1} + \varphi_n)/2 \ll \pi/2$, we obtain approximate expressions for the elongations:

$$D_0 = \left[\Delta u_n + \frac{1}{2}\Delta u_n^2 + \frac{1}{2}\Delta w_n^2\right],$$

$$D_1 = (a/\delta)\left[\Delta u_n - l\Delta\varphi_n + \frac{1}{2}\Delta u_n^2 + \frac{1}{2}\Delta w_n^2 + \frac{b}{\delta}\Delta w_n\Phi_n\right],$$

$$D_2 = (a/\delta)\left[\Delta u_n + l\Delta\varphi_n + \frac{1}{2}\Delta u_n^2 + \frac{1}{2}\Delta w_n^2 + \frac{b}{\delta}\Delta w_n\Phi_n\right],$$

$$\begin{aligned} D_3 = (a/\delta_1)\Bigg[&\frac{\delta}{\delta_1}\left(\Delta u_n - \frac{l}{a}\Phi_n\right) - \frac{2l}{\delta_1}\left(\Delta w_n + \frac{b}{a}\Phi_n\right) \\ &+ \frac{b}{\delta_1}\left(\Delta w_n\Phi_n + \frac{l}{b}\Delta u_n\Phi_n\right)\Bigg], \end{aligned} \tag{3}$$

$$\begin{aligned} D_4 = (a/\delta_1)\Bigg[&\frac{\delta}{\delta_1}\left(\Delta u_n + \frac{l}{a}\Phi_n\right) + \frac{2l}{\delta_1}\left(\Delta w_n + \frac{b}{a}\Phi_n\right) \\ &- \frac{b}{\delta_1}\left(\Delta w_n\Phi_n + \frac{l}{b}\Delta u_n\Phi_n\right)\Bigg]. \end{aligned}$$

Here, we retained only the linear and the principal quadratic terms for the spring elongations.

The potential energy associated with the deformation of the springs lying to the right of the particle *n* is determined by the formula

$$U_n = \frac{k_0}{2}(D_0^2 + \gamma D_0^3) + \frac{k_1}{2}(D_1^2 + D_2^2) + \frac{k_2}{2}(D_3^2 + D_4^2). \tag{4}$$

In choosing the form of the function U_n, we assumed that the major force is applied to the central springs connecting the centers of mass of the particles, and, therefore, in the expression for the energy of the central springs, we retained the cubic term γD_0^3. The horizontal springs (k_1) and the diagonal springs (k_2) are responsible for the relatively weak moment interactions of particles, which are related to rotations, and their energy is represented by only the quadratic terms. Then, correct to cubic terms, the expression for the potential energy per unit cell of the structure under study has the form

$$\begin{aligned} U_n = \frac{1}{2}\Bigg(&K_1\Delta u_n^2 + K_2\Delta w_n^2 + K_3 l^2\Delta\varphi_n^2 + \frac{K_2}{4}\Phi_n^2 \\ &+ K_2\Delta w_n\Phi_n\Bigg) + h_1\Delta u_n^3 + h_2\Delta u_n\Delta w_n^2 \\ &+ h_3\Delta u_n\Delta w_n\Phi_n + h_4\Delta w_n^2\Phi_n. \end{aligned} \tag{5}$$

Here, the first two terms describe the energy related to the longitudinal and shear deformations, the third and fourth terms describe the energy related to the noncentral (moment) interactions of particles, and the fifth term describes the coupling energy of the transverse and rotational degrees of freedom of the particles. The remaining terms with the coefficients h_n (n = 1–4) describe the energy of nonlinear interactions. We note that, owing to the symmetry of the system, Eq. (5) contains no cubic term proportional to $\Delta u_n^2\Phi_n$. The coefficients responsible for the linear effects are expressed

through the parameters of the micromodel and the elastic constants of the springs:

$$K_1 = k_0 + 2\frac{a^2}{\delta^2}k_1 + 2\frac{a^2\delta^2}{\delta_1^4}k_2 = k_0 + \frac{l^2}{4\delta^2}K_2 + K_3,$$
$$K_2 = 8\frac{a^2l^2}{\delta_1^4}k_2, \quad K_3 = 2\frac{a^2}{\delta^2}k_1. \tag{6}$$

The coefficients responsible for the nonlinear interactions have the form

$$h_1 = \frac{(1+\gamma)}{2}k_0 + \frac{a^2}{\delta^2}k_1 = \frac{1+\gamma}{2}k_0 + \frac{K_3}{2},$$
$$h_2 = \frac{1}{2}k_0 + \frac{a^2}{\delta^2}k_1 = \frac{k_0}{2} + K_3,$$
$$h_3 = 2a^2\left(\frac{b}{\delta^3}k_1 - 4\frac{l^2}{\delta_1^4}k_2\right) = \frac{b}{\delta}K_3 - K_2, \tag{7}$$
$$h_4 = 8\frac{a^2lb}{\delta_1^4}k_2 = \frac{b}{l}K_2.$$

It should be noted that, in the approximation under study, the nonlinear interaction constants h_3 and h_4 are of a "geometric" nature and originate from the presence of noncentral (moment) interactions of particles in the granular medium. The same interactions give rise to the corrections proportional to K_3 to the nonlinear constants h_1 and h_2 of the classical theory of elasticity. The shape of the microparticles strongly affects the values of the nonlinear interaction constants h_3 and h_4. For example, when the width of a particle decreases ($b \longrightarrow 0$) while $l \neq 0$, the constant h_4 tends to zero and the constant h_3 changes sign. If the particles are material points ($b = 0$ and $l = 0$), the elastic constants K_2, h_3, and h_4 are equal to zero.

The differential-difference equations describing the nonlinear dynamic processes in the system under consideration can be derived from the Hamilton variational principle using the Lagrange function $L = \sum(T_n - U_n)$, where T_n is the kinetic energy per unit cell of the chain:

$$T_n = \frac{m}{2}(\dot{u}_n^2 + \dot{w}_n^2) + \frac{J}{2}\dot{\varphi}_n^2.$$

Here, m is the grain mass and $J = m(l^2 + b^2)/3 = md^2/3$ is the grain moment of inertia about the axis passing through the center of mass. The point above a symbol denotes the derivative with respect to time. The differential-difference equations, which are not presented here because of their rather cumbersome explicit form, are convenient for a numerical simulation of the response of the system to external dynamic actions. In addition, on the basis of these equations, it is possible to construct the hierarchy of the quasi-continuous models of a granular medium.

CONTINUOUS MODEL OF A GRANULAR MEDIUM

In a typical case, the characteristic spatial scale of deformation (e.g., the elastic wavelength λ) is much greater than the chain period ($\lambda \gg a$). In this case, it is possible to change from the discrete variable j, which determines the cell number, to a continuous spatial variable $x = ja$, and the functions determined at discrete points can be interpolated by continuous expressions. The conditions of a one-to-one correspondence between the functions of the discrete argument and the continuous analytical functions, as applied to the theory of media with microstructure, are considered in detail in [2, 5].

If we consider the expansion up to the terms of the order of $O(a^2)$, the linear density of the Lagrange function L takes the form

$$L = \frac{\rho}{2}(u_t^2 + w_t^2 + r^2\varphi_t^2)$$
$$-\frac{1}{2a}\left(K_1u_x^2 + K_2w_x^2 + l^2K_3^*\varphi_x^2 + \frac{K_2}{4}\varphi^2 + K_2w_x\varphi\right) \tag{10}$$
$$-\frac{1}{a}(h_1u_x^3 + h_2u_xw_x^2 + h_3u_xw_x\varphi + h_4w_x^2\varphi).$$

Here, $\rho = m/a$ is the effective linear density of the granular medium, $r = \sqrt{J/m} = d/\sqrt{3}$ is the radius of inertia of the particles of the medium with respect to the center of mass, d is the length of the particle diagonal, and $K_3^* = K_3 + (a^2/16l^2)K_2$. From the Lagrangian (10), we easily derive a system of differential equations, which describe the interaction of different types of waves in a granular medium:

$$u_{tt} - c_1^2u_{xx} = \frac{\partial}{\partial x}[\alpha_1u_x^2 + \alpha_2w_x^2 + \alpha_3w_x\varphi_x],$$
$$w_{tt} - c_2^2w_{xx} - \beta^2\varphi_x = \frac{\partial}{\partial x}[\alpha_2u_xw_x - (\alpha_3u_x - \alpha_4w_x)\varphi],$$
$$\varphi_{tt} - c_3^2\varphi_{xx} + \omega_0^2\varphi + (\beta/r)^2w_x \tag{11}$$
$$= (\alpha_3/r^2)w_xu_x - (\alpha_4/r^2)w_x^2.$$

The physical meaning of the constants involved in these equations is as follows:

$$c_1 = \sqrt{K_1/\rho a} = \sqrt{\frac{1}{m}\left(k_0 + \frac{2a^2}{\delta^2}k_1 + \frac{2\delta^2a^2}{\delta_1^4}k_2\right)} \tag{12}$$

is the propagation velocity of longitudinal waves,

$$c_2 = \sqrt{K_2/\rho a} = 2\frac{al}{\delta_1^2}\sqrt{\frac{k_2}{m}} \quad (13)$$

is the propagation velocity of shear waves,

$$c_3 = (l/r)\sqrt{K_3^*/\rho a} = \frac{la}{r\delta}\sqrt{\frac{2}{m}\left(k_1 + \frac{a^2\delta^2}{4\delta_1^2}k_2\right)} \quad (14)$$

is the propagation velocity of particle microrotation waves (the spin waves), $\omega_0 = \sqrt{K_2/4a\rho r^2} = c_2/2r$ is the critical frequency of a spin wave, and $\beta = c_2$ is the linear coupling parameter of the transverse and spin waves.

From the equations derived above, one can see that the shear and rotational waves interact with each other already in the linear approximation, and the longitudinal waves are coupled with them by only the nonlinear effects. The nonlinear coupling of waves is also asymmetric. The nonlinear coupling coefficients have the form $\alpha_i = h_i/\rho a$ (i = 1–4). In a granular medium, in addition to the known second-order (K_1 and K_2) and third-order (h_1 and h_2) elastic constants, we have three new constants: one second-order constant K_3^* and two third-order constants h_3 and h_4, which are absent in the classical theory of nonlinear elastic media.

EFFECT OF MICROSTRUCTURE ON THE ACOUSTIC CHARACTERISTICS OF A MEDIUM

A granular material can be considered as a continuous medium consisting of two components (or phases) [20]. One component is represented by rigid particles of mass m and inertia J, and the other component is the porous space between the particles. In the model under consideration, the porous space is a massless nonlinear elastic medium through which the force and moment actions are transferred. To reveal the relation between the microscopic and macroscopic properties of a granular medium, we analyze the dependence of the velocities of acoustic waves on the parameters of the micromodel (microstructure). The structure of a granular medium is characterized by the distance between the particle centers a (the chain period) and by the geometric dimensions of the particles, b and l. However, these quantities are not always convenient for consideration. To correlate the theoretical calculations with the experimental data, it is more convenient to use the dimensionless parameters characterizing the shape of the particles $f = l/b$ and the volume porosity of the medium q, which is determined as the ratio of the cavity volume to the representative volume of the medium:

$$q = \frac{\delta}{a} = \left(1 - \frac{2b}{a}\right). \quad (15)$$

The porosity of the medium under consideration varies from zero to unity and coincides with the porosity parameter of a two-phase medium [20]. From Eq. (15), it follows that the quantities q, f, and the characteristic grain size d are related to each other by the formula:

$$q = 1 - \frac{2d}{a(1 + f^2)^{1/2}}. \quad (16)$$

From this expression, one can see that, as the grain size increases, the porosity of the medium decreases and can even become zero, which is physically incorrect. This result is related to the adopted rectangular shape of the particles and their ordered orientation. For another particle shape, relation (16) can be different.

The effective line density of the medium ρ, which is determined as the mass of the substance per unit length of the chain $\rho = m/a$, is related to the porosity and the line density of the grains $\rho_1 = m/2b$ by the relation $\rho = (1 - q)\rho_1$. In terms of these parameters, expressions (12)–(14) for the velocities of elastic waves in a granular medium have the form:

$$c_1 = c_{10}\sqrt{1 + \frac{2}{q^2}\left(\frac{k_1}{k_0}\right) + \frac{2q^2}{[q^2 + f^2(1-q)^2]^2}\frac{k_2}{k_0}}, \quad (17)$$

$$c_2 = 2r\omega_0 = \frac{c_{20}f(1-q)}{[q^2 + f^2(1-q)^2]^2}, \quad (18)$$

$$c_3 = \frac{c_{20}f}{q}\sqrt{\frac{4}{1 + f^2}\left(\frac{k_1}{k_2} + \frac{q^2}{4[q^2 + f^2(1-q)^2]^2}\right)}. \quad (19)$$

Here, $c_{10} = \sqrt{k_0/\rho a}$ and $c_{20} = \sqrt{k_2/\rho a}$ are the longitudinal and transverse wave velocities, respectively, in the absence of moment interactions between the particles of the medium, i.e., when $q = 0$ and $f = 0$.

The graphical analysis of the dependences of the acoustic wave velocities c_1, c_2, and c_3 on the porosity of the medium q and the shape parameter f is shown in Figs. 3–6. The values of the coefficients k_1 and k_2 in Eqs. (17)–(19) are chosen in an arbitrary way for a qualitative study of the properties of the model.

Figure 3 presents the relative value of the longitudinal wave velocity c_1/c_{10} as a function of q and f for $k_1/k_0 = k_2/k_0 = 0.3$. One can see that, as the porosity increases, the longitudinal wave velocity monotonically decreases and tends to a limiting value, which depends on the force constants k_1 and k_2. Since, at a fixed shape parameter f, the porosity of the medium q and the characteristic grain size d are linearly related by Eq. (16), one can use this plot to qualitatively estimate the dependence of the longitudinal wave velocity on grain size. As the shape parameter f increases (when $f < 1$, the particles are elongated in the direction of the x axis, and when $f > 1$, they are elongated along the

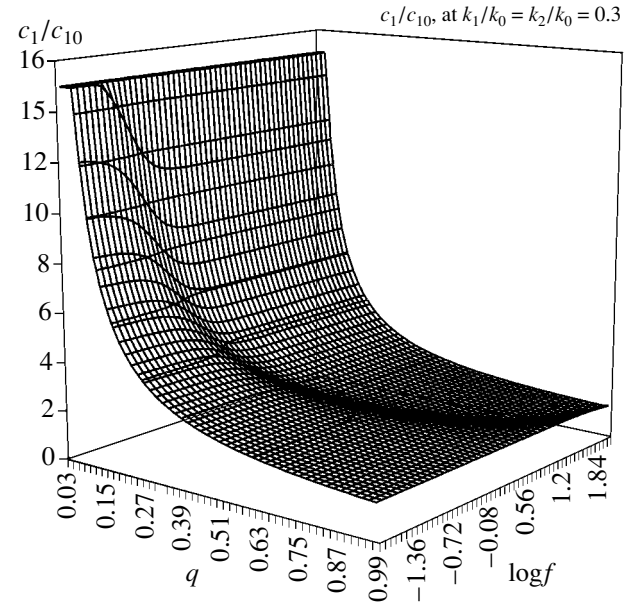

Fig. 3. Dependence of the longitudinal wave velocity on the porosity parameter of the medium and on the particle shape for the force constants $k_1 = k_2 = 0.3k_0$.

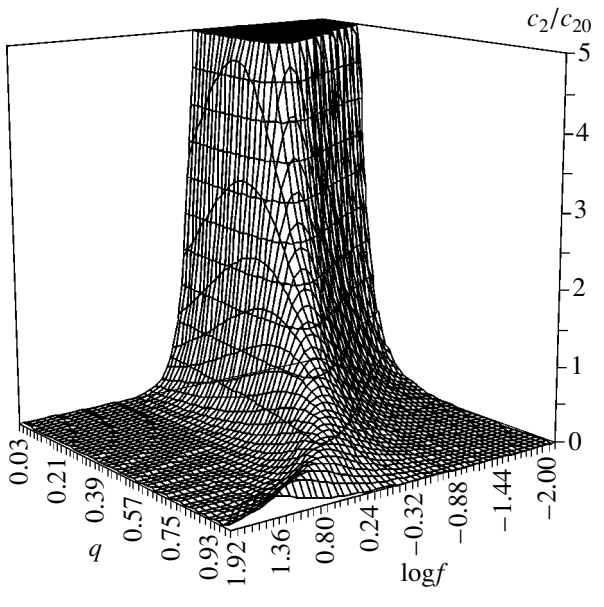

Fig. 4. Same as in Fig. 3 for the relative velocity of a shear wave.

y axis), the longitudinal wave velocity decreases. Simultaneously, the region of the transition from higher values of c_1/c_{10} to lower ones with increasing porosity is shifted to the right.

Figure 4 presents the behavior of the relative value of the shear wave velocity c_2/c_{20}. One can see that this behavior is of a "resonance" character, i.e., the dependences $c_2(q, f = \text{const})$ and $c_2(f, q = \text{const})$ reach their maximums and then decrease practically down to zero.[1] The plot also reveals the changes in the critical frequency of the rotational wave ω_0, because it is related to the quantity c_2 by a simple algebraic dependence given by Eq. (18).

Figure 5 presents the relative velocity of rotational waves c_3/c_{20} at equal values of the force constants $k_1 = k_2$ responsible for the moment interaction. One can see that c_3 monotonically decreases with the increasing porosity of the material q, and, for $q > 0.5$, it flattens out at a constant value, which depends on the particle shape. At low porosity values $q < 0.15$, the dependence $c_3(f, q = \text{const})$ exhibits a local maximum and a local minimum in the region where the shape of the particles is close to square (i.e., when $f \approx 1$).

Figure 6 shows the ratio of the shear wave velocity to the longitudinal wave velocity c_2/c_1 as a function of the porosity of the medium and the particle shape. The behavior of this quantity is also of a "resonance" character. It should be noted that, at some values of q and f, the ratio c_2/c_1 can be higher than unity. However, from experience it is well known that, in any material, the shear wave velocity never exceeds the longitudinal wave velocity. Hence, presumably, the ratio between

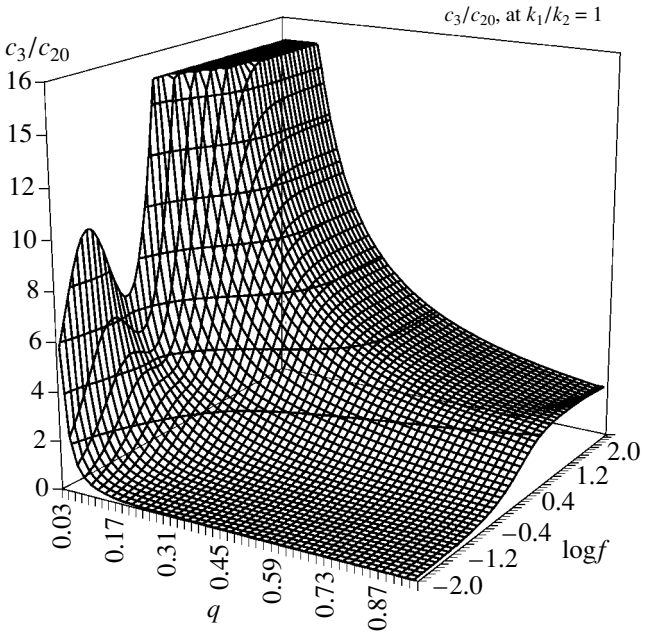

Fig. 5. Same as in Fig. 3 for the relative velocity of a rotational wave at $k_1 = k_2$.

[1] The values of the porosity parameter q close to unity are physically meaningless, because in this case the granular medium must be a vacuum.

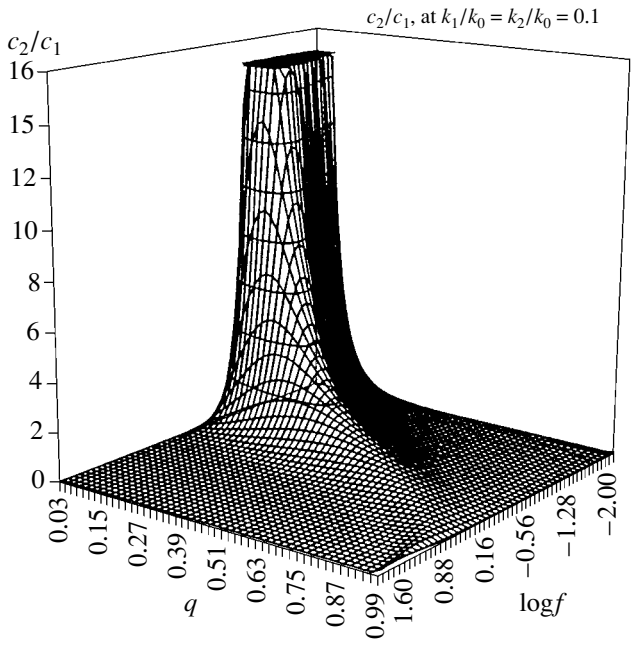

Fig. 6. Dependence of the ratio of the shear wave velocity to the longitudinal wave velocity for $k_1 = k_2 = 0.1k_0$.

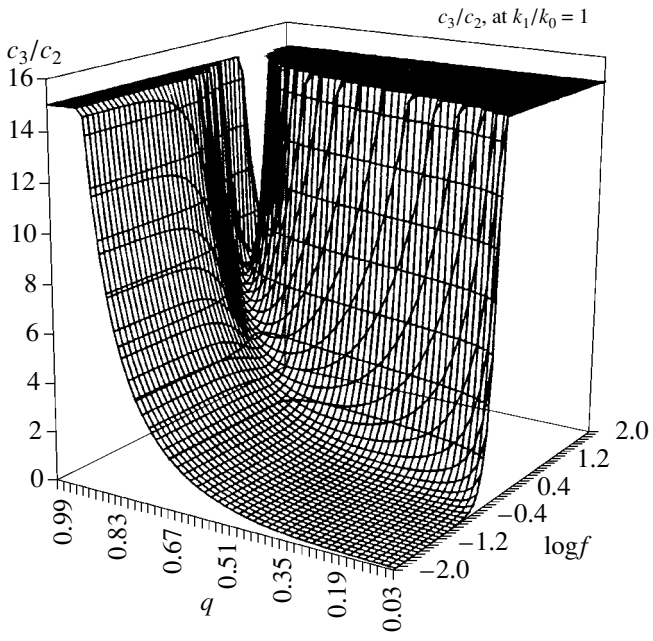

Fig. 7. Same as in Fig. 6 for the ratio of the rotational wave velocity to the shear wave velocity at $k_1 = k_2$.

the parameters q and f cannot be arbitrary and must satisfy some additional physical conditions, which are absent in the given model of the medium.

The behavior of the ratio of the rotational wave velocity to the shear wave velocity c_3/c_2 is shown in Fig. 7. This behavior is more complex than that of c_2/c_1. For $f < 1$, this ratio monotonically increases with increasing porosity, and for $f > 1$, the dependence $c_2(q)$ has a minimum whose magnitude and position are determined by the ratio of the parameters q and f.

Experimental data reported in [21] testify that, in artificially manufactured granular materials, the velocity of rotational waves can exceed the shear wave velocity. However, it should be noted that the virtual absence of experimental data on the material constants of structured media [21] and the lack of adequate methods for their study [22–24] represent one of the main factors that hinder the development of the models of nonclassical media and their application for calculating the dynamic and strength characteristics of composite and microinhomogeneous materials.

APPROXIMATION OF THE COSSERAT THEORY OF ELASTICITY

If the frequencies of acoustic waves are lower than ω_0, the spin wave does not propagate, i.e., the microrotations of particles in the medium are not free and are determined by the displacement field. By the method of successive approximations, we determine the approximate relationship between φ and w:[2]

$$\varphi(x, t) \approx \frac{\beta^2}{r^2\omega_0^2} w_x - \frac{\beta^2}{r^2\omega_0^4}\frac{\partial}{\partial x}(w_{tt} - c_3^2 w_{xx}).$$

In this approximation, the local rotations of the particles (the microrotations of structural elements) differ from the curl of the displacement field, and the relative value of this difference is determined by the small parameter of the particle "microinertia" ($r^2 = I/\rho$). Substituting Eq. (18) in the first two equations of Eqs. (11), we obtain

$$u_{tt} - c_1^2 u_{xx} = \frac{\partial}{\partial x}(\alpha_1 u_x^2 + \gamma_1 w_x^2),$$

$$w_{tt} - c_{2*}^2 w_{xx} - \beta_*^2 \frac{\partial^2}{\partial x^2}(w_{tt} - c_{3*}^2 w_{xx}) \qquad (21)$$

$$= \frac{\partial}{\partial x}(2\gamma_1 u_x w_x - \gamma_2 w_x^2),$$

where $c_{2*} = c_2\sqrt{1 - c_2^2/(r^2\omega_0^2)}$ is the shear wave velocity, $c_{3*}^2 = 2c_3^2(\beta^2 - c_2^2)/(2\beta^2 - c_2^2)$, $\beta_*^2 = \beta^2(2\beta^2 - c_2^2)/r^2 w_0^4$, and $\gamma_1 = (\alpha_2 - \alpha_3\beta^2/r^2\omega_0^2)$ and $\gamma_2 = \alpha_4\beta^2/r^2\omega_0^2$ are the nonlinearity coefficients.

[2] Here, the nonlinear terms are neglected, because they cause corrections of a higher order of smallness.

Equations of the type of Eqs. (21) are called equations of the Cosserat theory of elasticity. Their form is similar to that of the nonlinear equations describing longitudinal and flexural vibrations of a beam under tension with allowance for the inertia of rotations of transverse cross sections. The essential difference is that the equation describing the transverse waves in our model involves a quadratic nonlinearity, which is absent in the classical theory of elasticity. From the nonlinear elasticity theory, it is known that, in a homogeneous isotropic solid, the generation of the second shear harmonic of acoustic waves is forbidden for symmetry reasons. At the same time, in real materials, such a generation is observed in the experiment. This fact is usually explained by the presence of defects in the medium [25].

SUMMARY

From the micromechanical representation of a granular medium as a system of elastically interacting particles, we derived the equations of nonlinear acoustics, which take into account both translational and rotational degrees of freedom. The structure of these equations is invariant with respect to the shape and dimensions of the particles. The changes in the latter affect only the values of the coefficients involved in the equations. The inclusion of microrotations and the related moment interactions of particles leads to the formation of a microrotational wave in the medium. The dispersion properties of this wave are similar to the dispersion properties of a spin wave in a magnetoelastic medium [26]. Therefore, the microrotational wave propagating in a granular medium can also be called a spin wave. The spin wave exists when its frequency is higher than some threshold value. At frequencies below the threshold one, the wave becomes nonpropagating (forced), and the three-mode model of a granular medium is transformed to a two-mode model. In this case, higher derivatives and terms with a quadratic nonlinearity appear in the equation for the transverse mode, whereas such components are absent in the classical limit of the nonlinear elasticity theory. The quadratic nonlinearity is associated with the block structure of the medium and occurs because of the violation of symmetry in the moment interactions of blocks (particles) in the presence of transverse displacements and rotations. The nonlinearity vanishes when the particle width tends to zero and the symmetry of the moment interactions is restored ($b > 0$ and $\alpha_4 > 0$). This result agrees with the fact that, in a layered crystal formed as a chain of mechanical dipoles with $b = 0$ and $l > 0$, the quadratic nonlinearity of the transverse mode is not observed [11]. Thus, the proposed model allows one to explain the presence of the second shear harmonic in a medium with a block structure and to relate the characteristics of a wave to the structural parameters of the medium. The latter property opens up possibilities for obtaining additional information on the structure of a medium.

ACKNOWLEDGMENTS

The paper is based on the studies that were started by A. Potapov at the Institute of Mechanics of Materials at the University of California, San Diego. Potapov is grateful to Prof. M. Mayers for the chance to work at the Institute of Mechanics and for the support of the aforementioned studies. Later on, the work was continued by the authors from Russia and supported in part by the INTAS (project no. 96-2370), the Russian Foundation for Basic Research (project no. 00-02-16582), the Presidential Program in Support of the Leading Scientific Schools of Russia, and the Fediral Special-Purpose Program “Integratsiya”.

REFERENCES

1. *Physical Mesomechanics and Computer Simulation of Materials*, Ed. by V. E. Panin (Nauka, Novosibirsk, 1995), Vols. 1 and 2.
2. I. A. Kunin, *Theory of Elastic Media with Microstructure* (Nauka, Moscow, 1975).
3. A. C. Eringen, *Microcontinuum Field Theories. 1: Foundation and Solids* (Springer, New York, 1999).
4. G. Capriz, in *Springer Tracts in Natural Philosophy*, Ed. by C. Truesdell (Springer, New York, 1989), Vol. 35.
5. N. Triantafullidis and S. Bardenhagen, J. Mech. Phys. Solids **44**, 1891 (1996).
6. J. Christoffersen, M. M. Mehrabadi, and S. A. Nemat-Nasser, ASME Trans. J. Appl. Mech. **48**, 339 (1981).
7. C. S. Chang and L. Ma, Int. J. Solids Struct. **28**, 67 (1991).
8. C. S. Chang and J. Gao, J. Eng. Mech., No. 1, 52 (1997).
9. C. S. Chang and J. Gao, Int. J. Non-Linear Mech., No. 2, 111 (1995).
10. I. Y. Belyaeva, L. A. Ostrovsky, V. Y. Zaitsev, *et al.*, J. Acoust. Soc. Am. **99**, 1360 (1996).
11. T. N. Dragunov, I. S. Pavlov, and A. I. Potapov, Fiz. Tverd. Tela (St. Petersburg) **39**, 137 (1997).
12. V. I. Erofeyev and A. I. Potapov, Int. J. Non-Linear Mech. **28**, 483 (1993).
13. H. B. Muhlhaus and F. Oka, Int. J. Solids Struct. **33**, 2841 (1996).
14. V. F. Nesterenko, *Pulse Loading of Heterogeneous Materials* (Nauka, Novosibirsk, 1992).
15. A. N. Bogdanov and A. T. Skvortsov, Akust. Zh. **38**, 408 (1992) [Sov. Phys. Acoust. **38**, 224 (1992)].
16. V. G. Bykov, Akust. Zh. **45**, 169 (1999) [Acoust. Phys. **45**, 138 (1999)].
17. A. I. Potapov, I. S. Pavlov, and S. A. Potapova, in *New Advances in Modal Synthesis of Large Structures*, Ed. by

L. Jezequel (Balkema, Rotterdam, the Netherlands, 1997), pp. 399–410.

18. A. I. Potapov, S. A. Lisina, and V. F. Nesterenko, in *Proceedings of the 4th EUROMECH Solid Mechanics Conference* (Metz, France, 2000), Vol. 2, p. 722.
19. T. D. Shermergor, *Theory of Elasticity of Microinhomogeneous Media* (Nauka, Moscow, 1977).
20. G. M. Lyakhov, *Waves in Soils and Porous Multicomponent Media* (Nauka, Moscow, 1982).
21. R. D. Gauthier, in *Mechanics of Micropolar Media* (World Sci., Singapore, 1982), pp. 395–463.
22. V. I. Erofeev and V. M. Rodyushkin, Akust. Zh. **38**, 1116 (1992) [Sov. Phys. Acoust. **38**, 611 (1992)].
23. V. A. Vakhnenko, Prikl. Mat. Teor. Fiz. **37** (5), 35 (1996).
24. A. I. Potapov and V. M. Rodyushkin, Akust. Zh. **47**, 407 (2001) [Acoust. Phys. **47** (3), 347 (2001)].
25. L. K. Zarembo, V. A. Krasil'nikov, and O. Yu. Serdobol'skaya, in *Nonlinear Acoustics*, Ed. by V. A. Zverev and L. A. Ostrovskiĭ (Inst. Prikl. Fiz., Akad. Nauk SSSR, Gorki, 1980), pp. 189–219.
26. A. J. Akhiezer, V. G. Bar'yakhtar, and S. V. Peletminskiĭ, *Spin Waves* (Nauka, Moscow, 1967; North-Holland, Amsterdam, 1968).

Translated by E. Golyamina

Acoustical Physics, Vol. 47, No. 5, 2001, pp. 607–610. Translated from Akusticheskiĭ Zhurnal, Vol. 47, No. 5, 2001, pp. 694–697.

The Scattering of Flexural Waves by Random Fractal Inhomogeneities in a Thin Plate

M. L. Lyamshev

Wave Research Center, General Physics Institute, Russian Academy of Sciences, ul. Vavilova 38, Moscow, 119991 Russia

e-mail: lyamshev@kapella.gpi.ru

Received December 29, 2000

Abstract—The scattering of flexural waves by small statistical fractal inhomogeneities in a thin plate is considered. An expression for the average intensity of the fluctuations of the scattered wave field is obtained. A relation of the intensity to the plate parameters and to the fractal dimension of the inhomogeneities is determined. An expected frequency dependence of the attenuation of flexural waves in a plate due to the scattering by fractal inhomogeneities is discussed. © *2001 MAIK "Nauka/Interperiodica".*

Scattering of flexural waves by random inhomogeneities in a plate was considered earlier [1, 2]. Krasil'nikov studied the scattering of flexural waves by weak random inhomogeneities in a plate lying on a halfspace filled with an incompressible liquid [1]. The effect of fluctuations of the plate rigidity that were caused by the variability of the plate thickness (roughness of its surface) and the elastic properties of its material on the propagation and attenuation of flexural vibrations in the ice cover of the Arctic seas was studied. The scattering field was calculated using the perturbation method. It was assumed that the correlation function of inhomogeneities obeyed the Gaussian law. The propagation of flexural waves in a plate with random delta-correlated inhomogeneities was studied in [2] under the assumption of multiple scattering. A one-dimensional problem was solved.

Now there is evidence in favor of the fact that inhomogeneities of an ice cover are fractal [3]. Fractal properties are also characteristic of random inhomogeneities in thin films. Films of various materials with different physical properties form the basis of modern electronic devices and laser technology. Considerable advances has been made in their production. For example, it is possible to grow diamond films of a large area (up to thousands of square centimeters) with the thickness of the order of 1–2 mm [4]. Diamond films can be used for the production of diamond windows for powerful CO_2 lasers. The surface of any film is rough (uneven). Specifically, this is connected with the technological processes of the film growth from the gas phase of the growing substance. The film roughness can reach up to 10% of the film thickness. It is necessary to note that the surfaces of real bodies are always rough. Even when they seem perfectly even (smooth), they are rough in reality. The point is only the scale of this roughness [5]. For example, it was reported recently that statistical roughness with fractal properties is always present at the surfaces of computer hard disks along with the regular unevenness carrying the signal information [6]. The physical properties (mechanical, electrical, magnetic, and other properties) of films are largely affected by their internal structure. The microscopic structure of films is often disordered and fractal. This is quite true for a film (a layer) of an amorphous semiconductor, for example [7].

From the acoustical point of view, films and an ice cover can be treated as thin plates with surface roughness and microscopic inhomogeneities of internal structure. Here, we consider the scattering of flexural waves by inhomogeneities in a thin plate. The inhomogeneities are assumed to be random, statistically homogeneous, and small (weak). The perturbation method is used to solve the problem. The results obtained can be of interest in connection with acoustic diagnostics of inhomogeneities in films, as applied to the nondestructive testing of films and the investigation of the effect of random inhomogeneities on the propagation of flexural vibrations in an ice cover.

As one can see, inhomogeneities in both films and an ice cover have fractal properties. Fractal structures are characterized by scaling. As a consequence, the correlation functions and the spectra of statistical fractals are described by power laws with fractional exponents [5]. The statistical models of inhomogeneities that are adopted in [1, 2] can be inadequate to real inhomogeneities in plates and films.

1063-7710/01/4705-0607$21.00

Let the displacements $u(x, y)$ of a plate performing flexural vibrations be described by an equation [8]

$$[\Delta^2 - k^4(x, y)]u(x, y) = \frac{F(x, y)}{g}, \quad (1)$$

where

$$\Delta \equiv \frac{\partial^2}{\partial x^2} + \frac{\partial^2}{\partial y^2}; \quad g = \frac{Eh^3}{3(1-\sigma^2)},$$

$$k^4(x, y) = k^4(1 + \mu(x, y))^4,$$

$$k^4 = [3\omega^2\rho(1-\sigma^2)]/Eh^2,$$

g is the flexural rigidity, E is the Young modulus, σ is the Poisson ratio, $2h$ is the thickness, ρ is the density of the plate material, ω is the circular frequency of modulation of the laser radiation intensity, k is the wave number of propagating flexural waves (vibrations) in the plate, $\mu(x, y)$ is the random statistically homogeneous function characterizing the inhomogeneities in the plate, $\langle\mu(x, y)\rangle = 0$, $|\mu(x, y)| \ll 1$, and $F(x, y)$ is the external force set at a limited part of the plate at its center.

Let us represent the plate displacements in the form

$$u(x, y) = u_0(x, y) + u_1(x, y) + \ldots, \quad (2)$$

where $u_1(x, y)$ represents the displacements caused by the scattering of flexural waves of "zero" approximation with the displacements $u_0(x, y)$.

Substituting Eq. (2) into Eq. (1), we obtain the following equations for $u_0(x, y)$ and $u_1(x, y)$:

$$(\Delta^2 - k^4)u_0(x, y) = \frac{F(x, y)}{g}, \quad (3)$$

$$(\Delta^2 - k^4)u_1(x, y) = -4k^4\mu(x, y)u_0(x, y). \quad (4)$$

Using the Green function method, we can write down the solution to Eqs. (3) and (4) in the form

$$u_i(x, y) = \int_S Q_i(x_0, y_0)G(x_0, y_0/x, y)ds(x_0, y_0), \quad (5)$$

where $Q_i(x, y)$ are the functions describing the right-hand sides of Eqs. (3) and (4) and $G(x_0y_0/x, y)$ is the Green function, which is the solution to the equation

$$(\Delta^2 - k^4)G(x_0, y_0/x, y) = \delta(x_0 - x)\delta(y - y_0) \quad (6)$$

and satisfies the condition of radiation at infinity.

Let us assume that the curvature of the wave front of the "zero" flexural wave incident on inhomogeneities does not affect the scattering process, and the wave front can be considered as plane on the correlation scales of inhomogeneities. We consider the field of the scattered waves in the Fraunhofer zone with respect to the values of the correlation radii of inhomogeneities. In this case, as it follows from the reciprocity theorem, it is sufficient to know the asymptotics of the Green function in order to determine the plate displacements $u_1(x, y)$, as well as $u_0(x, y)$ [9]. The asymptotics of the Green function has the form [8]

$$G(x_0, y_0/x, y) = -\frac{\exp(ikR)}{\sqrt{32\pi ik^5R}}\exp(ik_xx_0 + ik_yy_0), \quad (7)$$

where $R = \sqrt{x^2 + y^2}$, (x, y) are the coordinates of the observation point, (x_0, y_0) are the coordinates of the source, and $k^2 = k_x^2 + k_y^2$.

Thus, we consider the fluctuations of the plate displacements in the field of a scattered wave under the assumption that the wave front of the incident zero wave is plane in the region with correlated inhomogeneities.

The solution to Eq. (4) can be represented by the expression

$$u_1(x_1, y_1) = A_0\frac{k^2}{\sqrt{2\pi ik}}\frac{\exp(ikR_1)}{\sqrt{R_1}}\int_S \mu(x_0, y_0) \times \exp[ik_xx_0 + ik_yy_0]\exp[-ik_xx_0 - ik_yy_0]ds(x_0, y_0). \quad (8)$$

Here, $A_0 \equiv u_0(x, y)$ characterizes the amplitude of the incident zero wave in the region of inhomogeneities, $\mathbf{r}_0(x_0, y_0)$ represents the coordinates of the point with inhomogeneities, and $\mathbf{r}_1(x_1, y_1)$ are the coordinates of the point of observation of the scattered wave.

Multiplying Eq. (8) by the complex conjugate, we obtain for the mean square fluctuation of the plate displacements in a scattered wave

$$\langle|u_1(x_1, y_1)|^2\rangle = |A_0|^2\frac{k^3}{2\pi R_1}\iint_S B(x_0', y_0', x_0'', y_0'') \times \exp[ik(\mathbf{n} - \mathbf{n}')(\mathbf{r}_0' - \mathbf{r}_0'')]ds(x_0', y_0')ds(x_0'', y_0''), \quad (9)$$

where $B(x_0', y_0', x_0'', y_0'') \equiv \langle\mu(x_0', y_0')\mu^*(x_0'', y_0'')\rangle$ is the correlation function of random inhomogeneities and $\mathbf{n}$ and $\mathbf{n}'$ are the vectors characterizing the directions of the incident (zero) and scattered (first-approximation) waves, respectively.

We introduce the relative coordinates $\xi = x_0' - x_0''$ and $\eta = y_0' - y_0''$ and the coordinates of the gravity center $\rho_1 = 1/2(x_0' + x_0'')$ and $\rho_2 = 1/2(y_0' + y_0'')$. Taking into account that the correlation function of statistically homogeneous processes depends only on the difference of the coordinates and integration over the coordinates

of the gravity center gives the value of the plate area S, we obtain

$$\langle |u_1(x_1, y_1)|^2 \rangle = |A_0|^2 \frac{k^3}{2\pi R_1} S \int_{-\infty}^{+\infty} B(\mathbf{r}') \exp(i\mathbf{q}\mathbf{r}') d\mathbf{r}'. \quad (10)$$

The finite integration limits determined by the value of the plate area S are replaced in Eq. (10) by $\pm\infty$ by virtue of the fact that the value of the correlation function rapidly tends to zero beyond the limits of the correlation region of inhomogeneities, and we have

$$\mathbf{q} = k(\mathbf{n} - \mathbf{n}'), \quad \mathbf{r}(x', y'). \quad (11)$$

The integral in Eq. (10) is the spatial energy spectrum of the inhomogeneity fluctuations, to within the factor $(2\pi)^{-2}$:

$$G(\mathbf{q}) = (2\pi)^{-2} \int_{-\infty}^{+\infty} B(\mathbf{r}') \exp(i\mathbf{q}\mathbf{r}') d\mathbf{r}'. \quad (12)$$

Now, as is done commonly in statistical wave theory, we determine the scattering coefficient m_s, which is determined by the energy flux through the boundary of a closed contour with the radius R at the plate surface. Taking into account Eqs. (10) and (12), we obtain

$$m_s \sim 2\pi k^3 G(\mathbf{q}). \quad (13)$$

The most important feature of fractal models of inhomogeneities is the power-law form of the fluctuation spectrum, which can be represented as

$$G(q) \sim q^{\alpha}, \quad (14)$$

where the index α is characterized by a fractional value and, for inhomogeneities with a fractal boundary (fractal surface), it is determined by the expression

$$\alpha = D - 2d. \quad (15)$$

Here D is the fractal dimension and d is the dimension of the embedding space. In order to describe random fractal inhomogeneities, we take the correlation function in the form (see [10] for example)

$$B(\mathbf{r}) = \langle \mu^2 \rangle [2^{\nu-1}\Gamma(\nu)]^{-1} (\mathbf{r}/\mathbf{r}_0)^{\nu} K_{\nu}(\mathbf{r}/\mathbf{r}_0), \quad (16)$$

where $\Gamma(\nu)$ is the gamma function, $K_{\nu}(u)$ is the Macdonald function of order ν, and r_0 is the correlation radius of inhomogeneities.

For the energy spectrum, we have the expression

$$G(q) = \langle \mu^2 \rangle \nu r_0^2 [\pi(1 + q^2 r_0^2)^{\nu+1}]^{-1}. \quad (17)$$

Substituting Eq. (16) into Eq. (13), we obtain for the scattering coefficient

$$m_s \sim \langle \mu^2 \rangle 2\pi\nu k^3 r_0^2 [\pi(1 + q^2 r_0^2)^{\nu+1}]^{-1}. \quad (18)$$

It follows from Eq. (18) that, for $q^2 r_0^2 \ll 1$, the fractal properties of inhomogeneities do not play any role in wave scattering. On the contrary, for $qr_0 \gg 1$, we obtain

$$m_s \sim \langle \mu^2 \rangle 2k^3 (qr_0)^{-2-2\nu}. \quad (19)$$

Let us evaluate the frequency dependence of the attenuation of flexural waves that is caused by the scattering by inhomogeneities:

$$\beta(\omega) \sim \oint_{\Gamma} m_s d\Gamma. \quad (20)$$

Let us consider the case of inhomogeneities in the form of structures with fractal boundaries. It is known that, in the case of such structures, the fractal dimension can lie within the limits $D \approx 1.3$–1.7 (see [2] for example). Substituting this value of fractal dimension into Eq. (15) and taking into account the fact that $d = 2$, we obtain $\alpha = -(2.7$–$2.3)$. Setting α equal to the value of the exponent of q in Eq. (19), we obtain the value of ν characterizing the order of the Macdonald function: $\nu = 0.35$–0.15. Taking into account that $q \sim k$, we obtain the following frequency dependence of the attenuation coefficient:

$$\beta(\omega) \sim \omega^{0.3-0.7}. \quad (21)$$

One can see that the exponent in the frequency dependence of scattering is fractional. This is caused by the fractal properties of inhomogeneities. The exponent can be a measure of fractality of the inhomogeneities [11]. It is necessary to note that the theory of ultrasonic attenuation in solids that is caused by the presence of dislocations leads to the dependence $\beta(\omega) \sim \omega^{-1}$, i.e., to a nonfractal dependence: the exponent in the frequency dependence of attenuation is equal to an integer. It follows from Krasil'nikov's result [1] that the scattering of flexural waves by random inhomogeneities in an ice cover, when the inhomogeneities are described by a Gaussian correlation function, leads to a quadratic frequency dependence of attenuation, i.e., also to a nonfractal dependence.

ACKNOWLEDGMENTS

This work was supported by the Russian Foundation for Basic Research, project no. 99-02-16334, and by the INTAS, project no. 97-31680.

REFERENCES

1. V. N. Krasil'nikov, Akust. Zh. **8**, 183 (1962) [Sov. Phys. Acoust. **8**, 141 (1962)].
2. S. A. Rybak, Akust. Zh. **17**, 412 (1971) [Sov. Phys. Acoust. **17**, 345 (1971)].
3. A. T. Manninen, J. Geophys. Res. C **102**, 1119 (1997).

4. *Handbook of Industrial Diamonds Films*, Ed. by M. A. Prulas, L. Popovie, and L. Bigelow (Marcel Dekker, London, 1997).
5. J. Feder, *Fractals* (Plenum, New York, 1988).
6. T. Karaback, Y.-P. Zhao, T. Liew, *et al.*, J. Appl. Phys. **88**, 3361 (2000).
7. Z. Chen, S. Zhang, and S. O. Tan, J. Appl. Phys. **89**, 783 (2001).
8. P. M. Morse and U. K. Ingard, *Theoretical Acoustics* (McGraw-Hill, New York, 1968).
9. L. M. Lyamshev, *Laser Thermooptical Excitation of Sound* (Nauka, Moscow, 1989).
10. Y.-P. Zhao, G.-C. Wang, and T. M. Lu, Phys. Rev. B **58**, 7300 (1998).
11. B. J. West and M. F. Shlesinger, J. Stat. Phys. **36**, 779 (1984).

Translated by M. Lyamshev

Acoustical Physics, Vol. 47, No. 5, 2001, pp. 611–617. Translated from Akusticheskiĭ Zhurnal, Vol. 47, No. 5, 2001, pp. 698–705.

Characteristics of Receiving Antenna Arrays Measured in a Shallow Sea

D. A. Orlov and V. I. Turchin

Institute of Applied Physics, Russian Academy of Sciences, ul. Ul'yanova 46, Nizhni Novgorod, 603600 Russia
e-mail: turchin@hydro.appl.sci-nnov.ru

Received September 20, 2000

Abstract—A diagnostic technique for receiving hydroacoustic antenna arrays operating in a shallow sea is presented. The technique reconstructs the hydrophone transfer coefficients, the array profile, and its position relative to the surface and the bottom. A stepped-frequency source and a special receiving element with a known transfer coefficient are used. The technique is illustrated by experimental hydroacoustic data, and the error in reconstructing each of the parameters is estimated. *© 2001 MAIK "Nauka/Interperiodica".*

After a stationary receiving hydroacoustic antenna array is deployed, its characteristics—the transfer coefficients of all hydrophones and their coordinates relative to the bottom (including the array profile as a whole)—are usually measured. Although the transfer coefficients, which relate the acoustic pressure (in pascals) at the input of the hydrophone to the voltage (in volts) at its output, are first measured in laboratory conditions, they may change after the deployment, because the temperature and other conditions may be different and because of the effect of various structural components of the array (the frame, the mechanical bindings, etc.), which are rather difficult to take into account in laboratory measurements. It is also clear that, if the array is flexible or semirigid, its shape after the deployment may differ from the desired one. At the same time, modern signal processing methods (see, e.g., [1]) require that the transfer coefficients, as well as the positions of the receiving elements, should be known to a sufficiently high accuracy. For example, if the error in the element positions exceeds $\lambda/10$ (where λ is the wavelength), the antenna gain decreases on the average by 1 dB [2].

Various techniques for retrieving the transfer coefficients of the receiving elements [3, 4] and the array profile [5–8] are known and currently used in practice. These techniques determine the positions of the receiving elements using a set of acoustic sources (usually explosive) placed at a sufficiently long distance from the array. This circumstance significantly limits the accuracy achieved with these methods, because the medium strongly affects the propagation of sound, which makes it difficult to predict the distribution of the received signal over the antenna [9].

This paper reports on the results of a theoretical and experimental study of a diagnostic technique for linear hydroacoustic antenna arrays operating in a shallow sea. The technique uses a stepped-frequency acoustic source placed at a small (smaller than the depth of the sea) distance from the antenna and an additional hydrophone with a known transfer coefficient. The advantage of this technique is that the source resides at a small distance from the antenna. Reverberation is also present in this arrangement, and it is more regular and predictable. Therefore, it can be efficiently suppressed.

One of the simplest methods for determining the transfer coefficients of the hydrophones is the so-called comparison method. This method compares the acoustic signals received by the array elements with the signal received by a special reference hydrophone whose transfer coefficient is known exactly. The complex transfer coefficient K_n of the nth array element ($|K_n|$ is measured in pascals per volt) is then determined as

$$K_n = \frac{U_n G_{\text{ref}}}{U_{\text{ref}} G_n} K_{\text{ref}}, \tag{1}$$

where K_{ref} is the known transfer coefficient of the reference hydrophone; U_n and U_{ref} are the voltages at the outputs of the nth element and the reference hydrophone, respectively; and G_n and G_{ref} (both measured in m^{-1}) are the acoustic transmission coefficients from the source to the nth element and to the reference hydrophone, respectively. In free space, $G_n/G_{\text{ref}} = (r_{\text{ref}}/r_n)\exp ik(r_n - r_{\text{ref}})$, where r_n and r_{ref} are the distances from the source to the nth element and to the reference hydrophone, respectively; $k = 2\pi f/c$; f is the frequency of the transmitted tone signal; and c is the sound velocity. To describe the transmission coefficients G in a shallow sea, we use the multipath propagation model. In particular, for the receiving array elements,

$$G_n = \sum_{l=1}^{L} V_n^{(l)} \frac{\exp(ikr_n^{(l)})}{r_n^{(l)}}, \tag{2}$$

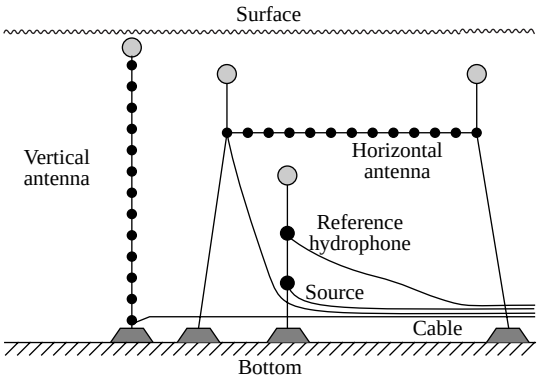

Fig. 1. Geometry of the experiment.

where $r_n^{(l)}$ is the distance from the lth image source to the nth hydrophone; $V_n^{(l)}$ is the product of the reflection coefficients for the lth ray; and L is the number of rays taken into account ($l = 1$ refers to the direct ray; $l = 2$ and 3, to the first-order reflections from the surface and bottom, respectively, etc.). We assume that the source, the receiving elements, and the reference hydrophone are omnidirectional. We have also neglected the ray curvature due to the vertical profile of the sound velocity in Eq. (2), because the distances between the source and the receiving elements are small.[1] It can be assumed that Eq. (2) describes the actual transfer coefficients as a function of distance, frequency, etc., to a sufficient accuracy, unlike the case of the long-range propagation of sound in a shallow sea, in which the interference structure of the field is difficult to predict (see, e.g., [9]).

Although the comparison method, which uses Eqs. (1) and (2), allows one to obtain the transfer coefficients of all hydrophones as a function of not only the hydrophone index but also frequency, it has a significant drawback when applied to an array operating in a shallow sea: it is sensitive to a possible mismatch between the parameters used in Eq. (2) and their true values (this refers in particular to various geometric parameters, such as depths, distances, etc.) and to a disagreement between model (2) and real conditions. Therefore, it is reasonable first to assume that the transfer coefficients of the receiving elements weakly depend on frequency (which is usually valid in practice) and to develop a procedure that will be capable of determining the average transfer coefficients in a certain frequency band, as well as the profile of the antenna array and the position of an element relative to the antenna. After that, Eqs. (1) and (2) can be used to refine the frequency dependence of the transfer coefficients.

[1] Nevertheless, if the vertical profile of the sound velocity $c(z)$ is known, it may partially be taken into account by characterizing each ray in Eq. (2) by its particular averaged sound velocity.

The appropriate measurement procedure can be as follows. At a distance of ~0.2 to 0.5 of the sea depth H from the array, an acoustic source is placed. The source is stepped in frequency with a fixed step size Δf in the range from f_b to f_e. Each mth frequency f_m is transmitted during a time interval sufficiently long for the narrow-band filtering. A reference hydrophone is placed at a small known distance r_{ref} from the source (at a different depth), as shown in Fig. 1.

With the above assumption that the transfer coefficients of the receiving elements are weakly dependent on frequency, we construct the output $U_{n,m}$ of the narrow-band filter versus the indexes of the receiving element, n, and of frequency, m, and normalize the function by the output $U_{ref,m}$ of the reference hydrophone in order to compensate for the irregularity of the frequency characteristic of the source:[2] $U_{n,m}^{(norm)} = U_{n,m}/U_{ref,m}$. Further, we calculate the Fourier transform $Y_{n,k}$:

$$Y_{n,k} = \frac{1}{J}\sum_{m=0}^{J-1} U_{n,m}^{(norm)} e^{-2\pi i \frac{km}{J}}, \qquad (3)$$

which turns the frequency dependences of the output signals into time samples taken at the moments $t_k = k\Delta t - r_{ref}/c$, where $\Delta t = (Jf_\Delta)^{-1}$ and $f_\Delta = f_e - f_b$. Formula (3) actually synthesizes a pulse with the waveform $\exp(2\pi i f_{av} t)\sin c(\pi f_\Delta t)$, where $f_{av} = (f_b + f_e)/2$. Next, we apply a time window to select the entries of the array $Y_{n,k}$ produced by the direct signal. We use the delay time $t_n^{(1)}$ of the direct signal to calculate the distances $r_n^{(1)} = ct_n^{(1)} + r_{ref}$ between the source and each nth hydrophone. Subsequently, we calculate the magnitudes $|K_n|$ of the transfer coefficients from Eq. (1) with the maximum $|Y_n^{(max)}| = \max_k |Y_{n,k}^{(1)}|$ taken as the ratio $|U_n/U_{ref}|$ at each n, and $|G_n/G_{ref}| = r_{ref}/r_n^{(1)}$; here, one should take into account that the signals are normalized by the output of the reference hydrophone. Clearly, the result represents the transfer coefficients averaged over the frequency range from f_b, to f_e.

To reconstruct the three-dimensional profile of the array, in addition to $r_n^{(1)}$, one should use at least one more set of distances, for example, $r_n^{(2)}$ (associated with rays reflected from the surface). Consider the Cartesian coordinate system (x, y, z) with the z axis looking downward and passing through the source, the y axis directed from the source to the nearest array element,

[2] Although the signals reflected from the surface and bottom will contribute to $U_{ref,m}$ less than $U_{n,m}$, because the reference hydrophone is close to the source, the reverberation component should be preliminarily suppressed, for example, by smoothing the frequency dependences of the amplitude and phase of $U_{ref,m}$ in order to increase the accuracy.

and the origin residing at the surface. Then, the source has the coordinates $(0, 0, z_s)$, where z_s is the depth of the source, which we consider to be known. The array profile will be characterized by the coordinates of its elements, (x_n, y_n, z_n), $n = 1, \ldots, N$. For example, for an ideal horizontal array with elements uniformly spaced a distance d apart, we have $x_n = (n - n_0 + \nu)d$, $y_n = y_0$, and $z_n = z_0$, where z_0 is the array depth, y_0 is the horizontal distance between the source and the line passing through the array elements, n_0 is the index of the element that is closest to the source, and the parameter ν allows for the fact that the perpendicular, dropped from the source to the line that carries the array elements, may intersect it between the hydrophones ($|\nu| \le 0.5$). Using the evident relationships

$$r_n^{(1)} = \sqrt{\rho_n^2 + (z_n - z_s)^2}, \quad r_n^{(2)} = \sqrt{\rho_n^2 + (z_n + z_s)^2}, \quad \rho_n^2 = x_n^2 + y_n^2, \tag{4}$$

we find $z_n = ((r_n^{(2)})^2 - (r_n^{(1)})^2)/4z_s$ and ρ_n. To find x_n and y_n, one can use the recurrent procedure for calculating the node coordinates of a polygonal line with a given distance d between the nodes, which can be derived from simple geometrical considerations:

$$x_{n+1} = \frac{1}{\rho_n^2}(x_n a_{n+1}^2 + y_n b_{n+1}^2), \quad y_{n+1} = \sqrt{\rho_{n+1}^2 - x_{n+1}^2}, \tag{5}$$

where

$$a_{n+1}^2 = \frac{1}{2}(\rho_{n+1}^2 + \rho_n^2 + (z_{n+1} - z_n)^2 - d^2),$$

$$b_{n+1}^2 = \sqrt{(\rho_{n+1}\rho_n)^2 - a_{n+1}^4}.$$

The procedure begins with the index $n = n_0$ and the coordinates $x_{n_0} = -\nu d$ and $y_{n_0} = \sqrt{\rho_{n_0}^2 - (\nu d)^2}$. The parameter ν is calculated by minimizing the differences between the determined values of $y_n(\nu)$ and a constant. Note that this procedure is very sensitive to even small random errors in each of the distances $r_n^{(1,2)}$. Therefore, prior to using it, one should smooth the experimental $r_n^{(1)}$ and $r_n^{(2)}$ as a function of the index n.

It can often be assumed that the profile of horizontal arrays with neutral buoyancy differs from a straight line mostly in the vertical plane and that it can be approximated by a catenary curve

$$z_n = A\cosh\frac{x_n - B}{A} + C, \tag{6}$$

where the parameters A, B, and C are to be estimated. They can be determined along with the unknown position of the source relative to the array in the horizontal plane by minimizing the rms deviation between the experimental distances $r_n^{(l)}$, $l = 1, 2, \ldots$ and the distances calculated from Eq. (6).

As we noted above, the frequency dependences of the transfer coefficients K_n can be refined through substituting the estimates x_n, y_n, and z_n obtained at the frequencies $f_b, \ldots, f_e$ into Eqs. (1) and (2). Note that, unlike the above procedures for estimating the average transfer coefficients and the array profile, the procedure for calculating the frequency dependences of the transfer coefficients is more sensitive to the model of the medium.

The technique described above was used to reconstruct the parameters of 64-element linear hydroacoustic arrays with elements spaced a distance $d = 0.19$ m apart (with a total length of ~12 m) deployed in the vertical or horizontal position in a lake. The arrays had the form of piezoceramic hydrophones with preamplifiers built in a cable. The cable was attached with foam plastic fasteners to an aluminum pipe 0.05 m in diameter in order to impart a certain rigidity to the system (the array as a whole, had almost neutral buoyancy). The experiments were carried out in the Sankhar lake (Vladimir oblast) in 1997–1999. At the place where the arrays were deployed, the depth was ~15 m and the bottom (sand covered with silt) was sufficiently flat. The experiments differed mostly in the array arrangement (horizontal or vertical) and in the technique used to attach the array to the pipe (in size and number of foam plastic fasteners).

In compliance with the above reconstruction procedure, a wideband acoustic source was placed at a distance of several meters from the array and an 8101 B&K hydrophone with a known transfer coefficient was placed 1 m above it. The source depth was chosen so as to provide the maximal path-length difference between the direct ray and the first-order reflections from the surface and bottom. The source was either a ring piezoceramic transmitter with a ~0.5-kHz bandwidth or a second 8101 B&K hydrophone operated in the reversed mode.[3] The frequency was stepped within a range of ~1 to 3 kHz.

Figure 2 presents $Y_{n,k}$ calculated with procedure (3) for the horizontal and vertical array arrangements. Both plots clearly show the arrival times of the direct rays (*1*) and of the rays arrived after one reflection from the surface (*2*). The first-order bottom reflection (*3*) is less pronounced, because the bottom reflection coefficient was rather small. Note that, for the horizontal array, the lines corresponding to different rays are almost parallel, whereas, for the vertical array, the lines associated with the surface and bottom rays always intersect.

The amplitude and phase of the frequency-averaged transfer coefficients for two different antenna arrays are given in Fig. 3. Each panel displays the results of three

[3] The piezoceramic transmitter was not omnidirectional: in the vertical direction, its radiation level was higher than in the horizontal direction. This effect was taken into account in the calculations.

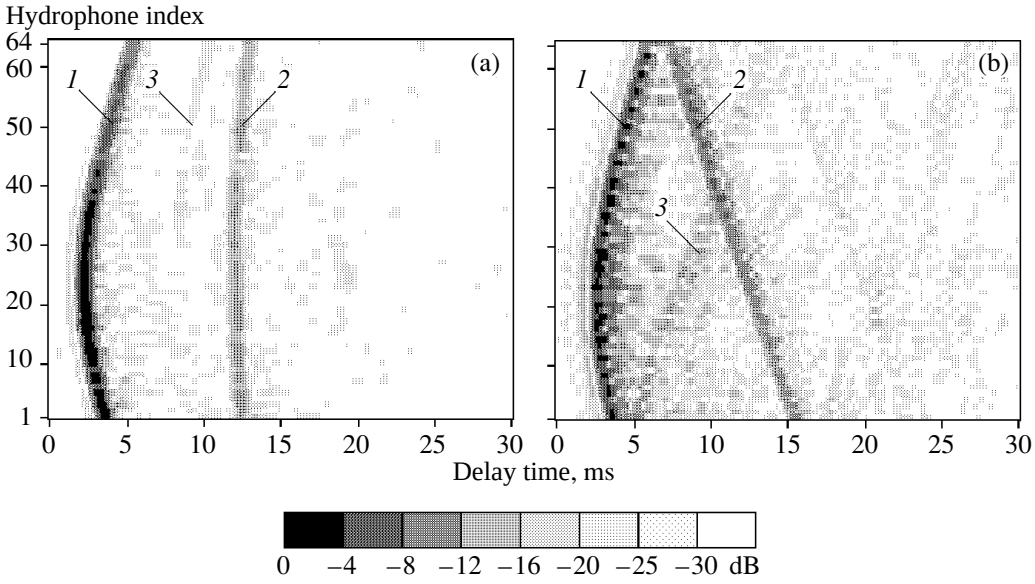

Fig. 2. Amplitude of the received signal on the delay time–hydrophone index plane for the (a) horizontal and (b) vertical antennas: (*1*) the direct ray and the first-order (*2*) surface and (*3*) bottom reflections.

independent measurements performed with different positions of the source and the reference hydrophone relative to the same antenna array. The spread in the results represents an error associated primarily with inaccurate calculation of the acoustic field transmission coefficients (see below). The results of reconstructing an improper arrangement of the receiving array are shown in Fig. 3b: the amplitude and phase of the transfer coefficients exhibit relatively strong periodic (with a period of 3 hydrophones) variations, because, in this experiment, we attached the antenna to the metal pipe with larger fasteners applied at three-element intervals (also refer to Fig. 2b). This effect was removed later on.

The error in reconstructing the transfer coefficients by the above technique depends on many factors. For example, the contributions made by the error in the transfer coefficient of the reference hydrophone and the error in the distance between the source and the reference hydrophone to the overall error can easily be calculated. Most specific of this technique is the error associated with incomplete suppression of all spurious rays when extracting the direct signal, in particular, because the frequency range of the stepped-frequency signal is finite (terms determined by the sidelobe level of the synthesized pulse for the surface, bottom, and other reflected rays are added to $Y_n^{(\max)}$). This error component was studied by numerical simulations. As an example, we consider a horizontal array of length $D = H$, where H is the sea depth at the array location. Figure 4 shows the element-averaged rms error in the transfer coefficients versus the dimensionless frequency range $\xi = f_\Delta D/c$ (the antenna length in terms of spatial resolution elements) for different source depths z_s (the horizontal distance between the source positioned opposite to the central element and the array, as well as the antenna depth, were $0.5H$). As can be seen from Fig. 4, the accuracy of reconstructing the transfer coefficients on average improves with increasing frequency range, and the optimal source depth for this arrangement is $H/2$. In this case, the surface and bottom rays are at the maximal distance from the direct one. When the source moves towards the surface or bottom, the surface or bottom ray, respectively, moves closer to the direct one and its sidelobes introduce a higher error into the results of calibration. As follows from Fig. 4, for a moderate frequency range of the stepped-frequency signal (ξ = 10–20), the error is no higher than 5–10%.

Generally speaking, the effect of the sidelobes can be reduced by using Fourier transform (3) with a window, for example, the cosine one. However, it was shown that the use of these windows in processing real data produces almost no effect on the noise level in $Y_{n,k}$, because it is determined not only by the sidelobe level, but also by the limited applicability of model (2) in real conditions. On the other hand, the window decreases the time resolution, and, therefore, the use of such windows for calculating the transfer coefficients is usually unreasonable.

The total experimental error can be estimated by comparing the transfer coefficients calculated for the same antenna hydrophones with different source positions. These estimates obtained from the results similar to those plotted in Fig. 3a show that the error is about 10–15%. This value is greater than that obtained from simulations primarily due to the phase component (the amplitude error is almost the same as that given by simulations).

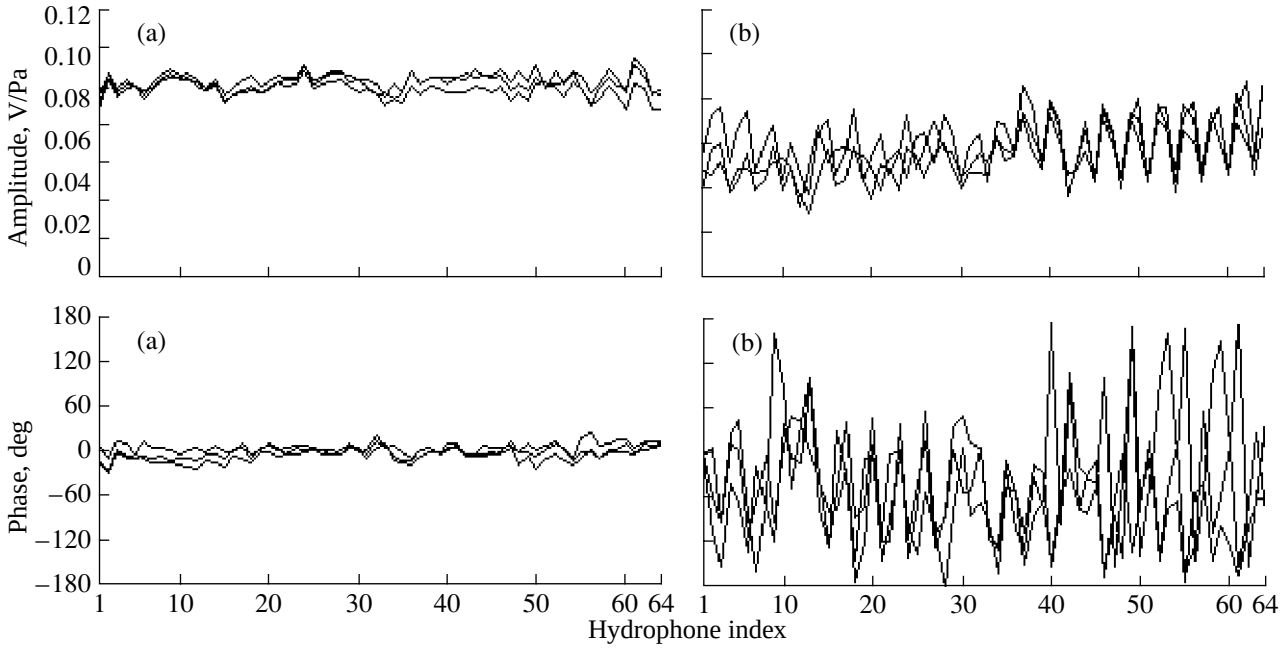

Fig. 3. Amplitude and phase of the transfer coefficients of the antenna arrays hydrophones for (a) horizontal and (b) vertical antennas. Each panel presents the plots obtained for three different source positions with the same array arrangement.

Figure 5 displays the results of reconstructing the profiles of horizontal arrays for two installation techniques: (a) with the help of two wires under tension directed at an angle and buoys creating the tensile stress, as shown in Fig. 1, and (b) by attaching the pipe to a Π-shaped vertical frame. The experimental estimates of the distances $r_n^{(1)}$ and $r_n^{(2)}$ were smoothed with second-order splines with one matching point, after which procedure (5) was used. Clearly, the profile reconstruction accuracy is determined only by the accuracy of the acoustic measurements of the distance, this accuracy being proportional to the spatial resolution $\Delta_r = c/f_\Delta$ (in the experiment, $\Delta_r = 0.75$ m). Since Eqs. (5) represent a nonlinear algorithm, the profile reconstruction accuracy as a function of the distance error was determined by numerical simulations. The errors were generated as independent random variables with equal standard deviations σ_r. For the array and source arrangement used in the experiment, we obtained that, when σ_r is within 0.05–0.3 m, the rms profile reconstruction error is within 0.02–0.1 m; i.e., it is comparable with the rms distance error (the maximal deviations of the reconstructed profile from the true one were higher than the rms error by a factor of 2.3–2.6).[4] The experimental rms distance error was estimated from the deviations of the experimental data from a smooth approximating function; it was 0.03–0.09 m (i.e., 4–12% of the spatial resolution) for different arrangements. Based on these estimates and on the estimates obtained from simulations, we can assume that the profiles presented in Fig. 5 are reconstructed with an rms error of 0.03 m. The results of the profile reconstruction with different positions of the source relative to the same array confirmed this estimate.

Formula (2) was obtained for a homogeneous medium bounded by a flat surface and a flat bottom. Its applicability in real conditions can be estimated as follows. Since the frequency characteristic of the source is sufficiently smooth, we approximate the frequency

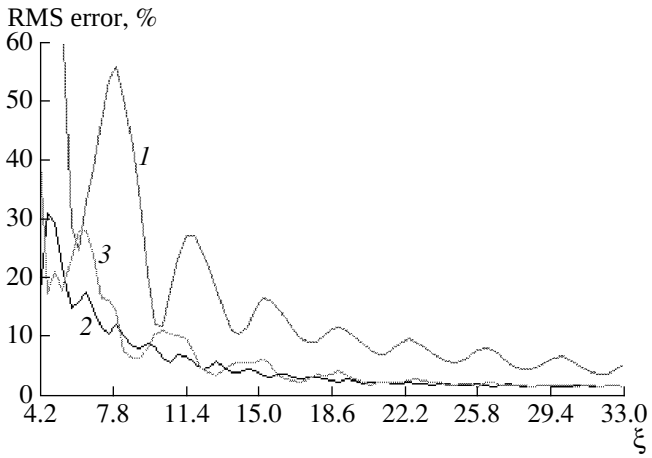

Fig. 4. Root-mean-square error in the calculated transfer coefficients normalized by the true value versus the dimensionless parameter ξ for the source depths (*1*) 0.2*H*, (*2*) 0.5*H*, and (*3*) 0.8*H*, as obtained from the simulations.

[4] A small reconstruction error due to the approximation of the distance as a function of the element index was also taken into account.

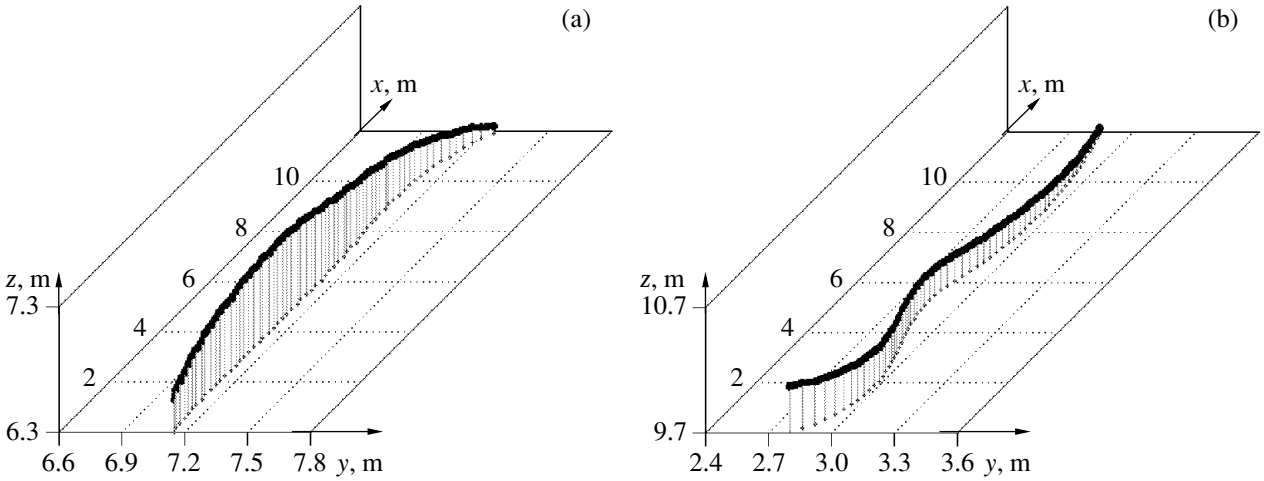

Fig. 5. Experimentally reconstructed three-dimensional array profiles for two array arrangements.

dependence of the signal received by the reference hydrophone with a smoothing function and divide the received signal by this smooth frequency dependence. Clearly, the result can be compared with calculations from Eq. (2). Figure 6 shows the result of such a comparison for the reference hydrophone (Fig. 6a) and for one of the antenna hydrophones (Fig. 6b). It can be seen that, for the reference hydrophone, model (2) provides a sufficiently good description of the received signal: the experimental positions of the interference maximums and minimums and the depth of the interference-related amplitude variations of the received signal are in good agreement with the model. In the case of the array hydrophone, the accuracy of the model is lower, presumably, because the distance from the source to the hydrophone is much longer than that to the reference hydrophone, which results in an increase in the effect of interference on the received signal and causes much greater errors in the reconstruction of the geometrical parameters. Errors in the low-order spline approximation of the frequency characteristics of the source and the hydrophone can also affect the accuracy of the result. Figure 6 illustrates the error in the reconstructed frequency characteristic of an individual hydrophone. Clearly, this error can be reduced by averaging the frequency dependence of the transfer coefficients over all hydrophones.

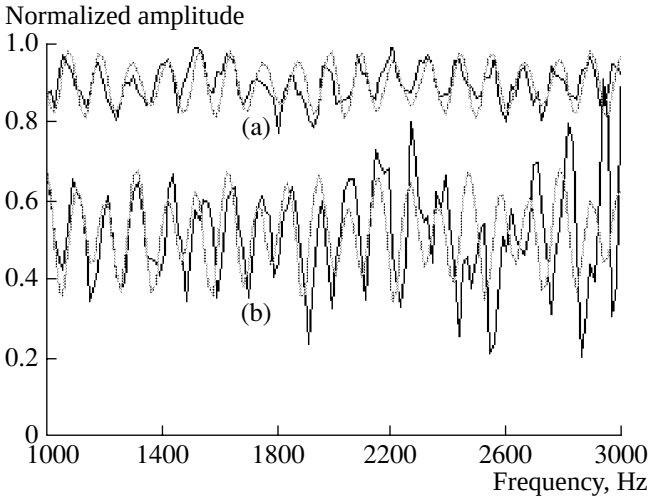

Fig. 6. Amplitude of the received signal normalized by the frequency dependence obtained by the spline approximation of the received signal (the black curves) and the simulated signal (the gray curves) for (a) the reference hydrophone and (b) one of the array hydrophones (no. 30).

The above experimental results were obtained with 12-m-long arrays operated in the frequency range of ~0.3 to 3.0 kHz at a test site with a depth of ~15 m. Clearly, due to the similitude principle and to the correspondence between the lake and sea conditions [10], similar results can be obtained for appropriately scaled low-frequency hydroacoustic arrays at frequencies from tens to hundreds of hertzs in a shallow sea at a depth of 100–300 m.

Thus, in this paper, we described an integrated technique for reconstructing the parameters of receiving hydroacoustic linear antenna arrays after they are deployed: the transfer coefficients of individual receiving elements, the profile of the array, and its position relative to the surface and the bottom. The technique can also be used to answer an important practical question concerning the applicability of the model that represents a shallow sea as a homogeneous medium bounded by a flat surface and a flat bottom in real conditions. The efficiency of the technique for the diagnostics of receiving hydroacoustic antennas is confirmed experimentally.

ACKNOWLEDGMENTS

We are grateful to V.V. Pikalev, P.I. Korotin, B.M. Salin, V.A. Tyutin, I.Sh. Fiks, and other staff

members of the Institute of Applied Physics, Russian Academy of Sciences, who took part in the experiments and discussions.

This work was supported by the Russian Foundation for Basic Research, project no. 00-02-16438.

REFERENCES

1. A. B. Baggeroer, W. A. Kuperman, and P. N. Mikhalevsky, IEEE J. Ocean. Eng. **18**, 401 (1993).
2. W. S. Hodgkiss, D. E. Ensberg, J. J. Murray, *et al.*, IEEE J. Ocean. Eng. **21**, 393 (1996).
3. Z. Lazreq and J. M. Ville, J. Acoust. Soc. Am. **100**, 364 (1996).
4. J. F. Zalesak, J. Acoust. Soc. Am. **105**, 2342 (1999).
5. R. C. Shockley, J. A. Rice, and P. Hursky, J. Acoust. Soc. Am. **95**, 2809 (1994).
6. H. T. Vincent, II and S.-L. J. Hu, J. Acoust. Soc. Am. **102**, 3099 (1997).
7. S. E. Dosso and M. R. Fallat, J. Acoust. Soc. Am. **104**, 846 (1998).
8. S. E. Dosso and B. J. Sotirin, J. Acoust. Soc. Am. **106**, 3445 (1999).
9. B. G. Katsnel'son and V. G. Petnikov, *Acoustics of a Shallow Sea* (Nauka, Moscow, 1997).
10. V. A. Zverev, P. I. Korotin, A. I. Matveev, *et al.*, in *Proceedings of the US–Russia Workshop on Experimental Underwater Acoustics* (Nizhni Novgorod, Russia, 2000), p. 117.

Translated by A. Khzmalyan

Acoustical Physics, Vol. 47, No. 5, 2001, pp. 618–622. Translated from Akusticheskiĭ Zhurnal, Vol. 47, No. 5, 2001, pp. 706–710.

Acoustic Characteristics of a Multichannel Long Line of the Flexural Type

V. V. Tyutekin

Andreev Acoustics Institute, Russian Academy of Sciences, ul. Shvernika 4, Moscow, 117036 Russia

e-mail: bvp@akin.ru

Received February 15, 2001

Abstract—The properties of an acoustic object represented by a multichannel long line of the flexural type are considered. Analytical formulas are obtained for the basic acoustic characteristics of a multichannel long line with an arbitrary number of flexurally oscillating single lines constituting it: the input impedance, the resonance frequencies, and the reflection and transmission coefficients are determined for an insulating multichannel long line, including the case of a cascade connection. Numerical calculations are performed and the plots are presented for the frequency dependences of the reflection and transmission coefficients for various parameters of the constituting lines. It is demonstrated that the acoustic characteristics of insulating multichannel long lines have certain advantages in comparison with the characteristics of similar objects based on single lines. © *2001 MAIK "Nauka/Interperiodica".*

The problem of absorption and insulation of sound and vibration remains important from both theoretical and practical points of view. Lately, the so-called active methods have become popular in this field of acoustics [1–7]. However, traditional methods of absorption and insulation of waves continue to develop (see [8] for example). One of such methods is described in a previous paper [9], which is devoted to the study of the characteristics of a new acoustic object, namely, a so-called multichannel long line for longitudinal waves.

This paper develops the method of multichannel long lines for flexural waves. As in the previous paper [9], we calculate the acoustic characteristics of multichannel long lines of the flexural type: the resonance frequencies, the input impedance, and the reflection and transmission coefficients for a flexural wave.

We assume that a multichannel long line of the flexural type consists of single long lines in the form of flat rods (strips) parallel to each other, which perform flexural oscillations with the frequency ω. We characterize each single line by the following parameters: the length l equal for all lines, the rod mass per its unit width $m_j = \rho_j h_j$ (it is assumed that the latter is much smaller then the flexural wavelength), the density ρ_j, the thickness h_j, the flexural rigidity $B_j = E_j h_j^3/12$, and the Young modulus E_j, where $j = 1$–N is the rod number.

The considered model of a multichannel long line presumes that the left ends of all lines ($x = 0$) are connected to each other, as well as their right ends ($x = l$) (see Fig. 1a). The connections are provided by weightless and undeformable plates in such a way that the transverse displacements w_j of each end are the same for all lines and the values of w_j' are equal to zero.

The latter condition can be provided by a large value of the flexural rigidity of the multichannel long line, which, in turn, can be achieved by setting the single lines at a sufficient distance from the center line of the multichannel long line.

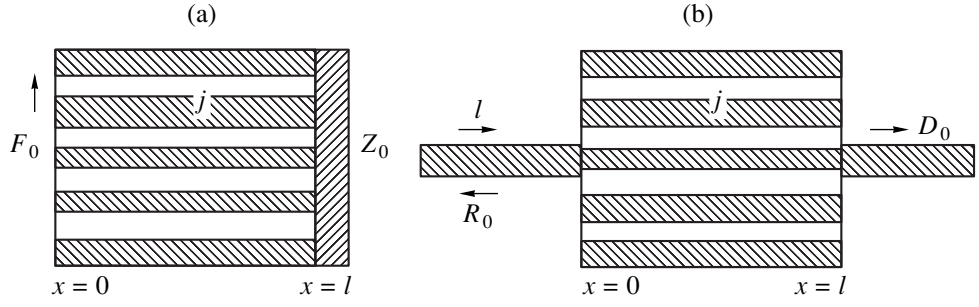

Fig. 1. Illustration of the derivation of the equations for the acoustic characteristics of multichannel long lines.

1063-7710/01/4705-0618$21.00 © 2001 MAIK "Nauka/Interperiodica"

In accordance with the selected model, we assume that the transverse displacements w_j in each single long line satisfy the equation for the flexural vibrations of a rod

$$\frac{d^4 w_j}{dx^4} - k_j^4 w_j = 0, \tag{1}$$

the solution to which can be selected in the form

$$w_j = a_j \cos k_j x + b_j \cosh k_j x + c_j \sin k_j x + d_j \sinh k_j x. \tag{2}$$

In Eqs. (1) and (2), $k_j^4 = \dfrac{m_j \omega^2}{B_j}$ and k_j is the wave number of flexural waves in the jth line. The boundary conditions can be written in the form

$$w_j(0) = w_0, \quad w_j(l) = w_l, \tag{3}$$

$$w_j'(0) = w_j'(l) = 0, \tag{4}$$

$$\sum_{j=1}^{N} F_j(0) + F_0 = 0, \quad \sum_{j=1}^{N} F_j(l) + F_l = 0, \tag{5}$$

where w_0, w_l and F_0, F_l are the unknown displacements and intersecting forces. Substituting the solution in the form of Eq. (2) into the boundary conditions given by Eqs. (3) and (4), we obtain (after simple transformations) the values of the unknown coefficients a_j, b_j, c_j, and d_j:

$$a_j = -b_j = \frac{1}{2\Delta_j}(T_j w_0 - S_j w_l), \tag{6a}$$

$$c_j = \frac{1}{2\Delta_j}(-G_j^- w_0 + C_j w_l), \tag{6b}$$

$$d_j = \frac{1}{2\Delta_j}(G_j^+ w_0 + C_j w_l). \tag{6c}$$

Here, we introduced the notations

$$\Delta_j = 1 - \cosh\varphi_j \cos\varphi_j;$$

$$T_j = \cosh\varphi_j \sin\varphi_j + \cos\varphi_j \sinh\varphi_j; \quad S_j = \sinh\varphi_j + \sin\varphi_j;$$

$$G_j^{\pm} = 1 - (\cosh\varphi_j \cos\varphi_j \pm \sinh\varphi_j \sin\varphi_j);$$

$$C_j = \cosh\varphi_j - \cos\varphi_j; \quad \varphi_j = k_j l.$$

Substituting Eqs. (6a)–(6c) into Eq. (2), it is possible in principle to obtain the fields of flexural waves in any single long line. To determine the effect of all lines combined in a multichannel long line, it is necessary to use the boundary conditions given by Eqs. (5). The intersecting forces in each single line are determined by the known formula

$$F_j(x) = -B_j \frac{d^3 w_j}{dx^3} = -B_j k_j^3(-a_j \cos k_j x + b_j \cosh k_j x + c_j \sin k_j x + d_j \sinh k_j x). \tag{7}$$

We introduce the parameters B_0 and k_0 of a "comparison" line and the dimensionless quantities

$$\Psi_j = \frac{B_j k_j^3}{B_0 k_0^3} = \frac{m_j c_f^j}{m_0 c_f^0},$$

for convenience of further consideration. Here, $c_f^{j,0}$ are the corresponding velocities of flexural waves. Taking into account Eqs. (6), the expressions for $F_j(0)$ and $F_j(l)$ can be represented in the form

$$\frac{F_j(0)}{B_0 k_0^3} = \frac{\Psi_j}{\Delta_j}(T_j w_0 - S_j w_l); \tag{8a}$$

$$\frac{F_j(l)}{B_0 k_0^3} = \frac{\Psi_j}{\Delta_j}(S_j w_0 - T_j w_l). \tag{8b}$$

Substituting Eqs. (8) into Eqs. (5), we obtain

$$\frac{F_0}{B_0 k_0^3} = f_0 = Z_{11} w_0 + Z_{12} w_l; \tag{9a}$$

$$\frac{F_l}{B_0 k_0^3} = f_l = Z_{21} w_0 + Z_{22} w_l. \tag{9b}$$

Here, Z_{ik} are the dimensionless impedances, which have the values

$$Z_{11} = -Z_{22} = -\sum_{j=1}^{N} \frac{\Psi_j}{\Delta_j} T_j;$$

$$Z_{12} = -Z_{21} = \sum_{j=1}^{N} \frac{\Psi_j}{\Delta_j} S_j. \tag{10}$$

We note that all formulas given above are obtained under the assumption that all rods are of the same

width. However, the variability of their widths can provide an opportunity to vary the values of ψ_j and, therefore, the impedances given by Eq. (10) in a wide range. In this case, we have

$$\psi_j = \frac{B_j k_j^3 H_j}{B_0 k_0^3 H_0} = \frac{m_j H_j c_f^j}{m_0 H_0 c_f^0}.$$

Equations (9) and (10) are initial for the determination of the basic acoustic characteristics of multichannel long lines of the flexural type.

Let us determine the input impedance of a multichannel long line. By definition, $Z_{in} = \frac{f_0}{w_0}$ is the input impedance and $Z_0 = \frac{f_l}{w_l}$ is the impedance of the multichannel long line load. We note that the impedances given above are scalar quantities due to the specific boundary conditions, whereas, in the general case of flexural vibrations, they have a matrix character. Equations (9) can be represented in the form

$$Z_{in} = Z_{11} + Z_{12}\frac{w_l}{w_0},$$

$$Z_0 = Z_{21}\frac{w_0}{w_l} + Z_{22}.$$

Taking into account Eqs. (10), we obtain from the above formulas:

$$Z_{in} = Z_{11} - \frac{Z_{12}^2}{Z_{11} + Z_0}. \quad (11)$$

We should note that Eq. (11) coincides in its form with the expression for the input impedance of a multichannel long line of the longitudinal type [10], but differs from it in the values of the impedances Z_{ik}. It is possible to determine the resonance frequencies from the conditions $Z_{in} = 0$ and $Z_{in} = \infty$ (under the condition $Z_0 = 0$) and the antiresonance frequencies from the relations $Z_{11} = \pm Z_{12}$ and $Z_{11} = 0$.

Now, let us consider such acoustic characteristics of multichannel long lines as the coefficients of reflection and transmission of a flexural wave. The model selected for the calculation is given in Fig. 1b. A single long line is connected to a multichannel long line on the left and on the right. We describe the parameters of this line, B_0 and k_0, by the index $j = 0$. (Physically, it can pass through the multichannel line and be one of the components of the latter.) A harmonic wave of unit amplitude propagates along this line:

$$w = \exp(ik_0 x).$$

This wave produces two waves reflected from the system: one homogeneous wave and one inhomogeneous wave decreasing in amplitude as $x \longrightarrow -\infty$:

$$w_1 = R\exp(-ik_0 x) + G\exp(k_0 x).$$

The transmission through a multichannel long line is accompanied by the formation of similar waves at its output:

$$w_2 = D\exp[ik_0(x-l)] + E\exp[-k_0(x-l)].$$

Here, R and D are the desired coefficients of reflection and transmission of the flexural wave.

Using the boundary conditions (Eqs. (4) and (5)), which are also valid for the reflected and transmitted waves, we can obtain the relations for the displacements

$$w_0 = (1+i)R + (1-i); \quad w_l = (1+i)D_1,$$

where $D_1 = D\exp(ikl)$, as well as relations for the intersecting forces and the impedance Z_0:

$$f_0 = 2i(1-R); \quad f_l = 2iD_1; \quad Z_0 = 1+i.$$

Using these relations, it is easy to obtain the expressions for the reflection and transmission coefficients

$$R = \frac{iZ_{in} + Z_1}{Z_{in} + Z_1}; \quad (12)$$

$$D_1 = -\frac{2Z_{12}}{(Z_{in} + Z_1)(Z_{11} + Z_0)}. \quad (13)$$

Here, $Z_1 = 1 + i$ and the quantities Z_{in}, Z_{11}, and Z_{12} are determined by Eqs. (10) and (11). It is evident that, in the absence of losses, $|R|^2 + |D_1|^2 = 1$.

It is interesting to consider a cascade connection (in series) of several multichannel long lines with different sets of single long lines. In this case, the latter can be described by the parameters and functions with two indices, for example:

$$\varphi_j^{(n)} = k_j^{(n)} l_n,$$

$$T_j^{(n)} = \cosh\varphi_j^{(n)}\sin\varphi_j^{(n)} + \cos\varphi_j^{(n)}\sinh\varphi_j^{(n)},$$

$$Z_{11}^{(n)} = -\sum_{j=1}^{N}\frac{\psi_j^{(n)}}{\Delta_j^{(n)}}T_j^{(n)}$$

and so on. Here, $j = 1$–$N^{(n)}$ and n is the number in the sequence of multichannel long lines (they are counted from the side of the transmitted wave).

A recurrent sequence for the quantities $Z_{in}^{(n)}$ can be obtained from Eq. (11):

$$Z_{in}^{(n)} = Z_{11}^{(n)} - \frac{(Z_{12}^2)^{(n)}}{Z_{11}^{(n)} + Z_{in}^{(n-1)}}, \quad (14)$$

where, evidently, $Z_{in}^{(0)} = Z_0$. The expression for the reflection coefficient $R^{(n)}$ is obtained from Eq. (12) by replacing Z_{in} by $Z_{in}^{(n)}$:

$$R^{(n)} = \frac{iZ_{in}^{(n)} + Z_1}{Z_{in}^{(n)} + Z_1}. \quad (15)$$

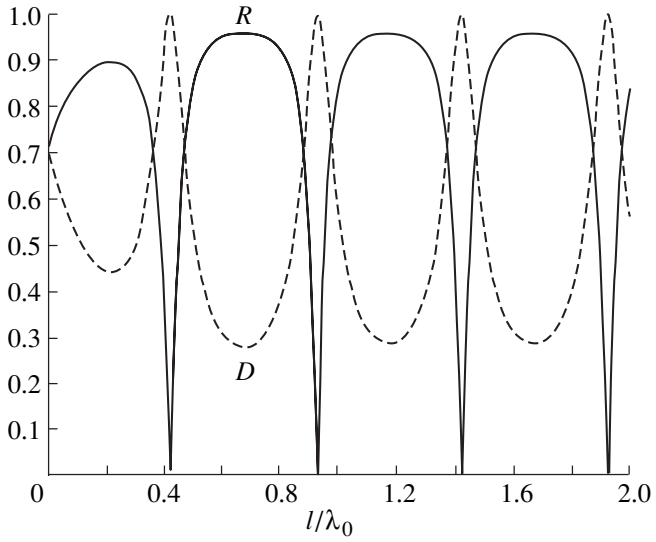

Fig. 2. Absolute values of the reflection R and transmission D coefficients for a single-channel insulator with the boundary conditions given by Eqs. (3)–(5).

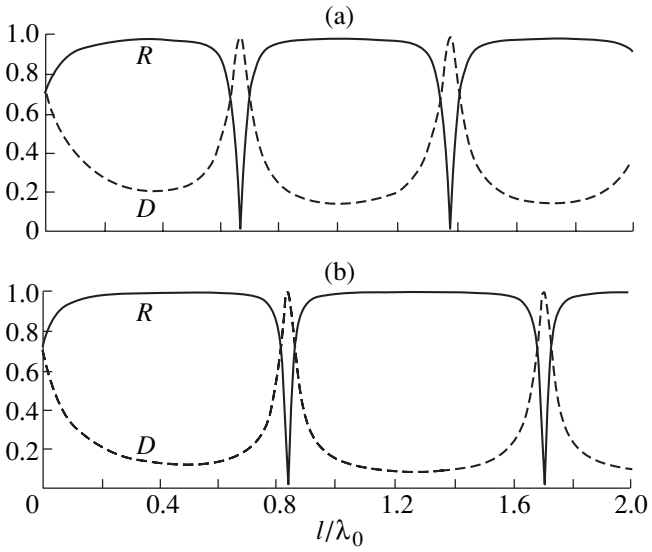

Fig. 3. Same as in Fig. 2 for a two-channel long line: (a) $h_1 = h_2 = 2h_0$ and (b) $h_1 = h_2 = 3h_0$.

It is possible to obtain the expression for the transmission coefficient $D^{(n)}$ by taking Eq. (9a) for the intersecting forces at the "left" ends of each of multichannel long line:

$$f^{(n)}(0) = Z_{11}^{(n)}(l_n)w^{(n)}(0) + Z_{12}^{(n)}(l_n)w^{(n)}(l_n);$$
$$f^{(n-1)}(l_n) = Z_{11}^{(n-1)}(l_{n-1})w^{(n-1)}(l_n) + Z_{12}^{(n-1)}(l_{n-1})w^{(n-1)}(l_{n-1});$$
$$\ldots\ldots\ldots\ldots\ldots\ldots$$
$$f^{(1)}(l_2) = Z_{11}^{(1)}(l_1)w^{(1)}(l_2) + Z_{12}^{(1)}(l_1)w^{(1)}(l_1).$$

(The value of l_1 corresponds to the "right" end of the terminal multichannel long line.)

Dividing each of these equalities by the value of the displacement at the left end of each of the multichannel long lines and taking into account the relation $w^{(k)}(l_k) = w^{(k-1)}(l_k)$, we obtain a system of equalities

$$Z_{\text{in}}^{(n)} = Z_{11}^{(n)}(l_n) + Z_{12}^{(n)}(l_n)\frac{w^{(n-1)}(l_n)}{w^{(n)}(0)};$$
$$Z_{\text{in}}^{(n-1)} = Z_{11}^{(n-1)}(l_{n-1}) + Z_{12}^{(n-1)}(l_{n-1})\frac{w^{(n-1)}(l_{n-1})}{w^{(n-1)}(l_n)};$$
$$\ldots\ldots\ldots\ldots\ldots\ldots$$
$$Z_{\text{in}}^{(1)} = Z_{11}^{(1)}(l_1) + Z_{12}^{(1)}(l_1)\frac{w^{(1)}(l_1)}{w^{(1)}(l_2)}.$$

Determining the ratios of the displacements and performing their multiplication, we obtain

$$\frac{w^{(1)}(l_1)}{w^{(n)}(0)} = \prod_{k=1}^{n}\frac{Z_{\text{in}}^{(k)} - Z_{11}^{(k)}(l_k)}{Z_{12}^{(k)}(l_k)}. \tag{17}$$

Then, taking into account Eqs. (12), we obtain the equalities

$$w^{(1)}(l_1) = Z_0 D_1^{(n)},$$
$$w^{(n)}(0) = (1+i)R^{(n)} + (1-i), \tag{18}$$

where

$$D_1^{(n)} = D^{(n)}\exp\left(ik_0\sum_{k=1}^{n} l_k\right).$$

Substituting Eqs. (18) into Eq. (17) and taking into account Eq. (15), we obtain the final expression for the transmission coefficient $D_1^{(n)}$:

$$D_1^{(n)} = \frac{2}{Z_{\text{in}}^{(n)} + Z_1}\prod_{k=1}^{n}\frac{Z_{\text{in}}^{(k)} - Z_{11}^{(k)}(l_k)}{Z_{12}^{(k)}(l_k)}. \tag{19}$$

One can easily see that, with allowance for Eq. (11), at $n = 1$, Eq. (19) transforms to Eq. (13). It is necessary to note that, deriving Eq. (19), we used the same technique as in the book by Brekhovskikh [10].

In Figures 2–4, we give illustrative examples of the characteristics of multichannel long lines of the flexural type, which were calculated by Eqs. (12) and (13). Figure 2 presents the frequency dependences of the absolute values of the reflection and transmission coefficients (R and D, respectively) for a single line of the

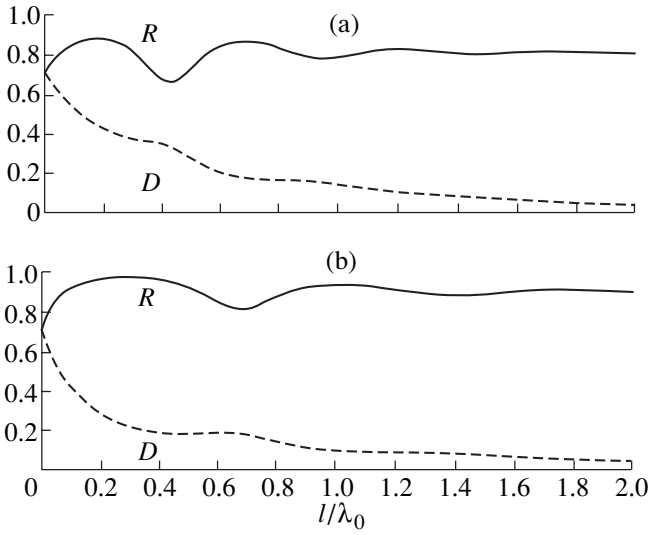

Fig. 4. Same as in Fig. 2 for a two-channel long line with internal losses $\eta = 0.2$: (a) $h_1 = h_2 = h_0$ and (b) $h_1 = h_2 = 2h_0$.

flexural type with the same parameters as the initial line (Fig. 1b). In this case, the conditions given by Eqs. (3)–(5) are set at the line ends. We note that such a model is artificial, since it is impossible to implement these conditions for a single line in practice, but this figure demonstrates a specific result caused by them. The specificity consists in the fact that, at $k_0 l = 2\pi l/\lambda_0 \longrightarrow 0$, the given quantities R and D tend not to zero and unity, respectively, which is characteristic of single long lines, but to the value 0.707. When the frequency increases, we observe their common changes due to the interference.

The same quantities for a two-channel line with the thickness of the rods constituting it $h_1 = h_2 = 2h_0$, where h_0 is the thickness of the initial line, are given in Fig. 3a. Figure 3b presents the similar data for $h_1 = h_2 = 3h_0$. One can see from comparison of these figures and also Fig. 2 that, as the thickness increases, the region of large values of R (≈ 1) extends towards high frequencies with a simultaneous decrease in the value of D.

It is possible to assume that the introduction of internal losses in multichannel long lines can improve their frequency characteristics. Figures 4a and 4b present the results for two-channel lines with the respective thicknesses $h_1 = h_2 = h_0$ and $h_1 = h_2 = 2h_0$. Internal losses in the lines are characterized by the loss coefficient η divided by the velocity of flexural waves: $c_{fl} = c_0(1 - i\eta)$. In both cases, we take the value $\eta = 0.2$. One can see from Fig. 4 that the introduction of losses "stabilizes" the value of R and causes a monotonic decrease in the value of D.

The theoretical and calculated results presented above demonstrate that, even in the case of two lines constituting a multichannel long line, it is possible to realize insulating multichannel long lines of the flexural type that have much better acoustic characteristics than analogous acoustic objects designed on the basis of single flexural lines. Specific design parameters of multichannel long lines (in particular, their cascade connection) can be determined by the calculation according to the given formulas, including the application of the optimization techniques, depending on the specific purposes.

REFERENCES

1. V. V. Tyutekin, Akust. Zh. **43**, 238 (1997) [Acoust. Phys. **43**, 202 (1997)].
2. A. I. Boĭko and V. V. Tyutekin, Akust. Zh. **45**, 454 (1999) [Acoust. Phys. **45**, 402 (1999)].
3. J. Guo, J. Pan, and C. Bao, J. Acoust. Soc. Am. **101**, 1492 (1997).
4. Z. Wu, V. K. Varadan, and V. V. Varadan, J. Acoust. Soc. Am. **101**, 1502 (1997).
5. K. Wicker and E. Arens, Acust. Acta Acust. **85**, S47 (1999).
6. C. R. Fuller and P. E. Cambou, Acust. Acta Acust. **85**, S102 (1999).
7. E. V. Korotaev and V. V. Tyutekin, Akust. Zh. **46**, 84 (2000) [Acoust. Phys. **46**, 71 (2000)].
8. *Handbook of Acoustics*, Ed. by Malkom J. Crocker (Wiley, New York, 1997).
9. V. V. Tyutekin, Akust. Zh. **46**, 809 (2000) [Acoust. Phys. **46**, 710 (2000)].
10. L. M. Brekhovskikh, *Waves in Layered Media*, 2nd ed. (Nauka, Moscow, 1973; Academic, New York, 1960).

Translated by M. Lyamshev

Acoustical Physics, Vol. 47, No. 5, 2001, pp. 623–625. Translated from Akusticheskiĭ Zhurnal, Vol. 47, No. 5, 2001, pp. 711–713.

SHORT COMMUNICATIONS

Acoustic Measurements in the Cathedral of Christ the Savior in Moscow and the Problem of Speech Intelligibility in Large Orthodox Cathedrals

M. Yu. Lannie* and V. N. Sukhov**

**All-Russia Research Institute for Television and Broadcasting, Tret'ya Khoroshevskaya ul. 12, Moscow, 123238 Russia*
e-mail: m_lannie@mail.magelan.ru

***Moscow Research and Design Institute for Culture, Leisure Sports, and Public Health Construction, Vtoraya Brestskaya ul. 29a, Moscow, 123056 Russia*

Received November 27, 2000

In the last few years, the construction of new churches and cathedrals and the reconstruction of old ones have become widespread in Russia. The most prominent example is the reconstruction of the Cathedral of Christ the Savior (CCS) in Moscow. This large building can be divided into two parts. The first part, the basement, is a new structure that contains the Council Hall and the Transfiguration Church with a volume of 8380 m^3. The acoustics of the latter was considered in a special publication [1]. The second, upper, part includes the reconstructed CCS, which is the object of this study.

The CCS is a large cathedral with a volume of 88 400 m^3. It is built on the Greek-cross plan, with each of its four sides being about 36 m in length (Fig. 1). The central section of the cathedral is covered by a dome 71 m in height. The history and architecture of the cathedral are described in many publications (e.g., [2]). The space-planning decision is schematically represented by the computer-simulated acoustic model (Fig. 2). In planning the reconstruction of the cathedral, the acoustical specialists had to find a design that would reduce the reverberation time in the hall inside the cathedral to the values providing an acceptable speech intelligibility. Unfortunately, this problem was not solved. The interior surfaces of the reconstructed room were covered with the same materials as those used in the previous cathedral (a stone floor; stone-covered

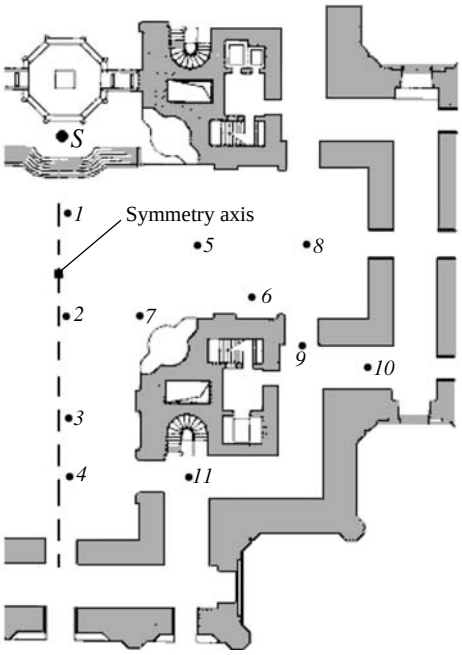

Fig. 1. Part of the cathedral plan with the points showing the positions of the measuring microphone.

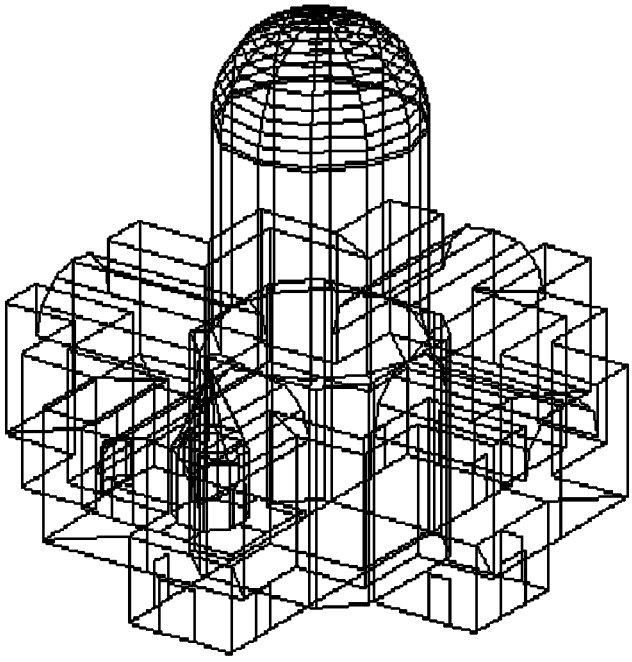

Fig. 2. Izometric representation of the CCS.

1063-7710/01/4705-0623$21.00

Table 1. Measured RASTI values

Point number (the microphone position)	Measurement conditions	
	with sound reinforcement system off	with sound reinforcement system on
1	0.57	0.44
2	0.26	0.51
3	0.24	0.49
4	0.24	0.48
5	0.36	0.44
6	0.26	0.43
7	0.24	0.47
8	0.24	0.45
9		0.27
10		0.30
11	Less than 0.20	0.30

lower parts of the walls; and plastered surfaces of the walls, arches, and the dome painted with frescoes). Thus, the CCS should be considered as an example of a large cathedral typical of the Russian architecture of the nineteenth century rather than a building constructed according to a modern architectural acoustic design.

The recent publication [3] devoted to the acoustics of the CCS presents only the measured values of the reverberation time (RT60), which is insufficient for an objective evaluation of the sound quality in the cathedral. The aim of our study is to determine speech intelligibility in the CCS. The measurements were performed when the room was empty. To determine the speech intelligibility in natural conditions, we used Bruel & Kjer equipment. A type 4225 source, which simulated a human voice, was positioned before the holy gates (point *S* in Fig. 1), and a type 4419 receiver whose display showed the RASTI values was positioned sequentially at eleven different points of the cathedral, which are also shown in Fig. 1. The results obtained after an appropriate averaging are presented in the left column of Table 1.

To determine the speech intelligibility in the case of the operation of the sound reinforcement system, a microphone was installed in front of the type 4225 source. The signal from the microphone output was supplied to the input of the system and, after an electric amplification, was transmitted by the acoustic systems. The hall was equipped with two acoustic systems produced by the DURAN company. Each system consisted of a linear set of active radiators. The loudness levels of the signal corresponded to the levels received in the case of the sound reinforcement of a church service. The measurements with the use of a type 4419 receiver were performed at the same eleven points in the same conditions. In addition, the RASTI values were measured for a test signal in the form of maximal-length sequences (MLS) generated by the SIA SMAART PRO program, which was fully installed on a computer with a professional (24 bit) VX pocket sound card (produced by the Digigram company). From the sound outputs of the card, the signal was supplied to the two acoustic systems installed in the hall. The measuring microphone was placed in turn at the same eleven points of

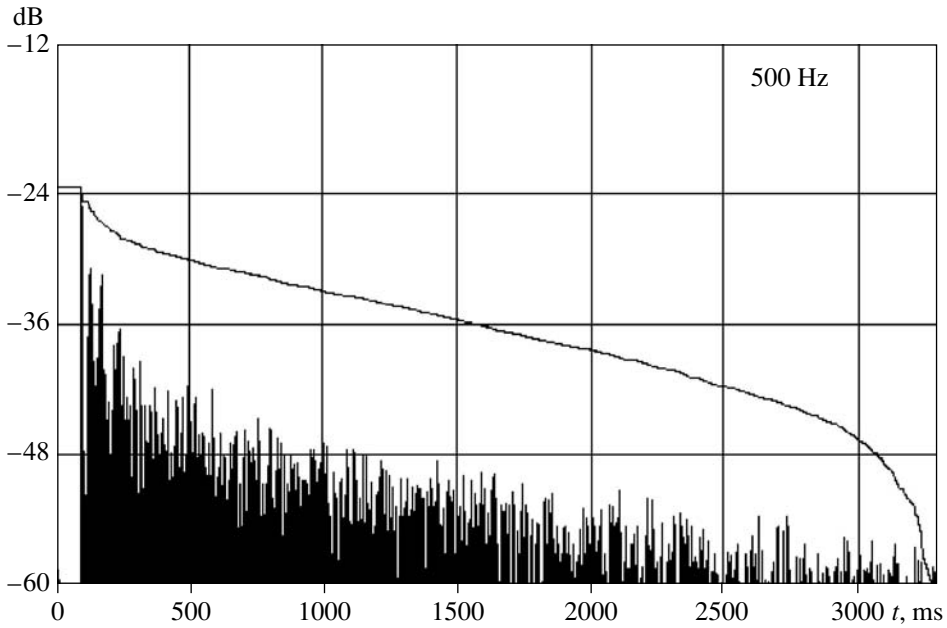

Fig. 3. Example of the impulse response of the room with the microphone placed at the point M2. The 500-Hz octave band.

Table 2. Values of the reverberation time measured in empty cathedrals (in seconds)

No.	Room	Octave band frequencies, Hz					
		125	250	500	1000	2000	4000
1	Upper church of the CCS (V = 88400 m^3)	9.6	9.1	8.7	8.3	7.2	4.2
2	Isaac Cathedral (V = 75400 m^3)	8.3	8.1	7.9	7.4	6.5	4.9
3	Kazan Cathedral (V = 40000 m^3)	6.7	6.3	5.9	5.1	4.5	4.0
4	Trinity-Izmailovo Cathedral (V = 52000 m^3)	7.0	6.6	5.9	5.0	4.5	3.5

the hall, and the signal from the microphone output was amplified and supplied to the input of the sound card, after which it was processed by the program. As a result, we calculated the RASTI values, the main acoustic parameters of the room (RT60, C80, and C50), and the structures of the sound reflections. It should be noted that both aforementioned methods of intelligibility measurements performed with the sound reinforcement system turned on provided practically identical results within admissible error. These results are presented in the right column of Table 1. The RT60 values averaged over the room are shown in row no. 1 of Table 2. Figure 3 presents a typical example of the impulse response of the cathedral.

Analyzing the results obtained from this study in comparison with the results of acoustic measurements performed earlier by M. Lannie and A. Chesnokov in the three largest cathedrals of St. Petersburg, we arrive at the following conclusions:

(1) Large Orthodox cathedrals with volumes greater than 40000 m^3 are characterized by a very long reverberation time, which tends to increase with increasing volume (see Table 2). The RT60 values far exceed the values that were recommended for Orthodox churches in [4] and included in the standard documentation [5]. The calculations show that, even when the cathedrals are full of people, the RT60 values taken at medium frequencies exceed 3 s. Such a situation is also characteristic of large churches of other confessions [6, 7].

(2) An acceptable speech intelligibility is observed only in the immediate vicinity of the priest or the chorus. At a distance of more than 10–12 m from the source, the speech intelligibility becomes unacceptable (RASTI < 0.35).

(3) When no special acoustic measures are taken to reduce the reverberation time, an acceptable speech intelligibility can be achieved only with the use of carefully designed sound amplification systems. The system installed in the CCS is a good example of using acoustic systems with narrow beams in the vertical plane. From Table 1, it follows that, even in the empty room, this system provides an acceptable intelligibility. An exception is the gallery zone (points *9–11* in Fig. 1), which is not insonified.

(4) In designing new Orthodox churches, is necessary to take special measures (which are known from practical acoustics) to reduce the reverberation time. This is important not only for large cathedrals such as the one considered above, but also for smaller churches with volumes of 5000–12000 m^3 [4]. An exception can be some of the space-planning solutions characteristic of Russian church architecture. In particular, in tent-shaped churches, when the horizontal dimensions of the room are much smaller than the height, an acceptable intelligibility (RASTI > 0.5) is obtained with relatively high RT60 values, such as ~3–4 s [8].

REFERENCES

1. M. Yu. Lannie, IN/OUT, Nos. 21–22, 13 (1997).
2. E. I. Kirichenko, *The Cathedral of Christ the Saver in Moscow* (Planeta, Moscow, 1992).
3. L. A. Borisov and Kh. A. Shchirzhetskiĭ, in *Proceedings of X Session of the Russian Acoustical Society* (Moscow, 2000), p. 17.
4. M. Yu. Lannie, A. N. Chesnokov, and Kh. A. Shchirzhetskiĭ, Akust. Zh. **44**, 498 (1998) [Acoust. Phys. **44**, 426 (1998)].
5. SP 31-103-99, *Buildings, Constructions, and Complexes of Orthodox Cathedrals* (Moscow, 2000).
6. M. K. Abdelazeez, R. N. S. Hammad, and A. A. Mustafa, J. Acoust. Soc. Am. **90**, 1441 (1991).
7. J. Brummer, Preprint No. 4248 (AES, Copenhagen, 1996).
8. M. Yu. Lannie and V. N. Sukhov, in *Proceedings of X Session of the Russian Acoustical Society* (Moscow, 2000), p. 49.

Translated by E. Golyamina

Acoustical Physics, Vol. 47, No. 5, 2001, pp. 626–628. Translated from Akusticheskiĭ Zhurnal, Vol. 47, No. 5, 2001, pp. 714–716.

SHORT COMMUNICATIONS

The Scattering of Flexural Waves Propagating in a Plate from a Chain of Resonators Mounted on It

A. D. Lapin

Andreev Acoustics Institute, Russian Academy of Sciences, ul. Shvernika 4, Moscow, 117036 Russia

e-mail: bvp@akin.ru

Received December 27, 2000

It is well known that flexural waves excited in a plate can be insulated by attaching resonators to it [1–7]. The simplest resonator has the form of a spring with a load [8–10]. Such a resonator positioned normally to the plate and connected to it by a spring causes an intense scattering of flexural waves propagating in the plate. The problem of the scattering of flexural waves by a single resonator with dissipation was solved earlier [11]. The scattering cross-section of a single resonator without dissipation is equal to $2\lambda/\pi$, where λ is the flexural wavelength. An effective means for insulating flexural waves in rods and plates are the waveguide insulators [3–6]. A waveguide insulator mounted on a plate is made in the form of an array of identical resonators fixed to the plate at small distances from each other. It is of interest to consider the problem of the scattering of a flexural plane wave propagating in a plate from a chain of resonators for any chain period in the case of an oblique incidence. Below, this problem is solved and it is shown that, when the period of the chain is less than $\frac{\lambda}{1+\sin\theta}$, where θ is the angle of incidence, the flexural wave is totally reflected from the chain.

Let a plate lie in the xy plane and identical resonators be attached to it at the points lying along the x axis: $x = x_s \equiv sL$, where $s = 0, \pm1, \pm2, \ldots$. Each resonator has a mass m and an elastic coefficient $\kappa(1 - i\varepsilon)$, where ε is the dissipation factor. From the plate $y > 0$, a harmonic flexural wave is incident on the resonators. The wave is characterized by the displacement

$$w^{(0)}(x, y, t) = A\exp[i(k_x^0 x - k_y^0 y - \omega t)], \qquad (1)$$

where k_x^0 and $-k_y^0$ are the projections of the wave vector of the incident wave on the x and y axes, respectively; A is the wave amplitude; and ω is the circular frequency. The wave causes the excitation of the resonators, and the latter generate the field $w^{(1)}(x, y, t)$. The total field w in the plate is equal to $w^{(0)} + w^{(1)}$. We denote the displacement of the load belonging to the resonator of number s (and attached to the plate at the point $(x_s, 0)$) by $w_s'(t)$. The equation of motion for this load has the form

$$m\frac{d^2 w_s'}{dt^2} = -F_s(t), \qquad (2)$$

where the force F_s is determined by the formula

$$F_s(t) = \kappa(1 - i\varepsilon)[w_s'(t) - w(x_s, 0, t)]. \qquad (3)$$

The equation for the plate connected with the resonators can be represented in the form

$$\rho\frac{d^2 w}{dt^2} + G\Delta^2 w = \sum_{s=-\infty}^{\infty} F_s(t)\delta(x - x_s)\delta(y), \qquad (4)$$

where ρ and G are the surface density and the flexural rigidity of the plate, respectively; Δ is the Laplace operator; and $\delta(y)$ is the delta-function. Since the incident wave $w^{(0)}$ is a free wave, the quantity w on the left-hand side of Eq. (4) can be replaced by $w^{(1)}$.

The structure of the scattered field is determined by the period of the scattering array (chain) of resonators, and the quantity $w^{(1)}(x, y, t)\exp(-ik_x^0 x)$ is a function periodic in x with the period L. Then, in the presence of the incident wave given by Eq. (1), the force $F_s(t)$ can be represented as

$$F_s(t) = F\exp[i(k_x^0 x_s - \omega t)], \qquad (5)$$

where F is the force amplitude at $s = 0$. The equation describing the forced harmonic vibrations of the plate can be recast as follows:

$$\Delta^2 w^{(1)} - k^4 w^{(1)} = \frac{F}{G}\exp[i(k_x^0 x - \omega t)]\delta(y)\sum_{s=-\infty}^{\infty}\delta(x - x_s), \qquad (6)$$

where $k = \left(\frac{\rho}{G}\omega^2\right)^{1/4}$ is the wave number of the flexural wave.

1063-7710/01/4705-0626$21.00

We seek the solution to Eq. (6) in the form of a Fourier series

$$w^{(1)}(x, y, t) = \exp[i(k_x^0 x - \omega t)] \times \sum_{n=-\infty}^{\infty} u_n(y) \exp\left(i\frac{2\pi}{L} n x\right). \quad (7)$$

Substituting this series into Eq. (6) and applying the inverse Fourier transform, we obtain an ordinary differential equation in $u_n(y)$:

$$\frac{d^4 u_n}{dy^4} - 2(k_x^n)^2 \frac{d^2 u_n}{dy^2} - [k^4 - (k_x^n)^4] = \frac{F}{LG}\delta(y), \quad (8)$$

where $k_x^n = k_x^0 + \frac{2\pi}{L} n$. Its solution has the form

$$u_n(y) = \frac{iF}{4k^2 LG} \times \left\{\frac{1}{k_y^n}\exp(\pm i k_y^n y) + \frac{i}{\sqrt{k^2 + (k_x^n)^2}}\exp(\mp\sqrt{k^2 + (k_x^n)^2}\, y)\right\},$$

where $k_y^n = \sqrt{k^2 - (k_x^n)^2}$; the upper and lower signs correspond to $y > 0$ and $y < 0$, respectively.

Substituting $u_n(y)$ in Eq. (7), we obtain an expression for $w^{(1)}$:

$$w^{(1)}(x, y, t) = \sum_{n=-\infty}^{\infty} \frac{iF}{4k^2 LG}\left\{\frac{1}{k_y^n}\exp[i(k_x^n x \pm k_y^n y - \omega t)] + \frac{i}{\sqrt{k^2 + (k_x^n)^2}}\exp[i(k_x^n x - \omega t) \mp \sqrt{k^2 + (k_x^n)}\, y]\right\}. \quad (9)$$

Here, the first term in the braces represents a homogeneous plane wave for $|k_x^n| < k$ and an inhomogeneous plane wave for $|k_x^n| > k$; the second term always represents an inhomogeneous wave.

We select the amplitude of the force F so as to satisfy Eq. (3). According to Eq. (2), the displacement of the load will be expressed as

$$w_s'(t) = \frac{F_s(t)}{m\omega^2} = \frac{F}{m\omega^2}\exp[i(k_x^0 x_s - \omega t)]. \quad (10)$$

Substituting Eqs. (1), (9), and (10) into Eq. (3), we derive the desired force amplitude

$$F = i\omega A \times \left\{\left[\mathrm{Re}Y + \frac{\varepsilon\omega}{\kappa(1+\varepsilon^2)}\right] + i\left[\mathrm{Im}Y + \frac{1}{m\omega} - \frac{\omega}{\kappa(1+\varepsilon^2)}\right]\right\}^{-1}, \quad (11)$$

where

$$Y = \frac{-i\omega w^{(1)}(x_s, 0, t)}{F_s(t)} = \sum_{n=-\infty}^{\infty} \frac{\omega}{4k^2 GL}\left\{\frac{1}{k_y^n} + \frac{i}{\sqrt{k^2 + (k_x^n)^2}}\right\}. \quad (12)$$

We determine the scattered field from Eq. (9) by substituting the quantity F into it. The resonance scattering occurs at the frequencies determined by the equation

$$\mathrm{Im}Y + \frac{1}{m\omega} - \frac{\omega}{\kappa(1+\varepsilon^2)} = 0.$$

At a resonance frequency, the amplitude of the nth scattered uniform spectrum (of a scattered homogeneous plane wave) is equal to

$$A_n = \frac{iF}{4k^2 GLk_y^n} = -\frac{\omega A}{4k^2 GLk_y^n}\left\{Y_1 + \frac{\varepsilon\omega}{\kappa(1+\varepsilon^2)}\right\}^{-1}, \quad (13)$$

where

$$Y_1 = \mathrm{Re}Y = \sum_s{}' \frac{\omega}{4k^2 GLk_y^s}; \quad (14)$$

the prime means that the summation is performed over all s at which k_y^s is real. The amplitude of the transmitted flexural wave is equal to $(A + A_0)$.

When the period of the chain is smaller than $\frac{\lambda}{1+\sin\theta}$, where $\theta = \arcsin\frac{k_x^0}{k}$ is the angle of the wave incidence and $\lambda = \frac{2\pi}{k}$, only the zero spectra are uniform in the scattered field (9). Then, from Eqs. (13) and (14), we derive the relations

$$Y_1 = \frac{\omega}{4k^2 GLk_y^0}, \quad A_0 = -A\left\{1 + \varepsilon\frac{4k^2 GLk_y^0}{\kappa(1+\varepsilon^2)}\right\}^{-1},$$

and the amplitude of the transmitted flexural wave is approximately equal to $\varepsilon\frac{4}{\kappa}k^2 GLk_y^0 A$. In the absence of dissipative loss in the resonators ($\varepsilon = 0$), the incident wave (1) is totally reflected from the chain of resonators.

When the period of the chain is greater than $\lambda(1 + \sin\theta)^{-1}$, the scattered field (9) contains nonzero homogeneous spectra. Then, the chain of resonators will be unable to provide an effective reflection of flexural waves.

REFERENCES

1. I. I. Klyukin, Akust. Zh. **6**, 213 (1960) [Sov. Phys. Acoust. **6**, 209 (1960)].
2. I. I. Klyukin and Yu. D. Sergeev, Akust. Zh. **10**, 60 (1964) [Sov. Phys. Acoust. **10**, 49 (1964)].
3. M. A. Isakovich, V. I. Kashina, and V. V. Tyutekin, in *Marine Instrument Making* (Acoustics Inst., Russ. Acad. Sci., Moscow, 1972), No. 1, pp. 117–125.
4. M. A. Isakovich, V. I. Kashina, and V. V. Tyutekin, USSR Inventor's Certificate No. 440509, Byull. Izobret., No. 31 (1974).
5. M. A. Isakovich, V. I. Kashina, and V. V. Tyutekin, Akust. Zh. **23**, 384 (1977) [Sov. Phys. Acoust. **23**, 214 (1977)].
6. L. S. Tsil'ker, Akust. Zh. **26**, 606 (1980) [Sov. Phys. Acoust. **26**, 336 (1980)].
7. R. J. Nagem, I. Velikovik, and G. Sandri, J. Sound Vibr. **207**, 429 (1997).
8. *Acoustics Handbook*, Ed. by Malcolm J. Crocker (Wiley, New York, 1977).
9. M. Gurgoze and H. Batan, J. Sound Vibr. **195**, 163 (1996).
10. M. Gurgoze, J. Sound Vibr. **223**, 667 (1999).
11. A. D. Lapin, Akust. Zh. **33**, 278 (1987) [Sov. Phys. Acoust. **33**, 164 (1987)].

Translated by E. Golyamina

Acoustical Physics, Vol. 47, No. 5, 2001, pp. 629–631. Translated from Akusticheskiĭ Zhurnal, Vol. 47, No. 5, 2001, pp. 717–719.

SHORT COMMUNICATIONS

The Relation between the Tangential Stresses on a Rigid Wall and the Pressure Fluctuations Generated in a Turbulent Boundary Layer

S. A. Rybak

Andreev Acoustics Institute, Russian Academy of Sciences, ul. Shvernika 4, Moscow, 117036 Russia
e-mail: bvp@akin.ru

Received August 24, 2000

Pressure fluctuations that occur in a turbulent boundary layer as a result of the nonlinear interactions between the eddy field components are the object of many theoretical and experimental studies (see, e.g., the review [1] and papers [2, 3]). At the same time, the mechanism of the linear transformation of vortex waves to longitudinal ones on a rigid or elastic wall is rather poorly understood. This paper continues our previous study [4] and considers the relation between the pressure fluctuations and the shear (viscous) stresses on the wall.

To describe the pressure field in a turbulent boundary layer, we use the Lighthill equation

$$\frac{1}{\mathbf{c}^2}\frac{\partial^2 p}{\partial t^2} - \Delta p = \frac{\partial^2}{\partial x_i \partial x_k} T_{ik}. \tag{1}$$

At the boundary, because of the adhesion condition, the nonlinear terms on the right-hand side can be considered as negligibly small, as compared to the linear viscous terms. Then, on the right-hand side of Eq. (1), we first take into account only the linear term that describes the shear viscosity:

$$T_{ik} = -\mu\left(\frac{\partial v_i}{\partial x_k} + \frac{\partial v_k}{\partial x_i} - \frac{2}{3}\delta_{ik}\frac{\partial v_s}{\partial x_s}\right) = -\sigma_{ik}, \tag{2}$$

where μ is the viscosity coefficient. One can easily see that, for the shear (eddy) component of the velocity field in which the turbulent energy is concentrated away from the wall, the right-hand side of Eq. (1) is identically equal to zero, because the condition

$$\frac{\partial v_i}{\partial x_i} = 0. \tag{3}$$

is satisfied. Hence, in a turbulent flow, the right-hand side of Eq. (1) is absent and, therefore, no generation of pressure fluctuations by viscous stresses takes place. Here, it should be noted that we consider a homogeneous liquid. If the viscous parameter $\mu(\mathbf{r})$ is inhomogeneous along the liquid flow, the above statement fails. However, the situation is different near the wall, because the reflection of the shear component from the wall leads to the generation of the longitudinal component of the velocity field $\mathbf{U}(\mathbf{x_i}, \mathbf{t})$ [4].

Using Green's function for a free space, we obtain an expression for the Fourier component $\mathbf{p}(\omega, \mathbf{x_i})$:

$$\begin{aligned} p(\omega, \mathbf{x}_i) &= \int \mathbf{G}(\omega, |x_i - y_i|)\frac{\partial^2 T_{kl}}{\partial y_k \partial y_l}\mathbf{d}^3\mathbf{y} \\ &= \oint_s \mathbf{G}\frac{\partial T_{kn}}{\partial y_k}\mathbf{ds} - \int \frac{\partial \mathbf{G}}{\partial y_k}\frac{\partial T_{kl}}{\partial y_l}\mathbf{d}^3\mathbf{y} = 0. \end{aligned} \tag{4}$$

$$\mathbf{G} = -\frac{1}{4\pi}\frac{\exp(i\mathbf{k}_0\mathbf{r})}{\mathbf{r}}; \quad \mathbf{r} = |\mathbf{x} - \mathbf{y}| \cdot k_0 = \frac{\omega}{c}. \tag{5}$$

The zero value of the right-hand side of Eq. (4) is a result of the combined contributions of the surface and volume integrals.

Now, in the surface integral in Eq. (4), we consider the contribution of the component T^l_{ik}, which corresponds to the longitudinal field component [5]:

$$T^l_{ik} = -2\mu\left(\frac{\partial u_i}{\partial y_k} - \frac{1}{3}\delta_{ik}\frac{\partial u_l}{\partial y_l}\right) - \zeta\delta_{ik}\frac{\partial u_l}{\partial y_l} = -\sigma^l_{ik} \tag{6}$$

(ζ is the second viscosity). The pressure fluctuations generated by the components of the viscous tensor T^l_{ik} are described by the expression

$$p(\omega, x_i) = \int_s \mathbf{G}(\omega, |\mathbf{x} - \mathbf{y}|)\frac{\partial T^1_{kn}}{\partial k_k}(\mathbf{ds}). \tag{7}$$

Here, the integration is performed over the wall plane.

The components of the velocity tensor can be expressed in terms of the scalar potential

$$u_i = \frac{\partial \varphi}{\partial x_i}. \tag{8}$$

1063-7710/01/4705-0629$21.00

Then, we have [5]

$$T_{ik}^{l} = -\sigma_{ik}^{l} = -2\mu\left(\frac{\partial^2\varphi}{\partial x_i \partial x_k} - \frac{1}{3}\delta_{ik}\Delta\varphi\right) - \zeta\delta_{ik}\Delta\varphi$$
$$= -\left(\lambda\delta_{ik}\Delta\varphi + 2\mu\frac{\partial^2\varphi}{\partial x_i \partial x_k}\right), \quad (9)$$
$$\lambda = \zeta - \frac{2}{3}\mu.$$

The relation between the pressure fluctuations and the potential φ is determined from the Navier–Stokes equation:

$$\rho_0\frac{\partial^2\varphi}{\partial t \partial x_i} = -\frac{\partial p}{\partial x_i} + \frac{\partial\sigma_{ik}^{l}}{\partial x_k}$$
$$= -\frac{\partial p}{\partial x_i} + (\lambda + 2\mu)\frac{\partial}{\partial x_i}\Delta\varphi, \quad (10)$$
$$p = -\rho_0\frac{\partial\varphi}{\partial t} + (\lambda + 2\mu)\Delta\varphi.$$

From Eq. (10) and the continuity equation

$$\frac{\partial p}{\partial t} = -\rho_0 c^2\Delta\varphi, \quad (11)$$

we obtain the wave equation for longitudinal waves in a viscous medium

$$c_1^2\Delta\varphi - \frac{\partial^2\varphi}{\partial t^2} = 0. \quad (12)$$

Here, the operator is

$$c_1^2 = c^2 + \frac{\lambda + 2\mu}{\rho_0}\frac{\partial}{\partial t}, \quad \left(\lambda + 2\mu = \zeta + \frac{4}{3}\mu\right). \quad (13)$$

The relation of the Fourier transform to the corresponding quantities at the wall is determined by the Kirchhoff formula [6]:

$$\varphi(\omega, x_i) = -\int_s\left(\varphi\frac{\partial}{\partial\mathbf{n}} - \frac{\partial\varphi}{\partial\mathbf{n}}\right)\mathbf{G}(\omega, |x_i - y_i|\,\mathbf{ds},$$
$$\mathbf{G} = -\frac{1}{4\pi\mathbf{r}}\exp(i\mathbf{qr}), \quad q = \frac{\omega}{c_1(\omega)}. \quad (14)$$

The derivatives in Eq. (14) are taken along the normal to the flow. It should be noted that, when an infinite plane wall represents a single boundary of the flow, Eq. (14) is replaced by a simpler expression

$$\varphi(\omega, x_i) = \int_s\varphi_n 2\mathbf{G}(\mathbf{ds}). \quad (15)$$

At the boundary $z = 0$, the resulting component of the velocity vector, which is the sum of the shear incident v_i and reflected w_i components and the longitudinal component u_i, is zero:

$$v_i + w_i + u_i = 0$$
$$v_i = v_{0i}\exp i(k_x x + k_z z), \quad (16)$$
$$w_i = w_{0i}\exp i(k_x x - k_z z), \quad u_i = u_{0i}\exp i(k_x x - q_z z).$$

In addition, the following equations are satisfied [5]:

$$k_x^2 + k_z^2 = k^2 = \frac{i\omega\rho}{\mu}, \quad (17)$$

for shear (viscous) waves and

$$k_x^2 + q_z^2 = q^2 = \frac{\omega^2}{c_1^2(\omega)}. \quad (18)$$

for longitudinal waves.

We express all velocity components at the boundary through the horizontal component of the incident shear wave by using Eqs. (16)–(18):

$$v_z = -\frac{k_x}{k_z}v, \quad w_x = \frac{-k_z q_z + k_x^2}{\Delta}\frac{v}{u},$$
$$w_z = \frac{k_x}{k_z}w_x, \quad u_x = ik_x\varphi = \frac{-2k_x^2}{\Delta}v, \quad (19)$$
$$u_z = -iq_z\varphi = \frac{2k_x q_z}{\Delta}v, \quad v = v_x, \quad \Delta = k_z q_z + k_x^2.$$

Now, it is easy to relate the fluctuations of shear stresses on the wall to the potential φ:

$$\sigma_{iz} = \sigma_{iz}^{t}(v) + \sigma_{iz}^{t}(w) + \sigma_{iz}^{l}(u). \quad (20)$$

Using Eqs. (2), (6), (9), (10), (18), and (19), we derive

$$\sigma_{xz}^{t}(v) = i\frac{\mu}{k_z}(k_z^2 - k_x^2)v, \quad \sigma_{xz}^{t}(w) = \frac{k_z q_z - k_x^2}{\Delta}\sigma_{xz}^{t}(v), \quad (21)$$
$$\sigma_{xz}^{l}(u) = 2\mu k_x q_z\varphi, \quad \varphi = i\frac{2k_x}{\Delta}v, \quad p = i\rho_0\omega\frac{c^2}{c_1^2}\varphi.$$

Combining all three components of σ_{xz} according to Eq. (20), we obtain

$$\sigma_{xz} = -\frac{2\rho_0\omega q_z}{\Delta}v = \frac{i\omega\rho_0 q_z}{k_x}\varphi = \frac{q_z}{k_x}\frac{c_1^2}{c^2}p. \quad (22)$$

Using Eq. (22), we can determine the pressure fluctuations generated by the shear stresses arising on the wall in a turbulent boundary layer:

$$p(\omega, k_x q_z) = \frac{k_x}{q_z}\frac{c^2}{c_1^2}\sigma_{xz}(\omega, k_{x,} k_{z,} q_z). \quad (23)$$

Relationship (23) expresses the pressure fluctuations directly and exclusively through the tangential stresses on the wall, and the correlation structure of these

stresses can be measured in the experiment (see [7]). Thus, the relation between the pressure fluctuations in a turbulent boundary layer and the fluctuations of the tangential stresses has now become more evident, as compared to previous publications (see e.g. [8]).

The expressions obtained above can be easily generalized to the case of the incidence of a plane wave at an arbitrary angle ϕ to the Cartesian coordinate system in the XY plane. For this purpose, we apply the following substitutions:

$$\begin{aligned} k_x &\longrightarrow k_x\cos\phi + k_y\sin\phi = k_l, \\ k_x &= k_l\cos\phi, \quad k_y = k_l\sin\phi \\ k_x v &\longrightarrow k_l v_l, \quad \sigma_{xz}k_x \longrightarrow \sigma_{xz}k_x + \sigma_{yz}k_y. \end{aligned} \tag{24}$$

The relation between the spectral intensity of the wall pressure fluctuations and the spectral intensity of the components of the viscous stress tensor follows from Eq. (23):

$$\begin{aligned} &\langle p(\omega, k_x, k_y, q_z)p^*(\omega, k_x, k_y, q_z)\rangle \\ &\quad = \left|\frac{1}{q_z}\frac{c^2}{c_1^2}\right|^2 \langle |k_x\sigma_{xz} + k_y\sigma_{yz}|^2\rangle. \end{aligned} \tag{25}$$

Here, the quantities σ_{iz} are determined according to Eqs. (20)–(23).

We note that viscous stresses also occur at a compliant boundary, e.g., when the boundary is represented by an elastic plate. In this case, the flexural and longitudinal vibrations of the plate are determined by the set of the components of the viscous stress tensor σ_{iz}, according to the right-hand sides of Eqs. (14) from our previous publication [9]:

$$\begin{aligned} Z_W W &= \sigma_{zz} - p - \frac{ik_x h}{2}\sigma_{xz}, \\ Z_W &= \frac{Eh^3}{12(1-\nu^2)}k_x^4 - \rho h\omega^2, \\ Z_U U &= \sigma_{xz} - \frac{\nu}{1-\nu}ik_x h(\sigma_{zz} - p), \\ Z_U &= \frac{Eh}{1-\nu^2}k_x^2 - \rho h\omega^2. \end{aligned} \tag{26}$$

Here, ν is the Poisson ratio. Relationships (26) refer to the Fourier components of the longitudinal U and transverse W displacements of the plate. In this case, the right-hand sides of Eqs. (16) should involve the quantities $i\omega U$ for the horizontal components of the velocity field and $i\omega W$ for the vertical ones.

All quantities derived above can also be determined in the case of the elastic wall by using Eqs. (26). In particular, the amplitude of the wall pressure fluctuations will have the form

$$p = -\rho\omega\frac{2k_x v - i\omega(-k_x U + k_z W)}{\Delta}\frac{c^2}{c_1^2}. \tag{27}$$

If we subject the elastic wall to additional external stresses, σ_{zz}^1 and σ_{xz}^1, so as to make the numerator of Eq. (27) equal to zero, the corresponding Fourier component of the pressure fluctuations $p(\omega, \mathbf{k})$ will also become zero. If the stresses satisfy the conditions

$$\begin{aligned} \sigma_{zz}^1 &= -\sigma_{zz} + p, \\ \sigma_{xz}^1 &= -\sigma_{xz}, \end{aligned}$$

the longitudinal and transverse vibrations of the elastic wall, $\underline{U}$ and W, will be zero for the same component $(\omega, \mathbf{k})$.

Obviously, the possibility of such a compensation in a given frequency band requires special analysis.

ACKNOWLEDGMENTS

This work was supported by the Russian Foundation for Basic Research (project no. 99-02-16161a) and the INTAS (project no. 99-0088).

REFERENCES

1. A. Powell, J. Vibr. Acoust. **112**, 145 (1990).
2. M. A. Hove and P. L. Shah, J. Acoust. Soc. Am. **99**, 3401 (1996).
3. S. Glegg, J. Acoust. Soc. Am. **107**, 2823 (2000).
4. K. A. Naugol'nykh and S. A. Rybak, Tr. Akust. Inst. Akad. Nauk SSSR, No. 16, 129 (1971); Akust. Zh. **26**, 890 (1980) [Sov. Phys. Acoust. **26**, 502 (1980)].
5. L. D. Landau and E. M. Lifshitz, *Course of Theoretical Physics*, Vol. 6: *Fluid Mechanics* (Nauka, Moscow, 1986; Pergamon, New York, 1987), Chap. 2.
6. H. Hönl, A. W. Maue, and K. Westpfahl, *Theorie der Beugung* (Springer, Berlin, 1961; Mir, Moscow, 1964), Chap. 1.
7. B. M. Efimtsov and V. A. Sysoev, Akust. Zh. **43**, 358 (1997) [Acoust. Phys. **43**, 307 (1997)].
8. A. G. Shustikov, Akust. Zh. **29**, 693 (1983) [Sov. Phys. Acoust. **29**, 409 (1983)].
9. S. A. Rybak and B. D. Tartakovskiĭ, Akust. Zh. **9**, 66 (1963) [Sov. Phys. Acoust. **9**, 51 (1963)].

Translated by E. Golyamina

Acoustical Physics, Vol. 47, No. 5, 2001, p. 632. Translated from Akusticheskiĭ Zhurnal, Vol. 47, No. 5, 2001, p. 720.

INFORMATION

XII Session of the Russian Acoustical Society and the IX Workshop on Ocean Acoustics Dedicated to the 85th Birthday of Academician L.M. Brekhovskikh

The session and the workshop will be held May 27–30, 2002, in the Large Conference Hall of the Shirshov Institute of Oceanology of the Russian Academy of Sciences, Nakhimovskiĭ pr. 36, Moscow.

Organizing committee:

L.M. Brekhovskikh—Honorary Chairman

N.A. Dubrovskiĭ—Chairman

Yu.A. Chepurin—Vice Chairman

O.A. Godin—Vice Chairman

E.V. Yudina—Vice Chairman for Organizational Problems

V.M. Tarasenko—Organizing Secretary

V.S. Gostev—Technical Secretary

Program Group:

I.B. Andreeva—Chairman

A.V. Furduev—Vice Chairman

E.A. Kopyl

Yu.P. Lysanov

V.V. Goncharov

Scope:

Sound propagation in the ocean

Acoustic tomography

Ambient noise in the ocean

Scattering and reflection of sound

Signal processing

Acoustic methods and means for ocean studies

Oceanological characteristics important for underwater acoustics

Ecological aspects of underwater acoustics

Deadlines:

November 1, 2001: Submission of the abstracts of papers. An abstract should not exceed 200 words. The authors are requested to indicate the corresponding scope item.

December 1, 2001: Decision of the Organizing Committee about the list of accepted papers. Simultaneously, the authors will receive directions for the paper layout.

January 1, 2002: Submission of the papers.

Address:

Organizing Committee of the Workshop on Ocean Acoustics, Shirshov Institute of Oceanology, Russian Academy of Sciences, Nakhimovskiĭ pr. 36, Moscow, 117851 Russia

Tel: (095) 129-1936; (095) 126-9835

Fax: (095) 124-5983; (095) 126-0100

e-mail: rav@rav.sio.rssi.ru

Web: http://rav.sio.rssi.ru/school9.html

Information:

The speakers can apply for the support of travel expenses and lodging (the support will be limited and distributed by the Organizing Committee).

It is recommended that the authors submit the abstracts of papers through e-mail in the form of MS-Word files with the Times New Roman font.

All information about the event, as well as the news and the current status, can be found on the Internet:

http://rav.sio.rssi.ru/school9.html

The proceedings of the IX Workshop on Ocean Acoustics are planned to be published by the beginning of the event with the abstracts given in Russian and in English.

The authors will be given the proceedings free of charge.

The full text of the papers in Russian will show up on Internet. The English versions of the papers, if any will be presented by the authors, can also be located on Internet.

The Organizing Committee will appreciate your transferring the information on the IX Workshop on Ocean Acoustics to your colleagues.

1063-7710/01/4705-0632$21.00 © 2001 MAIK “Nauka/Interperiodica”